Quark localization and the Anderson transition in lattice quantum chromodynamics

JUSTUS-LIEBIG-UNIVERSITÄT GIESSEN

Institut für Theoretische Physik

Zur Erlangung des Grades
eines Doktors der Naturwissenschaften
(Dr. rer. nat)

vorgelegte Dissertation von

M.Sc. Lukas Holicki
aus Darmstadt

Referent: Prof. Dr. Lorenz von Smekal
Korreferent: Prof. Dr. Christian S. Fischer

Tag der Einreichung: 02.04.2019
Tag der Prüfung: 16.05.2019

Für meine Eltern.

Selbstständigkeitserklärung

Ich erkläre: Ich habe die vorgelegte Dissertation selbstständig und ohne unerlaubte fremde Hilfe und nur mit den Hilfen angefertigt, die ich in der Dissertation angegeben habe. Alle Textstellen, die wörtlich oder sinngemäß aus veröffentlichten Schriften entnommen sind, und alle Angaben, die auf mündlichen Auskünften beruhen, sind als solche kenntlich gemacht. Ich stimme einer evtl. Überprüfung meiner Dissertation durch eine Antiplagiat-Software zu. Bei den von mir durchgeführten und in der Dissertation erwähnten Untersuchungen habe ich die Grundsätze guter wissenschaftlicher Praxis, wie sie in der "Satzung der Justus-Liebig-Universität Gießen zur Sicherung guter wissenschaftlicher Praxis" niedergelegt sind, eingehalten.

Gießen, den 02.04.2019

(Lukas Holicki)

Zusammenfassung

Die Erforschung der fermionischen Eigenschaften stark wechselwirkender Quantenfeldtheorien ist von fundamentaler Bedeutung für unser Verständnis der grundlegenden Prinzipien der Physik. Die Lösungen der Dirac-Gleichung, die Quark-Wellenfunktionen, zeigen überraschenderweise ein Lokalisierungsverhalten bei niedrigen Energien, das sehr ähnlich dem Verhalten von Elektronen in ungeordneten Festkörpern ist.

Zuerst werden wir das Lokalisierungsphänomen in der Quantenchromodynamik (QCD) auf dem Gitter studieren, wobei wir eine gemischte Wirkung aus Twisted-Mass-Wilson-Fermionen als Seequarks und Overlap-Fermionen, wegen ihrer chiralen Eigenschaften, als Valenzquarks benutzen. Wir diagonalisieren den Dirac-Operator in einem weiten Temperaturbereich in der chiral restaurierten Phase, und extrahieren die Delokalisierungsenergie, die "Mobilitätskante", die eine lineare Temperaturabhängigkeit aufweist und am chiralen Übergang verschwindet. Wir identifizieren eine Analogie zwischen der Verteilung des Polyakov Loops und dem ungeordneten Potential des Anderson-Modells in kondensierter Materie, da die niederliegenden Moden in Senken der lokalen Polyakov-Linie lokalisiert sind.

Wir untersuchen dann die topologischen Eigenschaften von QCD bei endlicher Temperatur und den Effekt von Gradient Flow auf topologische Invarianten. Wir finden, dass die Diskrepanz zwischen der gluonischen und der fermionischen Definition bei endlicher Flow-Zeit im Wesentlichen überwunden wird, und dass lokalisierte Quarkmoden topologische Ladung tragen. Außerdem suchen wir nach lokal selbstdualen Objekten in den Eichfeldkonfigurationen, wie zum Beispiel Instantonen, Caloronen oder Dyonen.

Desweiteren untersuchen wir Zweifarb-QCD (QC$_2$D) bei endlichem chemischen Potential mit Staggered Quarks, und zeigen, dass der korrekte Kontinuumslimes dieser speziellen Diskretisierungsmethode erhalten ist. Die anti-unitäre Symmetrie des Dirac-Operators restauriert, wenn die Diskretisierungsartefakte aus der Bulk-Phase reduziert werden. Wir bilden den Diquark-Onset ab und präsentieren die Eigenmoden des Staggered-Operators bei endlichem chemischen Potential. Wir beobachten, dass das endliche μ sowohl Lokalisierung als auch Niveauabstoßung unterdrückt.

Wir beschließen diese Arbeit mit einer Untersuchung von QC$_2$D mit Overlap-Seequarks vor einem Hintergrund reiner Eichtheorie bei endlicher Temperatur. Wir bilden ebenfalls die Temperaturabhängigkeit der Mobilitätskante dieser Theorie ab und finden ein lineares Verhalten bei großen Temperaturen, ähnlich wie in QCD, aber beobachten auch die Anwesenheit eines Krümmungsterms in der Nähe des Deconfinement-Übergangs. Wir schließen mit der Beobachtung, dass der Polyakov Loop wieder die Rolle eines Unordnungsterms spielt, der Lokalisierung verursacht.

Abstract

The exploration of the fermionic features of strongly interacting quantum field theories is of fundamental importance for our understanding of the basic principles of physics. The solutions to the Dirac equation, the quark wave functions, surprisingly show a localization behaviour at low energies, which is very similar to the behaviour of electrons in disordered solids.

Firstly, we will study this localization phenomenon in quantum chromodynamics (QCD) on the lattice using a mixed lattice action of twisted mass Wilson fermions as sea quarks and overlap fermions as valence quarks, due to their chiral properties. We diagonalize the overlap Dirac operator for a wide temperature range in the chirally restored phase and extract the delocalization energy, the "mobility edge", which exhibits a linear temperature dependence and vanishes at the chiral transition. We identify an analogy between the Polyakov loop distribution and the disordered potential from the Anderson model of condensed matter, as the low-lying modes are localized in sinks of the local Polyakov line.

We then study the topological features of finite temperature QCD and the effect of gradient flow on topological invariants. We find, that the discrepancy between the gluonic and the fermionic definition are mostly remedied at finite flow time and that localized quark modes carry topological charge. We also scout for local selfdual objects within the gauge configurations, such as instantons, calorons, or dyons.

Furthermore we study two-colour quantum chromodynamics (QC$_2$D) at finite chemical potential with staggered quarks and show that the correct continuum limit of this particular discretization method is maintained. The anti-unitary symmetry of the Dirac operator is restored when the discretization artifacts from the bulk phase are reduced. We map the diquark onset and present the eigenmodes of the staggered operator at finite chemical potential. We observe that finite μ both counteracts localization and level repulsion.

We conclude this work with an investigation of QC$_2$D with overlap sea quarks on a background of a pure gauge theory at finite temperature. We also map the temperature dependence of the mobility edge in this theory and find a linear behaviour at large temperatures, similar to QCD, but also observe the presence of some curvature term close to the deconfinement temperature. We close with the observation that the Polyakov loop plays the role of a disorder term here as well, thus causing localization.

Contents

1. Introduction 1

1.1. QCD in the continuum . . . 3
1.2. QCD on the Lattice . . . 4
    1.2.1. Lattice gauge transporters . . . 5
    1.2.2. Wilson's plaquette action . . . 5
    1.2.3. Symanzik's rectangle action . . . 6
    1.2.4. Iwasaki's renormalization group improved action . . . 7
    1.2.5. The continuum limit and the physical scale . . . 8
    1.2.6. Lattice fermions . . . 9
    1.2.7. Finite chemical potential on the lattice . . . 10
    1.2.8. The lattice path integral for QCD . . . 11
1.3. Chiral symmetry . . . 12
    1.3.1. Chiral symmetry on the lattice and the Ginsparg-Wilson relation . . . 13
    1.3.2. Domain wall fermions . . . 14
    1.3.3. The overlap operator . . . 16
1.4. Monte Carlo simulations of lattice QCD . . . 17
    1.4.1. The hybrid Monte Carlo method . . . 17
    1.4.2. HMC with fermions . . . 18
    1.4.3. The sign problem of QCD at finite chemical potential . . . 19
1.5. Gradient flow . . . 19
    1.5.1. Yang-Mills gradient flow at small gauge coupling . . . 21
    1.5.2. Renormalization . . . 22
    1.5.3. Gradient flow on the lattice . . . 22
    1.5.4. Setting the scale with gradient flow . . . 23
1.6. Chiral random matrix theory for Euclidean QCD . . . 24
1.7. The Anderson model for disordered solids . . . 26

2. The QCD Anderson transition 29
2.1. Lattice setup . . . 29
    2.1.1. Configurations . . . 29
    2.1.2. Eigenmode projection . . . 30
2.2. The Banks-Casher gap . . . 32
2.3. The temperature dependence of the mobility edge . . . 34
2.4. Morphology of quark wave functions . . . 42
    2.4.1. Fractal dimensions . . . 42
    2.4.2. The distribution of the chiral density . . . 46
    2.4.3. Moments of eigenmodes . . . 55
    2.4.4. Chirality overlap . . . 57
    2.4.5. Morphological properties of quark eigenmodes . . . 58
2.5. Unfolded level spacing distributions . . . 60
2.6. Localization through Polyakov loops . . . 63
    2.6.1. Smoothing the gauge configurations with gradient flow . . . 64
    2.6.2. Polyakov line clusters . . . 64

2.6.3. Local correlations with quark modes 67
2.7. Summary 74

3. The topological structure of QCD **75**
3.1. Topology and the Anderson transition 77
3.2. Gradient flow and topological structure 77
3.3. Topological overlap with quark wave functions 82
3.4. Local self-duality 85
3.5. Summary 89

4. Localization in two-colour QCD **91**
4.1. Anti-unitary symmetry of fundamental and adjoint QC_2D 92
4.2. The action of QC_2D with diquark sources 93
4.3. Bulk artifacts and the continuum limit 94
4.4. Zero temperature QC_2D with staggered quarks 97
4.4.1. Lattice setup 97
4.4.2. The Wigner-Dyson class of staggered QC_2D 97
4.4.3. The diquark condensation transition 99
4.4.4. Quark modes at finite chemical potential 103
4.5. Quenched QC_2D at finite temperature 107
4.5.1. Fixed scale without physical parameters 107
4.5.2. Lattice setup 108
4.5.3. Finite size effects 109
4.5.4. The Banks-Casher gap 111
4.5.5. The mobility edge 113
4.5.6. The unfolded level spacing distribution 116
4.5.7. Localization and the Polyakov loop 118
4.6. Summary 120

5. Conclusion **121**

Appendix A. Generating gauge configurations **123**
A.1. Local update algorithms 123
A.2. Hybrid Monte Carlo and equations of motion in molecular dynamics 123
A.2.1. Gauge sector 124
A.2.2. Molecular dynamics with pseudofermions 125
A.2.3. Dynamical staggered quarks 125
A.2.4. Dynamical Wilson quarks 126
A.2.5. Dynamical domain wall quarks 127
A.3. Rooting 127
A.3.1. The multishift conjugate gradient solver 128
A.3.2. The Remez exchange algorithm 129
A.4. Symplectic integrators 131
A.5. Gradient flow 131

Appendix B. Implementation of the overlap operator **133**
B.1. Chebyshev polynomials 133
B.2. Zolotarev approximation 134
B.3. Projection to the low eigenmodes of the kernel operator 134

Bibliography **135**

While the results presented in this thesis are the author's original work, some are obtained in collaboration with other authors. The results presented in Chapter 2 are partly published in [1]. A further publication based on the Chapters 2 and 3 will follow subsequently to this thesis. Some of the results in Chapter 4 are published in [2] and [3].

1. Introduction

The standard model of particle physics is one of the most successful and extensively reviewed theories in physics. It incorporates three of the four fundamental forces in nature and their local gauge symmetries: The electromagnetic interaction with the gauge group $U(1)$, the weak nuclear force with the gauge group $SU(2)$ and the strong interaction between quarks and gluons with the gauge group $SU(3)$. The local symmetry group of the contemporary standard model is hence

$$U(1) \times SU(2) \times SU(3). \tag{1.1}$$

However, the grand unification of the standard model with gravitation was not yet achieved. It must further be extended to describe finite neutrino masses, dark matter and dark energy, and there are hints to physics beyond the standard model e.g. from the anomalous magnetic moment of the muon [4]. The generation of mass by the Higgs-mechanism [5] has been included in the standard model recently.

This work is dedicated to the study of the quantum field theory of the strong interaction, *quantum chromodynamics* (QCD), and theories similar to it. QCD is a Yang-Mills theory with the gauge group $SU(N_c)$, where the N_c is the dimension of the fundamental representation. The non-Abelian nature of this group gives rise to gluon self-interactions. Furthermore, QCD is strongly coupled, which makes a perturbative treatment of the path integral impossible.

Typically the gauge field interactions in QCD are too strong for a perturbative treatment of the theory. In fact QCD contains a number of non-perturbative phenomena, such as confinement, the spontaneous breaking of chiral symmetry or the colour-superconductivity at large densities. K. G. Wilson used a lattice regularisation in 1974 to show that at large bare couplings lattice Yang-Mills theories are confining. The effective couplings and the relevant degrees of freedom, however, are scale dependent. The *running coupling* ensures simultaneously the existence of asymptotic freedom and confinement. In 1973 Wilczek and Politzer [6] and Gross [7] showed that strong interaction dynamics based on non-Abelian gauge theories leads to Bjorken scaling.

At large energies (or small length scales respectively) the coupling of QCD is small, which guarantees the renormalizability of QCD, as it is applicable to any energy regime.

At lower energies ($\Lambda_{\mathrm{QCD}} \approx 250$ MeV) the theory becomes non-perturbative. In this energy regime QCD is a theory of mesons and baryons since the quarks become locked into hadrons. This is called confinement, the chromoelectric flux is entirely concentrated between two quarks which causes a linearly rising potential between colour sources. Chiral perturbation theory, as opposed to a perturbative treatment of QCD, is a successful tool to study the hadronic structure of QCD at low energies [8].

Most features of the QCD phase diagram in the temperature-density plane are known from effective theories and functional methods. A sketch of the conjectured phase diagram is shown in Figure 1.1.

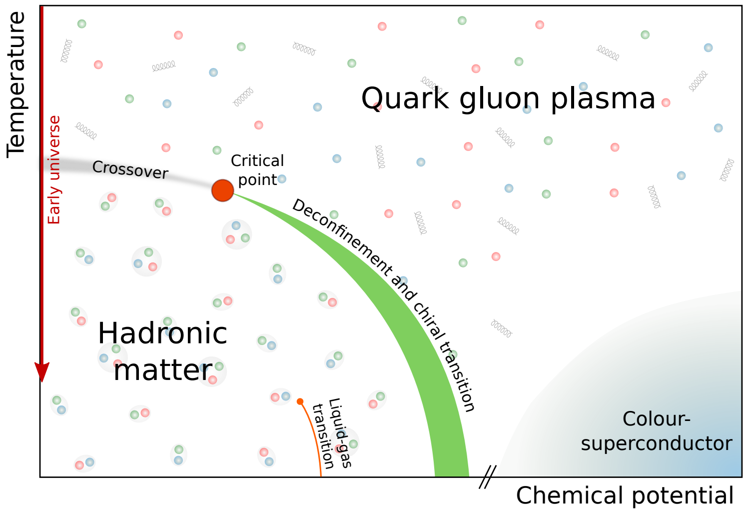

Figure 1.1.: The conjectured phase diagram of quantum chromodynamics in the temperature-chemical potential plane.

At low temperatures and chemical potential all degrees of freedom are locked inside of hadrons. In the quark-gluon plasma, at large temperatures, there are no bound hadronic states [9]. The temperature axis at vanishing baryon chemical potential reflects the situation of the early universe, with a perfect symmetry between matter and anti-matter. At $\mu = 0$ the deconfinement and chiral transition are rapid crossovers, with a transition temperature $T_c \approx 155$ MeV [10]. At intermediate μ a critical endpoint connects the crossover region with a first order phase transition that separates the hadronic phase from the quark gluon plasma. Within the hadronic phase at low temperatures there is a first order nuclear liquid-gas transition. At very large μ, outside the hadronic phase, a colour-superconducting phase is expected [11].

Chiral symmetry is spontaneously broken in the hadronic phase, such that the masses of parity partners are non-degenerate and a chiral condensate is formed. The Goldstone modes of this spontaneous symmetry breaking are the pions, whose light mass is caused by the explicit symmetry breaking by the finite quark mass.

Below the deconfinement transition the centre symmetry is almost conserved and the Polyakov loop, the trace of the static quark propagator, is approximately vanishing. In the quenched limit, the Polyakov loop has the role of the order parameter of the deconfinement transition, whereas in the presence of fermions the centre symmetry is explicitly broken.

Experimentally the phase structure of QCD is being explored in accelerator facilities and deep inelastic scattering experiments in heavy ion collisions, for example at the ALICE experiment at the *Large Hadron Collider* (LHC) at CERN in Geneva, Switzerland [12], the *Relativistic Heavy Ion Collider* (RHIC) at the BNL in Brookhaven, USA [13], the *Nuclotron-based Ion Collider fAcility* (NICA) at the JINR in Dubna, Russia [14], or the *Facility for Antiproton and Ion Research* (FAIR) at GSI in Darmstadt, Germany [15]. These experiments target both the hadronic region of the phase diagram and the quark gluon plasma phase and attempt to verify the existence of the critical endpoint.

Theoretical approaches to QCD also have a longstanding history. Perturbative QCD is only applicable in the small coupling regime of the phase diagram. As an ab-initio method to study QCD at an infrared scale, *lattice QCD* has proven to be an invaluable tool. It provides precise predictions of hadron masses [16] and the extraction of hadron form factors for electromagnetic and strong decays [17]. Also nucleon scattering phases can be computed [18] using a generalization of Lüscher's finite volume method.

However, lattice calculations typically suffer from the sign problem, which renders the $\mu > 0$

sector inaccessible to lattice Monte Carlo integration techniques. Effective models, however, allow predictions for the $\mu > 0$ regime, like the Polyakov-loop enhanced Nambu-Jona-Lasinio (PNJL) model, which incorporates both chiral symmetry restoration and a deconfinement transition [19,20], the Polyakov-quark-meson models as effective theories for QCD [21] and two-colour QCD [22,23], and Dyson-Schwinger calculations [24]. A comprehensive review on the phase diagram of QCD and the properties of QCD at finite temperature from a Dyson-Schwinger approach is given in [25].

Also the *complex Langevin* method [26,27] and the integration over *Lefshetz thimbles* [28,29] have shown promising results.

This work is organized as follows: In Chapter 1 the theoretical background and the basic concepts, which are relevant to this work, are introduced. Chapter 2 is dedicated to the eigenmodes of the Dirac operator in QCD at finite temperature, their localization properties and the QCD Anderson transition, which separates the spectral regime of extended quark modes from the localized ones. Chapter 3 presents the topological structure of finite temperature QCD and 4 discusses two-colour QCD, both at finite chemical potential in the low temperature sector and at finite temperature. Our findings are concluded in Chapter 5.

1.1. QCD in the continuum

In their seminal paper from 1954 [30] Yang and Mills presented a generalization of Quantum Electrodynamics (QED) to non-Abelian gauge fields without any external fields. These theories are thus called *Yang-Mills theories.* The action of a Yang-Mills theory is invariant under local non-Abelian transformations and the covariant derivative is given by

$$D_\mu(x) = \left(\partial_\mu + iA_\mu(x)\right), \tag{1.2}$$

where the local gauge field $A_\mu(x) \in su(N_c)$ acts as a Christoffel symbol. Analogous to QED, the field strength tensor is given by

$$F_{\mu\nu} = -i\left[D_\mu(x), D_\nu(x)\right] = \partial_\mu A_\nu(x) - \partial_\nu A_\mu(x) + i\left[A_\mu(x), A_\nu(x)\right]. \tag{1.3}$$

The Lagrangian of a Yang-Mills theory with dynamical fermions is then

$$\mathcal{L}[A] = -\frac{1}{4}\operatorname{tr}\left(F_{\mu\nu}F^{\mu\nu}\right) - \overline{\psi}(i\gamma_\mu D^\mu - m)\psi. \tag{1.4}$$

The quantization of a $(d+1)$-dimensional Yang-Mills theory can be done using the path integral formalism, where classical fields become operators and the classical solution is the minimum of the action

$$S = \int d^{d+1}x\mathcal{L}[A]. \tag{1.5}$$

The generating functional of the theory not only contains the classical solution, but integrates over the complete phase space of the degrees of freedom in the theory, thus including any quantum fluctuation like

$$Z = \int \mathcal{D}A\mathcal{D}\psi\mathcal{D}\overline{\psi}e^{iS[A,\psi,\overline{\psi}]}. \tag{1.6}$$

Time-ordered expectation values of observables are now given by the path integral

$$\langle T\mathcal{O}\rangle = \frac{1}{Z}\int \mathcal{D}A\mathcal{D}\psi\mathcal{D}\overline{\psi}\mathcal{O}[A]e^{iS[A,\psi,\overline{\psi}]}. \tag{1.7}$$

In Minkowski space the measure $\mathcal{D}A\mathcal{D}\psi\mathcal{D}\overline{\psi}e^{iS_{\text{YM}}}$ is highly oscillating. This is unfeasible for numerical calculations, where one would wish for the states of the theory to be localized in one region of the phase space. It is therefore common to perform a so-called *Wick-rotation*, where the time coordinate is rotated to the imaginary axis $t \mapsto i\tau$. The metric $g_{\mu\nu} = \delta_{\mu\nu}$ thus becomes Euclidean and there is no distinction between co- and contravariant indices anymore. The Minkowskian Yang-Mills action then changes to

$$S \mapsto iS_{\mathrm{E}} = i\frac{1}{4}\int d\tau \int d^d x \mathcal{L}_E, \tag{1.8}$$

with the Lagrangian

$$\mathcal{L}_E[A] = \frac{1}{4}\operatorname{tr}\left(F_{\mu\nu}F_{\mu\nu}\right) + \overline{\psi}(\gamma_\mu D_\mu + m)\psi. \tag{1.9}$$

The Euclidean γ-matrices obey $\left\{\gamma_\mu, \gamma_\nu\right\} = 2\delta_{\mu\nu}$.

The convenience of this trick originates in the fact that the generating functional of the Euclidean theory has the form of a thermodynamical partition function with an exponentially decreasing probability weight, the Boltzmann factor e^{-S_E}. It is therefore possible to assign a temperature to the system by identifying the inverse temperature $\beta_T = \frac{1}{t}$, where T is the extent of the compact time integral in the action,

$$Z = \int \mathcal{D}A\mathcal{D}\psi\mathcal{D}\overline{\psi}\exp\left(-\int_0^{\beta_T} dt \int d^d x \mathcal{L}_E\right). \tag{1.10}$$

In order to obtain physical quantities from Euclidean expectation values, one has to perform an analytic continuation to real time, e.g. with the maximum entropy method [31] or Bayesian reconstruction [32].

Since Yang-Mills theories are non-Abelian generalizations of QED, the field theory of the strong interaction of N_c colour charges is constructed as a Yang-Mills theory with the gauge group

$$SU(N_c) = \left\{\Omega \in \mathbb{C}^{N_c} \times \mathbb{C}^{N_c}, \Omega^\dagger = \Omega^{-1}, \det\Omega = 1\right\}. \tag{1.11}$$

The degrees of freedom of this theory are the gauge fields $A_\mu^{c,d}(x)$, which describe the gluons, and the N_f Grassmann-valued fermionic fields $\overline{\psi}^f(x)_{\alpha,c}$ and $\psi^f(x)_{\alpha,c}$. Here greek letters indicate Dirac indices and latin letters indicate colour indices.

The local gauge transformation of the $SU(N_c)$ Yang Mills theory is then

$$\psi(x) \mapsto \psi'(x) = \Omega(x)\psi(x) \quad \text{and} \quad \overline{\psi}(x) \mapsto \overline{\psi}'(x) = \overline{\psi}(x)\Omega^\dagger(x), \tag{1.12}$$

and

$$\Rightarrow A_\mu(x) \mapsto A'_\mu(x) = \Omega(x)A_\mu(x)\Omega^\dagger(x) + i\left(\partial_\mu\Omega(x)\right)\Omega^\dagger(x), \tag{1.13}$$

where $\Omega \in SU(N_c)$. The field strength tensor transforms like

$$F_{\mu\nu}(x) \mapsto F'_{\mu\nu}(x) = \Omega(x)F_{\mu\nu}(x)\Omega^\dagger(x). \tag{1.14}$$

1.2. QCD on the Lattice

In order to solve the path integral of Euclidean QCD numerically, it is necessary to discretize the space-time volume of the action integral. The degrees of freedom of the theory then live on a discrete lattice

$$\Lambda = \left\{x \in \mathbb{Z}^{d+1}, 0 \le x_{1,2,3} < N_s, 0 \le x_4 < N_t\right\}, \tag{1.15}$$

with a lattice spacing a and the space-time volume is $a^4 V = (aN_s)^3 \times (aN_t)$. In order to compute expectation values in physical units, the lattice spacing must be identified with a physical scale, see

Section 1.2.5. How the lattice spacing depends on the parameters of the action strongly depends on the discretization chosen.

As we have seen in equation 1.10, the Wick-rotated generating functional has the form of a thermodynamic partition function, such that we can assign the temperature

$$T = \frac{1}{aN_t}, \tag{1.16}$$

to the system. The Boltzmann weight e^{-S} will later be used as a probability weight for solving the path integral with Monte Carlo methods [33–37], which is explained in Section 1.4.

1.2.1. Lattice gauge transporters

Since the space-time coordinate is now discrete and there is a finite lattice spacing a, the covariant derivative of the theory must be redefined on the discrete lattice. For this we will introduce *link variables*, which are gauge transporters between two lattice sites and correspond to the continuum gauge field A.

When discretizing the derivative we find that $\overline{\psi}(x)\psi(x+\hat{\mu}) \mapsto \overline{\psi}(x)\Omega^\dagger(x)\Omega(x+\hat{\mu})\psi(x+\hat{\mu})$ is not gauge invariant. Therefore we define the lattice gauge transporter

$$U_\mu(x) = P\left[e^{i\int_x^{x+\hat{\mu}} dz^\mu A_\mu(z)}\right] = e^{iaA_\mu(x)} \approx 1 + iaA_\mu(x), \tag{1.17}$$

that transforms like

$$U_\mu(x) \mapsto \Omega(x)U_\mu(x)\Omega^\dagger(x+\hat{\mu}). \tag{1.18}$$

Terms like $\overline{\psi}(x)U_\mu(x)\psi(x+\hat{\mu})$ are then gauge invariant, such that the covariant derivative can be discretized with a mid-point approximation

$$\left(\partial_\mu + iA_\mu(x)\right) \approx \frac{1}{2a}\left(U_\mu(x)\delta_{y,x+\hat{\mu}} - U_{-\mu}(x)\delta_{y,x-\hat{\mu}}\right), \tag{1.19}$$

where the link variables are defined to obey $U_{-\mu}(x) = U_\mu^\dagger(x-\hat{\mu})$.

Since by discretizing it, the measure of the path integral only changes by a constant, $\mathcal{D}A \propto \mathcal{D}U$, it can be written in terms of the link variables instead of the continuum gauge field. Note that the continuum gauge field lies in the algebra of the gauge group $A_\mu(x) \in su(N_c)$ and is non-compact, while the link variable lies in the group $U_\mu(x) \in SU(N_c)$ and is compact.

In the following we will discuss several approaches to discretize the action of QCD and QCD-like theories.

1.2.2. Wilson's plaquette action

From equation (1.18) we can see that the trace of a closed loop $\mathcal{W}$ of link variables is gauge invariant and thus gauge invariant objects can be constructed in terms of $\operatorname{tr}\left[\prod_{(x,\mu)\in\mathcal{W}} U_\mu(x)\right]$. The smallest non-trivial loop is called a *plaquette*

$$P_{\mu\nu}(x) = U_\mu(x)U_\nu(x+\hat{\mu})U_\mu^\dagger(x+\hat{\mu})U_\nu^\dagger(x), \tag{1.20}$$

which is sketched in Figure 1.2.

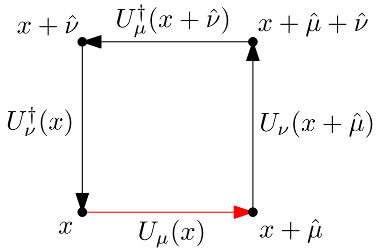

Figure 1.2.: The smallest non-trivial closed loop of link variables.

Using the Baker-Campbell-Hausdorff formula one and expand the plaquette in terms of the continuum gauge field such that

$$P_{\mu\nu}(x) \approx e^{ia^2 F_{\mu\nu}(x)+\mathcal{O}(a^3)} \approx 1 + ia^2 F_{\mu\nu} + \mathcal{O}(a^3). \tag{1.21}$$

This was used in 1974 by Kenneth G. Wilson [38] to propose a lattice discretization of the gauge part of the QCD action, the so-called *Wilson plaquette action*

$$S_g^{\text{Wilson}} = \frac{\beta}{N_c} \sum_{x,\mu} \sum_{\nu\neq\mu} \operatorname{Re}\operatorname{tr}\left[1 - P_{\mu\nu}(x)\right], \tag{1.22}$$

which reproduces $F^a_{\mu\nu}F^a_{\mu\nu}$ in the continuum limit. Note that this discretization is not unique.

1.2.3. Symanzik's rectangle action

Wilson's plaquette action can be improved by including larger loops of link variables in the action. Symanzik proposed to include planar 2×1 rectangles [39–44]. The Symanzik rectangle action then reads

$$S_g^{\text{Symanzik}} = -\frac{\beta}{N_c} \sum_{x,\mu} \sum_{\nu\neq\mu} \left(c_0 \operatorname{Re}\operatorname{tr} P_{\mu\nu}(x) + c_1 \operatorname{Re}\operatorname{tr} R_{\mu\nu}(x)\right), \tag{1.23}$$

with with rectangles $R_{\mu\nu}(x) = U_\mu(x)W_{\mu\nu}(x)$ and rectangle staples $W_{\mu\nu}(x)$. The rectangle contributions are sketched in Figure 1.3

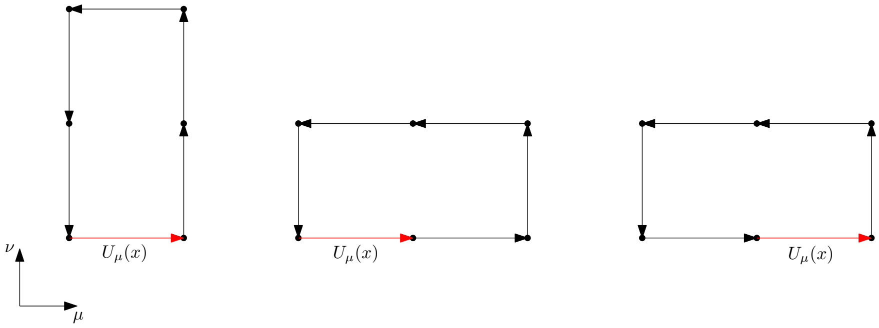

Figure 1.3.: The three different planar rectangles that are included in Symanzik's gauge action.

In order to contain the correct continuum limit the coefficient of this action have been determined [45] to be

$$c_0 = \frac{5}{3} \text{ and } c_1 = -\frac{1}{12}. \tag{1.24}$$

The Symanzik improvement of the action has been very successful, as it greatly improves the short distance scaling of the heavy quark potential and the energy density of SU(3) pure gauge theory [46] and has shown to greatly improve lattice discretization effects from a SU(3) lattice gauge theory with three flavours of Wilson fermions [47]. We will discuss how the Symanzik action improves upon discretization artifacts in two-colour QCD in Section 4.3.

1.2.4. Iwasaki's renormalization group improved action

The Symanzik rectangle action can further be improved by including non-planar 6-link Wilson loops in the gauge action [48–50]. These non-planar loops are sketched in Figure 1.4.

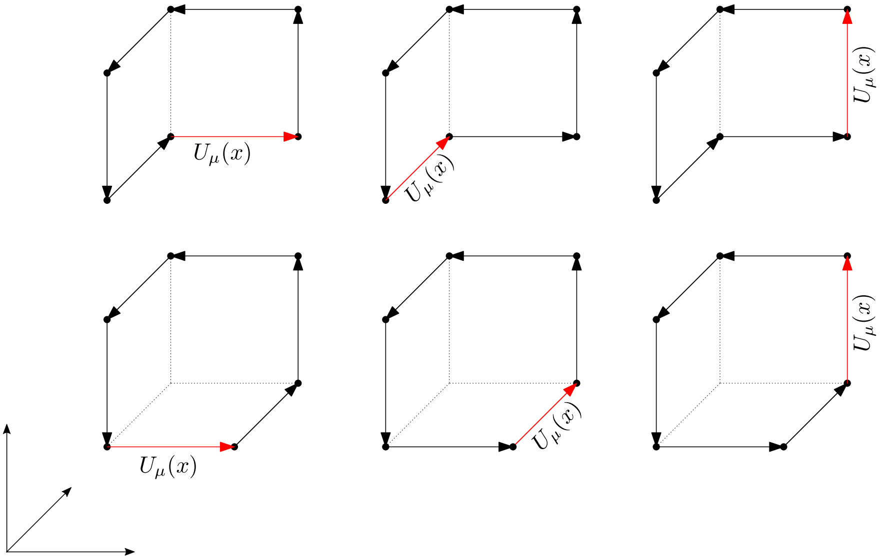

Figure 1.4.: The chair-like and cube-like six link Wilson loops that are included in Iwasaki's renormalization group improved gauge action.

The gauge action then takes the form

$$S_g^{\text{Iwasaki}} = -\frac{\beta}{N_c}\sum_{x,\mu}\sum_{\nu\neq\mu}\Bigg(c_0\,\mathrm{Re}\,\mathrm{tr}\,P_{\mu\nu}(x) + c_1\,\mathrm{Re}\,\mathrm{tr}\,R_{\mu\nu}(x) + \sum_{\rho\neq\mu,\rho\neq\nu}\left(c_2\,\mathrm{Re}\,\mathrm{tr}\,C^{\text{chair}}_{\mu\nu\rho}(x) + c_3\,\mathrm{Re}\,\mathrm{tr}\,C^{\text{cube}}_{\mu\nu\rho}(x)\right)\Bigg) \tag{1.25}$$

with now four couplings c_0, c_1, c_2 and c_3. These parameters must be chosen to fulfil the condition that the proper continuum expression $S = \frac{1}{4}\int d^4x \sum_{\mu\nu c}\left(F^c_{\mu\nu}\right)^2$ is maintained. When plugging the parallel transporters $U_\mu(x) = e^{iaA_\mu(x)}$ in the discretization anzsatz one obtains the normalization condition

$$c_0 + 8c_1 + 16c_2 + 8c_3 = 1. \tag{1.26}$$

The coefficients are then determined from a perturbative calculation. For this, one performs a block spin transformation of the gauge field variables like

$$A_\mu^{(i+1)}(x') = \frac{1}{8}\sum_{x\in x'} A_\mu^{(i)}(x), \tag{1.27}$$

such that each new link has the length $2a$. The action also evolves like $S^{(i)} \mapsto S^{(i+1)}$ and approaches the renormalized trajectory in the limit $i \mapsto \infty$. However, the coefficients are not unique and thus there are several different models for a proper discretization of the gauge action.

Iwasaki's original suggestion for the coefficients was

$$c_1 = -0.27 \text{ and } c_2 + c_3 = -0.04 \tag{1.28}$$

or almost equivalently, but much simpler to compute

$$c_1 = -0.331 \text{ and } c_2 = c_3 = 0. \tag{1.29}$$

In this work, the former Iwasaki action will be mostly used, due to its highly improved short range scaling.

1.2.5. The continuum limit and the physical scale

As mentioned before, physical observables and quantities on the lattice are only given in units of the lattice spacing, e.g. the temperature is given by $aT = 1/N_t$. The lattice spacing a is not a free parameter, but must be identified with a physical scale, for example by comparison to experimental data.

For this one often uses the *Sommer scale* r_0 [51]. From experiment it is possible to obtain the dimensionless quantity

$$r^2 \frac{dV(r)}{dr}\bigg|_{r=r_0} = 1.65, \tag{1.30}$$

where the Sommer parameter is $r_0 = 0.5$ fm and $dV(r)/dr$ is the force between two heavy quarks, which is calculated from $\bar{b}b$ and $\bar{c}c$ spectra. On the lattice one can compute the potential between two static colour sources and parametrize the potential like

$$aV(r) = aA + \frac{a^2 B}{ar} + a^2\sigma r, \tag{1.31}$$

where the *string tension* term $a^2\sigma r$ accounts for the linearly rising part of the potential that phenomenologically describes the flux tube between two confined colour sources.

While removing the lattice cutoff $a \mapsto 0$, all physical quantities should become independent of a. This is called the *continuum limit*. The infinite volume limit is called the thermodynamic limit.

In pure gauge theory there is only one coupling constant g, or the inverse coupling $\beta = 1/g^2$ respectively, which depends on the scale given by the lattice spacing. All bare parameters of the theory run with the coupling. For some observable O the continuum limit is given by

$$\lim_{a \mapsto 0} O(g(a), a) = O_{\text{cont}}, \tag{1.32}$$

which was described by Stückelberg, Peterman, Gell-Mann and Low for QED and by Callan and Symanzik for QCD.

The scale transformation is called *renormalization group* (RG) transformation and the RG equation for some observable is given by

$$\left(\frac{\partial}{\partial \ln a} + \frac{\partial g}{\partial \ln a}\frac{\partial}{\partial g}\right) O(g, a) = 0, \tag{1.33}$$

from which we can identify the β-function (which is not to be confused with the inverse coupling)

$$\beta(g) = -\frac{\partial g}{\partial \ln a}, \tag{1.34}$$

which can be expanded around $g = 0$ in perturbation theory

$$\beta(g) = -\beta_0 g^3 - \beta_1 g^5 + \mathcal{O}(g^7). \tag{1.35}$$

Solving the RG equation up to this order one obtains

$$a(g) = \frac{1}{C}(\beta_0 g^2)^{-\frac{\beta_1}{2\beta_0^2}} e^{-\frac{1}{2\beta_0 g^2}}(1 + \mathcal{O}(g^2)). \tag{1.36}$$

For a $SU(N_c)$ Yang-Mills theory with N_f massless fermions the expansion factors are given by

$$\beta_0 = \frac{1}{(4\pi)^2}\left(\frac{11}{3}N_c - \frac{2}{3}N_f\right) \tag{1.37}$$

and

$$\beta_1 = \frac{1}{(4\pi)^4}\left(\frac{34}{3}N_c^2 - \frac{10}{3}N_cN_f - \frac{N_c^2-1}{N_c}N_f\right). \tag{1.38}$$

With this one can estimate the lattice spacing in arbitrary units for a given gauge coupling g, as is plotted in Figure 1.5.

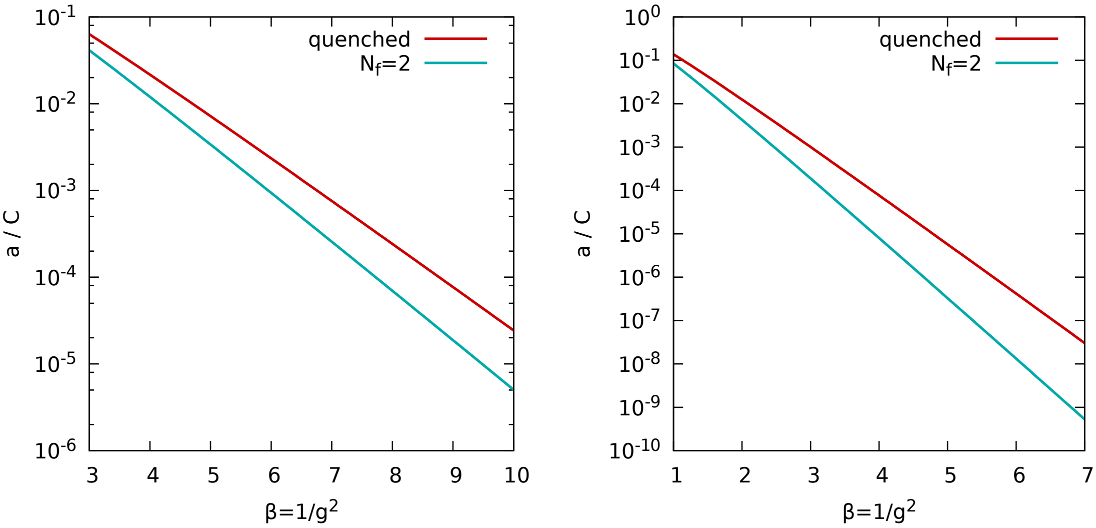

(a) $N_c = 3$

(b) $N_c = 2$

Figure 1.5.: The lattice spacing in arbitrary units up to second order for QCD and two-colour QCD.

1.2.6. Lattice fermions

As we have seen in Section 1.2.1 the covariant derivative can naively be discretized like

$$D_{x,y} = \sum_{\mu=1}^{4} \frac{\gamma_\mu}{2a}\left(U_\mu(x)\delta_{x+\hat{\mu},y} - U_{-\mu}(x)\delta_{x-\hat{\mu},y}\right). \tag{1.39}$$

However, this approach fails. For free fermions ($U_\mu(x) = 1 \forall x, \mu$) one can compute the quark propagator

$$\left(D_{x,y} + m\right)^{-1} = \frac{1}{V}\sum p \frac{m - \frac{i}{a}\sum_\mu \sin(p_\mu a)}{m^2 + \frac{1}{a^2}\sum_\mu \sin^2(p_\mu a)} e^{ip(x-y)a}, \tag{1.40}$$

which has a pole in each corner of the Brillouin zone. These 16 poles do not vanish in the continuum limit and are called *fermion doublers*. Such a discretization corresponds to 16 degenerate continuum flavours. It is therefore necessary to use some improved doubler-free quark discretization.

The Nielsen-Ninomiya No-Go Theorem [52] states that a real, local and doubler free lattice fermion action that is chirally and translationally invariant does not exist. There is however a vast variety of different quark discretizations, which are mostly based on two different approaches.

In Wilson's approach the doublers are removed by making them heavy enough to decouple from the theory. This is done by adding a second derivative term with a heavy mass to the doublers, which vanishes in the continuum limit. The Dirac operator for Wilson fermions then reads

$$D_{x,y} = \left(m + \frac{4}{a}\right)\delta_{x,y} - \frac{1}{2a}\sum_{\nu=\pm 1}^{\pm 4}(1-\gamma_\nu)U_\nu(x)\delta_{x+\hat{\nu},y}. \tag{1.41}$$

This discretization however suffers from an explicit chiral symmetry breaking due to the additional mass-like term.

The Wilson operator is often rephrased like

$$D_{x,y} := \delta_{x,y} - \kappa H_{x,y} \tag{1.42}$$

where $\kappa = \frac{1}{2am+4}$ is the Hopping parameter. For heavy quarks this can be expanded in κ, which is the so-called *hopping expansion*.

A very different approach to the fermion doubling problem was proposed by Kogut and Susskind in 1975 [53]. Here the fermion fields are diagonalized in Dirac space like

$$\psi(x) \mapsto \psi'(x) = \gamma_1^{x_1}\gamma_2^{x_2}\gamma_3^{x_3}\gamma_4^{x_4}\psi(x) \tag{1.43}$$

and

$$\overline{\psi}(x) \mapsto \overline{\psi}'(x) = \overline{\psi}(x)\gamma_4^{x_4}\gamma_3^{x_3}\gamma_2^{x_2}\gamma_1^{x_1} \tag{1.44}$$

such that there are four independent components to the fermion field. This is called the *staggered transformation*. Three of those components are then dropped and the number of doublers is reduced by a factor of four. These four remaining doublers are called *staggered tastes*. The new fermion field χ is a Dirac scalar and the staggered Dirac operator then reads

$$D_{x,y} = m\delta_{x,y} + \sum_\nu \frac{\eta_\nu(x)}{2a}\left(U_\nu(x)\delta_{x+\hat{\nu},y} - U_{-\nu}(x)\delta_{x-\hat{\nu},y}\right) \tag{1.45}$$

where the γ-matrices have been replaced by the staggered phases

$$\eta_\nu(x) = (-1)^{\sum_\sigma^{\nu-1} x_\sigma}. \tag{1.46}$$

This fermion discretization provides some remnant chiral symmetry (see also Section 1.3.1) like

$$\chi \mapsto \chi' = e^{ia\eta_5}\chi \text{ and } \overline{\chi} \mapsto \overline{\chi}' = \overline{\chi}e^{ia\eta_5} \tag{1.47}$$

but still has four remaining degenerate staggered tastes originating from the doublers. When staggered quarks are used one usually approximates the root of the fermion matrix to reduce the number of tastes in the theory [35].

1.2.7. Finite chemical potential on the lattice

It is generally assumed that the early universe is well approximated by QCD at vanishing chemical potential. In the following we denote the baryon chemical potential with μ_B and the quark chemical potential with $\mu = \mu_B/N_c$.

The grand canonical potential with a quark number n is given by

$$Z = \operatorname{tr} e^{-\beta(H-\mu n)} \tag{1.48}$$

and we see that the action obtains an additional term $-\mu \int_0^{1/T} dtn$ with

$$n = \int d^3x \overline{\psi}(x)\gamma_4\psi(x) = \int d^3x \psi^\dagger(x)\psi(x). \tag{1.49}$$

Charge conjugation symmetry implies that $Z(\mu) = Z(-\mu)$, which could be implemented by a term like $\overline{\psi}\gamma_4\psi \mapsto_C -\overline{\psi}\gamma_4\psi$.

However, simply adding $\mu\overline{\psi}\gamma_4\psi$ to the lattice action fails because the free energy density diverges in the continuum limit [54],

$$\lim_{a\mapsto 0} \epsilon = \lim_{a\mapsto 0} \frac{1}{V} \frac{\partial}{\partial(1/T)} \ln Z = \infty. \tag{1.50}$$

Fortunately the quark number is the Noether charge of the $U_V(1)$ symmetry such that $\mu n = \mu\overline{\psi}\gamma_4\psi$ looks like the time component of the fermion current coupling to an external gauge field. Therefore the chemical potential can be represented by an external temporal Abelian constant gauge field [36]

$$\mu n = -ig \int d^3x A_4 j_4 \tag{1.51}$$

where $A_4 = -i\frac{\mu}{g}$. This constant gauge field can be implemented on the lattice with constant temporal link variables

$$U_4^{\text{ext}} = e^{iagA_4} = e^{a\mu} \text{ and } U_{-4}^{\text{ext}} = e^{-iagA_4} = e^{-a\mu} \tag{1.52}$$

such that the gauge variables are modified to

$$U_\nu(x) \mapsto e^{a\mu\delta_{\nu,4}} U_\nu(x) \text{ and } U_{-\nu}(x) \mapsto e^{-a\mu\delta_{\nu,4}} U_{-\nu}(x). \tag{1.53}$$

This means that temporal forward quark propagation is favoured over temporal forward propagation of antiquarks. More generally the temporal link variables can be modified with some function [54]

$$U_\nu(x) \mapsto f(a\mu)U_\nu(x) \text{ and } U_{-\nu}(x) \mapsto f(-a\mu)U_{-\nu}(x) \tag{1.54}$$

that satisfies $f(-a\mu) = \frac{1}{f(a\mu)}$, for example $f(a\mu) = \frac{1+a\mu}{\sqrt{1-(a\mu)^2}}$ [55].

Due to the sign problem, see Section 1.4.3, one can not study full QCD at finite chemical potential with importance sampling methods. However, QCD-like lattice gauge theories without a sign problem have extensively studied. The action, the symmetries and the spectrum of two-colour QCD with staggered fermions has been investigated in [56], and the spectrum of QC$_2$D with Wilson fermions in [57, 58].

1.2.8. The lattice path integral for QCD

As we have seen before the path integral measure over the gauge field is proportional to the measure over the gauge transporters or link variables. This gauge-invariant integration measure over the whole group manifold is called the *Haar measure*

$$\mathcal{D}U = \prod_x \prod_{\mu=1}^{4} dU_\mu(x). \tag{1.55}$$

While the link variables connect two adjacent lattice sites, the fermion fields are anticommuting Grassmann numbers that live on the lattice sites. The corresponding integration measure reads

$$\mathcal{D}\overline{\psi}\mathcal{D}\psi = \prod_x \prod_{f,\alpha,c} d\overline{\psi}^f(x)_{\alpha,c} d\psi^f(x)_{\alpha,c}. \tag{1.56}$$

For a total action $S\left[\overline{\psi},\psi,U\right] = S_g[U] + S_f\left[\overline{\psi},\psi,U\right]$ the generating functional on the lattice then looks like

$$Z = \int \mathcal{D}U e^{-S_g[U]} \int \mathcal{D}\overline{\psi}\mathcal{D}\psi e^{-S_f\left[\overline{\psi},\psi,U\right]}. \tag{1.57}$$

The fermion action generically has the form $S_f\left[\overline{\psi},\psi,U\right] = \overline{\psi}\mathcal{M}\psi$ with a fermion kernel $\mathcal{M}$. The Gauss integral the Grassmann fields can explicitly be carried out using the Matthews-Salam formula [59] like

$$\int d\overline{\xi}_0 d\xi_0 ... d\overline{\xi}_N d\xi_N e^{\sum_{i,j}\overline{\xi}_i M\xi_j} = \det M, \tag{1.58}$$

so that the Haar measure of the theory with dynamical fermions includes the fermion determinant like

$$Z = \int \mathcal{D}U e^{-S_g[U]} \det \mathcal{M}(U). \tag{1.59}$$

This integral can then be numerically solved, for example with Monte Carlo methods.

1.3. Chiral symmetry

In massless QCD the Dirac operator can be written in a chiral basis, in which left- and right-handed components of the fermion fields decouple and the action is invariant under the chiral rotations [60, 61]

$$\begin{aligned} \psi \mapsto e^{i\alpha\gamma_5 T_a}\psi \text{ and } \overline{\psi} \mapsto \overline{\psi}e^{i\alpha\gamma_5 T_a}, \\ \psi \mapsto e^{i\alpha\gamma_5}\psi \text{ and } \overline{\psi} \mapsto \overline{\psi}e^{i\alpha\gamma_5} \end{aligned} \tag{1.60}$$

where T_a is a generator of $SU(N_f)$. The left- and right-handed components can be rotated independently, like $\psi_\pm \mapsto V_\pm\psi_\pm$ where $V_\pm \in U_\pm(N_f)$. That means that the action of massless QCD is invariant under the symmetry group

$$U_+(N_f) \times U_-(N_f) = SU_+(N_f) \times SU_-(N_f) \times U_V(1) \times U_A(1). \tag{1.61}$$

$SU_+(N_f) \times SU_-(N_f)$ corresponds to the independent rotation of left- and right-handed fermion components, $U_V(1)$ to the conservation of the baryon number and $U_A(1)$ to the axial anomaly. The Lagrangian of QCD is invariant under $U_A(1)$, but the fermion integration measure in the path integral is not. The axial symmetry is broken by quantization. A candidate for a Nambu-Goldstone boson would be the $\eta^{'}$, but it is much too heavy. A recent study of the behaviour of the $\eta^{'}$-mass at finite temperature in $N_f = 2 + 1 + 1$ lattice QCD is presented in [62].

A small quark mass breaks chiral symmetry explicitly. For N_f degenerate massive fermion flavours the left- and right-handed components can not be rotated independently anymore, the $SU_+(N_f) \times SU_-(N_f)$ symmetry is broken to the diagonal vector subgroup $SU_V(N_f)$ and the remaining symmetry is

$$SU_V(N_f) \times U_V(1). \tag{1.62}$$

Chiral symmetry can be written like

$$\{\gamma_5, D\} = 0. \tag{1.63}$$

This means that the eigenmodes of a chirally symmetric Dirac operator occur in conjugate pairs $(i\lambda,\psi)$ and $(-i\lambda,\gamma_5\psi)$. Zero modes of the Dirac operator are simultaneous eigenmodes to γ_5 and thus have a definite chirality. In a chiral basis, where the fermion fields are projected onto their chiral components with $P_\pm = \frac{1\pm\gamma_5}{2}$ such that $\psi = P_+\psi + P_-\psi = \psi_+ + \psi_-$ and $\overline{\psi} = \overline{\psi}_+ + \overline{\psi}_-$ the massless Dirac operator can be written like

$$\overline{\psi}D\psi = \overline{\psi}_+ D\psi_+ + \overline{\psi}_- D\psi_-. \tag{1.64}$$

A finite chiral condensate $\langle\overline{\psi}\psi\rangle = \langle 0|\overline{\psi}_+\psi_- + \overline{\psi}_-\psi_+|0\rangle$ spontaneously breaks chiral symmetry such that the degenerate masses of chiral partners split. This is a purely non-perturbative effect. The Goldstone bosons of this spontaneous symmetry breaking are the pions, whose light mass is originated in the small but finite quark mass, which explicitly but weakly breaks chiral symmetry. The chiral condensate transforms like a mass term. The *Banks-Casher relation* [63] connects the near-zero spectral density of the Dirac operator with the chiral condensate and reads

$$-\langle\overline{\psi}\psi\rangle \equiv \Sigma = \pi \lim_{\lambda\mapsto 0}\lim_{m\mapsto 0}\lim_{V\mapsto\infty}\rho(\lambda). \tag{1.65}$$

1.3.1. Chiral symmetry on the lattice and the Ginsparg-Wilson relation

The construction of a lattice discretization of the Dirac operator that contains chiral symmetry has continued to pose a serious problem that is originated in the doubling problem. Removing the doublers in a theory usually interferes with its chiral properties.

In the case of Wilson fermions the additional second derivative term acts as a mass, which becomes infinitely large in the continuum limit, and explicitly breaks chiral symmetry. The staggered transformation on the other hand replaces any γ_μ and γ_5 operator with some staggered phase, such that the chirality operator becomes a coordinate dependent local operator.

The solution to this problem was first presented by Ginsparg and Wilson in their seminal paper [64] from 1982. It was then rediscovered by Hasenfratz [65] in 1997.

Ginsparg and Wilson suggested to replace the continuum requirement for chiral symmetry with an anticommutation relation, that is continuously connected with the full continuum expression by the lattice spacing, such that it properly restores in the continuum limit. This remnant chiral symmetry on the lattice then reads

$$\{\gamma_5, D\} = \frac{a}{\rho}D\gamma_5 D, \tag{1.66}$$

with some real positive rescaling parameter ρ. This equation is called the *Ginsparg-Wilson relation.* It is, however, not unique, since higher order terms in a can in principle be added.

Fermion discretizations, that obey this relation are called Ginsparg-Wilson fermions. Two very popular examples are domain wall fermions, also called Kaplan fermions, see Section 1.3.2, and overlap fermions, also called Neuberger fermions, see Section 1.3.3.

The Ginsparg-Wilson equation can be written in terms of the propagator like

$$\left\{\gamma_5, D_{x,y}\right\} = \frac{a}{\rho}D_{x,y}\gamma_5 D_{x,y} \Leftrightarrow \left\{D^{-1}_{x,y}, \gamma_5\right\} = \frac{a}{\rho}\gamma_5\delta(x-y). \tag{1.67}$$

The symmetry of the propagator is thus only modified for $x = y$ by some contact term, that vanishes in the continuum limit.

It can also be rephrased like

$$D\gamma_5\left(1 - \frac{a}{2\rho}D\right) + \left(1 - \frac{a}{2\rho}D\right)\gamma_5 D = 0 \tag{1.68}$$

and we can see that the chiral rotations are modified to

$$\psi \mapsto e^{i\alpha\gamma_5\left(1-\frac{a}{2\rho}D\right)}\psi \text{ and } \overline{\psi} \mapsto \overline{\psi}e^{i\alpha\left(1-\frac{a}{2\rho}D\right)\gamma_5}. \tag{1.69}$$

Thus, on the lattice the projection operators to left- and right-handed components of the quark fields change to

$$P_{\pm} = \frac{1}{2}\left(1 \pm \gamma_5\left(1 - \frac{a}{\rho}D\right)\right). \tag{1.70}$$

Note that, using (1.66) one can show, that $\left(\gamma_5\left(1 - \frac{a}{\rho}D\right)\right)^2 = 1$ and the projections therefore remain idempotent.

The eigenvalues of a chirally symmetric Dirac operator in the continuum are purely imaginary. On the lattice, however, the eigenvalues of a Ginsparg-Wilson Dirac operator D have a non-vanishing real part. Let $|\psi\rangle$ be an eigenvector to D and $D|\psi\rangle = \lambda|\psi\rangle$, $\lambda \in \mathbb{C}$, then $\gamma_5 D \gamma_5 |\psi\rangle = D^\dagger|\psi\rangle = \lambda^*|\psi\rangle$. The eigenvalues then obey

$$\begin{aligned} \{\gamma_5, D\}\,|\psi\rangle &= \frac{a}{\rho}D\gamma_5 D|\psi\rangle \\ &\Leftrightarrow (D^\dagger + D)|\psi\rangle = \frac{a}{\rho}D^\dagger D|\psi\rangle \\ &\Rightarrow 2\,\mathrm{Re}\,\lambda = \frac{a}{\rho}|\lambda|^2, \end{aligned} \tag{1.71}$$

which means that λ lie on a circle with radius ρ/a through zero. This circle is called the Ginsparg-Wilson circle, and falls on the imaginary axis for $a \mapsto 0$, see Figure 1.6.

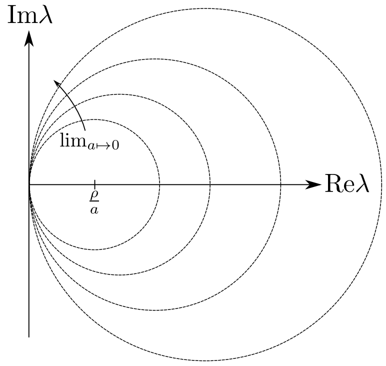

Figure 1.6.: The Ginsparg-Wilson circle falls onto the imaginary axis in the continuum limit and $\{\gamma_5, D\} = 0$ is restored.

1.3.2. Domain wall fermions

The first successful suggestion for a fermion discretization, that obeys the Ginsparg-Wilson relation was formulated by David B. Kaplan in 1992 [66], see also [67,68]. The Kaplan fermion discretization has become a successful approach to lattice fermions and are widely used. It has been shown by the HotQCD collaboration [69] that chiral and axial symmetry restore at finite temperature for these fermions, already at coarse lattices and small volumes ($N_s^3 \times N_t \times N_5 = 16^3 \times 8 \times 96$).

These so-called domain wall fermions implement an approximate chiral symmetry, such that lattice chiral symmetry is asymptotically preserved. The idea is to introduce an auxiliary dimension of length N_5, and distribute the left- and right-handed components of the quark fields as far from each other as possible in 5-direction. The chiral components then bulk at the domain walls and an explicit breaking of chiral symmetry can be implemented by coupling the to each other with some mass parameter, see Figure 1.7.

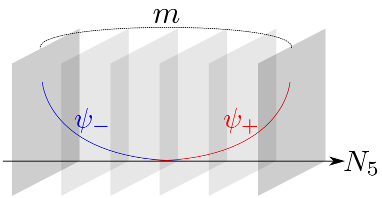

Figure 1.7.: A sketch of the fermion fields with the domain wall operator: The chiral components bulk at the domain walls of the auxiliary dimension.

The gauge field still lives on a 3+1 dimensional space-time and each space-time slice in 5-direction sees the same gauge field. On each of those slices live heavy Wilson quarks. When the two domain walls at $n_5 = 0$ and $n_5 = N_5 - 1$ are entirely decoupled, chiral symmetry is restored in the $N_5 \mapsto \infty$ limit.

The domain wall Dirac operator reads

$$D_{x,y;s,t} = \delta_{s,t} D^{\parallel}_{x,y} + \delta_{x,y} D^{\perp}_{s,t}, \tag{1.72}$$

where s, t are coordinates in the auxiliary direction. The parallel part is the standard Wilson operator with a large mass M_5

$$D^{\parallel}_{x,y} = (M_5 - 4)\,\delta_{x,y} + \frac{1}{2}\sum_{\nu=\pm1}^{\pm4}(1+\gamma_\nu)U_\nu(x)\delta_{x+\nu,y} \tag{1.73}$$

and the perpendicular part describes the interaction in N_5 direction, and thus separates the left- and right-handed chiral components,

$$\begin{aligned} D^{\perp}_{s,t} &= -\delta_{s,t} + \Theta_{s,t}\left(P_+\delta_{s+1,t} + P_-\delta_{s-1,t}\right), \\ \text{where } \Theta_{s,t} &= 1 - (m+1)\left(\delta_{t,0}\delta_{s,N_5-1} + \delta_{t,N_5-1}\delta_{s,0}\right). \end{aligned} \tag{1.74}$$

Chiral symmetry can explicitly be broken by coupling the diametrically opposed domain walls to each other with a mass parameter m, see equation (1.74).

From these five dimensional domain wall fermion fields the physical quark fields can be reconstructed like

$$\begin{aligned} \psi(x) &= P_-\phi(x,0) + P_+\phi(x,N_5-1) \\ \text{and } \overline{\psi}(x) &= \overline{\phi}(x,N_5-1)P_- + \overline{\phi}(x,0)P_+. \end{aligned} \tag{1.75}$$

With domain wall fermions, however, the Ginsparg-Wilson equation is only approximately obeyed. At $N_5 < \infty$ and $m = 0$ it is violated by some perturbation term η

$$\{\gamma_5, D\} = \frac{a}{\rho} D\gamma_5 D + \eta \Rightarrow 2\mathrm{Re}\lambda = \frac{a}{\rho}|\lambda|^2 + \xi, \tag{1.76}$$

where we have assumed that the domain wall fermion eigenmode is also an eigenvector to the perturbation term, $\gamma_5\eta|\psi\rangle = \xi(\lambda)|\psi\rangle$. That means that the eigenvalues of the "perturbed" domain wall operator at finite N_5 lie on concentric circles with radii $\frac{\rho}{a} + \xi(\lambda)$, and it is sufficient to radially project the eigenvalues on the Ginsparg-Wilson circle. As $N_5 \to \infty$ the chiral components decouple and the eigenvalues fall onto the circle.

The quark mass also gets an additive renormalization contribution due to finite N_5 and non-zero M_5. At tree-level it is possible to predict the effective quark mass [70], which then reads

$$\hat{m} = M_5(2 - M_5)m. \tag{1.77}$$

In the limit $N_5 \to \infty$ the domain wall degrees of freedom increase with N_5, but the physical degrees of freedom remain the same. These bulk divergences must be suppressed with heavy bosonic auxiliary fields, the Pauli-Villar fields [71,72], such that the determinant of the two-flavour Domain-Wall fermion kernel becomes becomes

$$\det \mathcal{M} = \frac{\det\left(D^\dagger(M_5,m)D(M_5,m)\right)}{\det\left(D^\dagger(M_5,1)D(M_5,1)\right)}. \tag{1.78}$$

1.3.3. The overlap operator

A very different approach to chiral lattice fermions was presented by Neuberger in 1998 [73–75]. The massless Neuberger operator reads

$$D(0) = \frac{\rho}{a}\left(1 + \mathrm{sgn}K\right), \tag{1.79}$$

where the sign function on the kernel operator is defined as $\mathrm{sgn}K = \frac{K}{\sqrt{K^\dagger K}}$ and the kernel operator itself only has to be γ_5-hermitian. For the kernel operator it is common to choose the Wilson operator with a negative mass $-\rho$.

This overlap Dirac operator solves the Ginsparg-Wilson equation exactly, since

$$\begin{aligned} \{(1 + \mathrm{sgn}K), \gamma_5\} &= (1 + \mathrm{sgn}K)\gamma_5(1 + \mathrm{sgn}K) \\ \Leftrightarrow \mathrm{sgn}K^\dagger \mathrm{sgn}K &= 1. \end{aligned} \tag{1.80}$$

It also implements the $U_A(1)$ anomaly on the lattice. Furthermore, it can be shown that overlap quarks are automatically $\mathcal{O}(a)$ improved [76].

The overlap operator can even be further improved. The operator

$$D_{\mathrm{imp}} = \left(1 - \frac{a}{2\rho}D\right)^{-1} D \tag{1.81}$$

fulfils the continuum equation $\{D, \gamma_5\} = 0$ in the same way as the eigenvalues on the Ginsparg-Wilson circle can be projected on their continuum counterparts on the imaginary axis, see Section 2.1.2.

The massive overlap operator is then given by

$$D(m_q) = \left(1 - \frac{am_q}{2\rho}\right)D(0) + m_q = \left(\frac{\rho}{a} - \frac{m_q}{2}\right)(1 + \mathrm{sgn}K) + m_q. \tag{1.82}$$

In most implementations of the overlap operator in lattice simulations the sign function is approximated with Chebyshev polynomials (see Section B.1) or a rational function (see Section B.2). A projection to the low eigenmodes on the kernel operator can massively improve the approximation of the low-lying modes of the overlap operator, since the sign function can then be treated exactly for these modes, see Section B.3.

An alternative formulation of overlap quarks using a staggered fermion kernel operator is called Adams fermions [77,78]. These fermions obey an index theorem but are computationally cheaper than overlap quarks with a Wilson kernel. The Ginsparg-Wilson relation however is obeyed only with respect to staggered phases $\Gamma_{55}(x) = (-1)^{\sum_\mu x_\mu}$ instead of γ_5.

1.4. Monte Carlo simulations of lattice QCD

Now that we have established a consistent lattice discretization of the Euclidean QCD partition function and a proper continuum limit, we can now solve the path integral numerically. A very popular method to do so is approximating the path integral using Monte Carlo integration over finite ensembles $\{U\}$ of gauge configurations. In order to obtain a sufficient approximation of expectation values, the set of configurations must cover all phase space and the configurations must be fairly decorrelated among each other. The expectation value is then approximated over N configurations like

$$\langle \mathcal{O} \rangle = \frac{1}{Z} \int \mathcal{D}U e^{-S_g[U]} \det \mathcal{M}(U) \mathcal{O}(U) \approx \frac{1}{Z} \sum_k^N e^{-S_g[U_k]} \det \mathcal{M}(U_k) \mathcal{O}(U_k). \tag{1.83}$$

If the configurations U are chosen according to the probability distribution $P(U) \propto e^{-S_g[U]} \det \mathcal{M}(U)$, the approximation simplifies to

$$\langle \mathcal{O} \rangle \approx \frac{1}{N} \sum_k^N \mathcal{O}(U_k). \tag{1.84}$$

Monte Carlo methods generally employ Markov processes that create configurations (or “events”) along a certain probability distribution. A *Markov chain* [79] is a sequence of events U_0, U_1,... where each element only depends on the previous, i.e. the Markov process has no memory. The transition probability for $U_i \mapsto U_j$ is described by the transition matrix $T_{i,j}$, which is positive definite, such that every event U with $P(U) > 0$ can be reached within a finite number of steps. This is called *ergodicity*. Also the processes $U_i \mapsto U_j$ and $U_j \mapsto U_i$ are equally likely, which can be phrased as

$$P(U_i) T_{i,j} = P(U_j) T_{j,i} \tag{1.85}$$

and is called *detailed balance*. This is equivalent to the reversibility of the Markov process.

In practice one starts with an arbitrary configuration U_0 and then performs the update algorithm repeatedly, until the proper equilibrium distribution of the gauge configuration is reached. After this first thermalization process, the first configurations are then discarded.

1.4.1. The hybrid Monte Carlo method

The hybrid Monte Carlo algorithm (HMC) uses molecular dynamics to generate a Markov chain. The consecutive gauge configurations are created from one another by introducing a fictitious time coordinate τ and evolving the gauge field in a random direction. Here the gauge field variables $U_\mu(x) \in SU(N_c)$ are interpreted to be generalized coordinates of a classical trajectory, which have conjugate momenta $\pi_\mu(x) \in su(N_c)$. These momenta are randomly sampled in the beginning of each Monte Carlo update, following the distribution of a classical heat-bath

$$P(\pi_\mu(x)) \propto e^{-\pi_\mu^2(x)}. \tag{1.86}$$

In order to ensure the proper equilibrium distribution of the gauge configuration, the classical equations of motion for the conjugate variables $U_\mu(x)$ and $\pi_\mu(x)$ are governed by the Hamiltonian

$$H = \frac{1}{2} \sum_{x,\mu} \mathrm{tr}(\pi_\mu(x)^2) + S \tag{1.87}$$

such that

$$\frac{d}{d\tau} U_\mu(x) = \frac{\partial H}{\partial \pi_\mu(x)} \quad \text{and} \quad \frac{d}{d\tau} \pi_\mu(x) = -\frac{\partial H}{\partial U_\mu(x)} \equiv F_\mu(x). \tag{1.88}$$

These solution to the equations of motion must be symmetric under Monte Carlo time reversal, in order to maintain detailed balance. The numerical integration scheme must therefore be symplectic, which is described in Appendix A.4.

Note that we have introduced a *force term* $F_\mu(x)$, which is the key element to the molecular dynamics evolution of the gauge field. It incorporates the minimization of the action and is given by

$$F_\mu(x) = U_\mu(x)\frac{\partial S[U]}{\partial U_\mu(x)}. \tag{1.89}$$

The derivations of molecular dynamics force terms for a variety of lattice actions are given in Appendix A.2.

The whole hybrid Monte Carlo update then consists of three steps:

1. Momentum heat-bath:
   The conjugate momenta are randomly sampled along a Gaussian distribution.

2. Molecular dynamics:
   The gauge variables and their momenta are integrated along the classical equations of motion. Here the computation of the force term is usually the most time consuming operation.

3. Metropolis check:
   To account for numerical integration errors, the candidate for the new gauge configuration is only accepted with a probability

   $$p_A = e^{-(S[U']-S[U])}. \tag{1.90}$$

   If the update candidate is rejected, return to step 1.

1.4.2. HMC with fermions

For numerical computations, the usage of Grassmann variables is difficult, if not unfeasible. We therefore replace the Grassmann fields $\overline{\psi}$, ψ by scalar fields $\phi^\dagger$, ϕ by rewriting the fermion determinant like

$$\int \mathcal{D}\overline{\psi}\mathcal{D}\psi e^{-\overline{\psi}\mathcal{M}\psi} = \det\mathcal{M} = \frac{1}{\det\mathcal{M}^{-1}} = \int \mathcal{D}\phi^\dagger\mathcal{D}\phi e^{-\phi^\dagger\mathcal{M}^{-1}\phi}. \tag{1.91}$$

The new field variables $\phi^\dagger$ and ϕ are called *pseudofermions*. This method however requires the inversion of the fermion matrix $\mathcal{M}$, which in most cases is numerically very expensive. The pseudofermion field is initialized randomly at the beginning of every HMC trajectory with the probability distribution

$$P(\phi) = e^{-\phi^\dagger(D^\dagger D)^{-1}\phi} = e^{-\rho^\dagger\rho} \text{ with } \phi = D\rho. \tag{1.92}$$

As we have seen in Section 1.2.6 some fermion actions require an additional rooting procedure, where the fermion kernel $\mathcal{M}$ is approximated to some fractional power $\mathcal{M}^{n/m}$ in order to regulate the number of fermion flavours in the theory. This is both used to remove the redundant staggered tastes as well as perform computations with odd numbers of Wilson flavours and many other applications.

In principle, rooting is possible with a variety of different approximations. A widely used choice is the so-called *Zolotarev approximation* or simply *rational approximation* [35, 44]

$$r_\gamma(\mathcal{M}) = c + \sum_{j=0}\frac{\alpha_j}{\mathcal{M}+\beta_j} \approx \mathcal{M}^\gamma. \tag{1.93}$$

The coefficients for this series are determined from a min-max optimization using the Remez algorithm, which is explained in Section A.3.2. For practical applications the multiple inversions of the shifted fermion kernel $\mathcal{M} + \beta_j$ are performed simultaneously using the multishift conjugate gradient solver [80–82], which is described in detail in Appendix A.3.1.

1.4.3. The sign problem of QCD at finite chemical potential

At finite chemical potential the path integral can not simply be solved with Monte Carlo integration. The fermion determinant is real, if the Dirac operator is γ_5-hermitian, which means that

$$\gamma_5 \not{D} \gamma_5 = \not{D}^\dagger. \tag{1.94}$$

When a chemical potential is included, this equation changes to

$$\gamma_5 \left(i\gamma_\mu D_\mu - \gamma_4 \mu \right) \gamma_5 = \left(i\gamma_\mu D_\mu + \gamma_4 \mu^* \right)^\dagger \tag{1.95}$$

and the fermion determinant is not real anymore. It obtains a complex phase

$$\det \mathcal{M} = |\det \mathcal{M}| e^{i\varphi}, \tag{1.96}$$

and any expectation value now oscillates immensely like

$$\frac{1}{Z} \int \mathcal{D}U e^{-S_g[U]} \det \mathcal{M}(U) \mathcal{O}[U] = \frac{\langle O e^{i\varphi} \rangle}{\langle e^{i\varphi} \rangle}. \tag{1.97}$$

With finite computing resources it is close to impossible to appropriately sample observables with an importance sampling method.

There are, however, several approaches to circumvent the sign problem in Lattice QCD. A possible approach is the *complex Langevin method*, which was independently invented by Parisi [83] and Klauder [84] in 1983, and is based on stochastic quantization. The complex integration measure is represented with an only mildly oscillating measure on a complexified field space and the SU(3) gauge group is extended to SL(3,$\mathbb{C}$). A contemporary review on the status of complex Langevin is given in [27].

It has also proven worthwhile, to study Yang-Mills theories on the lattice, which are similar to QCD but do not have a sign problem. This is for example the case for adjoint QCD, QCD at finite isospin chemical potential or two-colour QCD [57,85–87]. The latter has an orthogonal anti-unitary symmetry, and the matrix elements of the Dirac operator are real. We studied several aspects of two-colour QCD on the lattice in Chapter 4.

It is also interesting to study the exceptional Lie group G_2 as gauge group [88, 89]. This group contains SU(3), but the matrix elements of the Dirac operator are quaternion real, such that there is no sign problem present in G_2-QCD as well.

However, QCD-like theories do not directly relate to full QCD and can only be used to study qualitative aspects of strongly interacting matter or construct effective theories.

1.5. Gradient flow

In lattice gauge theory simulations the term “smoothing” generally means removing ultraviolet short range fluctuations in the gauge field with some kind of smearing technique. As this is analogous to reducing the temperature in a thermodynamic system, this is called “cooling” as well. Smoothing gauge configurations is of great importance for removing the contamination of two-point functions with excited states, for example in the computation of the static quark potential or hadron spectroscopy.

With many gauge cooling techniques the original “thin” links are replaced with local extended gauge paths, which are called ”fat” links. In 1987, the APE collaboration suggested in the seminal paper [90] a cooling method that replaces the original link at smearing step j with a linear combination like

$$U_\mu^{(j)}(x) \to U_\mu^{(j+1)}(x) = \mathcal{P}\left((1-\alpha)\, U_\mu^{(j)}(x) + \frac{\alpha}{6} \sum_{\nu\neq\mu} V_{\mu\nu}^{(j)}(x) \right), \tag{1.98}$$

where $V_{\mu\nu}^{(j)}(x)$ denotes the perpendicular staple at smearing step j and $\mathcal{P}$ is a projection to the gauge group.

The hypercubic block method (also called HYP smearing) [91, 92] as proposed by Hasenfratz *et al.* in 2001 consists of three steps of constructing fat links from paths within the hypercubes that are attached to the original thin link. These fat links are then combined into the new link with an APE-like smearing step.

Stout smearing [93] has been proposed by Morningstar and Peardon in 2004. This is an analytic procedure and the smearing operation is hence differentiable. The smeared links, also called stout links, have exactly the same symmetry transformation properties as the original links. The smearing operation is defined by

$$U_\mu^{(j)}(x) \to U_\mu^{(j+1)}(x) = e^{iq_\mu^{(j)}(x)} U_\mu^{(j)}(x) \quad \text{where} \quad q_\mu^{(j)}(x) = \sum_{\pm\nu\neq\mu} \rho_{\mu\nu} V_{\mu\nu}^{(j)}(x) U_\mu^\dagger(x) \Big|_{\mathrm{TA}} \in su(N), \tag{1.99}$$

with perpendicular staples $V_{\mu\nu}^{(j)}(x)$ and real tunable parameters $\rho_{\mu\nu}$. The subscript TA denotes the projection to the traceless antihermitian part. A popular choice for these parameters is the spatial smearing $\rho_{ik} = \rho \neq 0$ and $\rho_{4\mu} = \rho_{\mu 4} = 0$, which leaves temporal links unchanged. These three methods have been compared in [94].

Quite recently a gauge cooling method based on stochastic quanization has been presented and applied to a two-dimensional scalar field theory in [95]. In this approach the Langevin equation, which evolves the field with a noise term to incorporate quantum fluctuations, is modified by introducing an ultraviolet regulator to the noise.

The gradient flow method, which was first formulated by Lüscher [96–99], is based on a diffusion equation, that evolves, i.e. “flows”, the gauge field gauge-covariantly in an auxiliary time direction. It can be shown that local observables and correlation functions determined from the flowed gauge field do not require additional renormalization. The gauge field is thus mapped on a smooth renormalized gauge field.

For a non-Abelian gauge theory in the continuum the equation of motion, or flow equation, for the gauge field reads

$$\frac{d}{d\tau} B_\mu = D_\nu G_{\nu\mu}, \tag{1.100}$$

with the initial condition $B_\mu\big|_{\tau=0} = A_\mu$. The auxiliary time dimension coordinate is denoted with τ. The flowed field strength tensor reads

$$G_{\mu\nu} = \partial_\mu B_\nu - \partial_\nu B_\mu + \left[B_\mu, B_\nu\right], \tag{1.101}$$

and the covariant derivative on the flowed gauge field is given by

$$D_\mu = \partial_\mu + \left[B_\mu, \frac{d}{d\tau}\right]. \tag{1.102}$$

The fermion fields follow diffusion equations like

$$\frac{\partial}{\partial\tau}\chi = \Delta\chi \text{ and } \frac{\partial}{\partial\tau}\overline{\chi} = \overline{\chi}\overleftarrow{\Delta}, \tag{1.103}$$

with the initial conditions $\chi\big|_{\tau=0} = \psi$ and $\overline{\chi}\big|_{\tau=0} = \overline{\psi}$. The flowed gauge covariant Laplace operator is $\Delta_\mu = D_\mu D_\mu$.

Gradient flow evolves the action monotonically towards its stationary points up to the point, where quantum fluctuations are entirely smoothed out. In a finite volume, the flow evolution is unique.

The next few sections follow closely the line of reasoning as presented in [96].

1.5.1. Yang-Mills gradient flow at small gauge coupling

In order to verify that the flowed variables have a well-defined continuum limit, we will study a perturbative expansion of the gauge field in the small gauge couplings g_0 for a $SU(N)$ Yang-Mills gauge theory with N_f flavours of massless quarks. We shall now illustrate how the gauge field changes when gradient flow is applied, and find that in leading order it is smeared over a sphere with a radius that increases with the flow time.

The flow equation is invariant under τ-independent gauge transformations. The gauge dependent contributions to the flow equation, that arise from an expansion in g_0, can be removed by adding a term, that is continuously connected with the original flow equation like

$$\frac{d}{d\tau} B_\mu = D_\nu G_{\nu\mu} + \lambda D_\mu \partial_\nu B_\nu. \tag{1.104}$$

The solution of this modified flow equation is thus connected to the original solution $B_\mu\big|_{\lambda=0}$ by a τ-independent gauge transformation

$$B_\mu = \Lambda B_\mu\big|_{\lambda=0} \Lambda^{-1} + \Lambda \partial_\mu \Lambda^{-1}, \tag{1.105}$$

which itself is governed by the flow equation

$$\frac{d}{d\tau} \Lambda = -\lambda \partial_\nu B_\nu \Lambda, \tag{1.106}$$

with the initial condition $\Lambda\big|_{t=0} = 1$. If $\lambda = 1$ is chosen, we end up with a diffusion equation.

When the original gauge field is rescaled with the gauge coupling $A_\mu \mapsto g_0 A_\mu$, higher orders of g_0 become dominant in the flowed gauge field B_μ at positive flow times, which can then expanded be like

$$B_\mu = \sum_{k=1}^{\infty} g_0^k B_{\mu;k} \text{ with } B_{\mu;k}\big|_{t=0} = \delta_{k,1} A_\mu. \tag{1.107}$$

Plugging this expansion in the modified flow equation gives

$$\frac{d}{d\tau} B_{\mu;k} - \partial_\nu \partial_\nu B_{\mu;k} = R_{\mu;k}, \tag{1.108}$$

which in leading order $R_{\mu;1} = 0$ has the form of a heat equation. In next-to-leading order we get $R_{\mu;2} = 2\left[B_{\nu;1}, \partial_\nu B_{\mu;1}\right] - \left[B_{\nu;1}, \partial_\mu B_{\nu;1}\right]$ and so on.

The leading order solution to this equation is

$$B_{\mu;1}(\tau, x) = \int d^d y K(\tau, x - y) A_\mu(y), \tag{1.109}$$

where K is the Green's function of the differential operator on the left side of the leading order flow equation, the so called "heat kernel" that is given by

$$K(\tau, z) = \int \frac{d^d p}{(2\pi)^d} e^{ipz} e^{-\tau p^2} = \frac{e^{-z^2/(4\tau)}}{(4\pi\tau)^{d/2}}. \tag{1.110}$$

From this we can see, that the gauge potential is smeared, or averaged, over a d-dimensional sphere. For $d = 4$ the radius of this sphere is $\sqrt{8\tau}$.

In higher orders of g_0 the solution for the flowed gauge field is generally given by

$$B_{\mu;k}(\tau, x) = \int_0^\tau ds \int d^d y K(\tau - s, x - y) R_{\mu;k}(s, y). \tag{1.111}$$

1.5.2. Renormalization

In this perturbative expansion in the bare gauge coupling g_0 we shall study the renormalization properties of gradient flow exemplarily with an expansion of the energy density $\langle E \rangle = \frac{1}{4}\langle G^a_{\mu\nu} G^a_{\mu\nu} \rangle$. In leading order this can be expanded like

$$\begin{aligned} \langle E \rangle &= \frac{1}{2} g_0^2 \frac{N^2 - 1}{(8\pi\tau)^{d/2}} (d-1) \left(1 + c_1 g_0^2 + \mathcal{O}(g_0^4)\right), \text{ where} \\ c_1 &= \frac{1}{16\pi^2} (4\pi)^\epsilon (8\tau)^\epsilon \left(N \left(\frac{11}{3\epsilon} + \frac{52}{9} - 3\ln 3 \right) - N_f \left(\frac{2}{3\epsilon} + \frac{4}{9} - \frac{4}{3}\ln 2 \right) + \mathcal{O}(\epsilon) \right). \end{aligned} \tag{1.112}$$

The $\overline{\text{MS}}$-scheme relates the bare coupling g_0 to the renormalized coupling g. Terms proportional to $1/\epsilon$ cancel. In terms of the running coupling $\alpha(q) = \frac{g^2(q)}{2\pi}$ at length scales $q = \sqrt{8\tau}$, the smearing radius, the energy density reads

$$\begin{aligned} \langle E \rangle &= \frac{(d-1)(N^2-1)}{32\pi\tau^2} \alpha(q) \left(1 + k_1 \alpha(q) + \mathcal{O}(\alpha^2)\right), \text{ where} \\ k_1 &= \frac{1}{4\pi} \left(N \left(\frac{11}{3}\gamma_E + \frac{52}{9} - 3\ln 3 \right) - N_f \left(\frac{2}{3}\gamma_E + \frac{4}{9} - \frac{4}{3}\ln 2 \right) \right), \end{aligned} \tag{1.113}$$

which is in leading order always finite at non-vanishing flow time. That means that at leading order $\langle E \rangle$ is a renormalized quantity. Generally gauge invariant operators that are constructed from the flowed gauge field $B_\mu(x,t)$ are automatically renormalized, since the high momentum modes in $A_\mu(x,t)$ are exponentially suppressed in the smearing process.

1.5.3. Gradient flow on the lattice

When putting the gradient flow method to use on the lattice not the algebra valued gauge field but the group valued link variables are flowed. In analogy to the continuum expression the flow equation for the gauge transporters reads

$$\frac{d}{d\tau} V_\mu(x) = -g_0^2 \underbrace{\frac{\partial S[V]}{\partial V_\mu(x)}}_{\in su(N)} V_\mu(x), \tag{1.114}$$

with $V_\mu(x)\big|_{\tau=0} = U_\mu(x)$. The group derivative is defined by

$$\frac{\partial}{\partial V_\mu(x)} f(V) = \sum_a T^a \frac{\partial}{\partial V^a_\mu(x)} f(V) = \sum_a \frac{\partial}{\partial \alpha} f(e^{i\alpha T^a} V_\mu(x))\Big|_{\alpha=0}, \tag{1.115}$$

and thus the “force” term in the lattice flow equation is algebra valued. This term also appears in the equations of motion of the hybrid Monte Carlo algorithm, see Section 1.4.1.

The simplest choice for a lattice action is the Wilson gauge action, see Section 1.2.2, and gradient flow using this action is also called Wilson flow. Likewise if one uses the Symanzik or Iwasaki gauge action, see Sections 1.2.3 and 1.2.4, it is called Symanzik flow or Iwasaki flow respectively. The action can naturally also include matter fields.

In order to monitor the gradient flow evolution it is also useful to discretize the energy density. The field strength tensor can be discretized with the plaquette-like Clover leaf term like

$$G_{\mu\nu} = \tfrac{1}{4}\mathrm{Im}$$
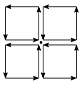

and the energy density is then simply given by its continuum expression $\langle E\rangle = \frac{1}{4}\langle G^a_{\mu\nu}G^a_{\mu\nu}\rangle$. Equivalently one can use the Wilson-like discretization of the energy density, which reads

$$E = 2\sum_x \sum_{\mu<\nu} \mathrm{Re}\,\mathrm{tr}\left[1 - P_{\mu\nu}(x)\right]. \tag{1.116}$$

The lattice flow equation then can numerically be solved with the Runge-Kutta integrator, see Appendix A.5.

1.5.4. Setting the scale with gradient flow

As we have seen before the higher orders of the bare coupling become more dominant with increasing flow time. The perturbative treatment of gradient flow is thus only applicable at small flow times ($q = \sqrt{8\tau} \approx 0.3$ fm or so). The energy density is independent of g_0 only in leading order. It develops a very non-trivial dependence on the flow time at next-to-leading order already. This means that the predictions from the perturbation series only hold while $\langle E\rangle$ is a renormalized, physical quantity, e.g. at small flow times.

Therefore, to fix the smearing radius of a gradient flow computation, we can set some dimensionless quantity to a suitable constant to fix the flow time and thus the smoothing scale.

A popular criterion to fix the scale was proposed by Lüscher [96]: from equation (1.113) we can see, that $\langle E\rangle \propto \frac{1}{\tau^2}$. A possible dimensionless quantity to set the scale would therefore be

$$\tau^2\langle E(\tau)\rangle\big|_{\tau=\tau_0} = c. \tag{1.117}$$

It has been observed, that $\tau^2\langle E(\tau)\rangle$ is approximately linear in τ at large flow times. From the requirement that the t'Hooft coupling $\lambda = g^2N$ for $SU(N)$ gauge theories remains approximately constant while $N \to N'$ in an $\frac{1}{N}$-expansion, Lüscher suggested

$$c = \begin{cases} 0.3 & \text{for } SU(3) \\ 0.2 & \text{for } SU(2) \end{cases}. \tag{1.118}$$

The t'Hooft coupling over a leading order perturbative expansion of $\tau^2\langle E(\tau)\rangle$ was plotted in Figure 1.8.

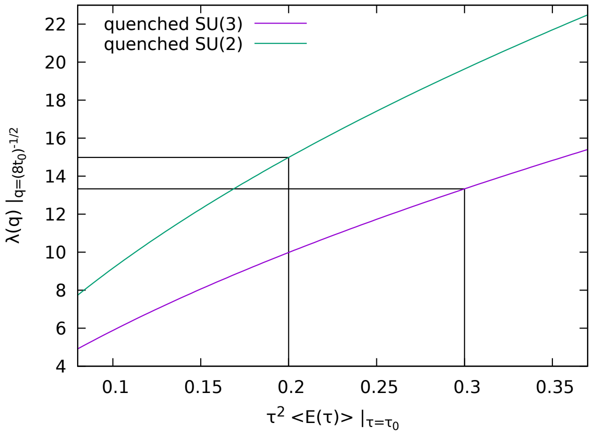

Figure 1.8.: The t'Hooft coupling over the dimensionless quantity $\tau^2\langle E(\tau)\rangle$ in quenched SU(N) gauge theory from a leading order expansion of the action density in the gauge coupling.

The Budapest-Marseille-Wuppertal collaboration suggested a similar criterion to fix the scale [100], that suffers less from discretization artifacts at small flow times. The dimensionless quantity that is being chosen is

$$W(\tau)\big|_{\tau=w_0^2} = \tau\frac{d}{d\tau}\left(\tau^2\langle E(\tau)\rangle\right)\big|_{\tau=w_0^2} = c, \tag{1.119}$$

and for $SU(3)$ one also chooses $c = 0.3$. While different values for $\tau^2\langle E(\tau)\rangle$ result in very different scales, different values for its derivative result in similar scales, since $\tau^2\langle E(\tau)\rangle$ is approximately linear at large flow times.

1.6. Chiral random matrix theory for Euclidean QCD

The Goldstone theorem states that the low-energy description of a theory is entirely dominated by its global symmetries. A spontaneous symmetry breaking creates massless particle excitations called *Goldstone bosons* [101]. For example the spontaneous symmetry breaking in a $O(3)$ spin system reduces the symmetry to $O(2)$ and the Goldstone modes are spin waves in the plane perpendicular to the polarization axis.

Low-energy QCD is well approximated with two light quarks and the pions are identified to be the Goldstone modes of the spontaneous chiral symmetry breaking, since their mass is much smaller than the mass of the other hadrons in the spectrum. As the quarks have a finite mass, chiral symmetry is also explicitly broken and the (pseudo-)Goldstone modes have a finite mass.

The fundamental assumption of random matrix theory (RMT) is that symmetries govern the whole theory and all interactions are equally likely [61]. The matrix elements of the Hamiltonian are replaced with uncorrelated random numbers such that all observables, for example energy levels, become averages over the random matrix elements. The global symmetries of the theory are obeyed by the random matrix and the distribution of matrix elements is conserved. This means that a random matrix ensemble of a theory can only reproduce its macroscopic and universal features, and microscopic properties of the theory are not reflected. This can especially be of great use for studying critical phenomena where the correlation lengths diverge. The observables thus do not depend anymore on microscopic features, which is commonly referred to as *scale separation*.

RMT has proven to be an invaluable tool for studying nuclear resonances [102]. It can, however, also be applied to discretized gauge theories. When applying RMT to a lattice gauge theory it is expected that the spectral properties of the theory on the scale of the average lattice spacing are universal. In the continuum limit, the inverse lattice spacing diverges, similar to a correlation length.

For low-energy QCD the Dirac matrix can readily be replaced with a random matrix with the same global symmetries, whose elements have no space-time dependence. Chiral symmetry breaking can be observed in the limit of infinitely large random matrices, and the partition function is then dominated by the Goldstone modes, the pions. The RMT model of low-energy QCD is then constructed, such that the eigenfunctions are distributed uniformly over the unitary unit sphere.

In order to extract spectral properties from a RMT of QCD any microscopic feature of the RMT must be removed, such that only universal features remain. For example the level spacings must be *unfolded*, which means rescaling, such that the average level spacing is unity. This is a common technique to study energy levels in many-body quantum theories, where the complete level spacing distribution is unobtainable or expensive to extract [103,104].

An ordered sequence of energy levels $\{\lambda_0, ..., \lambda_N\}$ is mapped on a new set of variables, the *unfolded levels* $\{\xi_0, ..., \xi_N\}$, and the system specific mean level density is removed. The cumulative spectral function of λ contains a smooth and a fluctuating part like

$$\eta(\lambda) = \int_{-\infty}^{\lambda} \sum_{n=0}^{N} \delta(\lambda' - \lambda_n) d\lambda' = \xi(\lambda) + \eta_{\text{fluct}}(\lambda) \tag{1.120}$$

and $\eta_{\text{fluct}}(\lambda)$ depends solely on the non-universal features while we identify the smooth part $\xi(\lambda)$ with the unfolded variable. The smooth cumulative levels are determined from a fit (in our computations with a polynomial function) and the fluctuating part is discarded. The unfolded level spacing variable is then

$$s_j = \frac{|\xi_{j+1} - \xi_j|}{|\langle \xi_{j+1} - \xi_j \rangle|}, \tag{1.121}$$

where $\xi_j = \xi(\lambda_j)$. The distribution of the spacing variable is called the *unfolded level spacing distribution* (ULSD).

For some random matrix ensembles a prediction for the ULSD is possible. For example for entirely uncorrelated eigenmodes the level spacings are uncorrelated as well and the ULSD is

$$P(s) = P_{\text{Poisson}}(s) = e^{-s}. \tag{1.122}$$

If the eigenmodes of the theory are not uncorrelated, the random matrix ensembles can be classified depending on the anti-unitary symmetries of the Dirac operator. The RMT prediction for the ULSD is then a Wigner surmise that approximates the level spacing density of 2×2 matrices with different anti-unitary symmetries. This Wigner surmise reads

$$P(s) = a(\beta_D) s^{\beta_D} e^{-b(\beta_D) s^2} \tag{1.123}$$

where β_D denotes the Dyson index and

$$a(\beta_D) = 2\frac{\left(\Gamma(\frac{\beta_D}{2} + 1)\right)^{\beta_D+1}}{\left(\Gamma(\frac{\beta_D+1}{2})\right)^{\beta_D+2}} \quad \text{and} \quad b(\beta_D) = \frac{\left(\Gamma(\frac{\beta_D}{2} + 1)\right)^2}{\left(\Gamma(\frac{\beta_D+1}{2})\right)^2}, \tag{1.124}$$

where $\Gamma(x) = \int_0^\infty t^{x-1} e^{-t} dt$ for $x \in \mathbb{R}$. The factors $a(\beta_D)$ and $b(\beta_D)$ are chosen, such that

$$\int_0^\infty ds P(s) = 1 \quad \text{and} \quad \langle s \rangle = \int_0^\infty ds P(s) s = 1. \tag{1.125}$$

The ULSDs for different anti-unitary symmetries are listed in Table 1.1 and plotted in Figure 1.9. As opposed to entirely uncorrelated eigenmodes, whose level spacings follow a Poisson distribution, the level spacings of these ensembles present a level repulsion as the Wigner surmise vanishes for zero distance and the repulsion of levels at short distances behaves like $\propto s^{\beta_D}$.

Table 1.1.: The Wigner surmise for the unfolded level spacing distributions of three different random matrix ensembles and Dyson indices β_D.

ensemble	β_D	matrix elements	ULSD
orthogonal	1	real	$P_{\beta_D=1}(s) = \frac{\pi}{2} s \exp(-\frac{\pi}{4} s^2)$
unitary	2	complex	$P_{\beta_D=2}(s) = \frac{32}{\pi^2} s^2 \exp(-\frac{4}{\pi} s^2)$
symplectic	4	quaternion real	$P_{\beta_D=4}(s) = \left(\frac{8}{3}\right)^6 \frac{1}{\pi^3} s^4 \exp(-\left(\frac{8}{3}\right)^2 \frac{1}{\pi} s^2)$

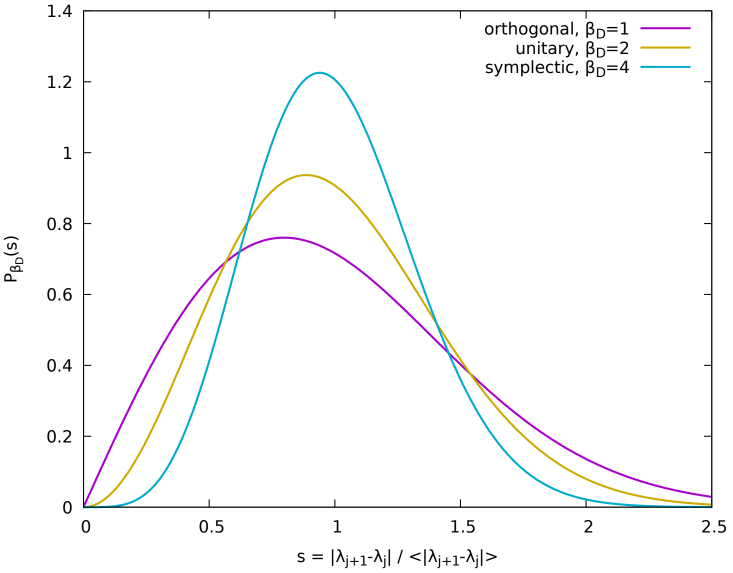

Figure 1.9.: The Wigner surmise for the unfolded level spacing distributions of three different random matrix ensembles. Note that due to the unfolding procedure, the average level spacing is unity.

1.7. The Anderson model for disordered solids

Electron dynamics in crystal structures or lattices are commonly described with the tight-binding approximation. In his seminal paper titled "Absence of Diffusion in Certain Random Lattices" [105] P. W. Anderson studied non-interacting electrons in a disordered crystal using a tight-binding model with a random on-site potential. It was observed that electron eigenstates exhibit an exponential decay in the presence of strong disorders, and that there is a metal-insulator transition within the spectrum of the Hamiltonian. This transition is commonly referred to as an *Anderson transition*, with the energy at which it occurs called the *mobility edge*. The random potential that models lattice defects in conducting crystals creates a localization of electron modes such that the conductivity vanishes. No potential well creates this localization, but rather interference of the wave functions, which "scatter" off the lattice impurities. Anderson localization thus has no classical analogon.

A comprehensive review on the physics of electron localization in disordered solids is given in [106].

In 1997 Slevin and Ohtsuki used a finite size scaling analysis in the Anderson model to obtain a prediction of the critical exponents for two different symmetry classes, orthogonal and unitary [107]. The spectral statistics of the Anderson models are described with Wigner-Dyson random matrix theories [108]. Anderson tight-binding Hamiltonians can have different universal symmetries, which are categorized with their Dyson index: the orthogonal ($\beta_D = 1$), the unitary ($\beta_D = 2$) and the symplectic ($\beta_D = 4$) Anderson model. The unfolded level spacing distributions for delocalized modes in each model follow the corresponding Wigner-Dyson surmises, see Table 1.1, while the localized level spacings follow a Poisson distribution.

In [109, 110] the time evolution of initially localized electron modes whose dynamics are governed by the Anderson Hamiltonian are studied by solving the time-dependent Schrödinger equation numerically. Electron diffusion was measured using the quadratic displacement $r^2(t) = \int d^d r r^2 \langle \psi(r,t) | \psi(r,t) \rangle$. For a particle which propagates according to "ordinary" diffusion this quantity goes like $\lim_{t\mapsto\infty} r^2(t) = Dt$, where D is the diffusion constant. For a localized particle the displacement is limited from above.

The multifractal properties of the critical modes at the Anderson transition for the three Wigner-Dyson classes in three dimensions are studied in [111], where the critical exponents are determined using a finite-size scaling analysis of generalized multifractal exponents.

The Wigner-Dyson class of an Anderson model is determined from the matrix elements of its Hamiltonian. For the *orthogonal Anderson model* the matrix elements are real and the Dyson index reads $\beta_D = 1$. The corresponding random matrix ensemble is orthogonal. This Anderson model contains both time reversal and spin rotation symmetry and its Hamiltonian is given by

$$H = \sum_r \rho(r) |r\rangle\langle r| + \kappa \sum_{\langle r,r'\rangle} |r\rangle\langle r'|, \tag{1.126}$$

where $\kappa \in \mathbb{R}$ (the hopping parameter) and $\langle r, r'\rangle$ denotes nearest neighbours. The random on-site potential is distributed like $\rho(x) \in \left[-\frac{w}{2}, \frac{w}{2}\right]$. The critical disorder for the $E = 0$ electron modes in the three-dimensional orthogonal Anderson model was determined in [108] to be $\frac{w_c}{\kappa} \approx 16.5$.

In the *unitary Anderson model* the matrix elements are generally complex and the Dyson index is $\beta_D = 2$. Time reversal symmetry is broken by an external magnetic field and the Hamiltonian reads

$$H = \sum_r \rho(r) |r\rangle\langle r| + \kappa \sum_{\langle r,r'\rangle} e^{-i2\pi\varphi\delta_{r,r'+\hat{z}}} |r\rangle\langle r'|, \tag{1.127}$$

where φ denotes the magnetic flux and $\hat{z}$ denotes the unit vector in the z-direction.

The *symplectic Anderson model* however exhibits both a broken time reversal and a broken spin rotation symmetry. When a spin-orbit coupling is added to the model, the matrix elements become quaternion-selfdual and the Wigner-Dyson symmetry class becomes symplectic ($\beta_D = 4$). In the symplectic model the Anderson transition already occurs in two dimensions, while for the orthogonal and unitary Anderson model it only occurs for three or more dimensions. The symplectic Anderson tight binding Hamiltonian reads

$$H = \sum_{r,\sigma} \rho(r) |r,\sigma\rangle\langle r,\sigma| + \sum_{\langle r,r'\rangle,\langle\sigma,\sigma'\rangle} \kappa_{r,r'}^{\sigma,\sigma'} |r,\sigma\rangle\langle r',\sigma'|, \tag{1.128}$$

where the hopping matrix consists of quaternion real 2×2 matrices in spinor space, which can be written like

$$\kappa_{r,r'} = 1 + i\mu \sum_{j=1}^{3} \kappa^j \sigma_j = \begin{pmatrix} 1 + i\mu\kappa^3 & \mu\kappa^2 + i\mu\kappa^1 \\ -\mu\kappa^2 + i\mu\kappa^1 & 1 - i\mu\kappa^3 \end{pmatrix}_{r,r'}. \tag{1.129}$$

The coefficients $\kappa^j \in \left[-\frac{1}{2}; \frac{1}{2}\right]$ are sampled uniformly random and σ_j are the Pauli matrices.

An Anderson model is called *chiral*, if the on-site term is vanishing but the hopping matrix elements are chosen randomly. This causes an additional chiral symmetry to arise between two sublattices.

As a measure for localization and delocalization a wave function can be assigned a so-called *inverse participation ratio* (IPR) of some order n, which reads

$$\nu_n^{-1} = \int d^d x \left(\psi^\dagger(x)\psi(x)\right)^n . \tag{1.130}$$

Its inverse is thus called *participation ratio* (PR). The second order PR ν_2 is proportional to the volume that is occupied by the wave function and can thus be used to quantify the degree of localization. This quantity will later be used to estimate the volume that is occupied by the eigenmodes of the QCD Dirac operator, see Section 2.3. In the Anderson model an extended wave function spreads over the volume like

$$\nu_2 \propto D\sqrt{t}. \tag{1.131}$$

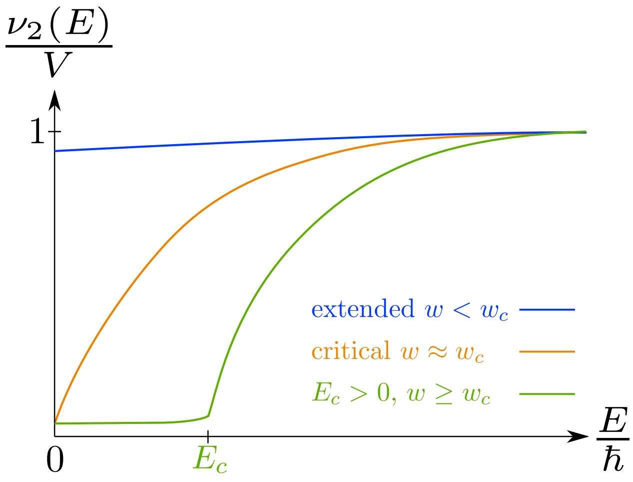

Figure 1.10.: A sketch of the normalized electron participation ratio ν_2/V for disorder terms w below, close to and above the Anderson transition in condensed matter.

The normalized participation ratio of electron modes $\frac{\nu_2(E)}{V}$ at an energy E is sketched in Figure 1.10. For disorders below the critical value all modes are extended over the whole volume. At the critical disorder w_c the ground state localized such that the conductivity vanishes. For larger disorder potentials the mobility edge E_c moves to finite values.

2. The QCD Anderson transition

In this chapter the quark mode localization in the lower spectral regime of the QCD Dirac operator will be studied. The transition from localized to extended quark wave functions within the spectrum of the Dirac operator is called the QCD Anderson transition, in analogy to the metal-insulator transition in the Anderson model from condensed matter physics (described in Section 1.7), and occurs at temperatures above the chiral transition.

For this examination of wave functions, the overlap operator was diagonalized and its lowest eigenmodes were analysed for several temperatures and for two different lattice spacings. This setup allows us to study the temperature dependence of the localization energy along with many other aspects of quark localization.

In the end of this chapter, we will present a mechanism driven by the local Polyakov loop that causes localization.

2.1. Lattice setup

To diagonalize the Dirac operator and to extract eigenvalues and -vectors we used the implicitly restarted Arnoldi method (IRAM), which was described by W.E. Arnoldi [112], as provided by the ARPACK library [113]. The software implementing the overlap operator, the Zolotarev approximation and the Remez algorithm, that was used for the following computations was specifically designed for this survey. The implementation is described in detail in Appendix B.

2.1.1. Configurations

For this project we used lattice configurations created by the twisted mass at finite temperature (tmfT) collaboration [114, 115]. These configurations are listed comprehensively in [116].

Since a fixed scale approach was employed, the generation of the configurations and the tuning of the twist parameter could be done analogous to the computations done by the European twisted mass collaboration (ETMC) for zero temperature calculations [117–120]. The lattice spacings are based on [121].

The finite temperature ensembles used here were generated with $N_f = 2 + 1 + 1$ dynamical flavours of twisted mass Wilson quarks at maximal twist, with two degenerate light fermions and two non-degenerate heavy fermions as described in [122], and the Iwasaki gauge action.

In the valence band we studied overlap fermions (see Section 1.3.3), since they provide a chiral symmetry with respect to the Ginsparg-Wilson equation and obey an Atiyah-Singer index theorem. The scaling parameter we used was $\rho = 1.4$ and the spectrum was computed at the quark mass $m_q = 0$.

For these finite temperature computations in QCD the sign function in the overlap operator was computed using the Zolotarev approximation, as described in Appendix B.2. An overview of the ensembles we used, the number of configurations, and the number of eigenmodes that were computed on each configuration is given in Table 2.1.

Table 2.1.: An overview of the tmfT ensembles used in this work, the number of configurations on which overlap eigenmodes were computed and the number of eigenmodes per configuration. The chiral transition temperatures T_c were taken from [115].

Ensemble	N_t	T / MeV	T/T_c	# conf.	$\frac{\text{modes}}{\text{conf}}$
A370 $N_s = 24$ $a = 0.0936(13)$ fm $m_\pi = 364$ MeV $T_c = 184(4)$ MeV	4	527.06(7.32)	2.86(07)	98	512
	5	421.65(5.86)	2.29(06)	63	512
	6	351.37(4.88)	1.91(05)	111	512
	7	301.18(4.18)	1.64(04)	101	512
	8	263.53(3.66)	1.43(04)	100	512
	9	234.25(3.25)	1.27(03)	101	512
	10	210.82(2.93)	1.15(03)	99	512
D370 $N_s = 32$ $a = 0.0646(7)$ fm $m_\pi = 369$ MeV $T_c = 184(4)$ MeV	3	1018.21(11.03)	5.53(13)	96	300
	6	509.11(5.52)	2.77(07)	71	300
	14	218.19(2.36)	1.19(03)	121	190
D210 $N_s = 48$ $a = 0.0646(7)$ fm $m_\pi = 213$ MeV $T_c = 152(5)$ MeV	4	763.66(8.27)	5.02(17)	7	160
	8	381.83(4.14)	2.51(09)	26	80

2.1.2. Eigenmode projection

Overlap fermions solve the Ginsparg-Wilson equation exactly, thus providing a remnant chiral symmetry on the lattice. From this it follows that the eigenvalues of the overlap Dirac operator lie on the Ginsparg-Wilson circle with radius ρ/a

$$\operatorname{Im}\lambda = \pm\sqrt{\frac{2\rho}{a}\operatorname{Re}\lambda - (\operatorname{Re}\lambda)^2}, \tag{2.1}$$

which is shown in Section 1.3.1. Due to the γ_5-hermiticity the non-zero eigenvalues come in complex conjugate pairs. For most computations we restrict our considerations on the positive branch $\operatorname{Im}\lambda > 0$.

The continuum limit of the spectral distribution of a Ginsparg-Wilson Dirac operator can be mimicked by projecting the eigenvalues onto the imaginary axis. For this we used a stereographic projection, which is illustrated in Figure 2.1.

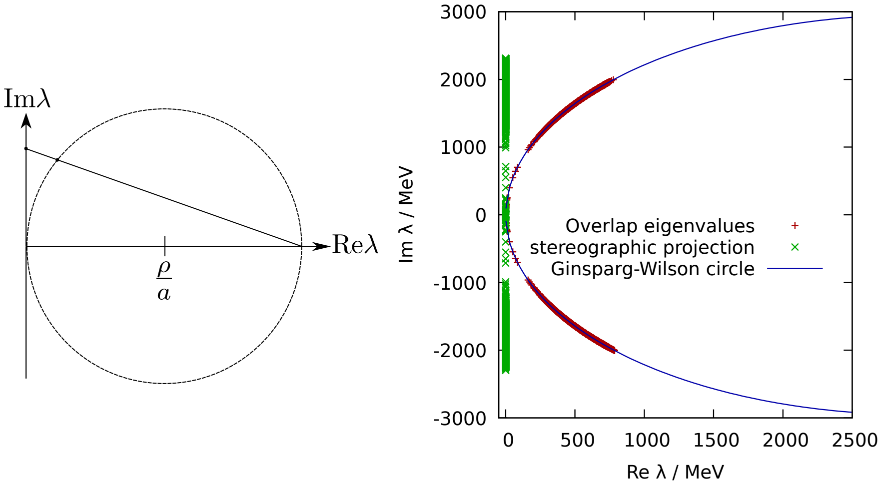

Figure 2.1.: *Left*: A sketch of the stereographic projection of the eigenvalues at finite a onto the imaginary axis. *Right*: The projection of the eigenvalues on a single configuration at T=421.65(5.86) MeV.

An eigenvalue on the circle is projected from the north pole (at $\mathrm{Re}\,\lambda = 2\rho/a$) to $\mathrm{Re}\,\lambda = 0$ like

$$\mathrm{Im}\,\lambda' = \frac{\frac{2\rho}{a}\,\mathrm{Im}\,\lambda}{\mathrm{Re}\,\lambda - \frac{2\rho}{a}}. \tag{2.2}$$

The parameter ρ can be adjusted to compare two different lattice spacings, since two Ginsparg-Wilson circles with (a, ρ) and (a', ρ') fall onto each other if $\frac{\rho}{\rho'} = \frac{a'}{a}$.

2.2. The Banks-Casher gap

The spectral density of a chiral Dirac operator can be related to the spontaneous breaking of chiral symmetry. The Banks-Casher relation (see equation (1.65)) relates the density of low eigenmodes with the chiral condensate: when chiral symmetry is broken, we find $\langle\overline{\psi}\psi\rangle \propto \lim_{\lambda\to 0}\rho(\lambda) > 0$, while a restored chiral symmetry is reflected in $\lim_{\lambda\to 0}\rho(\lambda) = 0$. This means that above the critical temperature for the chiral transition a gap opens in the spectral density of the Dirac operator.

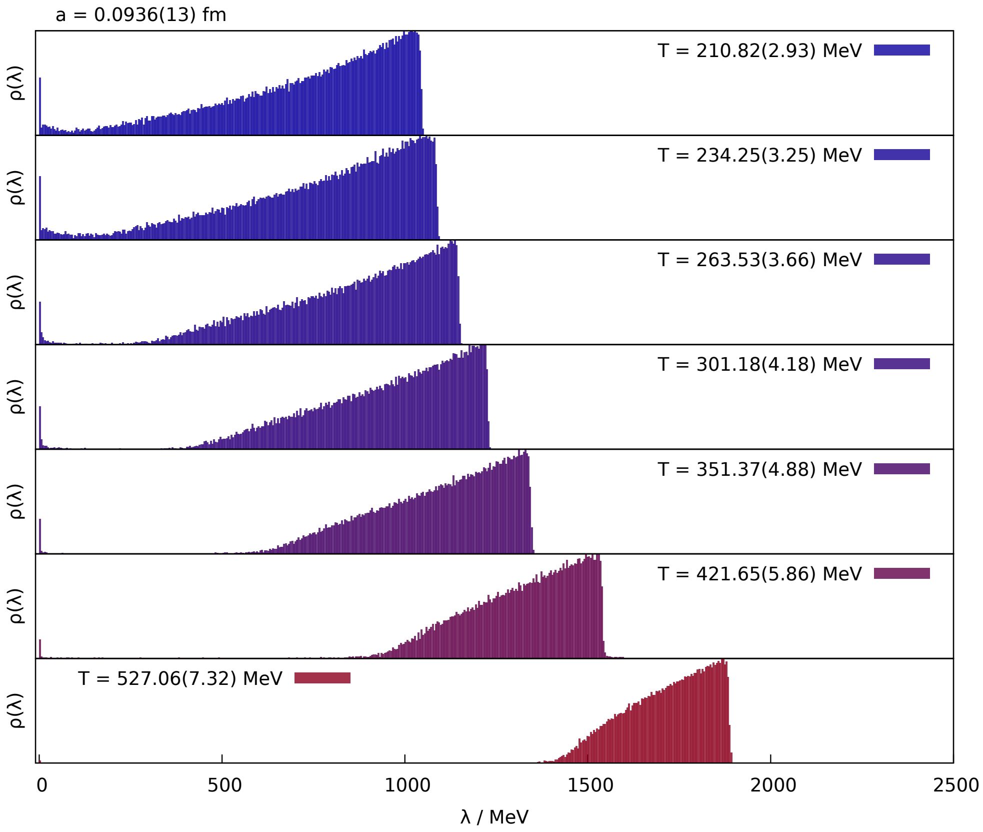

Figure 2.2.: The distribution of the overlap eigenvalues for the A370 meta ensemble (a = 0.0936(13) fm). Due to finite volume effects, there are still eigenmodes within the Banks-Casher gap at small temperatures.

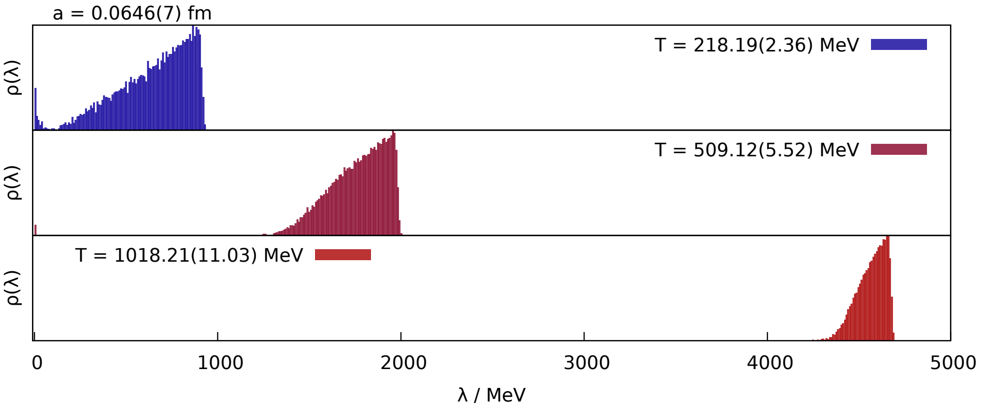

Figure 2.3.: The distribution of the overlap eigenvalues for the D370 meta ensemble (a = 0.0646(7) fm).

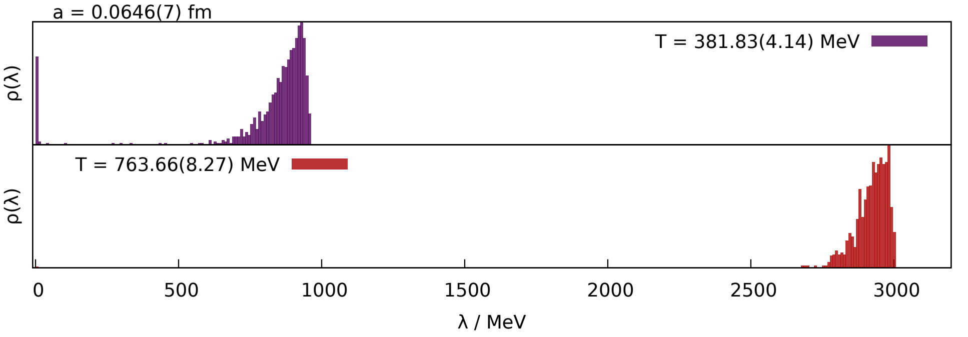

Figure 2.4.: The distribution of the overlap eigenvalues for the D210 meta ensemble (a = 0.0646(7) fm).

The distribution of eigenvalues on the A370, D370 and D210 meta ensembles are plotted for several temperatures in Figures 2.2, 2.3 and 2.4. The chiral transition for these temperatures occurs at T_c = 184(4) MeV [115]; all the presented temperatures are in the chirally restored phase. We observe, however, that at small temperatures in the vicinity of T_c there are still modes present within the Banks-Casher gap; it has not fully opened. This effect is caused by the finite physical volume and subject to closer inspection in Section 4.5.3.

Also, each ensemble contains zero modes which are eigenmodes to γ_5 and hence chiral. The spectral density thus does not vanish for $\lambda = 0$, but chiral symmetry is not broken by these modes.

2.3. The temperature dependence of the mobility edge

The spectral position below which the quark eigenmodes are localized is called the mobility edge λ_c. In the following we will define a criterion for the mobility edge, using the space-time volume, that is occupied by the eigenmodes, and study the dependence of λ_c on the temperature.

In a previous survey conducted by Giordano *et al.* in 2013 [123] it was shown that the QCD Anderson transition becomes of second order in the thermodynamic limit. It is also shown that the critical exponent of this transition within the Dirac operator spectrum $\nu_{\mathrm{QCD}} = 1.43(6)$ matches the critical exponent of the delocalization transition in the unitary Anderson model $\nu_{uA} = 1.43(4)$ (as computed in [107]) very well.

In [124] the temperature dependence of the Anderson transition point was studied from lattice simulations, using $N_f = 3$ unimproved staggered quarks with the Wilson gauge action. In this study the temperature was adjusted by the inverse gauge coupling, and thus the lattice spacing. In order to identify the mobility edge, the integrated unfolded level spacing distribution was computed, as it takes an universal value at the critical point. This model exhibits a sharp chiral transition at the temperature where λ_c becomes non-vanishing. It is hence conjectured that the temperature plays a similar role as the disorder parameter in the condensed matter Anderson model. We will present evidence based on the Polyakov loop that supports this conjecture in Section 2.6.

This method was also used in [125] where the Anderson transition was studied in quenched two colour QCD and in QCD with $N_f = 2 + 1$ dynamical flavours of staggered quarks at the physical point. The mobility edge was here identified as the scale-invariant fixed point of the level spacing distribution and it was found that it also vanishes at the chiral transition.

In this survey of the mobility edge in QCD, we use the relative volume that is occupied by an eigenmode to probe and quantify localization. We define λ_c to be either the spectral position of the inflection point of this relative eigenvector volume $r(\lambda)$, which is also the point of maximal fluctuations of the participation ratio, or the spectral position where $r(\lambda)$ has increased by some factor compared with the volume of localized modes.

The inverse participation ratio (IPR) of the n-th order is a well-known quantity from condensed matter physics. It is defined with respect to some density (in our case $\langle\psi(x)|\psi(x)\rangle$) and a volume (here V being the total number of lattice points) and reads

$$\nu_n^{-1} = \int_V d^d x \langle\psi(x)|\psi(x)\rangle^n. \tag{2.3}$$

A maximally localized mode only occupies one lattice site, thus $\langle\psi(x)|\psi(x)\rangle = \delta_{x,0}$. The n-th order IPR is then

$$\nu_n^{-1} = \int_V d^d x \delta_{x,0}^n = 1 \Rightarrow \nu_n = 1. \tag{2.4}$$

A maximally extended, thus homogeneously distributed eigenmode, where $\langle\psi(x)|\psi(x)\rangle = \frac{1}{V}$, on the other hand yields an IPR like

$$\nu_n^{-1} = \int_V d^d x \frac{1}{V^n} = \frac{1}{V^{n-1}} \Rightarrow \nu_n = V^{n-1}. \tag{2.5}$$

Since the second order participation ratio ν_2 is proportional to the volume that the eigenmode occupies we can define the relative eigenmode volume like

$$r(\lambda) = \frac{\nu_2(\lambda)}{V} \in (0,1]. \tag{2.6}$$

This quantity was computed for many eigenmodes and averaged in small bins of λ. The inflection point of r is located at the energy where the fluctuations among the participation ratios are maximal and the second moment peaks. This point was determined from a fit to $r(\lambda)$ and used as an estimate for the mobility edge like

$$\left.\frac{\partial^2 r(\lambda)}{\partial \lambda^2}\right|_{\lambda=\lambda_c} = 0. \tag{2.7}$$

The estimates for λ_c that were obtained this way are listed in Table 2.2.

Alternatively we studied the relative growth of eigenmodes with respect to the modes in the localized regime. We estimated the mobility edge with the spectral position where the eigenmodes have expanded their volume by a factor of n like

$$\left.\frac{r(\lambda)}{r(0)}\right|_{\lambda=\lambda_c} = n. \tag{2.8}$$

The estimated mobility edges from this criterion are listed in Table 2.3 for $n = 3$, $n = 4$ and $n = 5$. At the smallest temperatures this criterion was not applicable anymore, as a localized regime could not clearly be distinguished. Also the volume of localized modes is possibly not constant, as it was observed in [126], and can thus not be properly used as a scale for delocalization effects. Furthermore, in Section 4.5.3 it is found that the relative volume of the localized modes is easily polluted by finite volume effects, such that the latter criterion for the mobility edge will only be qualitatively studied here.

In Figures 2.5 and 2.6 the relative eigenvector volume is plotted for several temperatures on the A370 and the D370 meta ensemble, averaged in small bins of the size $a\Delta\lambda = 0.01$. The inflection points that were determined from a fit are indicated with a circle. In Figures 2.7 and 2.8 the local fluctuations in each bin of the eigenmode volume are plotted. The maxima of these susceptibilities coincide with the inflection points and can equivalently be used as an estimator for the mobility edge.

For both estimation methods the mobility edge agrees well with a linear extrapolation to T_c, which is shown in Figure 2.9 for the inflection point method and in Figure 2.10 for the relative growth method.

This linear extrapolation allows us to conclude that below T_c all eigenmodes are delocalized and the mobility edge vanishes. The Dirac operator and the correlations between its matrix elements are only governed by its global symmetries, and spectral statistics are entirely described with random matrix ensembles.

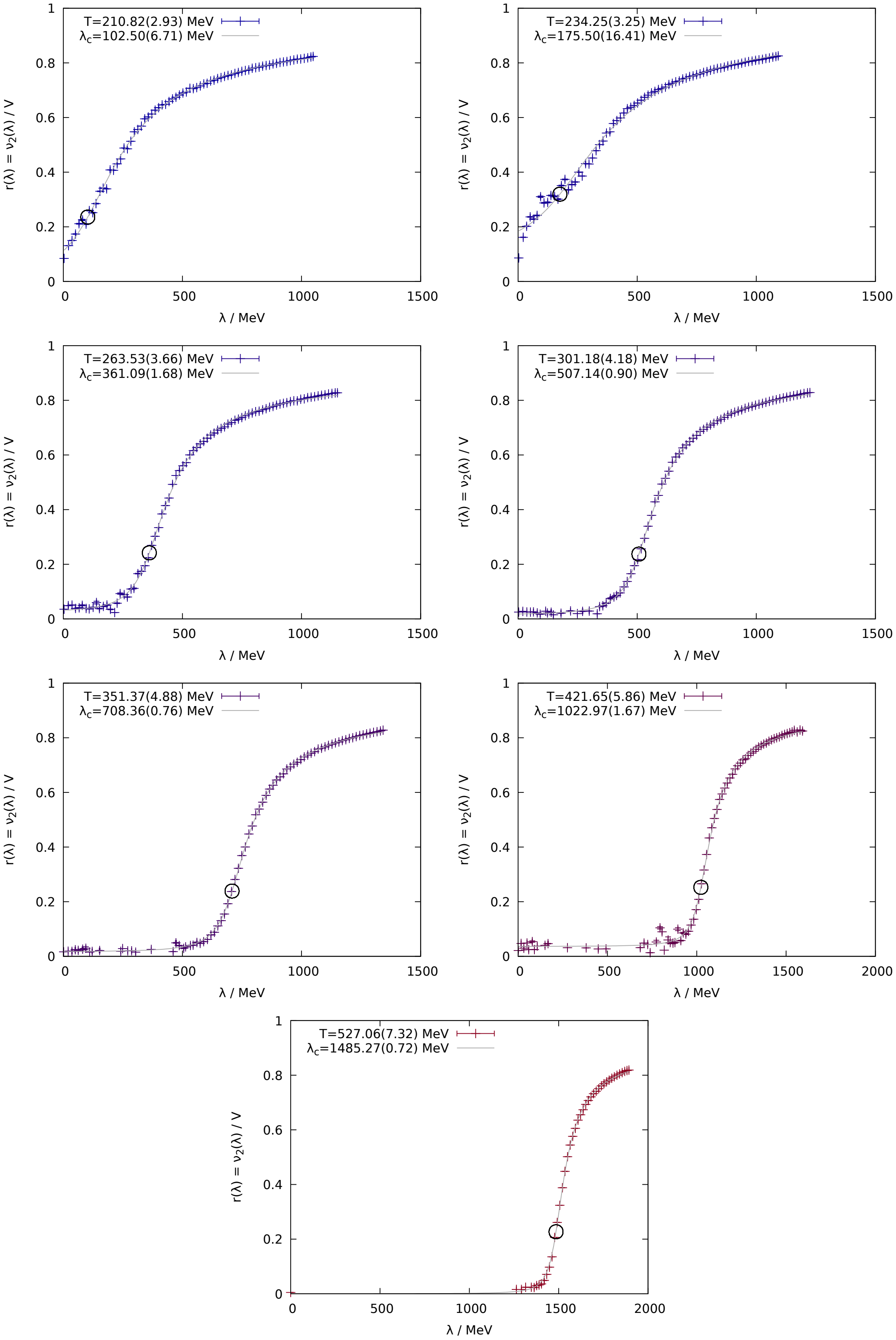

Figure 2.5.: The relative eigenvector volume over λ for several temperatures on the A370 meta ensemble. The inflection points (indicated by a circle) were determined by a fit.

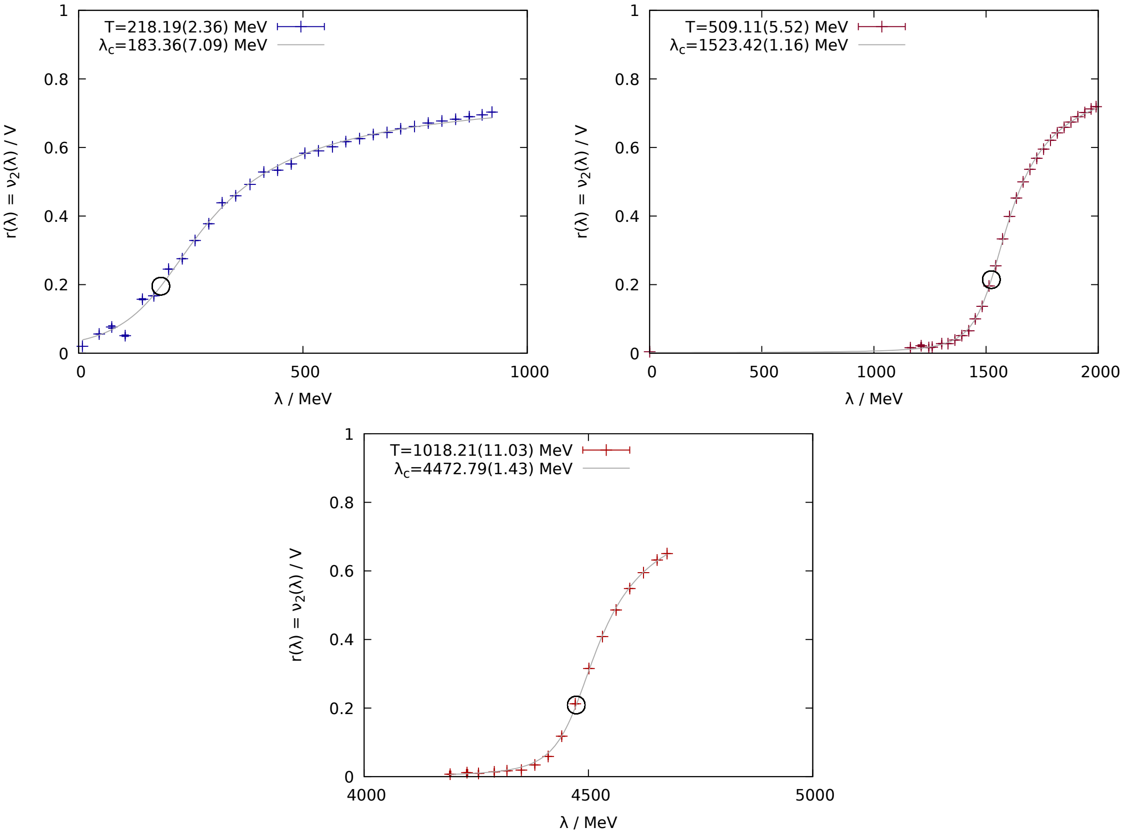

Figure 2.6.: The relative eigenvector volume over λ for several temperatures on the D370 meta ensemble.

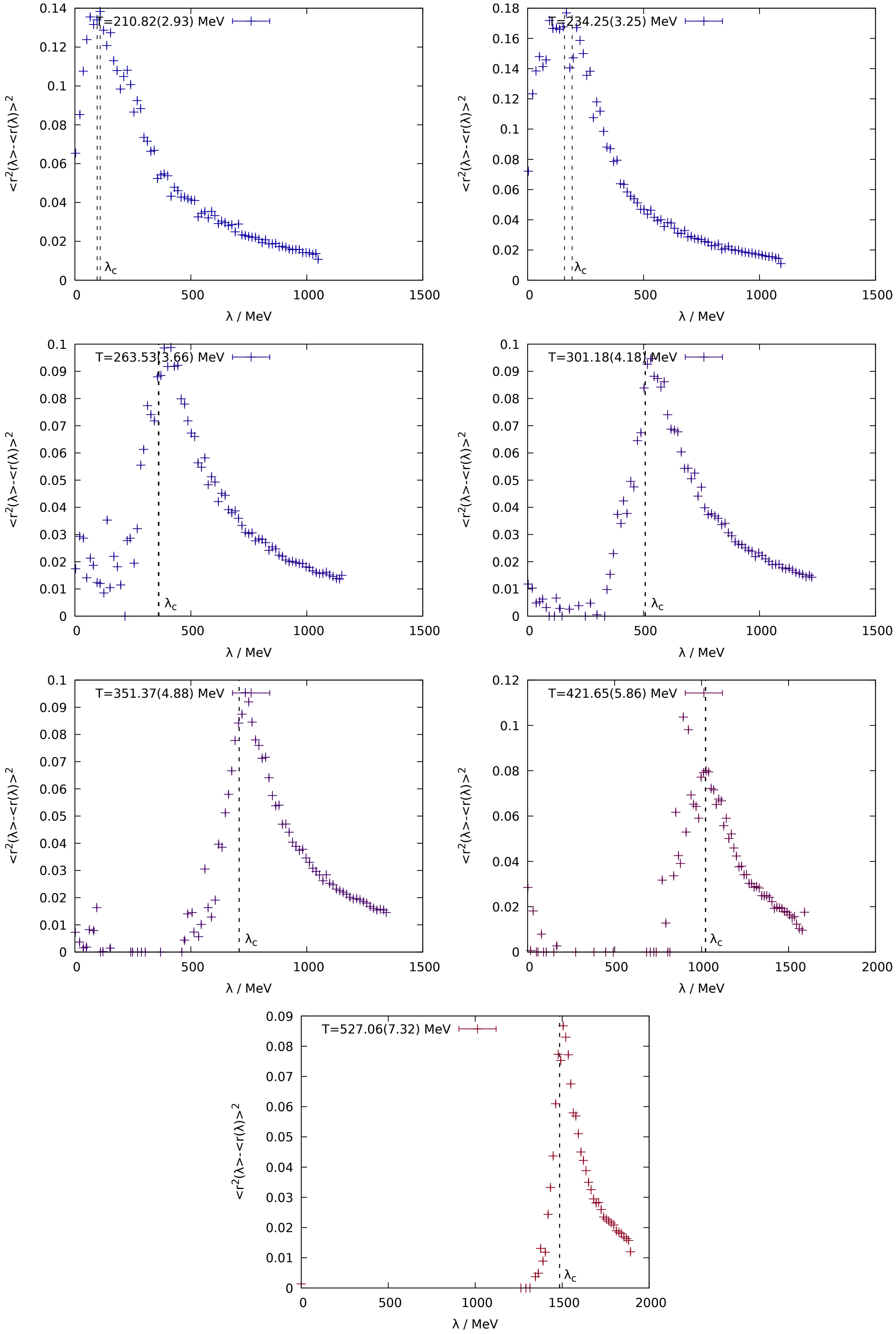

Figure 2.7.: The local fluctuations of the relative eigenmode volume on the A370 meta ensemble. The maximum of this susceptibility is well matched by the mobility edge, that was estimated with the inflection point of $r(\lambda)$ (vertical lines).

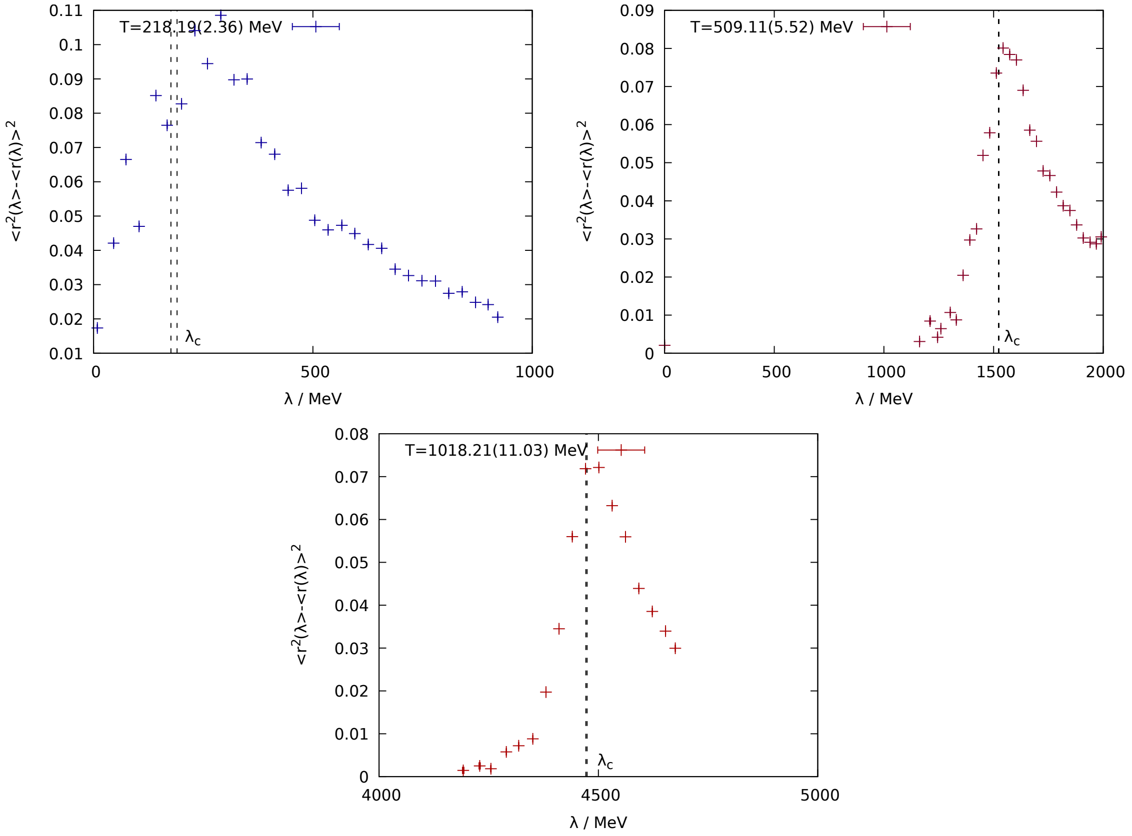

Figure 2.8.: The local fluctuations of the relative eigenmode volume on the D370 meta ensemble.

Table 2.2.: The mobility edges over the temperature, determined from the inflection point from the eigenmode volume $\frac{\partial^2 r(\lambda)}{\partial \lambda^2}\Big|_{\lambda=\lambda_c} = 0$, also plotted in Figure 2.9.

Ensemble	N_t	T / MeV	λ_c / MeV
A370	4	527.06(7.32)	1485.27(0.72)
	5	421.65(5.86)	1022.97(1.67)
	6	351.37(4.88)	708.36(0.76)
	7	301.18(4.18)	507.14(0.90)
	8	263.53(3.66)	361.09(1.68)
	9	234.25(3.25)	175.50(16.41)
	10	210.82(2.93)	102.50(6.71)
D370	3	1018.21(11.03)	4472.58(0.98)
	6	509.11(5.52)	1523.01(1.00)
	14	218.19(2.36)	181.68(6.38)

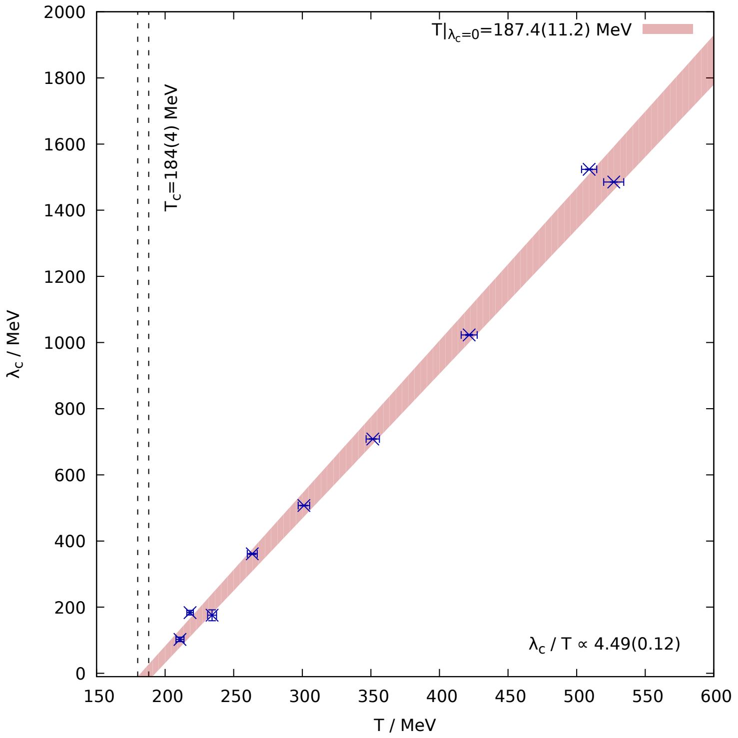

Figure 2.9.: The mobility edge over temperature, where λ_c was extracted from the inflection point of the relative eigenmode volume. $T_c = 184(4)$ MeV is the critical temperature for the chiral restoration transition taken from [115]. λ_c can be linearly extrapolated to zero at the chiral transition.

Table 2.3.: The mobility edges over the temperature, estimated from the point where the eigenmodes have delocalized by a factor n like $\frac{r(\lambda)}{r(0)}\big|_{\lambda=\lambda_c} = n$, also plotted in Figure 2.10. For the low temperatures the volume of localized modes could not be extracted.

Ensemble	N_t	T / MeV	λ_c / MeV for $n = 3$	λ_c / MeV for $n = 4$	λ_c / MeV for $n = 5$
A370	4	527.06(7.32)	1418.73(1.77)	1433.54(1.39)	1444.43(1.18)
	5	421.65(5.86)	954.34(3.11)	978.85(2.37)	995.69(2.02)
	6	351.37(4.88)	592.90(2.03)	622.22(1.51)	642.07(1.25)
	7	301.18(4.18)	393.82(2.18)	423.33(1.65)	443.90(1.38)
	8	263.53(3.66)	299.30(2.53)	326.80(2.09)	347.93(1.91)
	9	234.25(3.25)	-	-	-
	10	210.82(2.93)	-	-	-
D370	3	1018.21(11.03)	4361.35(4.46)	4381.16(3.42)	4395.28(2.83)
	6	509.11(5.52)	1327.13(5.35)	1361.77(3.92)	1386.17(3.14)
	14	218.19(2.36)	-	-	-

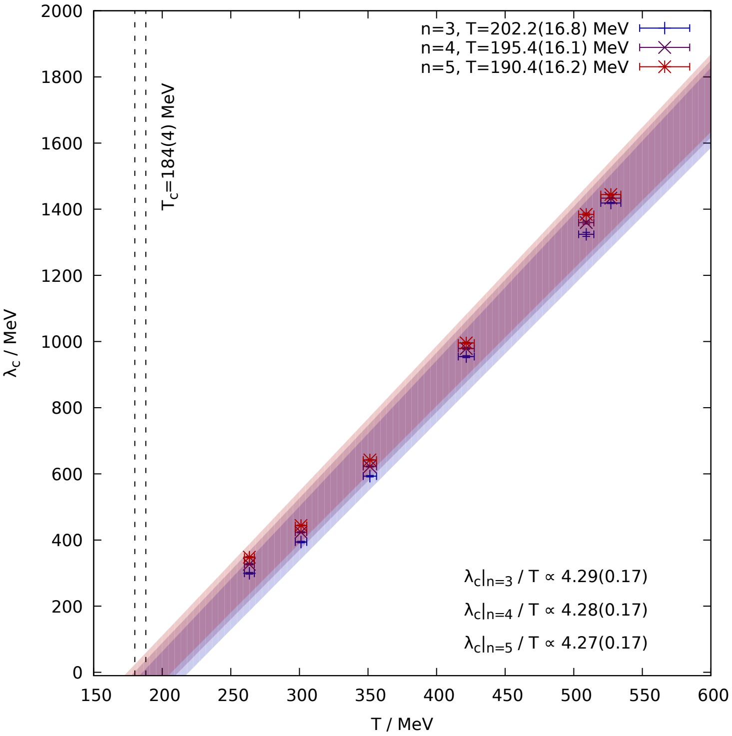

Figure 2.10.: The mobility edge over temperature, where λ_c was defined to be the spectral position, where the eigenmode volume has increased by a factor n. Here the linear extrapolation indicates as well, that the mobility edge vanishes at $T = T_c$.

We find, that the mobility edge vanishes, when the temperature is decreased to and below the chiral transition temperature and localized modes exclusively exist above the chiral transition temperature. The opening of a localized sector in the spectrum is connected to the restoration of chiral symmetry, as was already suspected in [124]. Our findings also allow to conclude, that the temperature dependence of the mobility edge is linear and the slope is

$$\frac{\lambda_c}{T} \propto 4.49(12). \tag{2.9}$$

2.4. Morphology of quark wave functions

In the following section we will study the different morphological and geometrical aspects of eigenmodes in the localized, the critical, and the extended eigenvalue regimes. It was found in [127] that critical eigenmodes provide a multifractal structure, and we will attempt to find indications for this in our setup. We will further study the correlation functions of the chiral densities for selected eigenmodes in order to shed some light on the local structure of quark wave functions and define moments of the wave functions and their chiral components, similar to the moments of inertia of a mass distribution. This will allow us to gain some insight in their geometry and spatial structure.

2.4.1. Fractal dimensions

In this section we will present the fractal dimensions of the quark eigenmodes, which were determined using the box counting method. For this the time integrated scalar density

$$p(x) = \int dt \langle \psi(x,t) | \psi(x,t) \rangle, \tag{2.10}$$

will be used, in order to study the spatial scaling of the quark modes. The lattice volume is divided in boxes with a side length l, which can overlap and intersect. On each box the scalar density is normalized

$$p_{\text{box}}(x) = \frac{p(x)}{\int_{\text{box}} d^3y p(y)}, \tag{2.11}$$

and an IPR $\overline{\nu}_n(x)$ is defined within a box at the spatial coordinate x like

$$\overline{\nu}_n^{-1}(x) = \int_x^{x+l} d^3y p_{\text{box}}^n(y). \tag{2.12}$$

In each box this IPR ranges between 1 and $l^{-3(n-1)}$ and we can define a relative occupied volume in each box like

$$r_{\text{box}}(x) = \frac{\overline{\nu}_2(x)}{l^3} \in (0,1]. \tag{2.13}$$

The average box occupation ratio is then

$$\langle r_{\text{box}} \rangle = \frac{\sum r_{\text{box}}(x)}{N_{\text{box}}}, \tag{2.14}$$

where N_{box} is the number of boxes, which depends on whether and how the boxes are chosen to overlap. The average occupation ratio is independent of the box counting scheme.

The scaling factor between the boxes and the total volume is $\epsilon = \frac{1}{N_{\text{box}}}$. The box counting dimension describes how the occupation ratio changes with the scaling factor ϵ and reads

$$d = \lim_{\epsilon \mapsto 0} \frac{\ln \langle r_{\text{box}} \rangle}{\ln \frac{1}{\epsilon}}. \tag{2.15}$$

This is sketched in Figure 2.11. The scaling exponent $d \in (0,3]$ is also called the fractal dimension and was determined by a linear fit to $\ln\langle r_{\text{box}} \rangle$ over $\ln l$, which worked with high precision.

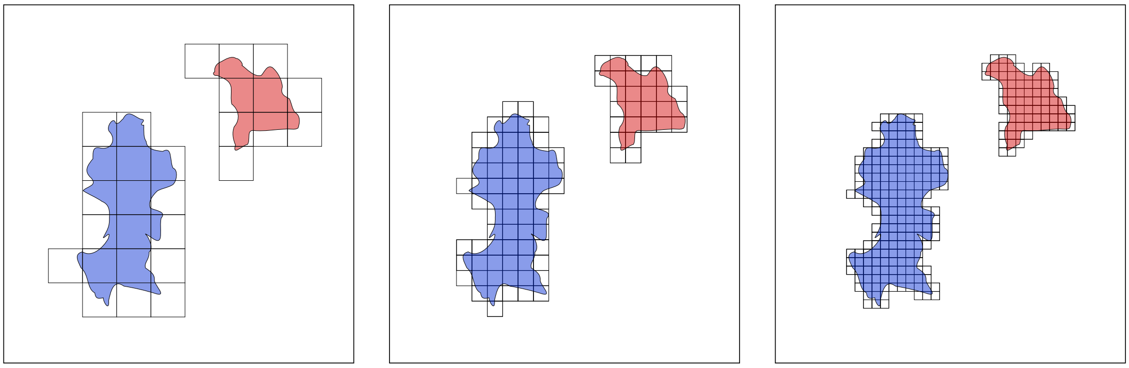

Figure 2.11.: A sketch of the box counting method for several ϵ (decreasing from left to right) in two dimensions. Only boxes with non-vanishing occupation ratio are shown.

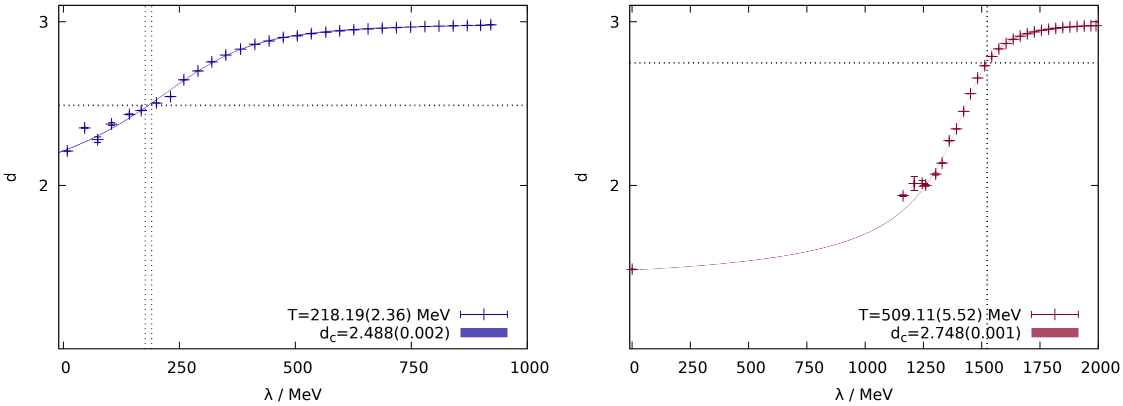

Figure 2.12.: The fractal dimension of eigenmodes in small bins of λ for several temperatures on the D370 meta ensemble. The vertical lines indicate the mobility edges λ_c and the horizontal lines the box counting dimension of the critical modes d_c.

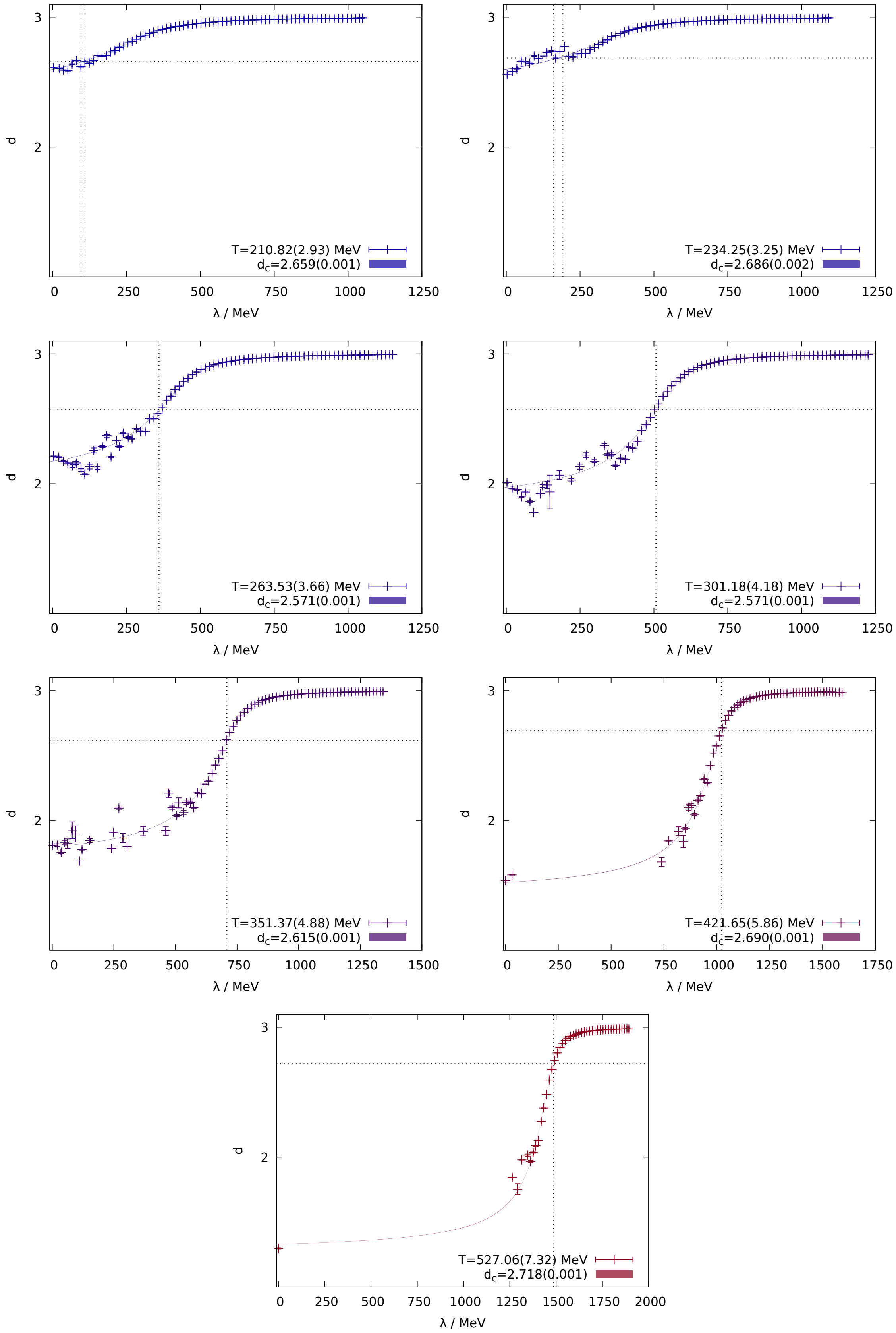

Figure 2.13.: The fractal dimension of eigenmodes in small bins of λ for several temperatures on the A370 meta ensemble.

In Figures 2.12 and 2.13 the fractal dimension of eigenmodes on the A370 and the D370 meta ensemble averaged in small bins of the size $a\Delta\lambda = 0.01$ are shown. We observe that localized mode present a fractal dimension which becomes smaller when the temperature is increased. Extended modes at larger eigenvalues scale three-dimensionally, as expected. The critical dimension $d_c := d(\lambda_c)$ and the zero mode dimension $d_0 := d(0)$ were determined from a fit to the averaged fractal dimension like $d(\lambda) \propto (\arctan\lambda)^2$.

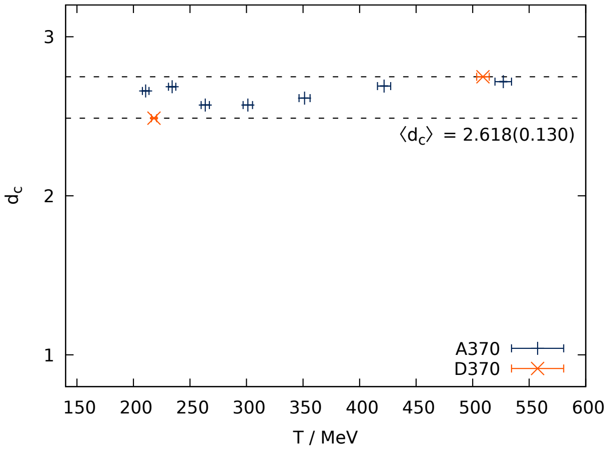

Figure 2.14.: The critical dimension over temperature on the A370 and the D370 meta ensemble.

The temperature dependence of the critical dimension is plotted in Figure 2.14. At the mobility edge the fractal dimension is consistent with a constant $d_c = 2.618(130)$. This means that critical modes scale very similar if not equal for all temperatures and their fractal dimension could be a universal quantity. However, this can not be confirmed with large certainty within the precision of this computation.

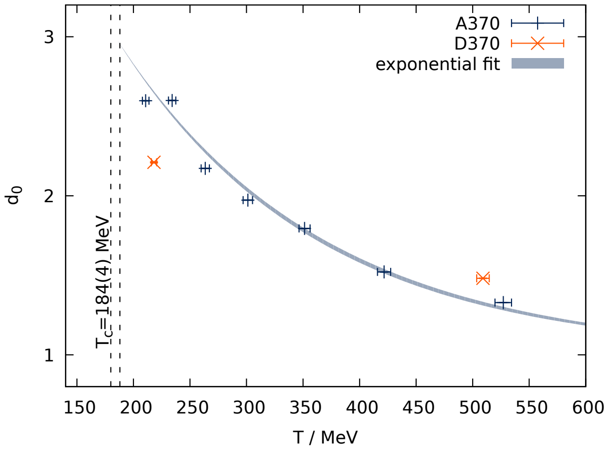

Figure 2.15.: The fractal dimension of zero modes over temperature on the A370 and the D370 meta ensemble. The chiral transition temperature $T_c = 184(4)$ MeV was again taken from [115].

The temperature dependence of the scaling dimension of zero modes is shown in Figure 2.15. We find that the zero mode dimension is well described with

$$d_0(T) = (3-1)e^{-(T-T_c)/\kappa} + 1, \tag{2.16}$$

where the only fit parameter was κ, which means that $d_0(T_c) = 3$ (the above fit was only applied to the data from the A370 meta ensemble, as d_0 appears to depend on the lattice spacing). We find that zero modes asymptotically become one-dimensional at large temperatures. With the instanton-liquid model in mind (see section 3.1) this finding comes as a surprise: (anti-)instantons, which induce chiral zero modes in the Dirac operator, are temporally and spatially localized such that one would rather assume the dimension zero (for point-like objects) or three (for spherical objects).

2.4.2. The distribution of the chiral density

It has been observed that quark modes contain distinct areas of positive and negative local chirality. Localized non-zero modes always come in conjugate pairs with very similar local distributions of scalar, pseudoscalar and chiral densities. Their total chirality vanishes.

This section is dedicated to the geometrical features of these local distributions. The two-point function of the four dimensional densities $p(x)$ and $q(x)$ is determined by using their Fourier transform $g(k) = \mathcal{F}(p(x))$ and $h(k) = \mathcal{F}(q(x))$. Their convolution is a product in Fourier space such that the volume averaged correlator can readily be extracted like

$$\langle p(0)q(r)\rangle = \mathcal{F}^{-1}\left(g^*(k)h(k)\right). \tag{2.17}$$

For negative distances r we also have

$$\langle p(0)q(-r)\rangle = \mathcal{F}^{-1}\left(h^*(k)g(k)\right). \tag{2.18}$$

In a finite volume with periodic boundary conditions negative distances create highly oscillating contributions to the Fourier transform, which creates a non-vanishing imaginary part of $g^*(k)h(k)$, such that the negative momenta in the Fourier transform can not be correctly reproduced.

We therefore restrict our considerations to positive momenta (and distances) by projecting the correlation functions like

$$\begin{aligned} g^*(k)h(k) + h^*(k)g(k) &= \int d^d r \int d^d x \left(p(x)q(x+r)e^{ikr} + q(x)p(x+r)e^{-ikr}\right) \\ &= \mathcal{F}\left(\langle p(0)q(r)\rangle - \langle q(0)p(-r)\rangle\right). \end{aligned} \tag{2.19}$$

For the homogeneous correlators, translational invariance automatically introduces a cutoff at negative momenta. For inhomogeneous correlators, however, we find $p(x)q(x+r)e^{ikr} \neq q(x)p(x+r)e^{-ikr}$ since $p(x) \neq q(x)$ and thus $g \neq h$, such that this projection becomes necessary.

In the following we will discuss the chiral densities

$$p^{\pm}(x,t) = \langle\psi(x,t)|\frac{1}{2}(1 \pm \gamma_5)|\psi(x,t)\rangle \tag{2.20}$$

and study the three correlation functions $\langle p^+(0)p^-(r)\rangle = \langle p^-(0)p^+(r)\rangle$ (the inhomogeneous correlator), $\langle p^+(0)p^+(r)\rangle$ and $\langle p^-(0)p^-(r)\rangle$ (the homogeneous correlators).

On the D370 meta ensemble at T=509.11(5.52) MeV we will further present the spatial distributions of the pseudoscalar density

$$p^5(x,t) = \langle\psi(x,t)|\gamma_5|\psi(x,t)\rangle \tag{2.21}$$

on three adjacent time slices to give an idea about the time evolution and fluctuations of the quark modes, together with the chiral correlators.

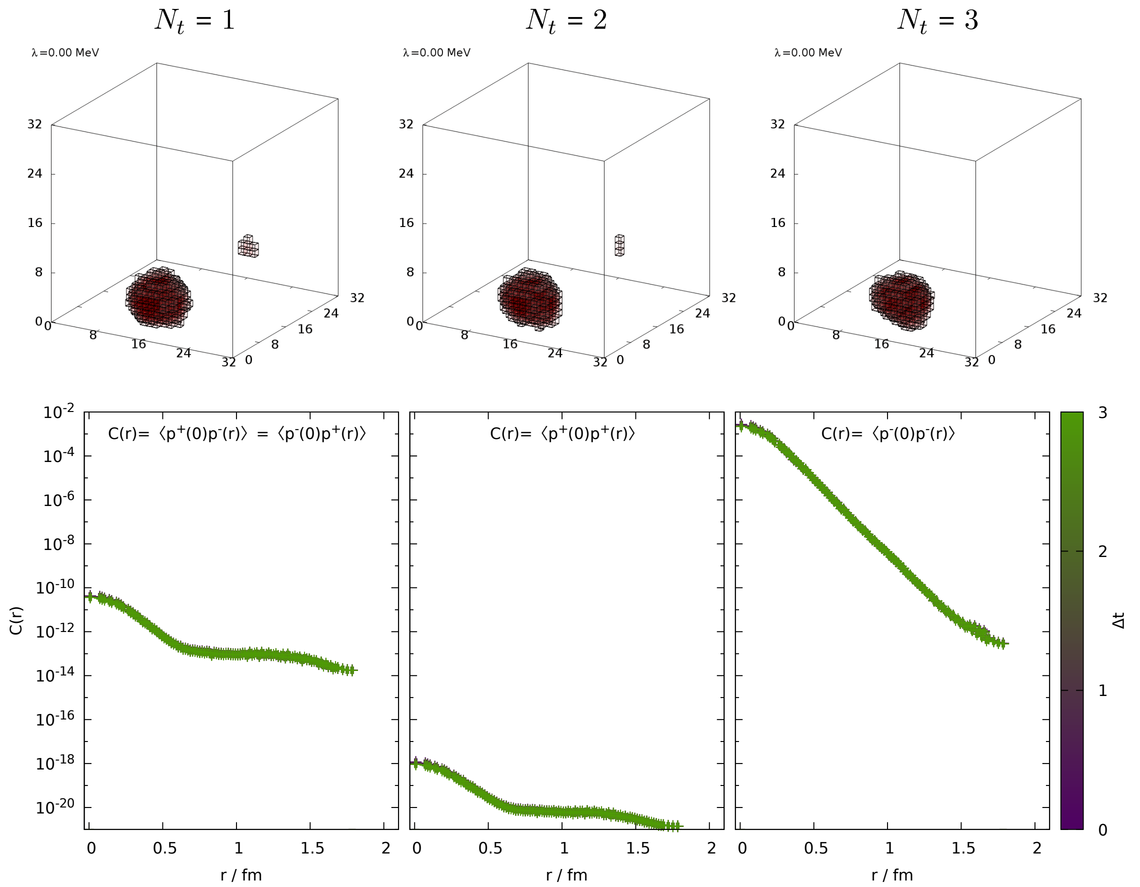

Figure 2.16.: Single centre zero mode, containing one lump of negative chirality. *Top*: The spatial distribution of the chiral density on three different time slices. *Bottom*: The correlation functions of the chiral density.

In Figure 2.16 a zero mode is shown, which only contains a single cluster of negative chirality. As the eigenvalue of this mode vanishes, it is also an eigenmode of γ_5 and therefore has a non-vanishing chirality.

In the top panels of Figure 2.16 the spatial distribution of the pseudoscalar density is plotted (where red indicates $p^5(x,t) < 0$ and blue $p^5(x,t) > 0$), where an artificial cutoff has been introduced in order to make the plots more lucid.

The bottom panels show the correlation functions of the chiral densities. We can see that the mixed correlator is relatively suppressed, as there is (within numerical precision) no p^+ contribution in the mode. The homogeneous positive channel $\langle p^+(0)p^+(r)\rangle$ is thus strongly suppressed.

The only cluster within the mode has negative chirality, and hence $\langle p^-(0)p^-(r)\rangle$ contains a clear exponential decay and a small centre at small distances. One can also observe that the correlation functions are independent from the temporal distance Δt. It can be concluded that the density distribution is constant in time.

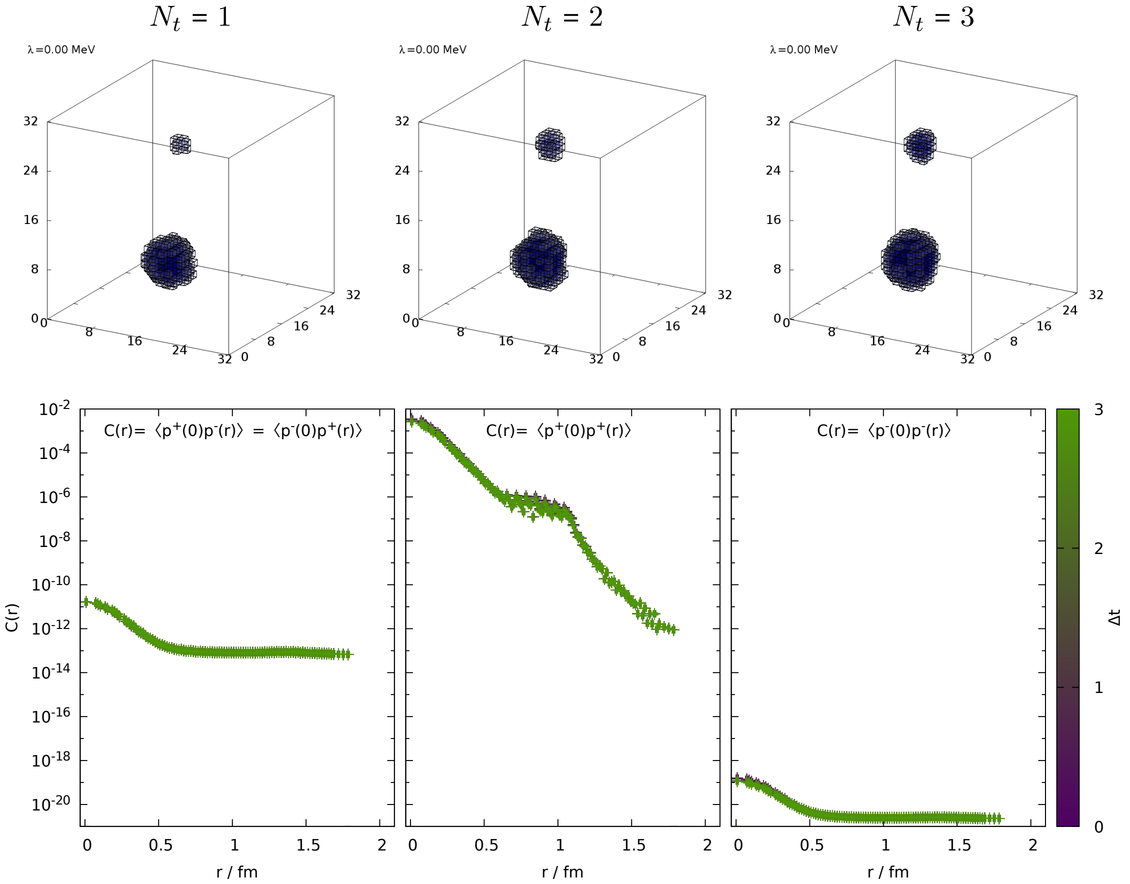

Figure 2.17.: Multi-centre zero mode, containing two lumps of positive chirality, one of which pulsates, but is not strictly time localized. *Top*: The spatial distribution of the chiral density on three different time slices. *Bottom*: The correlation functions of the chiral density.

Figure 2.17 shows a zero mode that has positive chirality and contains two distinct centres of positive pseudoscalar density. One of these centres pulsates very slightly in time but is never vanishing. The mixed correlation functions are again suppressed and the homogeneous negative correlator is vanishing within numerical resolution. The purely positive correlator contains two distinct exponential decays and a plateau that corresponds to the coexistence of the two positive clusters in this distance range.

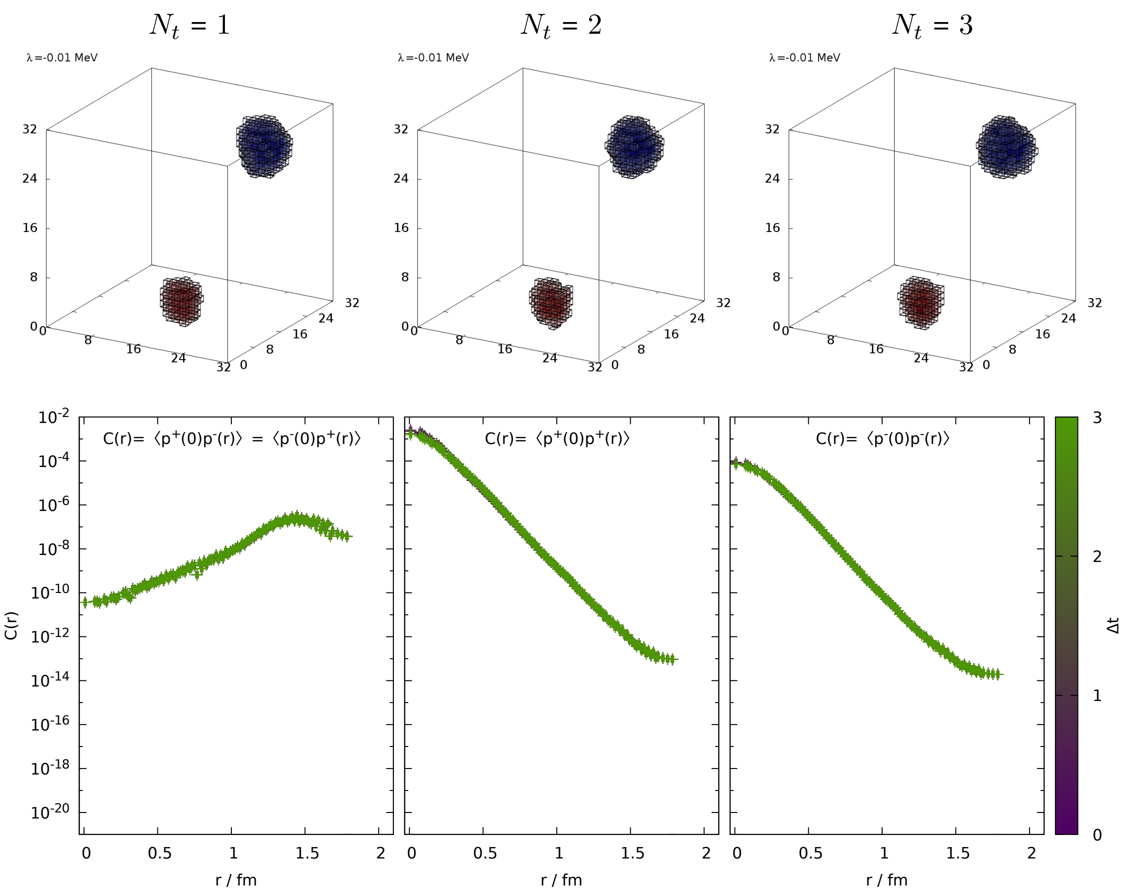

Figure 2.18.: A near zero mode at $|\lambda| = 0.01$ MeV $= 1.3 \cdot 10^{-5} \lambda_c$. *Top*: The spatial distribution of the chiral density on three different time slices. *Bottom*: The correlation functions of the chiral density.

When moving away from zero eigenvalues, the Dirac operator eigenmodes are no longer simultaneous eigenmodes of γ_5 and occur in complex conjugate pairs. An eigenmode very close to $\lambda = 0$ is shown in Figure 2.18.

This non-zero mode is strictly localized, similar to the zero modes. It contains, however, two centres of opposing sign in the pseudoscalar density, such that the total chirality vanishes. This can be seen in the upper panels where the $p^5(x,t)$ is plotted. The homogeneous correlation functions both contain an exponential decay with a "hard" centre at small distances, where the positive one is a little more prominent. The slight difference in the height of the correlators is caused by slightly different densities in the centres of the clusters.

The mixed correlator is small at small distances as there appears to be some repulsion between the two clusters. It increases with r up to a maximum, which corresponds to the characteristic distance between the two centres. This mode is also constant in time.

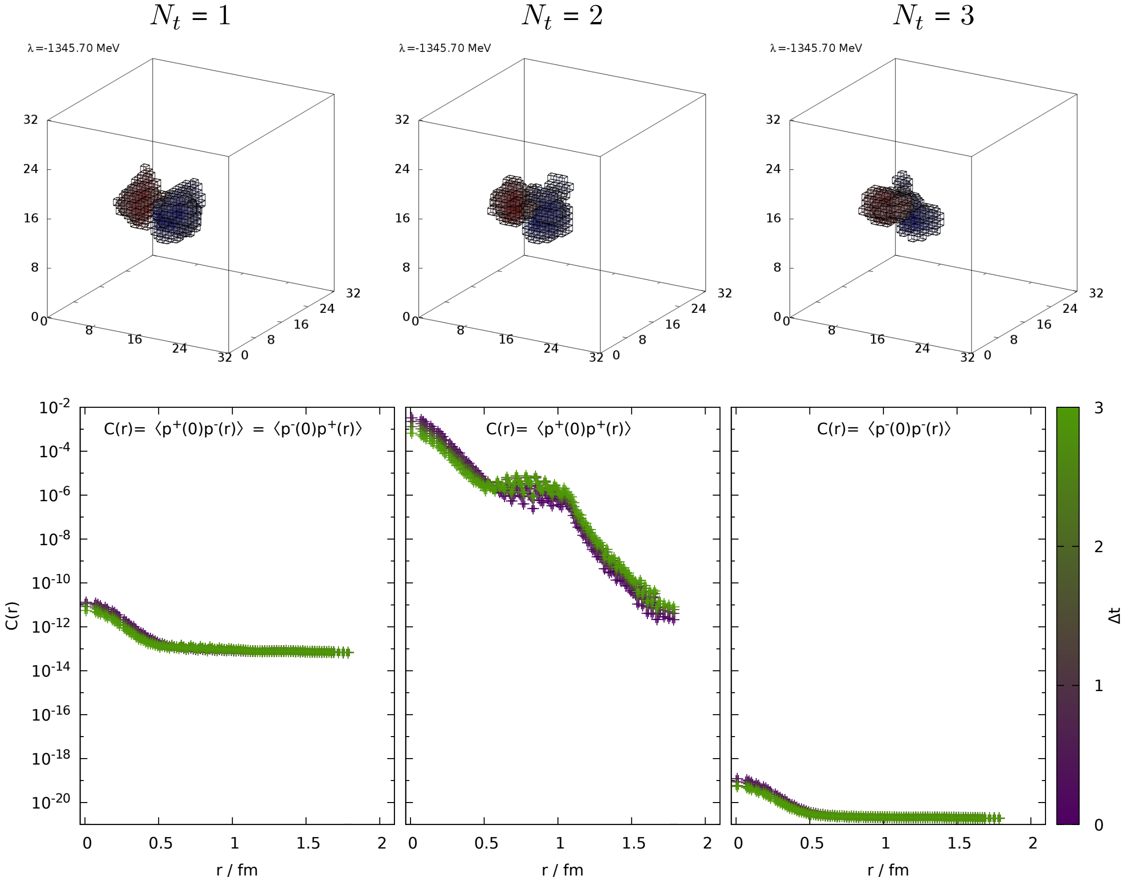

Figure 2.19.: A localized mode at $|\lambda| = 1345.7$ MeV $= 0.884\lambda_c$ which is constant in time. *Top*: The spatial distribution of the chiral density on three different time slices. *Bottom*: The correlation functions of the chiral density.

The eigenmodes of the Dirac operator remain localized up to the mobility edge λ_c, which was studied in the previous section. In Figure 2.19 a mode in the upper end of the localized regime is shown. It resides at $|\lambda| = 0.884\lambda_c$ and its spatial distribution is already more “fuzzy” than for the lower lying modes. There can still be two distinct centres of opposing chirality observed, which coexist within the mode at relatively small distances. It appears that the localization phenomenon is associated with a separation of local chiralities, which becomes weaker when approaching the delocalization transition.

For the localized mode in Figure 2.19 we find that the mixed correlators present a short exponential decay and a constant plateau, which indicates that both dense centres are embedded in a mostly homogeneous distribution of both positive and negative chiralities. The purely negative correlator is strongly suppressed, the negative cluster apparently encodes only very little of the total “chiral charge”. The positive cluster is very dominant and contains at least two dense centres, which coexist at a characteristic distance indicated by the plateau in the correlation function.

The spatial distribution of this mode is again mostly time-independent, since the correlators coincide for every temporal distance.

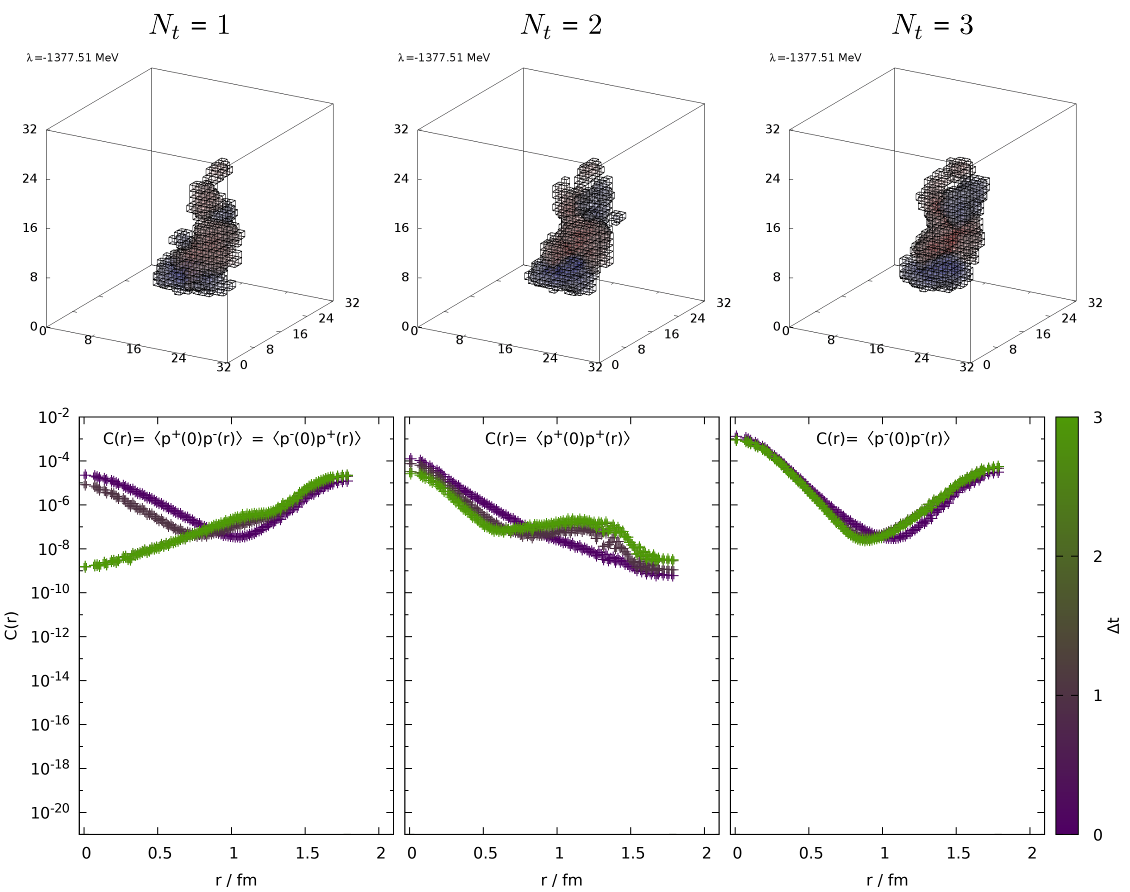

Figure 2.20.: A localized mode at $|\lambda| = 1377.51$ MeV $= 0.904\lambda_c$ that fluctuates slightly in time. *Top*: The spatial distribution of the chiral density on three different time slices. *Bottom*: The correlation functions of the chiral density.

In Figure 2.20 a localized mode close to the mobility edge is shown; its eigenvalue is $|\lambda| = 0.904\lambda_c$. Although this mode still lies within the localized area, it presents a distribution which fluctuates in time. The chirally positive component of the mode begins “wrapping” around the negative cluster. There appear to be multiple positive and negative centres, some of which being strongly localized in time, others time independent. Also temporal fluctuations become more prominent with larger λ.

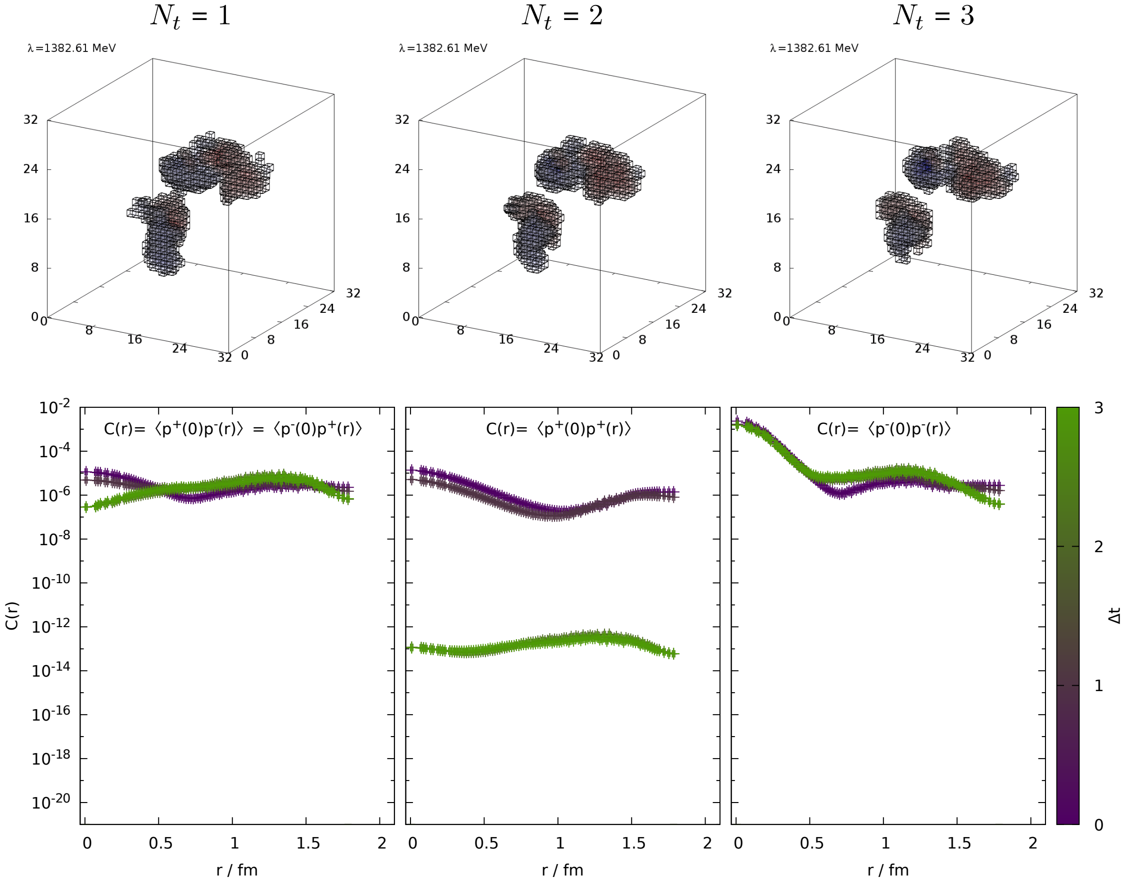

Figure 2.21.: A localized mode at $|\lambda| = 1382.61$ MeV $= 0.908\lambda_c$ that contains a time-localized chirally positive centre. *Top*: The spatial distribution of the chiral density on three different time slices. *Bottom*: The correlation functions of the chiral density.

It can also be seen in Figure 2.21 that temporal fluctuations become larger the closer λ is to the mobility edge. Especially the $\langle p^+(0)p^+(r)\rangle$ correlator in this mode hows a strong suppression at large time distances (colour-coded in green). This indicates that the chirally positive part of this mode contains areas or centres that are strongly localized in the time direction.

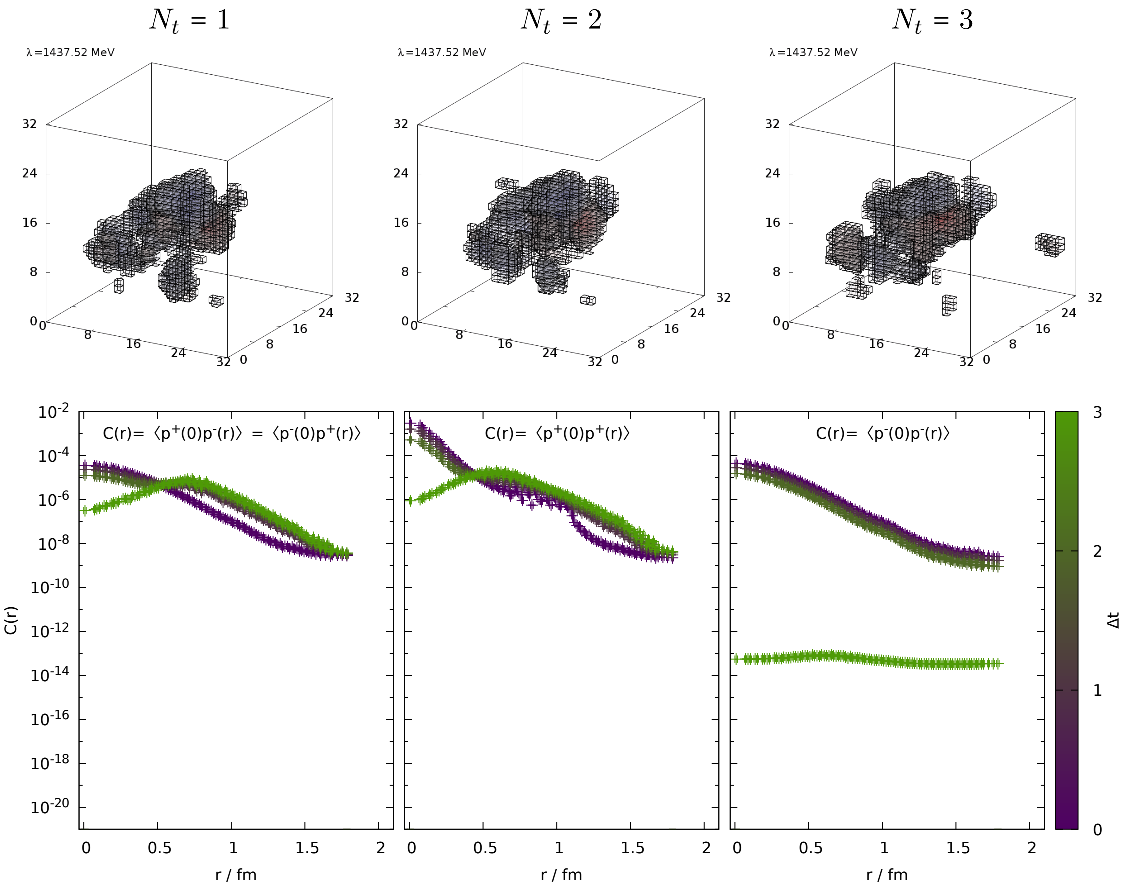

Figure 2.22.: A localized mode at $|\lambda| = 1437.52$ MeV $= 0.944\lambda_c$, that contains a time-localized chirally negative centre. *Top*: The spatial distribution of the chiral density on three different time slices. *Bottom*: The correlation functions of the chiral density.

Even further up the spectrum we find an almost delocalized mode: in Figure 2.22 an eigenmode to $|\lambda| = 0.944\lambda_c$ is plotted which already occupies a large fraction of the volume and whose distribution fluctuates in time. In particular, the negative centres are time-localized which is reflected in the $\langle p^-(0)p^-(r)\rangle$ correlator, and in the spatial distribution of the pseudoscalar density at $N_t = 3$ (upper panel) we can see a chirally negative lump on the right side, which only exists on this time slice. This mode also fluctuates spatially much more than the lower modes. The temporal correlations within eigenmodes obtain a rich structure in proximity to the mobility edge, which vanishes again once the modes are homogeneously extended.

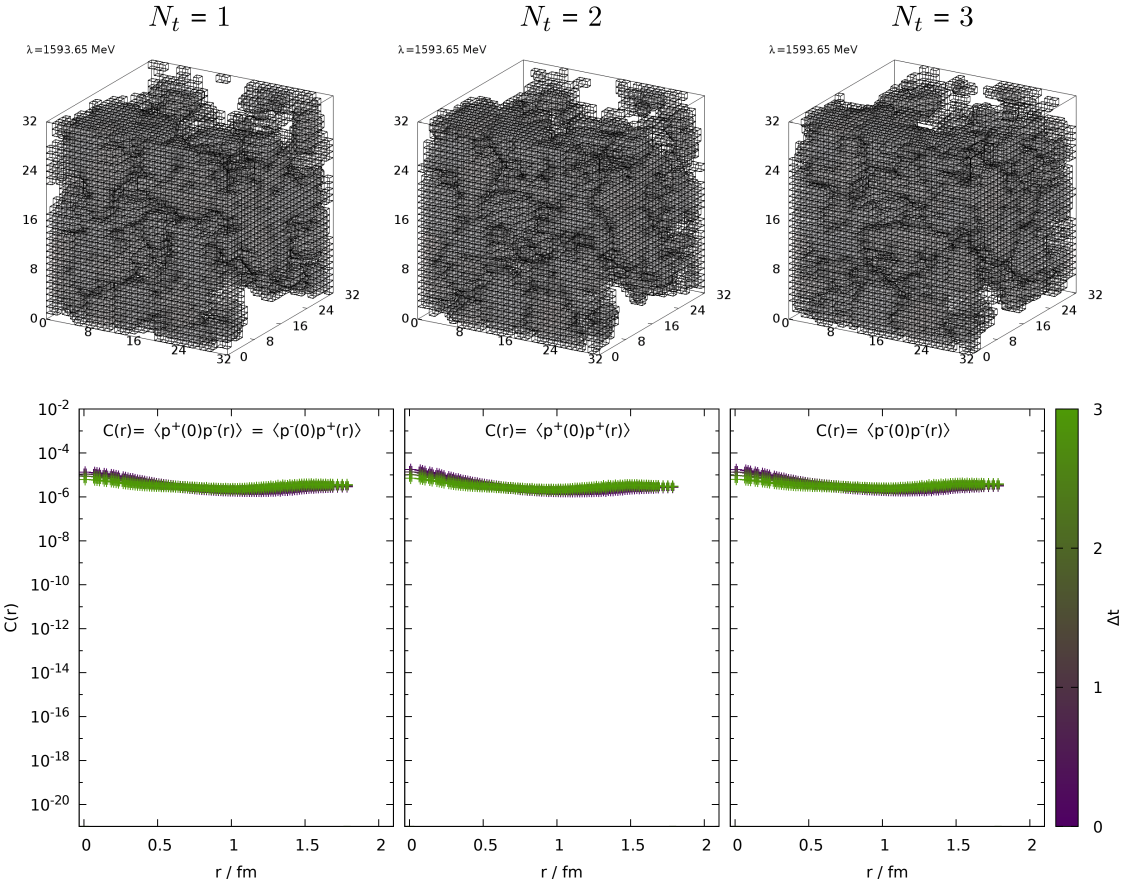

Figure 2.23.: An extended mode at $|\lambda| = 1593.65$ MeV $= 1.046\lambda_c$, that is spread almost homogeneously over the volume. *Top*: The spatial distribution of the chiral density on three different time slices. *Bottom*: The correlation functions of the chiral density.

Finally, in Figure 2.23 an extended quark mode just above the mobility edge at $|\lambda| = 1.046\lambda_c$ is shown. As the mode is spread homogeneously throughout the whole volume, all correlators are relatively large and almost constant. There is no time dependence remaining.

2.4.3. Moments of eigenmodes

For a geometrical interpretation of the distribution of a quark eigenmode in a finite volume, it is useful to study the principal moments of the spatial density of a mode which are the eigenvalues of the "inertia" tensor in analogy to the moments of inertia of a mass density.

This tensor is given by $(i, j = 1, 2, 3)$

$$\Theta_{ij} = \int d^d r \left(\sum_{k=1}^{3} r_k^2 - r_i r_j \right) p(r), \tag{2.22}$$

where d is the number of spatial dimensions and $r = r_0 - x$ is the distance from the centre of density with respect to periodic boundary conditions

$$r_0 = \int d^d x x p(x). \tag{2.23}$$

We study again the time integrated scalar density, as in Section 2.4.1, and the time integrated chiral densities

$$p^{\pm}(x) = \int dt \langle \psi(x,t) | \frac{1}{2} (1 \pm \gamma_5) | \psi(x,t) \rangle, \tag{2.24}$$

which allows to study the chiral components of a quark mode separately.

The eigenvalues of Θ are the moments of of the quark mode $\{\theta_k\}$ and the eigenvectors $\{\omega_k\}$ are the corresponding principal axes. The inertia tensor of a sphere with an exponentially decaying density $p(r) = p_0 e^{-r/\xi}$ (ξ being the correlation length) is given by

$$\Theta = 64\pi p_0 \xi^5 \begin{pmatrix} 1 & & \\ & 1 & \\ & & 1 \end{pmatrix}. \tag{2.25}$$

The correlation length thus takes the role of an effective radius. We can connect the moments of quark eigenmodes to the two-point functions of the chiral densities, from which the correlation lengths within cluster objects can be extracted (see Section 2.4.2). Due to the rotational symmetry the inertia tensor is diagonal and the eigenvalues are degenerate. This is expected for spherical density distributions among the localized modes or volume filling distributions of extended modes. For an ellipsoid geometry, the correlation length would depend on the principal axes of the density distributions. Prolate or even cylindrical density distributions present two θ_k which are approximately degenerate and one preferred rotation axis. From earlier considerations this is expected for localized modes, i.e. the local clusters of opposing chirality within. A filament structure presents no degenerate moments, which could also appear in localized modes.

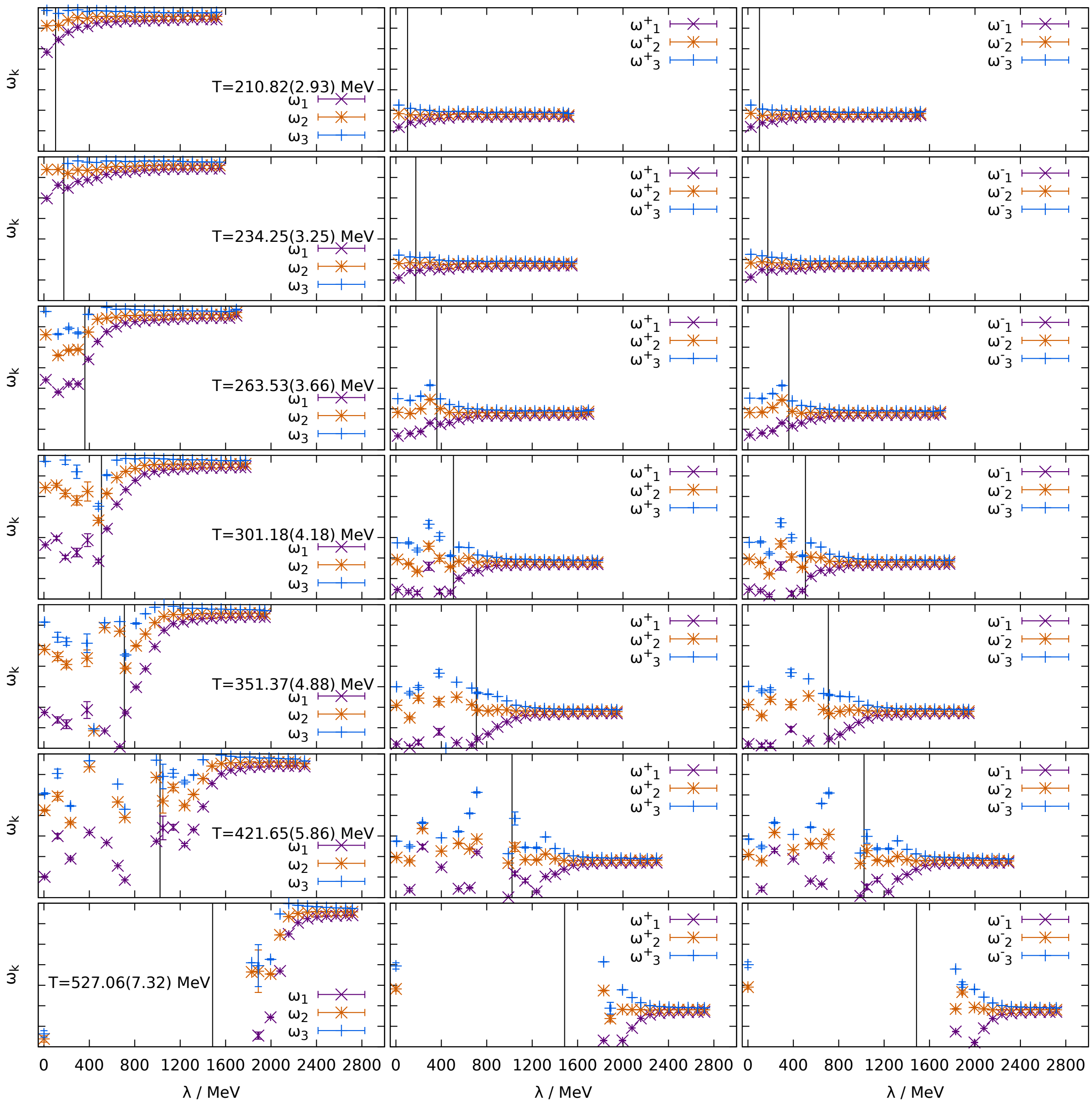

Figure 2.24.: The principal moments of the time integrated scalar (left), positive chiral (middle) and negative chiral (right) densities for several temperatures on the A370 meta ensemble. The vertical lines indicate the position of the mobility edge.

In Figure 2.24 the principal moments of the Dirac operator eigenmodes are plotted over the eigenvalue, averaged in bins of the size $a\Delta\lambda = 0.04$. In the extended regime the moments become degenerate as there is no distinguished axis anymore. Since the eigenmodes are almost homogeneously spread over the whole volume there is some spherical (cubical) symmetry. In the localized regime, however, we observe a splitting of ω_1, ω_2 and ω_3. The smallest moment deviates the most, but also the second moment splits from the largest. The largest, however, changes very little from the localized to the extended regime. We thus conclude that the localized modes present a ellipsoid geometry, where one rotation axis is much preferred above the other two. This means that these modes have a prolate distribution of densities. These “sticks” blow up at the mobility edge, where their moments of inertia degenerate.

We have seen above that the correlation length ξ of a symmetric sphere takes the role of a radius and contributes $\propto \xi^5$ to the moments. As these are split in the localized regime, we conclude that the correlation length becomes anisotropic here. The anisotropy of the density distributions becomes fuzzy and dissolves at the delocalization transition, the modes form homogeneous “clouds”. The chiral components of the quark modes present very similar moments of inertia, their geometries seem to mirror each other.

We have, however, not studied zero modes separately. We assume that their structure is different from localized non-zero modes, as we always observed spherical clusters of chiral density within zero modes.

2.4.4. Chirality overlap

We have seen in the previous sections that localized modes split in local clusters with different eigenvalues to γ_5. Once the modes become delocalized, the clusters with different chiral densities $p^{\pm}(x)$ diffuse into each other. Localization is reflected in a spatial separation of chiral clusters.

In this section we will study how the local chiral clusters overlap. The overlap of the chiral densities $p^{\pm}(x)$ is defined as

$$O^{\chi}(\lambda_j) = \frac{\int d^4x p_j^+(x) p_j^-(x)}{\int d^4x \left((p_j^+(x))^2 + (p_j^-(x))^2\right)}. \tag{2.26}$$

In Figure 2.25 this overlap is plotted over λ, averaged in bins of the size $a\Delta\lambda = 0.01$. For the low quark modes the local chiral components are widely separated from each other. Above the mobility edge the local chiral distribution becomes homogeneously mixed. This transition from clearly separated lumps to a cloud distribution is, however, a very smooth one. Still the mobility edge separates mostly unmixed from mostly mixed modes. The chiral overlap of zero modes drops to zero, as there are no opposing chiral lumps within zero modes.

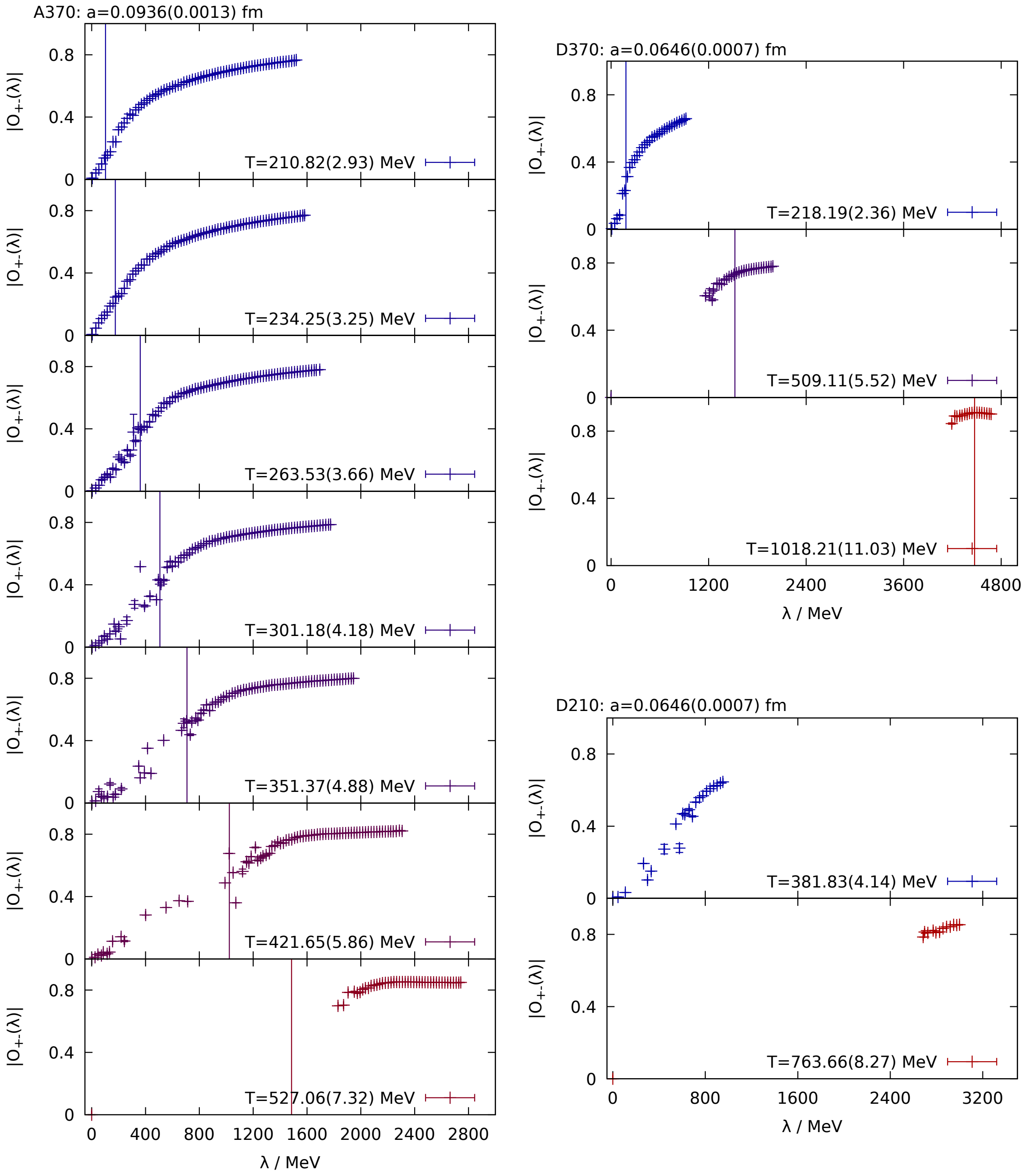

Figure 2.25.: Overlap of regions with positive and negative chirality on the A370 (*Left*), the D370 (*Top right*) and the D210 meta ensemble (*Bottom right*). Localization is reflected with a low overlap, the vertical lines indicate the mobility edges that were determined from the relative eigenvector volume.

2.4.5. Morphological properties of quark eigenmodes

To summarize this morphology survey of the structure and geometry of quark wave functions we find that around the mobility edge Dirac operator eigenmodes are multifractal, which confirms earlier findings [127]. We observe that, while the dimension of critical modes is consistent with a constant in the temperature, the dimension of zero modes exponentially decreases with the temperature.

Furthermore, we used the correlation functions of the chiral densities $p^{\pm}(x)$ to study the geometry of the eigenmodes. It was found that zero modes are strictly localized and present an exponential decay within the boundaries of the clusters, in the case of multicentre zero modes the correlator shows a plateau that corresponds to the characteristic distance between these modes and localized modes contain at least two distinct centres, such that their total chirality vanishes. These distinct centres are spatially well separated at low eigenvalues but stick closely together for larger eigenvalues. This separation is continuously lost when approaching λ_c from below. The time dependence of the eigenmodes becomes larger when the mobility edge is approached, and the spatial structure becomes diffuse. Modes that are close to the zero modes are mostly constant in time, but in rare cases zero modes contain pulsating clusters. The larger the eigenvalue, the more time-localized centres are present within a mode.

The eigenmodes can be assigned an "inertia" tensor when studying the time integrated scalar and chiral densities. The moments are split in the localized regime and smoothly degenerate in the extended regime, which indicates that the low eigenmodes have an ellipsoid geometry that becomes diffuse and vanishes when λ is increased. The correlation length of modes, which presented an exponentially decaying density within their clusters, takes the role of a radius in the inertia tensor. Since we now know that localized modes have (at least partially) exponentially decaying densities, we can conclude that the correlation length of the eigenmodes in the localized regime in anisotropic in space, and depends on the principal axes of the eigenmodes.

2.5. Unfolded level spacing distributions

The following section will present the level spacing distribution of the Dirac operator spectrum in QCD at finite temperatures. In the thermodynamic limit there is a non-analytic transition from a Poisson-like to a Wigner-Dyson regime. In [123] the universal mobility edge was mapped using finite size scaling, and it was found that the critical exponent of the correlation length is compatible with the critical exponent of the unitary Anderson model.

In Section 1.6 the unfolding procedure was outlined. The level spacings are rescaled to remove microscopic (and thus non-universal) features from the spectrum. For this, the cumulative spectral function is split in a smooth (universal) and a fluctuating (microscopic) part. In this survey, the smooth part was determined by a second order polynomial fit. After this, only the global symmetries of the Dirac operator govern the unfolded level spacing distribution (ULSD), and for different global anti-unitary symmetries of the Dirac matrix the level spacings follow different Wigner-Dyson surmises. In full QCD the Dyson index is $\beta_D = 2$ and the matrix elements are complex (as opposed for e.g. SU(2) Yang-Mills theory). This corresponds to a random matrix theory following a chiral Gaussian unitary ensemble (chGUE).

Since within the localized regime the quark modes are uncorrelated to each other, the level spacings follow a Poisson distribution. The Anderson transition is thus reflected in a transition from a Poisson-like ULSD to the chiral Gaussian unitary ensemble like

$$P_{\mathrm{Poisson}}(s) = e^{-s} \mapsto P_{\mathrm{chGUE}}(s) = \frac{32}{\pi^2} s^2 \exp\left(-\frac{4}{\pi} s^2\right). \tag{2.27}$$

As we have already seen, this transition is rather smooth. In [123] the integrated ULSD has been used to estimate the transition point, whereas [126] employed the variance of the ULSD to distinguish a Poisson-like regime from a Wigner-Dyson-like one.

Figure 2.26 shows the ULSD for several temperatures on the A370 meta ensemble, 2.27 on the D370 meta ensemble. In the top panels, the eigenvalue distribution and the spectral regimes in which the ULSDs were computed are plotted, where red indicates the localized, Poisson-like and blue the extended, Wigner-Dyson like regime. The bottom panels show the level spacing distributions in these spectral intervals and the prediction from chiral random matrix theory.

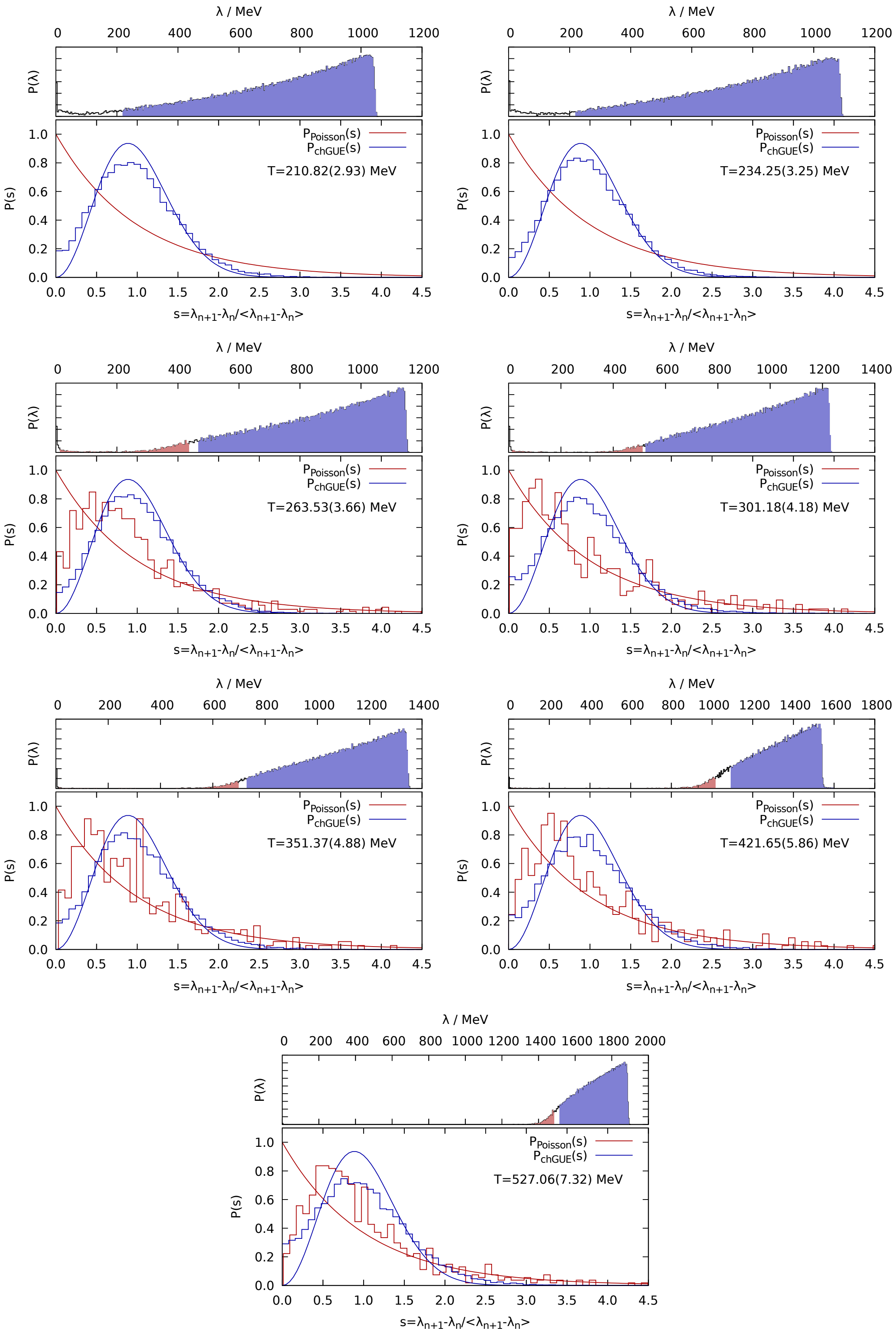

Figure 2.26.: The unfolded level spacing distributions for several temperatures on the A370 meta ensemble.

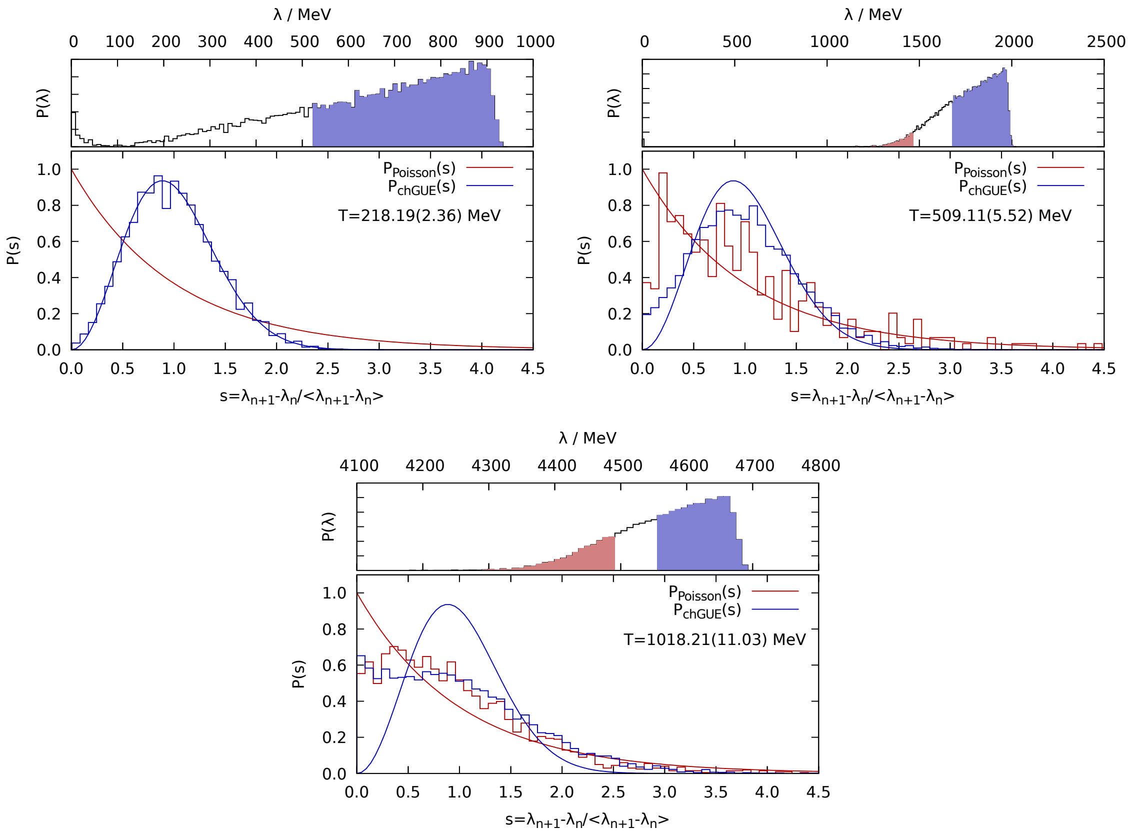

Figure 2.27.: The unfolded level spacing distributions for several temperatures on the D370 meta ensemble.

For these computations the λ intervals have been estimated from the mobility edges that were determined from the relative eigenvector volumes in Section 2.3. The Poisson sector unfortunately suffers from bad statistics, but clearly a transition between two sectors takes place. For the low temperatures there appears to be no distinguishable Poisson part in the spectrum, since all eigenmodes are more or less delocalized. This can be seen in Figures 2.5 and 2.6 where at low temperatures all modes have a relatively large volume. Although the mobility edge could be estimated for these low temperatures, there are too few eigenmodes below it to properly resolve a level spacing distribution.

2.6. Localization through Polyakov loops

After the previous sections the question remains: How is quark localization caused by the gauge field? Is it possible to identify a gauge invariant object that causes this effect?

Possible candidates for this are the local Polyakov line or topological charge density. As the latter is not uniquely defined, this section is dedicated to the correlation between localized quark modes and the local Polyakov line. It is defined as

$$l(x) = \frac{1}{N_c}\,\mathrm{tr}\, e^{\int dt A_4(x,t)} = \frac{1}{N_c}\,\mathrm{tr}\prod_t U_4(x,t), \tag{2.28}$$

and corresponds to the propagator of a static quark, which only evolves in time direction (the index 4 denotes the time direction). This is sketched in Figure 2.28.

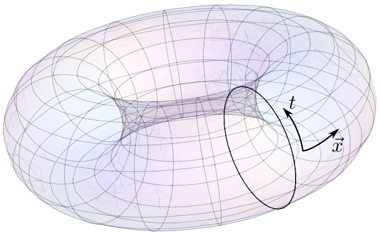

Figure 2.28.: A sketch of the Polyakov line on the space-time torus.

The expectation value of the volume averaged Polyakov line

$$\langle l\rangle = \frac{1}{Z}\int \mathcal{D}U e^{-S}\int dx l(x) \tag{2.29}$$

is called the Polyakov loop and serves as an order parameter for the breaking of the $Z(N_c)$ symmetry, which in pure gauge theory is equivalent to the deconfinement transition. Unquenching explicitly breaks this symmetry, as the fermion fields obey anti-periodic boundary conditions. In pure gauge theory the renormalized Polyakov loop can be related to the free energy of a static quark F_q like

$$\langle l^{\mathrm{ren}}\rangle = \frac{Z_q}{Z} \propto e^{-F_q/T}. \tag{2.30}$$

In the confined phase one requires an infinite amount of energy to remove a colour source from the system, such that we have $F_q = \infty$ and thus $\langle l^{\mathrm{ren}}\rangle = 0$, while in the deconfined phase $F_q < \infty$ such that $\langle l^{\mathrm{ren}}\rangle \lessgtr 0$.

In 2011 Bruckmann, Kovacs and Schierenberg [128] already studied this correlation and the localization of staggered and overlap eigenmodes in quenched two colour QCD. It was found that low-lying quark modes are “trapped” in local Polyakov loop fluctuations, which are far away from the centre element of SU(2) that breaks the centre symmetry. In 2015 Giordano, Kovacs and Pittler [129] described an effective model very similar to an Anderson model with continuous spins in three dimensions, which mimics the effect of Polyakov lines on the quarks, to extend the idea of quark modes that are trapped in local Polyakov loop fluctuations to a SU(3) gauge theory. In 2016 Cossu and Hashimoto studied the QCD Anderson transition, particularly the correlation with the Polyakov line, at high temperatures using Möbius domain wall fermions [130].

Since short-range fluctuations within the gauge field distort the Polyakov loop signal, the gauge configurations first have to be UV-smoothed.

2.6.1. Smoothing the gauge configurations with gradient flow

For the following computations the gauge configurations were smoothed using gradient flow (see Section 1.5) to suppress UV-fluctuations, which heavily distort the local structure of e.g. the Polyakov loop. Also this procedure renormalizes the Polyakov loop expectation value. We employed gradient flow with respect to the pure gauge theory, where the RG-improved Iwasaki gauge action was employed (see Section 1.2.4). This is also referred to as "Iwasaki flow". The tmfT gauge configurations were generated using this gauge action as well.

The integration of the flow equation on the lattice was done numerically using a step size $\Delta\tau = 2\cdot10^{-3}a^2$. In order to estimate an appropriate maximum flow time, the energy density was computed like

$$E = 2\sum_x \sum_{\mu<\nu} \mathrm{Re}\,\mathrm{tr}\left(1 - P_{\mu\nu}(x)\right), \tag{2.31}$$

and a dimensionless quantity was determined from that, as described in Section 1.5.4.

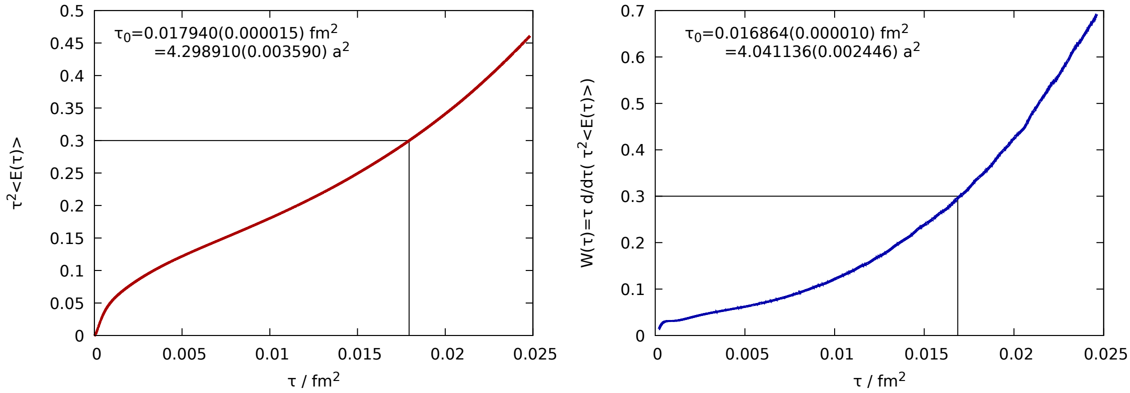

Figure 2.29.: Setting the flow time at $T = 509.11(5.52)$ MeV (D370), *Left*: with $\tau^2\langle E(\tau)\rangle = c$, as proposed by Lüscher [96], *Right*: with $\tau\frac{d}{d\tau}\left(\tau^2\langle E(\tau)\rangle\right) = c$, as proposed by the Budapest-Marseille-Wuppertal collaboration [100]

In Figure 2.29 the dimensionless quantities used to set the scale as proposed by Lüscher and the BMW collaboration are shown. As both procedures yield comparable results, we will use $\tau = 4a^2$ as the flow time in the following.

2.6.2. Polyakov line clusters

When the centre symmetry breaks the Polyakov loop acquires a non-vanishing expectation value. In the broken phase the distribution of local Polyakov loops accumulates around one of the centre elements, which be seen in Figure 2.30, where the distribution of $l(x)$ at flow time $\tau = 0$ is shown in the complex plane.

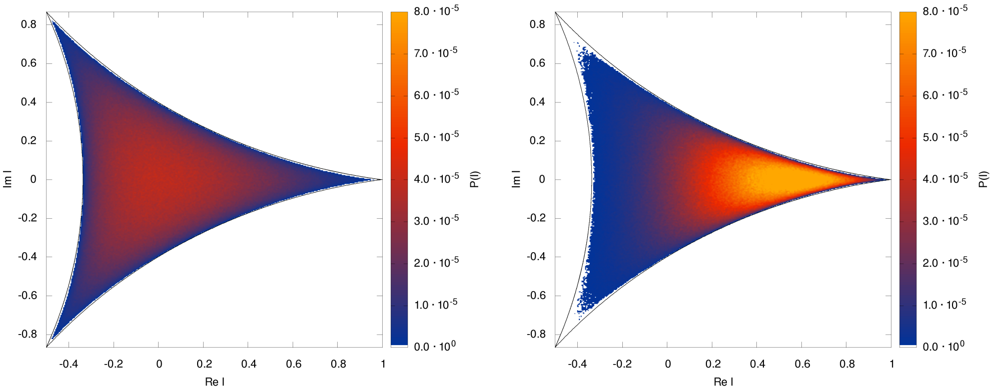

Figure 2.30.: The distribution of the local Polyakov loop $l(x)$ at zero flow time for T=210.82(2.93) MeV (*Left*) and T=527.06(7.32) MeV (*Right*). In the strongly broken phase the Polyakov loop bulks around the centre element 1. The solid lines indicate the area in the complex plane to which the trace of a SU(3) matrix is restricted.

At finite flow time, the expectation value becomes renormalized. In Figure 2.31 it is plotted for several flow times over the temperature, and one can see that it slowly approaches a plateau with increasing τ/a^2.

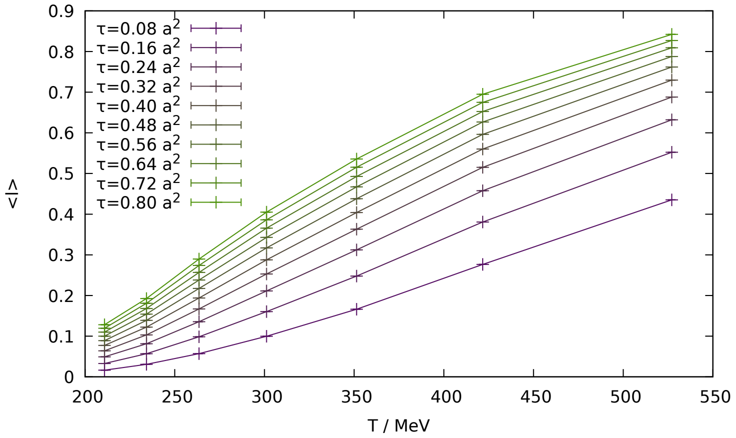

Figure 2.31.: The expectation value of the real part of the Polyakov loop over temperature on the A370 meta ensemble for different gradient flow times. $\langle l \rangle$ slowly approaches a plateau with increasing flow time.

The flow time used in the following ($\tau = 4a^2$) was chosen closely below what the Lüscher and the Budapest-Wuppertal-Marseille criterion for scale setting suggested. The distribution of the real part of the Polyakov loop at this flow time and at $\tau = 0$ is shown for two different temperatures in Figure 2.32: For the small temperature the distribution and thus the expectation value is small and changes relatively little during Iwasaki flow. For the larger temperature, however, the centre symmetry is more strongly broken and the expectation value is renormalized to a rather large value by Iwasaki flow.

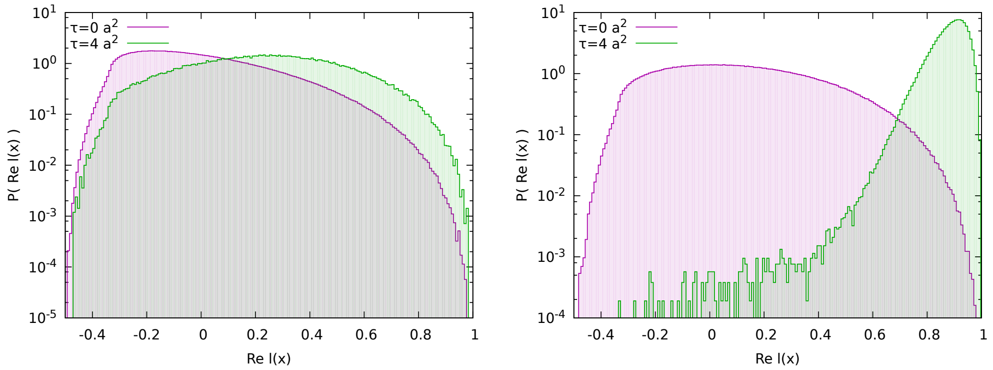

Figure 2.32.: *Left*: T=218.19(2.36) MeV: At low temperatures the Polyakov loop distribution is affected slightly by the Gradient flow, but the expectation value is still small. *Right*: 509.11(5.52) MeV: The Polyakov loop distribution strongly bulks around the centre element at finite flow time.

It is also worthwhile to note that we observe a localization of regions, where the Polyakov loop is small or negative, when the gauge field is smoothed. As the unsmoothed configurations exhibit strong short range fluctuations, the local Polyakov loop fills the available volume homogeneously. However, on the smoothed configuration the spatial distribution of $l(x)$ exhibits local sinks, where the holonomy has small values. This is shown in Figure 2.33, where the spatial distributions of regions of $\mathrm{Re}\, l(x) \leq 0.3$ are plotted at the temperature T=509.11(5.52) MeV.

On the smooth gauge configurations the sinks of the local Polyakov loop appear in connected and spatially localized lumps, very similar to the lumps we found in localized quark modes.

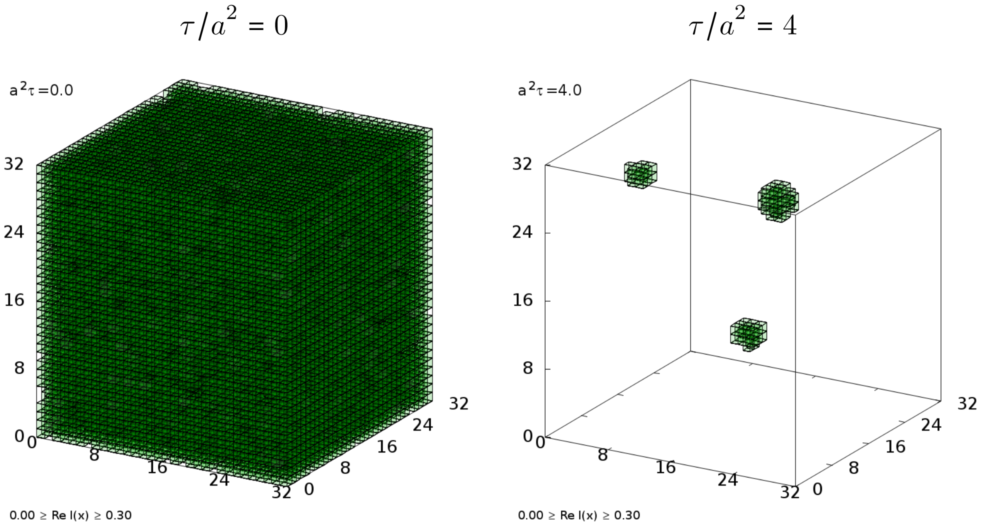

Figure 2.33.: The spatial distribution of the local Polyakov loop where $\mathrm{Re}\, l(x) \leq 0.3$ at flow time $\tau = 0a^2$ (left) and $\tau = 4a^2$ (right) at T=509.11(5.52) MeV. The regions of small values of $\mathrm{Re}\, l(x)$ come in localized lumps when UV-fluctuations are smoothed out via gradient flow.

2.6.3. Local correlations with quark modes

Therefore the question arises, whether the local distribution of Polyakov lines influence the localization features of quark modes. In the following we will study the correlation between the real part of the local holonomy $\mathrm{Re}\, l(x)$ and the local distribution of the time integrated scalar and pseudoscalar density of quark eigenmodes

$$\begin{aligned} p(x) &= \int dt \langle \psi(x,t) | \psi(x,t) \rangle \\ \text{and} \quad p^5(x) &= \int dt \langle \psi(x,t) | \gamma_5 | \psi(x,t) \rangle \end{aligned} \tag{2.32}$$

in order to determine if these local densities depend on the spatial structure of $l(x)$.

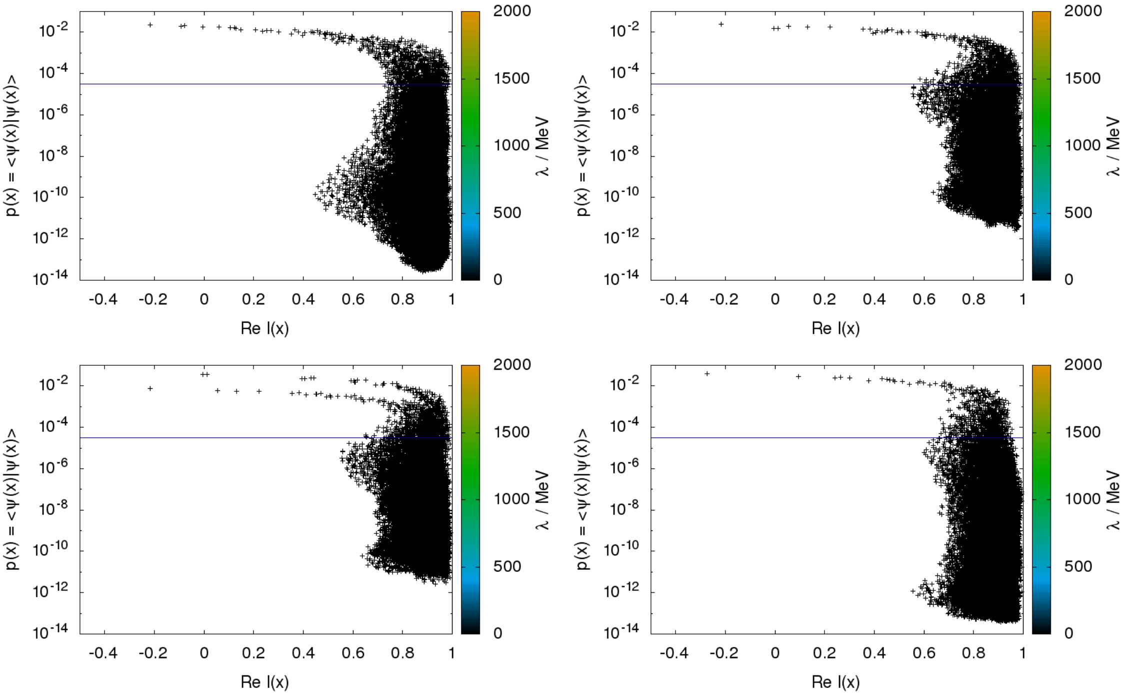

Figure 2.34.: T=509.11(5.52) MeV: Four zero modes from different configurations. These strongly localized eigenmodes present a strong anti-correlation with the local Polyakov loop. The dense regions of the zero modes coincide with regions where $\mathrm{Re}\, l(x)$ is small. In regions where $\mathrm{Re}\, l(x)$ is close to 1 the scalar density is suppressed by several orders of magnitude.

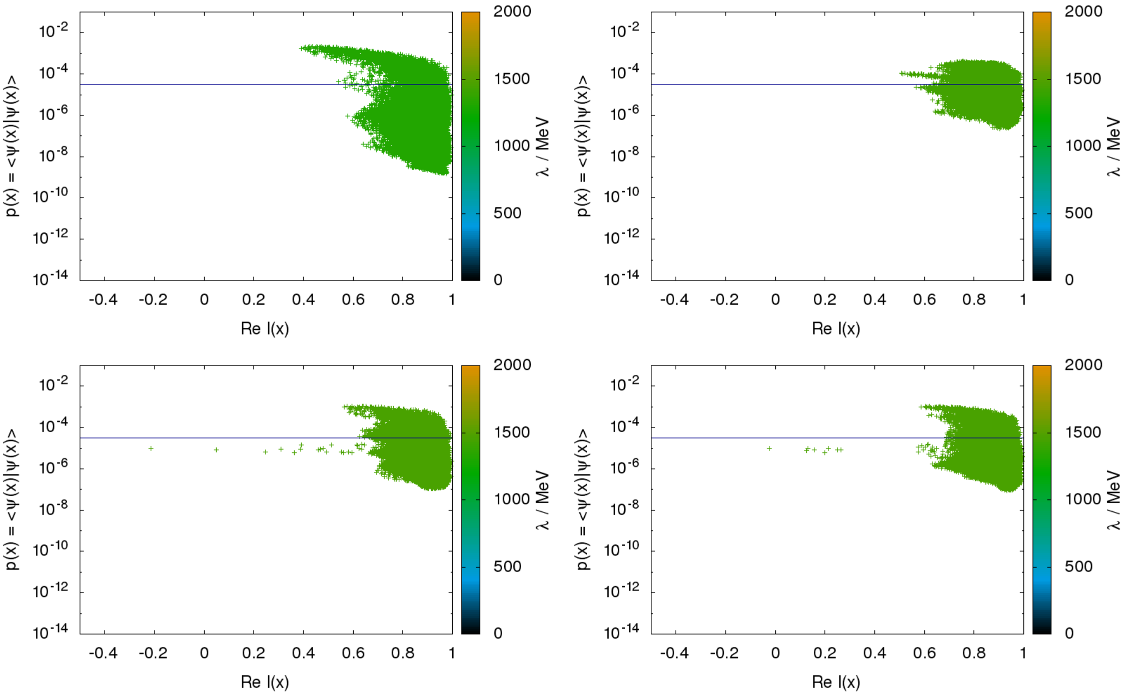

Figure 2.35.: T=509.11(5.52) MeV: Four localized modes from different configurations. *Top left*: λ = 1321.57 MeV $\approx 0.868\lambda_c$. *Top right*: λ = 1435.11 MeV $\approx 0.942\lambda_c$. *Bottom left*: λ = 1450.58 MeV $\approx 0.952\lambda_c$. *Bottom right*: λ = 1460.76 MeV $\approx 0.959\lambda_c$. The same suppression of $p(x)$ in regions where $\mathrm{Re}\, l(x)$ is large can be observed, however, to a smaller extent.

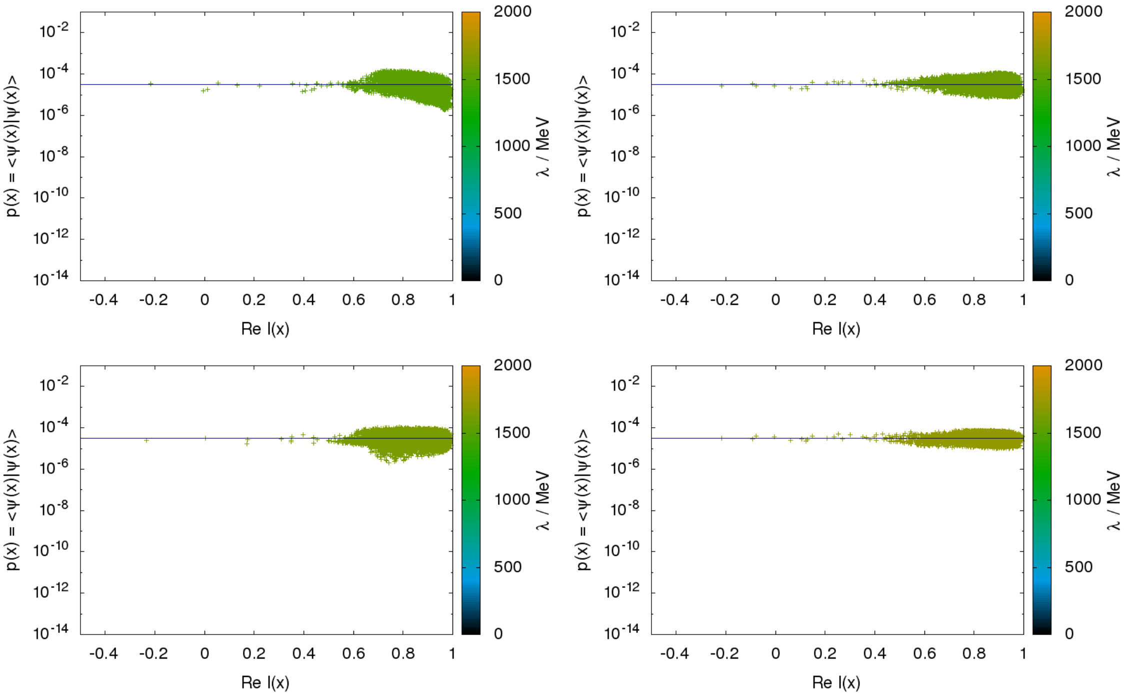

Figure 2.36.: T=509.11(5.52) MeV: Four modes in proximity of the mobility edge. *Top left*: $\lambda = 1518.49$ MeV $\approx 0.997\lambda_c$. *Top right*: $\lambda = 1578.94$ MeV $\approx 1.037\lambda_c$. *Bottom left*: $\lambda = 1627.34$ MeV $\approx 1.068\lambda_c$. *Bottom right*: $\lambda = 1721.70$ MeV $\approx 1.130\lambda_c$. Here the correlation of $p(x)$ and $\mathrm{Re}\, l(x)$ has vanished.

The correlation between the local Polyakov loop and the scalar density of selected quark modes are shown in Figure 2.34 for zero modes, in Figure 2.35 for localized non-zero modes and in Figure 2.36 for extended modes in proximity of the mobility edge. In these plots, the blue line indicates $p(x) = \frac{1}{V}$, where extended modes are closely distributed around.

In these figures, one finds, that the localized modes have a significantly smaller density in regions, where the local holonomy bulks around the centre element 1, and a large density, where the holonomy is small or negative. This is especially true for zero modes, which are most prominently localized as we have seen in Section 2.4.2. This means, that localized modes have, as opposed to delocalized modes, a clear anti-correlation to the local Polyakov loop, they are more present in sinks of $\mathrm{Re}\, l(x)$ and driven away from sources.

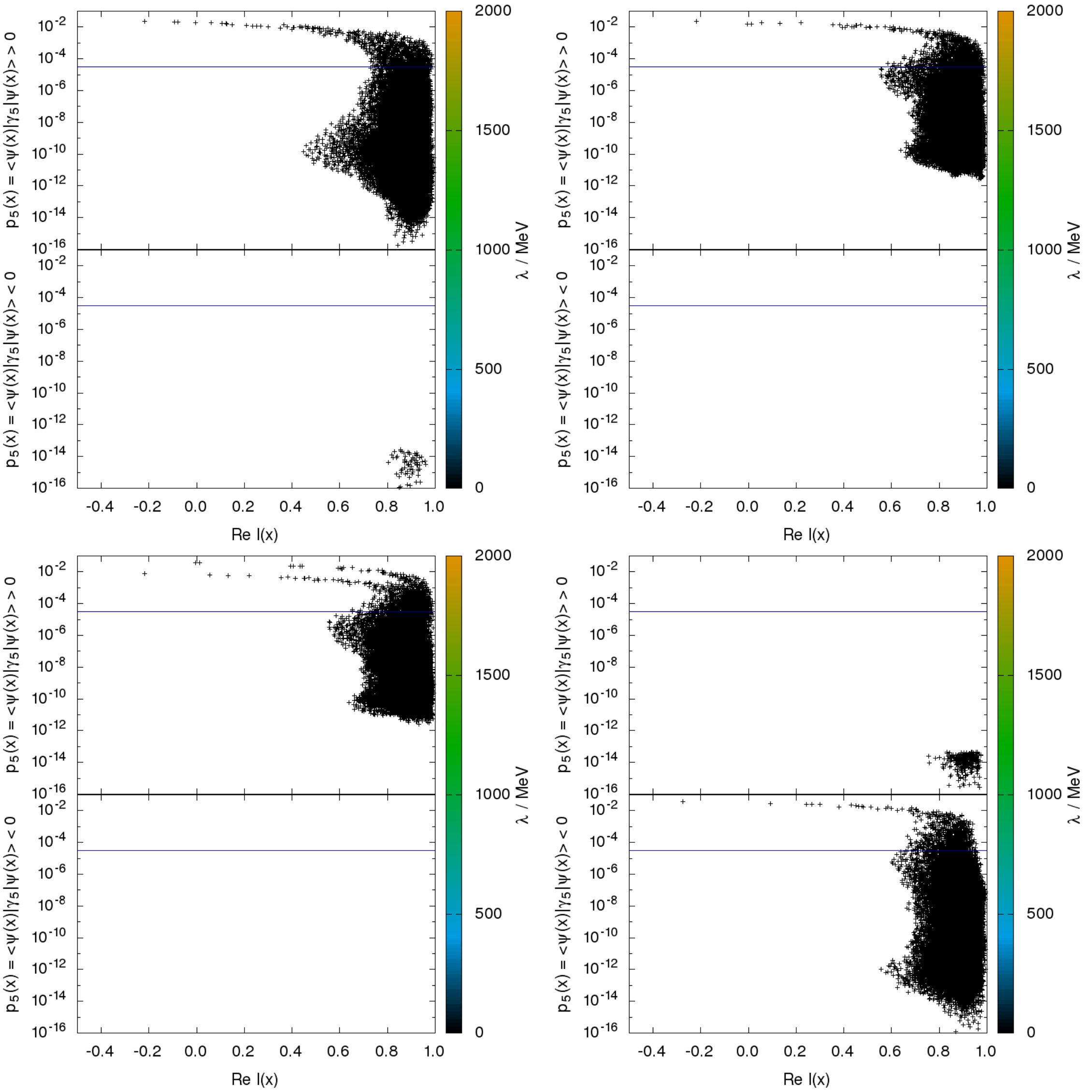

Figure 2.37.: T=509.11(5.52) MeV: Four zero modes from different configurations. Again, the dense regions coincide with small Re $l(x)$ and the pseudoscalar density is suppressed where the holonomy is close to the centre element. The positive and negative branches in $p^5(x)$ are separated among the zero modes and pollutions of opposite signs are small (see the upper left and the lower right panel).

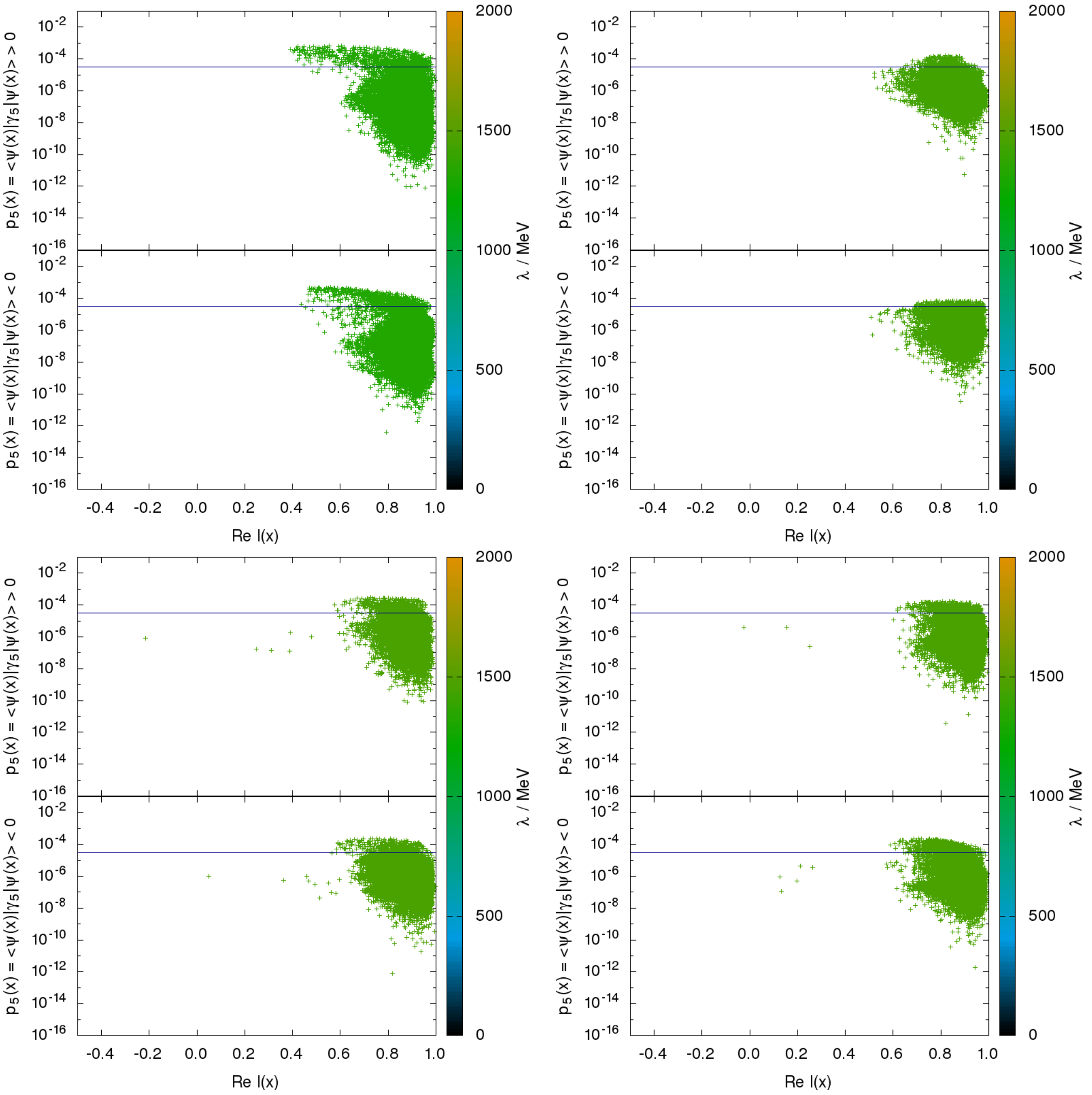

Figure 2.38.: T=509.11(5.52) MeV: Four localized modes from different configurations. *Top left*: λ = 1321.57 MeV $\approx$ 0.868λ_c. *Top right*: λ = 1435.11 MeV $\approx$ 0.942λ_c. *Bottom left*: λ = 1450.58 MeV $\approx$ 0.952λ_c. *Bottom right*: λ = 1460.76 MeV $\approx$ 0.959λ_c. These modes contain both positive and negative regions of $p^5(x)$, which “mirror” each other.

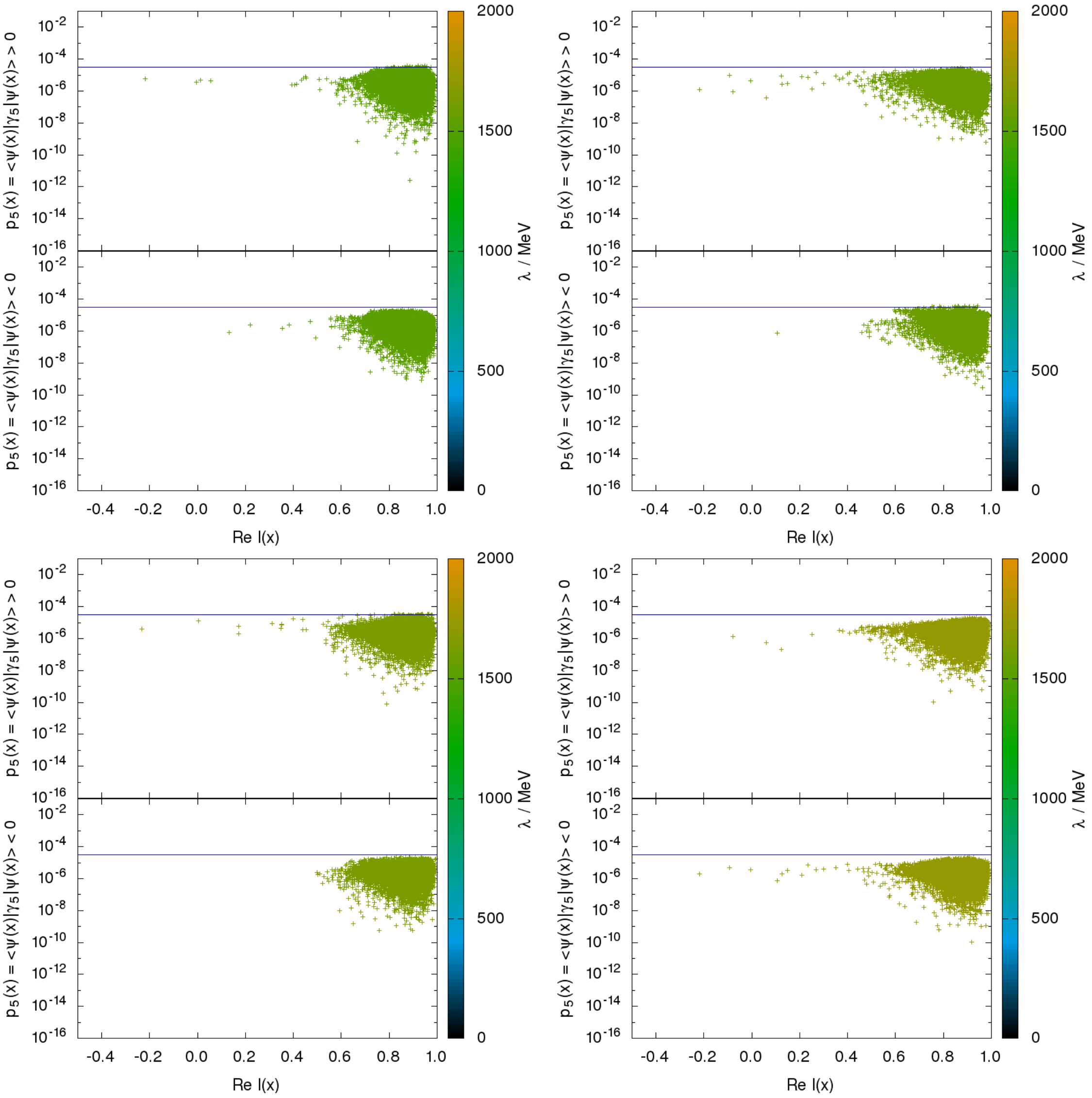

Figure 2.39.: T=509.11(5.52) MeV: Four modes in proximity of the mobility edge. *Top left*: $\lambda = 1518.49$ MeV $\approx 0.997\lambda_c$. *Top right*: $\lambda = 1578.94$ MeV $\approx 1.037\lambda_c$. *Bottom left*: $\lambda = 1627.34$ MeV $\approx 1.068\lambda_c$. *Bottom right*: $\lambda = 1721.70$ MeV $\approx 1.130\lambda_c$. The positive and negative regions of $p^5(x)$ again mirror each other.

The correlation between $\mathrm{Re}\, l(x)$ and the pseudoscalar density is shown in Figures 2.37, 2.38 and 2.39, where the upper panels show regions of positive and the lower panels regions of negative pseudoscalar density. Here we can also see that the low eigenmodes show the same behaviour, being "pushed away" by large $\mathrm{Re}\, l(x)$. The regions far away from the centre element $\mathrm{Re}\, l(x) = 1$ dominate the total chirality and thus the topological charge.

For zero modes, depicted in Figure 2.37, we find, that each mode mostly resides either at positive or negative pseudoscalar density, since zero modes have definite chirality. The pollution by opposing signs in $p^5(x)$ (which can be seen in the upper left and the lower right panel) is very small and only occurs in regions, where the mode is strongly suppressed.

Localized modes, as shown in Figure 2.38 exhibit a balanced, almost symmetric distribution of the pseudoscalar density in both signs, such that the total chirality agrees well with zero. Some localized modes contain stronger fluctuations, such that the pseudoscalar density has regions above the $1/V$-line. Similarly extended modes close to λ_c (figure 2.39) are also symmetric around $p^5(x) = 0$, but are bound from above by the $1/V$-line.

From this it is conjectured, that the local Polyakov loop plays the role of the lattice impurities, or the random on-site potential in the Anderson model from condensed matter physics. The fluctuations of the temporal links appear to be acting as a three-dimensional disorder and are governed by the temperature. This could be an explanation for the temperature dependence of the localized regime within the Dirac operator spectrum.

Since the eigenmode density at small energies causes chiral symmetry breaking by the Banks-Casher relation, and since the quark propagator and thus the chiral condensate are dominated by localized modes, it is further conjectured, that the localization of quark modes in QCD is the connection between the spontaneous breaking of centre symmetry and deconfinement, reflected in the Polyakov loop, and chiral symmetry breaking.

2.7. Summary

In this chapter we studied the localization properties of the QCD Dirac operator eigenmodes on the lattice, where we used the overlap discretization, on the tmfT lattice configurations for several temperatures. We extracted the volume that is occupied by the eigenmodes from the inverse participation ratio and devised an estimate for the mobility edge. Its temperature dependence showed to be linear.

We found that the modes below the delocalization transition present a multifractal structure and computed the fractal dimensions of the eigenmodes with a box counting method. We could conclude that the critical dimension is consistent with a constant while the zero mode dimension agrees with an exponential decay in the temperature and asymptotically approaches 1.

Furthermore, we presented selected eigenmodes throughout the spectrum (zero, localized, critical and extended modes) and the correlators of their chiral densities and found that they are time dependent only in the proximity of the mobility edge. Also small lumps that are strongly localized in time appear close to λ_c. The correlation functions allow a deep insight into the geometry of the eigenmodes, which was also studied with the spatial moments of the time integrated densities. It was found that the low-lying eigenmodes have an oblate structure and correlation length of the chiral density is spatially anisotropic. From the chirality overlap function it was concluded that the localized centres below the mobility edge strictly separate chiral components of the quark wave functions.

The distribution of level spacings agrees well with the predictions from random matrix theory above λ_c and presented a Poisson-like tail in the low energy regime. Statistics, however, did not allow an extraction of the mobility edge or critical exponents from the ULSDs. To choose the spectral intervals on which the level spacings were computed we used the mobility edge estimates from the relative eigenvector volume.

After UV-smoothing the gauge configurations with gradient flow it was possible to find a clear correlation between the local Polyakov loop and the wave functions. The local holonomy occurs in clusters and acts as disorder that causes the low energy wave functions to localize. This connects deconfinement to the chiral transition, as the Polyakov line triggers the localization of quark modes which dominate the quark propagator.

3. The topological structure of QCD

On a lattice with a finite spacing topology is not well-defined. One commonly tries to gain insight to the continuum quantities for sufficiently small lattice spacings and using different approaches to topologically invariant quantities: either by employing a gluonic definition of the topological charge, based on some discretization of the field strength tensor, or with a fermionic approach by studying the spectral properties of the Dirac operator. In this work both approaches shall be compared and used to study the topological structure of QCD at finite temperature.

The Euclidean action of QCD has classical solutions at saddle points of the partition function and can be decomposed like [131]

$$S_g = \frac{1}{4}\int d^4x F^a_{\mu\nu}(x)F^a_{\mu\nu}(x) = \frac{1}{4}\int d^4x\left(\pm F^a_{\mu\nu}(x)\tilde{F}^a_{\mu\nu}(x) + \frac{1}{2}\left(F^a_{\mu\nu} \mp \tilde{F}^a_{\mu\nu}\right)^2\right). \tag{3.1}$$

The dual field strength tensor is defined as

$$\tilde{F}^a_{\mu\nu}(x) = \frac{1}{2}\epsilon_{\mu\nu\rho\sigma}F^a_{\rho\sigma}(x), \tag{3.2}$$

where $\epsilon_{\mu\nu\rho\sigma}$ is the antisymmetric tensor. After decomposing the action this way, it is minimized by local self-dual fields, the so-called *instanton* solutions, which read

$$F^a_{\mu\nu} = \begin{cases} +\tilde{F}^a_{\mu\nu} & \text{“Instanton”} \\ -\tilde{F}^a_{\mu\nu} & \text{“Anti-Instanton”} \end{cases}. \tag{3.3}$$

These solutions locally solve the classical equations of motion $D^{ab}_\rho F^b_{\rho\sigma} = 0$. The first part of the action is invariant under continuous transformations of the gauge field and is proportional to the *topological charge*

$$Q = \frac{1}{16\pi^2}\int d^4x F^a_{\mu\nu}(x)\tilde{F}^a_{\mu\nu}(x). \tag{3.4}$$

The minimum the gauge action is the instanton action $S_g^{\text{instanton}} = 4\pi^2|Q|$. In Euclidean space instantons are strongly localized spherical fields, whereas in Minkowski space they are tunnel events between different vacua of QCD $|n\rangle$. The QCD ground state is then a superposition

$$|\Theta\rangle = \sum_n e^{in\Theta}|n\rangle. \tag{3.5}$$

If the vacuum angle Θ is non-vanishing, the QCD Lagrangian acquires a term $\mathcal{L}_\Theta = i\Theta Q$, which breaks the T- and CP-invariance of the theory. As CP-conservation is observed, this poses a puzzle, commonly referred to as the *strong CP problem*. The *axion* solution as proposed by Peccei and Quinn in 1977 [132, 133] explains the CP-conservation of QCD by introducing a pseudoparticle, called the axion, which couples to the topological charge. From the grand canonical partition function $Z(\Theta, T)$ of QCD with an axion source one can deduce the axion potential $F(\Theta, T)$ and the mass of the axion is then

$$(m_a(T)f_a)^2 = \left.\frac{\partial^2 F(\Theta,T)}{\partial\Theta^2}\right|_{\Theta=0} = \chi_q(T), \tag{3.6}$$

where f_a is the coupling of the axion to $\tilde{F}F$. The topological susceptibility χ_q can be computed from the local topological charge correlator like

$$\chi_q = \int d^d x \langle q(x) q(0) \rangle = \frac{\langle Q^2 \rangle}{V}, \tag{3.7}$$

and is proportional to the variance of the distribution of the topological charge in an ensemble since $\langle Q \rangle = 0$. Experimentally the vacuum angle was found to have an upper bound $\Theta \leq 10^{-10}$ by measuring the electric dipole moment of the neutron [134].

A fermionic approach to the topology of QCD can be achieved by employing the Atiyah-Singer index theorem. Counting the zero modes of the Dirac operator gives the topological charge like

$$Q = N_+ - N_-. \tag{3.8}$$

$N_\pm$ is the number of zero modes with chirality ±1. Non-zero modes have a vanishing chirality. The fermionic topological charge density then reads

$$q(x) = -\operatorname{tr}\left[\gamma_5 \left(1 - \frac{a}{2} D_{x,x}\right)\right]. \tag{3.9}$$

To compute this quantity on the lattice one requires in principle the full (continuous) spectrum of the Dirac operator. From our lattice calculations we have, however, only access to a limited number of eigenmodes of a discretized Dirac operator. The contribution of higher modes (which is very small already) is thus cut off with some regulator function $\mathcal{R}(|\lambda|)$. If all modes were taken into account, the conjugate pairs would cancel. We can then compute the topological charge density like

$$q(x) = -\sum_j \left(1 - \frac{\lambda_j}{2}\right) \langle \psi_j(x) | \gamma_5 | \psi_j(x) \rangle \mathcal{R}(|\lambda_j|), \tag{3.10}$$

where we chose the regulator

$$\mathcal{R}(|\lambda|) = \begin{cases} 1 & \text{for } \lambda \leq \lambda_0 \\ \exp(-\kappa(\lambda - \lambda_0)) & \text{for } \lambda > \lambda_0 \end{cases}. \tag{3.11}$$

On the lattice the gluonic topological charge density can be expressed like [135]

$$q(x) = \frac{1}{32\pi^2} \epsilon_{\mu\nu\rho\sigma} \operatorname{tr} G^P_{\mu\nu}(x) G^P_{\rho\sigma}(x) \tag{3.12}$$

where $G^P_{\mu\nu}(x)$ is the plaquette-like Clover leaf. This plaquette-like leaf has $\mathcal{O}(a^2)$ discretization errors. These discretization errors can be improved upon by including planar rectangle contributions

$$q(x) = \frac{1}{32\pi^2} \epsilon_{\mu\nu\rho\sigma} \operatorname{tr}\left(c_0 G^P_{\mu\nu}(x) G^P_{\rho\sigma}(x) + 2c_1 G^R_{\mu\nu}(x) G^R_{\rho\sigma}(x)\right), \tag{3.13}$$

which are sketched in Figure 3.1.

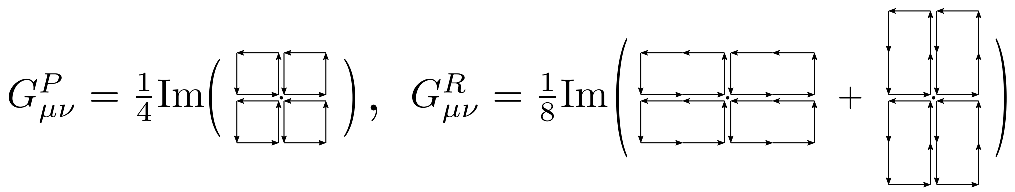

Figure 3.1.: The plaquette- and rectangle-contributions to the discretized field strength tensor, used for the gluonic topological charge from the lattice.

Weisz *et al.* proposed $c_0 = \frac{5}{3}$ and $c_1 = -\frac{1}{12}$, which reduces the discretization errors to $\mathcal{O}(a^4)$.

From the topological densities the total charge is computed like $Q = \int d^d x q(x)$. In a finite volume the gluonic topological charge is not necessarily an integer, this is only strictly true in the limit $V \to \infty$. Also, the gluonic topological charge is especially prone to UV-fluctuations, which is why gradient flow was used here to smooth the lattice gauge fields. The fermionic topological charge on the other hand could suffer from cutoff effects and must be renormalized as well.

3.1. Topology and the Anderson transition

t'Hooft found that the presence of an instanton induces a zero mode with negative chirality in the Dirac operator, an anti-instanton induces a zero mode with positive chirality. From this a model for chiral symmetry breaking based on the presence of local self-dual objects within a gauge configuration was deduced. The *instanton liquid model* (ILM) was proposed by Shuryak, Diakonov and Petrov [131,136,137] and describes a liquid of instanton and anti-instanton objects with a very low density, such that the semi-classical approximation is possible. The vacuum configurations are strongly localized (anti-)instantons which are surrounded by a weak gauge field. An instanton anti-instanton pair with large separation then induces a pair of zero modes with opposing chirality. If these modes begin to overlap, e.g. when more instanton objects are added, the degeneration of the modes is lost and the Dirac operator obtains two conjugate eigenmodes with non-vanishing λ. These non-zero modes are no longer eigenvectors of γ_5. The non-vanishing spectral density at the origin then induces a chiral condensate by the Banks-Casher mechanism, which breaks chiral symmetry.

Although the ILM provides an explanation for chiral symmetry breaking, it fails to explain confinement.

Models based on the ILM generally assume that the spectrum of the Dirac operator consists of modes that are the result of overlaps of zero modes. Based on the instanton-liquid model the dilute non-interacting caloron gas model was formulated by Gerhold, Ilgenfritz and Müller-Preussker [138]. This is an analogy to the Anderson transition in QCD:

In the ILM zero modes are bound to instantons, overlaps between neighbouring instantons, or their long-range interaction respectively, create a chiral condensate as the zero modes “delocalize” within the spectrum and obtain finite eigenvalues [139–141]. In the Anderson model the localized electron wave functions are bound to areas with low impurities. When less volume is occupied with impurities, which means that the random potential is weaker, these localized electrons begin to overlap and push each other to spatial delocalization.

As for the Anderson transition in the spectrum of the QCD Dirac operator, we found in Chapter 2 that localized quark modes are bound to sinks in the local Polyakov loop. When the local holonomy becomes homogeneous by lowering the temperature localized quarks begin to overlap and delocalize.

3.2. Gradient flow and topological structure

In order to determine the fermionic topological charge we need a reliable method to find the zero modes of the Dirac operator. Proper zero modes should have definite chirality

$$\chi_j = \int d^d x \langle \psi_j(x) | \gamma_5 | \psi_j(x) \rangle = \begin{cases} \pm 1 & \text{for } \lambda_j = 0 \\ 0 & \text{for } \lambda_j \neq 0 \end{cases} . \tag{3.14}$$

In principle the topological charge can then be read off the chiralities of each mode like

$$Q = -\sum_j \left(1 - \frac{\lambda_j}{2}\right)\chi_j. \tag{3.15}$$

Unfortunately we found zero modes with non-integer chirality in our calculations. Although this effect is very rare (it affects less than 0.1% of all modes in an ensemble) we need to verify that there is no systematic error present.

Since zero modes are infinitely close to each other, it is numerically very challenging to distinguish them from one another. UV-fluctuations mix modes which are close to each other, zero modes in particular. We hence use gradient flow with respect to the Iwasaki gauge action to “unmix” zero modes.

In the most problematic case one configuration contained three mixed modes close to zero and it was impossible to determine whether or not there is a proper zero mode in the spectrum.

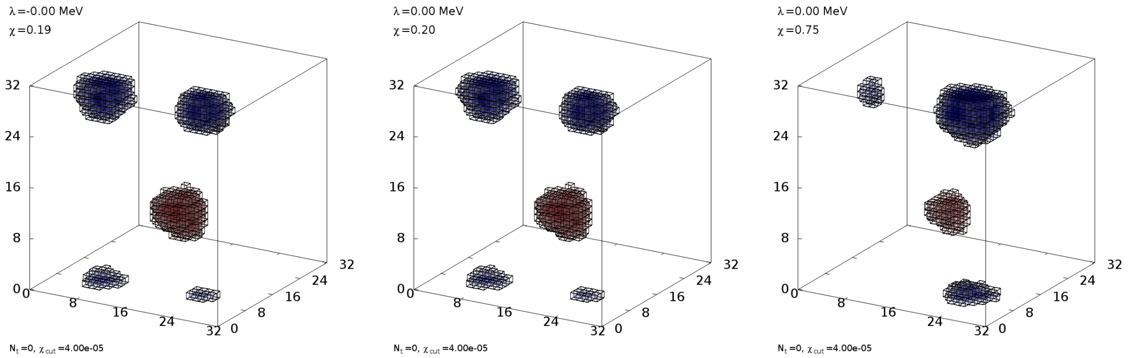

Figure 3.2.: $\tau/a^2 = 0$: Three zero mode candidates on a configuration from the D370 ensemble (T=509.11(5.52) MeV) which have the indefinite chiralities $\chi_0 \approx 0.19$, $\chi_1 \approx 0.20$ and $\chi_2 \approx 0.75$.

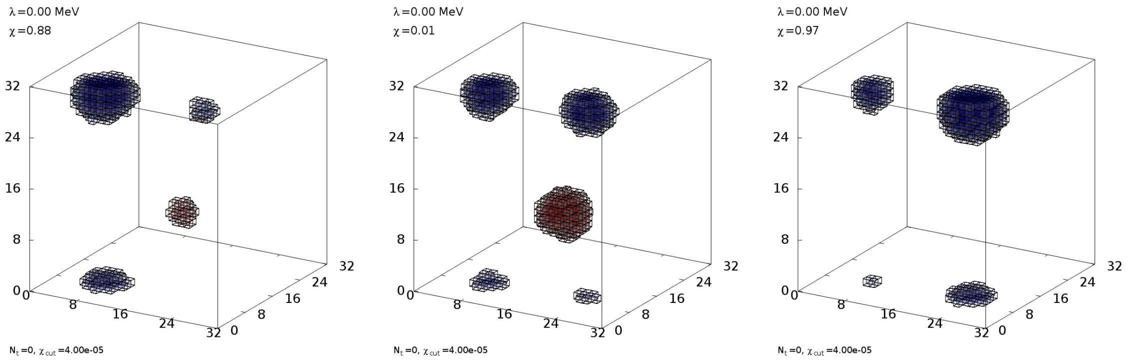

Figure 3.3.: $\tau/a^2 = 1$: The chiralities χ of the three aforementioned modes changed towards integer values, we find $\chi_0 \approx 0.88$, $\chi_1 \approx 0.01$ and $\chi_2 \approx 0.97$.

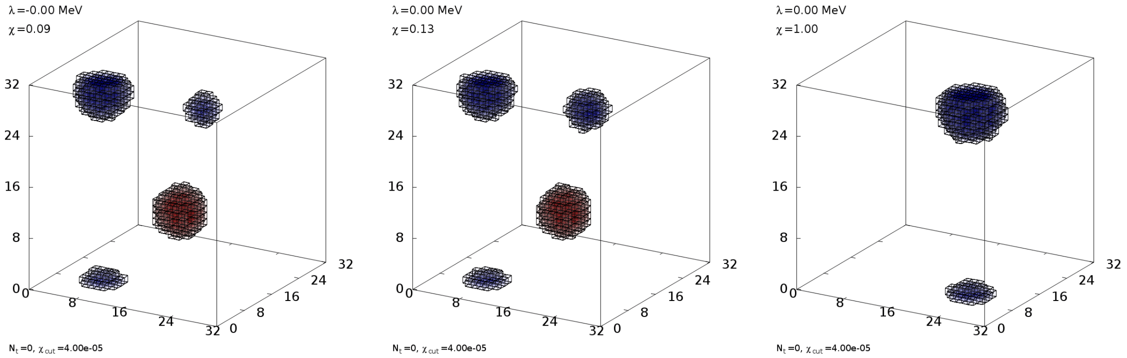

Figure 3.4.: $\tau/a^2 = 4$: Two modes seem to approach $\chi = 0$ while the third appears to be a proper zero mode with positive chirality. Note that all three modes still share a chirally positive cluster and are probably still not entirely unmixed.

In Figures 3.2, 3.3 and 3.4 the spatial distribution of the pseudoscalar density on a single time slice of three candidates for zero modes are shown, which are supposedly mixed by UV-fluctuations. At $\tau/a^2 = 0$ their chiralities are mixed and no proper zero mode can be identified, at large flow time one mode obtains a positive chirality and no negative cluster remains it its spatial distribution. The other two modes have a non-vanishing, but small remnant chirality.

We conclude that for a proper calculation of the topological charge by counting zero modes, it is imperative to smooth the gauge configurations first. However, as this problem occurred at very rare instances only, our estimates of Q without gradient flow are considered reliable.

An alternative method is the multiplicative renormalization as proposed in [94,142], which yields a renormalized topological charge $Q^{\text{ren}} = \text{round}\,(ZQ)$, where the renormalization constant $Z > 1$ minimizes

$$\chi^2 = \int \mathcal{D}U\,(ZQ(U) - \text{round}\,(ZQ(U)))^2\,. \tag{3.16}$$

This is depicted in Figure 3.5.

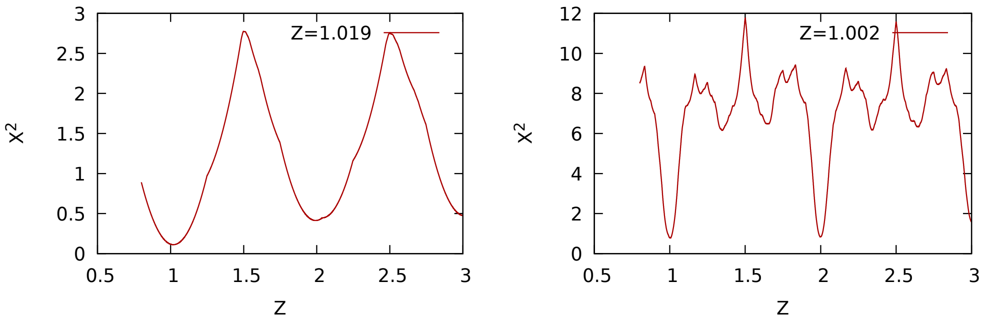

Figure 3.5.: The deviation from integer values over the multiplicative renormalization constant Z as in equation (3.16) for the fermionic topological charge. *Left*: T=527.06(5.52) MeV. *Right*: T=210.82(2.93) MeV.

Here we study the distribution of the gluonic and fermionic topological charge and compare the two. This is plotted in Figure 3.6. For computing the gluonic topological charge the gauge configurations have been smoothed using Iwasaki flow for flow times $\tau/a^2 \leq 0.5$, as this observable is very susceptible to UV-distortions.

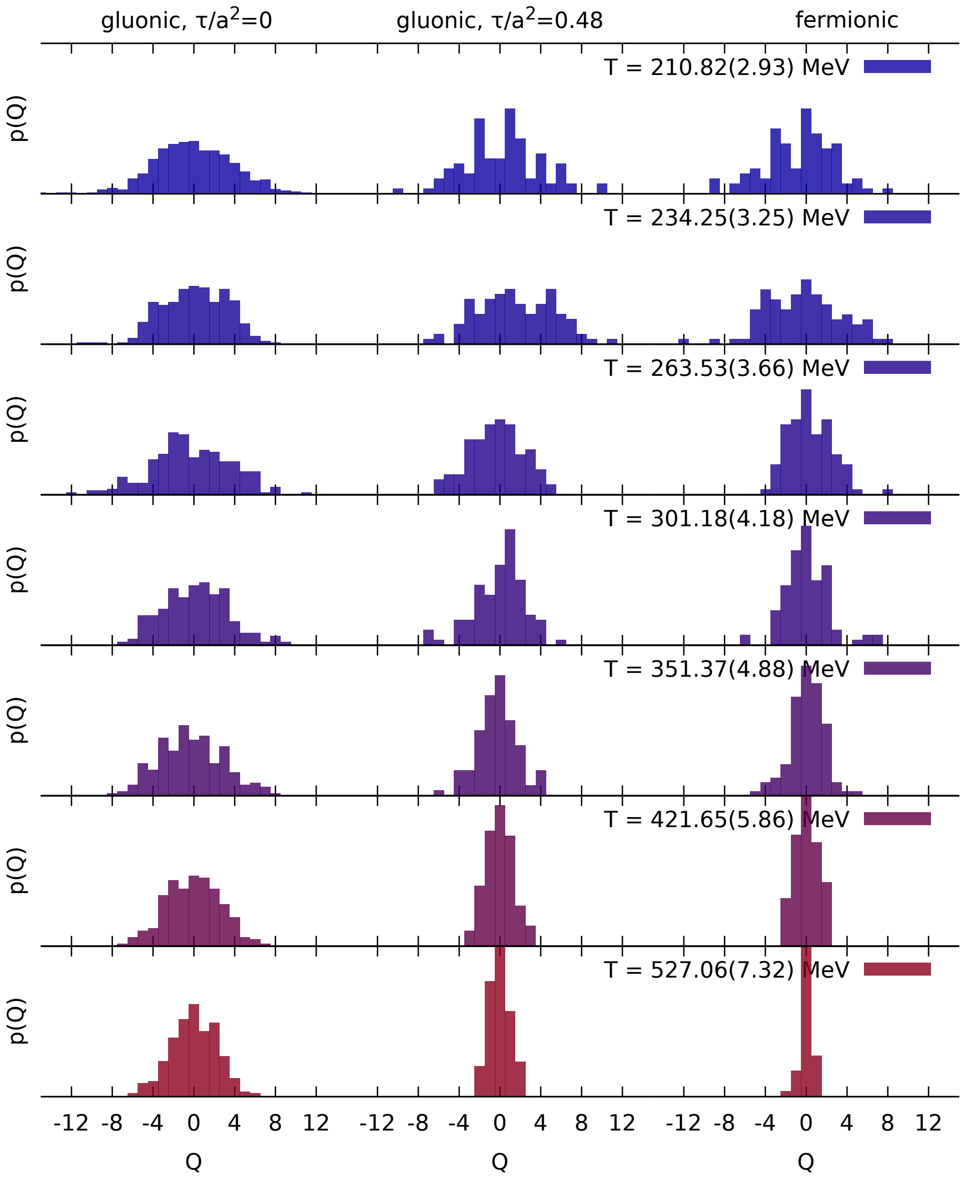

Figure 3.6.: The distribution of the topological charge from the gluonic definition at $\tau/a^2 = 0$ (*Left*), at $\tau/a^2 = 0.48$ (*Middle*) and from the fermionic definition (*Right*).

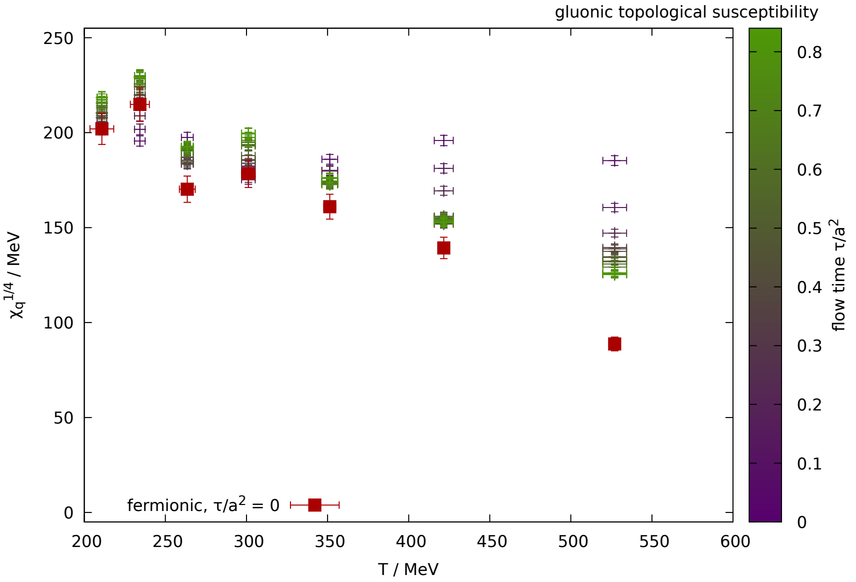

Figure 3.7.: The gluonic topological susceptibility compared with the fermionic on the A370 meta ensemble for several temperatures. At larger flow times the difference becomes smaller.

The topological susceptibilities was computed from the distribution of the total topological charge and is shown in Figure 3.7 for both the fermionic and the gluonic definition at several flow times. Although both quantities deviate, the gluonic approaches the fermionic susceptibility at larger τ. It seems, however, that it approaches a plateau at large temperatures, such that gradient flow does not suffice.

3.3. Topological overlap with quark wave functions

In this section we study how the quark wave functions that were computed in Chapter 2 relate to the topological charge density. We define the overlap function

$$O_5(\lambda_j) = \frac{\int d^4x p_j^5(x) q(x)}{\int d^4x \left((p_j^5(x))^2 + (q(x))^2 \right)}, \tag{3.17}$$

where the $p_j^5(x)$ is the pseudoscalar eigenvector density $p_j^5(x) = \langle \psi_j(x) | \gamma_5 | \psi_j(x) \rangle$ and $q(x)$ is a topological density

$$q(x) = \begin{cases} -\mathrm{Tr}\left[\gamma_5 \left(1 - \frac{a}{2} D_{x,x}\right)\right] & \text{(fermionic)} \\ \frac{g^2}{16\pi^2} \epsilon_{\mu\nu\rho\sigma} F^a_{\mu\nu}(x) F^a_{\rho\sigma} & \text{(gluonic).} \end{cases} \tag{3.18}$$

Since most of the eigenmodes were computed at vanishing flow time, the overlap between the eigenmodes and the topological charges was computed at $\tau/a^2 = 0$ as well.

The overlap of the pseudoscalar density and the gluonic topological charge density from the tmfT ensembles is shown in Figure 3.8, the overlap with the fermionic topological density in Figure 3.9. The vertical lines in the plots indicate the mobility edges at the respective temperatures. We find that localized modes carry (both fermionic and gluonic) topological charge, while the overlap drops to zero the more delocalized the modes are. It can be conjectured that topological charge appears in localized "lumps" as well, which are correlated to the eigenmode distributions.

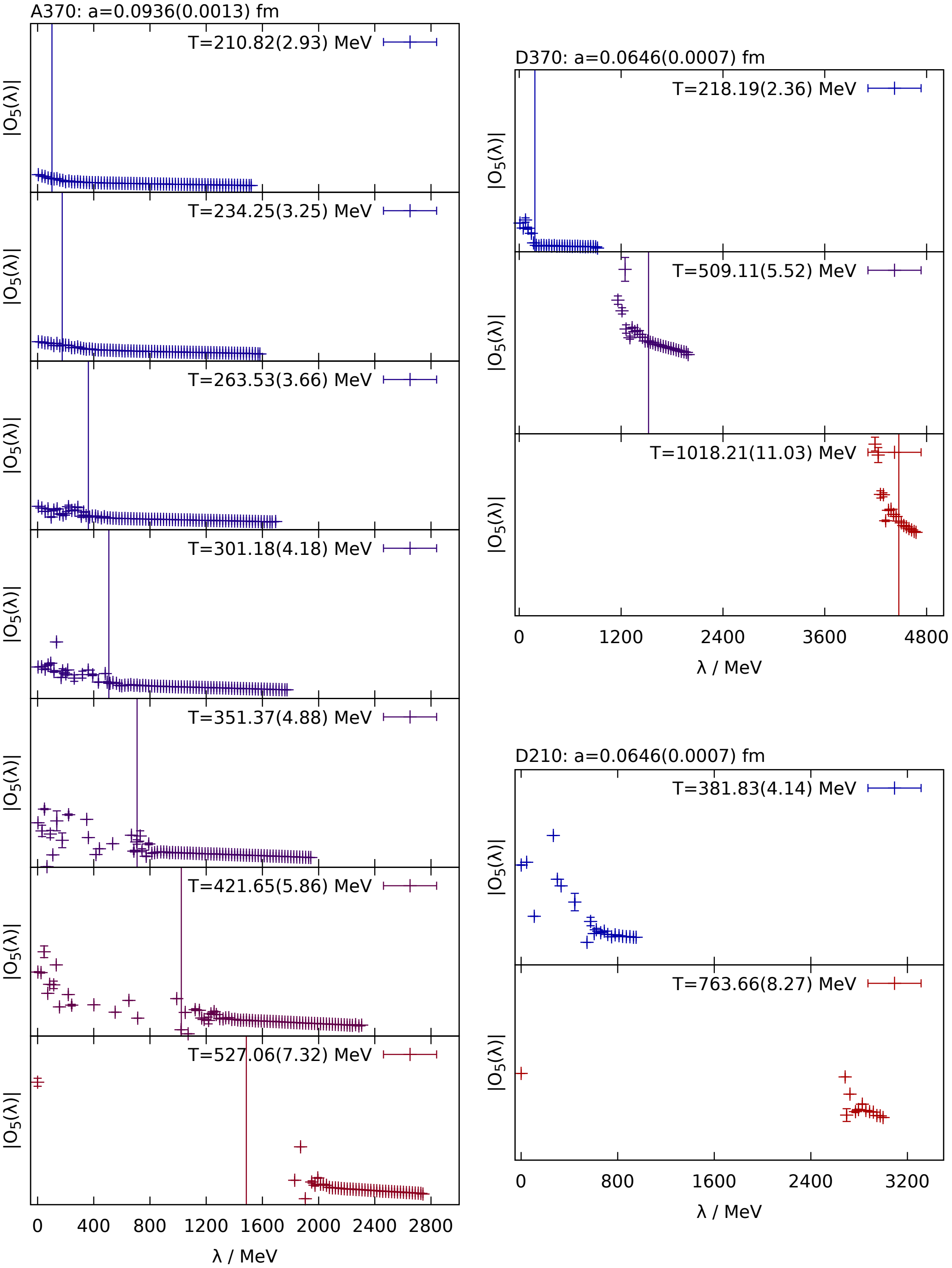

Figure 3.8.: Overlap of the gluonic topological charge with the pseudoscalar density. Vertical lines indicate the mobility edge as determined from the eigenmode volume.

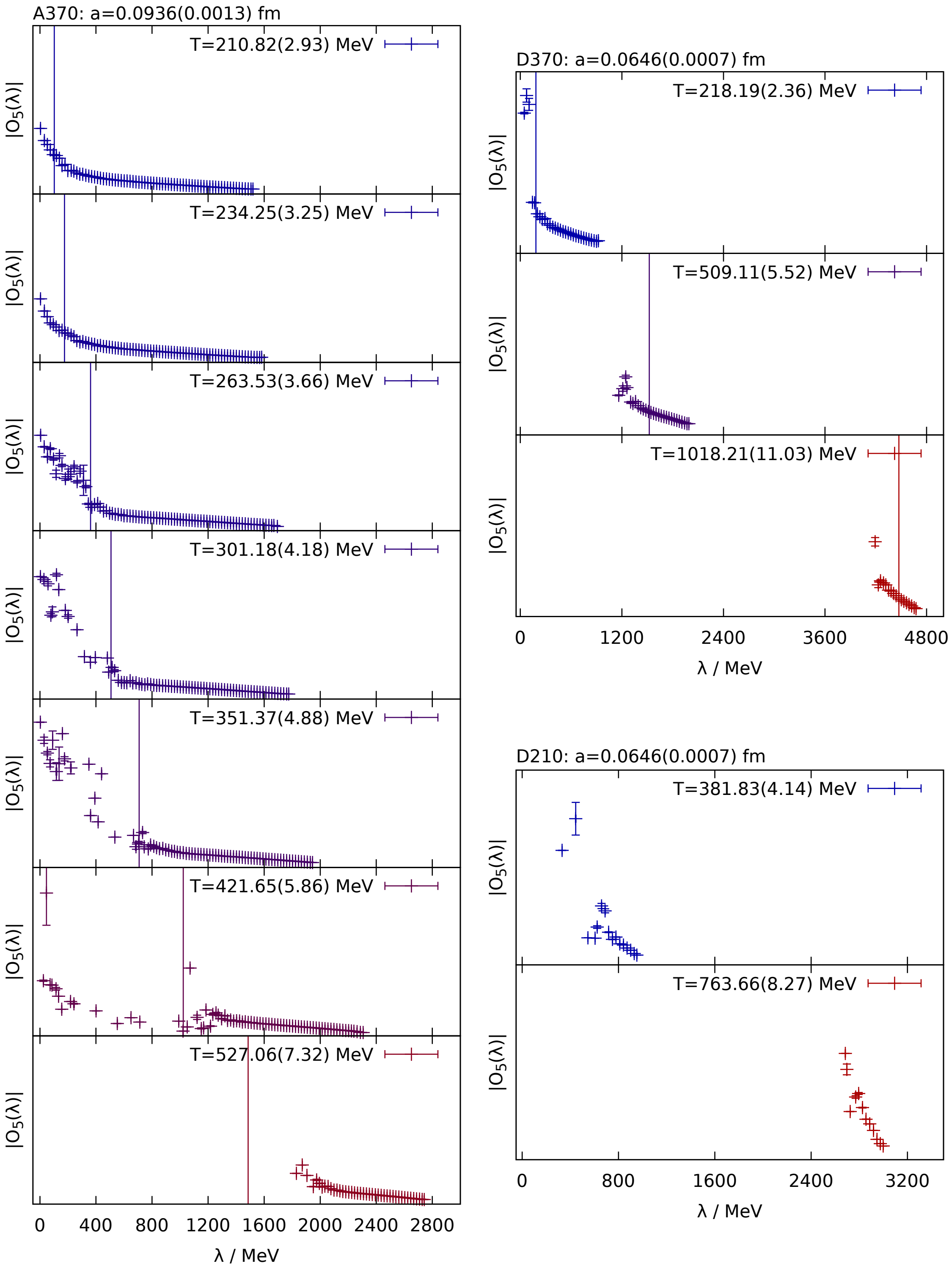

Figure 3.9.: Overlap of the fermionic topological charge with the pseudoscalar density. Vertical lines indicate the mobility edge as determined from the eigenmode volume.

3.4. Local self-duality

In [143] under-relaxed cooling and a pattern recognition method was used to identify instanton objects in the vacuum of SU(3) lattice gauge theory, and it was observed that small instantons form a dilute gas. The properties of an instanton liquid were studied for $N_f = 0$, $N_f = 2+1$ and $N_f = 2+1+1$ dynamical fermion flavours in [144], where gradient flow was used as a cooling method. It was found that the instanton density decreases with the flow time. Clusters of local topological charge were studied in [145], where the fractal dimension of such clusters was determined with a random walk algorithm. Selfdual and anti-self-dual peaks are identified in the gauge field and a correlation between the filtered topological density and the local chirality of localized quark modes is observed.

In this section we will compare the action density

$$s(x) = \frac{1}{32\pi^2} F_{\mu\nu}(x) F_{\mu\nu}(x) \tag{3.19}$$

against the topological density

$$q(x) = \frac{1}{32\pi^2} \tilde{F}_{\mu\nu}(x) F_{\mu\nu}(x) \tag{3.20}$$

to scout for self-dual excitations in the gauge field, using gradient flow to UV-smooth the configurations. The *local self-duality* reads

$$w(x) := \frac{q(x)}{s(x)} \in [-1, 1] \tag{3.21}$$

and if $w(x) = \pm 1$ the classical equations of motion are locally obeyed, which is a necessary requirement for the presence of instantons and anti-instantons. We will extract the number of self-dual centres and the volume of their clusters.

The weighted distribution of the local self-duality $wP(w)$ is shown in Figure 3.10. We find that gradient flow drives the distribution towards self-dual points, but this effect saturates after some flow time. Also, we observe a symmetry between self-dual and anti-self-dual points.

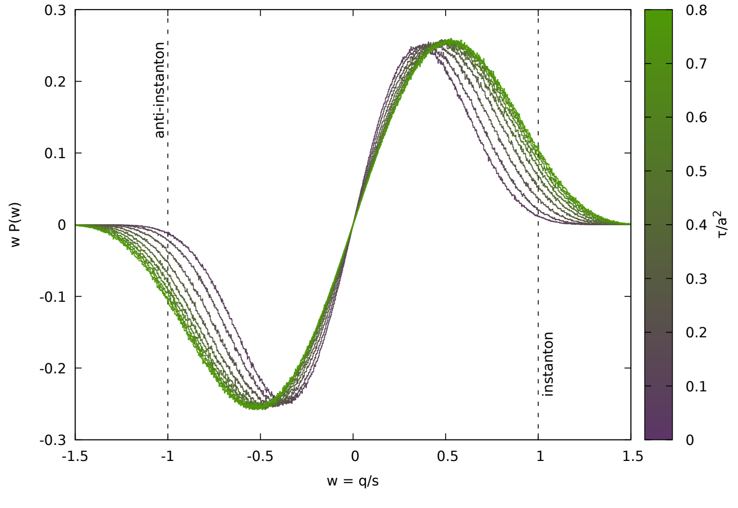

Figure 3.10.: The weighted distribution of the local self-duality at T=351.37(4.88) MeV on the A370 meta ensemble. Gradient flow drives the ratio of topological and action density in proximity to the self-dual points -1 and 1.

We fitted the weighted distribution of $w(x)$ with a function $\propto w \exp(-\left(\frac{w}{2\sigma}\right)^2)$ and determined the maxima, which are given by $w = \sigma$. These maxima are shown in Figure 3.11, and we find that although self-dual points become more prominent at larger flow times, the slope of σ becomes smaller such that we suspect that a plateau will be reached at some point.

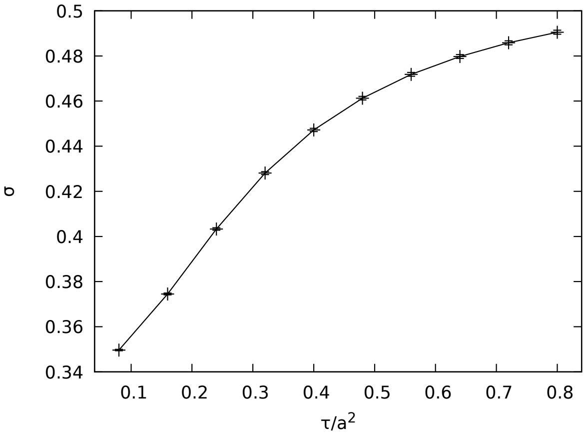

Figure 3.11.: The maxima of the weighted distribution of the local self-duality at T=351.37(4.88) MeV on the A370 meta ensemble.

In order to verify the presence of localized self-dual objects within the gauge configurations, we devised an algorithm to extract such clusters:

1. Filter self-dual centres for which
$$1 - |w(x)| \leq c. \tag{3.22}$$
These points usually come isolated, without neighbours.

2. For each of those centres estimate the extent of the surrounding self-dual cluster by assuming an exponential decay of the local topological density $q(x)$ within the lump like
$$q(x+r) = q(x)e^{-|r|/\kappa}. \tag{3.23}$$
Scan around the self-dual centres recursively and consider a point part of the cluster if $\log\left(\frac{q(x)}{q(x+r)}\right) \leq |r|/\kappa$. The exponential assumption is motivated by the spatial structure of localized quark modes, which carry topological charge (this is conjectured from Section 3.3) and the exponential decay of densities that was found within localized quark modes (see Section 2.4.2).

In Figure 3.12 we see the results of the above algorithm on an example gauge configuration at $T = 527.06(7.32)$ MeV ($N_t = 4$) with the parameters $c = 5 \cdot 10^{-4}$ and $\kappa = 5$ for the flow times $\tau = 0.08a^2$, $\tau = 0.48a^2$ and $\tau = 0.80a^2$. While the exact number of points that are identified as part of clusters depend on the parameters c (the self-duality tolerance) and κ (the cluster decay constant), the qualitative features of the clusters for a fixed set of parameters are comparable.

We find that gradient flow increases the number of self-dual points up to $\tau = 0.48a^2$, after this flow time the size of self-dual clusters seems to become smaller again. In this particular configuration we find at $\tau = 0.48a^2$ a region with $w(x) > 0$ (green) that appears to have a filament structure and a small but finite extent in time direction. All other cluster objects are strictly time localized and very small.

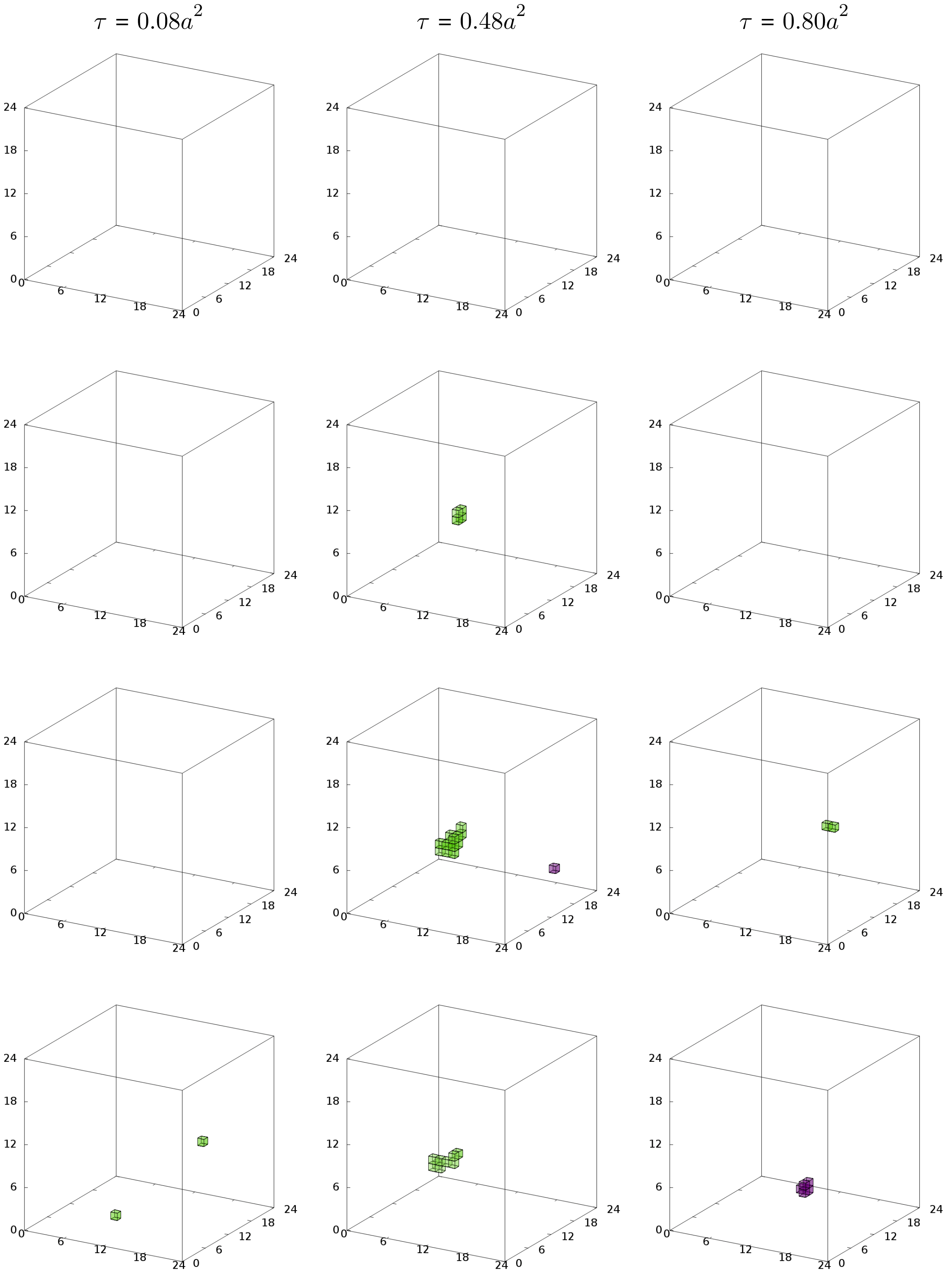

Figure 3.12.: The local self-duality distribution on the time slices $t/a = 0$ (top panels) through $t/a = N_t - 1$ (bottom panels) for the flow times $\tau = 0.08a^2$ (left panels), $\tau = 0.48a^2$ (middle panels) and $\tau = 0.80a^2$ (right panels) at $T = 527.06(7.32)$ MeV ($N_t = 4$). Green corresponds to $w(x) > 0$ and violet to $w(x) < 0$.

To get an idea about the abundance of self-dual objects we used the algorithm as described above and computed the number of self-dual and anti-self-dual centres $n(w > 0)$ and $n(w < 0)$ within each configuration at the flow time $\tau = 0.48a^2$ with the same parameters c and κ. The flow time was chosen to get the best signal of self-dual objects, as the instanton candidate density will decrease with increasing flow time but UV-fluctuations will obstruct local self-dualities for small flow times. For each configuration the average relative cluster volume $\langle v \rangle$ was computed from the number of points within each self-dual cluster normalized to the total volume and the number of centres.

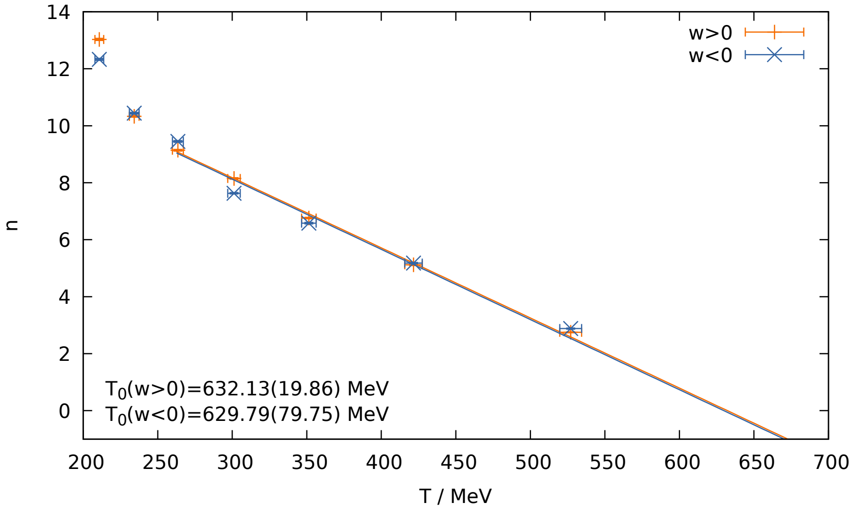

Figure 3.13.: The number of (anti-)self-dual points over the temperature from the A370 meta ensemble, $\tau = 0.48a^2$.

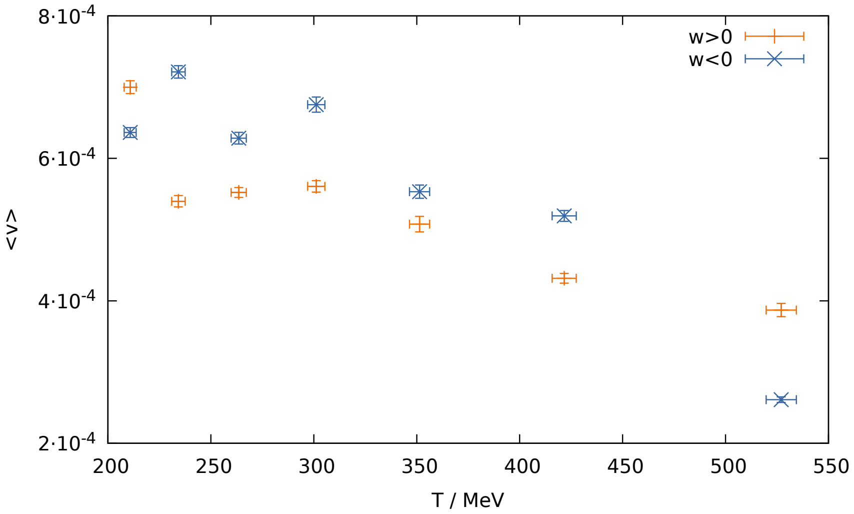

Figure 3.14.: The average volume of (anti-)self-dual clusters over the temperature from the A370 meta ensemble, $\tau = 0.48a^2$, with a cluster decay constant $\kappa = 5$.

The number of self-dual centres and the cluster volume were then averaged over all configurations. The temperature dependence of n and $\langle v \rangle$ are shown in Figures 3.13 and 3.14. We find that the number of candidates for instanton objects drops when the temperature is increased. At large temperatures $T \gtrsim 260$ MeV the number of self-dual centres drops is consistent with a linear extrapolation, which predicts that at $T \approx 630$ MeV n has dropped to zero. Furthermore, the average cluster volume becomes smaller. If the self-dual centres are instanton candidates the instanton gas becomes very thin at large temperatures. We also observe, that there is no asymmetry between self-dual and anti-self-dual objects; both come in similar abundances.

3.5. Summary

This chapter is dedicated to the topological structure of QCD on the lattice in the tmfT setup. Counting zero modes allows to determine the fermionic topological charge and we find that possible mixing issues caused by a finite numerical resolution are resolved by unmixing the modes with gradient flow. Furthermore we find that the gluonic and fermionic topological charge differ from each other, but after smoothing the gauge configurations they become similar; the same is true for the topological susceptibility. At large temperatures, however, gradient flow does not suffice.

The overlap of quark wave functions with the gluonic and fermionic topological charge indicates that localized quark modes carry topological charge while extended modes do not.

We have devised an algorithm to extract self-dual clusters and using this algorithm we could deduce that self-dual and anti-self-dual objects occur in the same abundance and become less abundant with increasing temperature.

4. Localization in two-colour QCD

The study of two-colour QCD (QC$_2$D) has a long history: especially the low temperature region of the QC$_2$D phase diagram has been subject to throrough investigation [57, 58, 87, 146–149]. The colour-singlet grand canonical potential in two-color matter and the static quark-anti-quark potential was recently studied in [150]. A lattice study of the phase diagram of two-colour QCD with quarks in the adjoint representation was presented in [85, 151]. The deconfinement transition at zero temperature and large quark chemical potential was studied on the lattice in [152, 153].

As the gauge group SU(2) is pseudoreal there is no sign problem at finite chemical potential. Two-colour lattice gauge theories have hence been a testing ground for the behaviour of strongly interacting theories at $\mu > 0$. Since the whole phase diagram is accessible with Monte-Carlo methods, ab-initio predictions in two-colour QCD can be compared to predictions from effective models (e.g. the quark-meson-diquark model [22]) using the functional methods like the functional renormalization group, Dyson-Schwinger calculations or effective descriptions in the framework of chiral perturbation theory.

Two-colour QCD both in the fundamental and in the adjoint representation of the gauge group provides an extended flavour symmetry because quarks and antiquarks are in equivalent representations of SU(2) [56]. A comprehensive review on the extended flavour symmetry is given in [154]. The symmetry breaking pattern for fundamental and adjoint two-colour QCD is sketched in Figure 4.1.

$$\begin{tikzcd}
 & SU(2N_f) \arrow[dl, "m_q > 0"'] \arrow[dr, "\mu > 0"] & \\
Sp(N_f) \arrow[dr, "\mu > 0"'] & & SU(N_f)_L \times SU(N_f)_R \times U(1)_B \arrow[dl, "m_q > 0"] \\
 & SU(N_f)_V \times U(1)_B \arrow[d, "\langle qq \rangle > 0"] & \\
 & Sp(N_f/2)_V &
\end{tikzcd}$$

$$\begin{tikzcd}
 & SU(2N_f) \arrow[dl, "m_q > 0"'] \arrow[dr, "\mu > 0"] & \\
SO(2N_f) \arrow[dr, "\mu > 0"'] & & SU(N_f)_L \times SU(N_f)_R \times U(1)_B \arrow[dl, "m_q > 0"] \\
 & SU(N_f)_V \times U(1) \arrow[d, "\langle qq \rangle > 0"] & \\
 & SO(N_f)_V &
\end{tikzcd}$$

Figure 4.1.: The extended flavour symmetry breaking pattern of two-colour QCD in the fundamental (*Left*) and the adjoint (*Right*) representation.

The baryonic degrees of freedom in two-colour QCD are bosonic. The lightest baryons are a pair of diquarks, which at $\mu = 0$ are degenerate with the pions. A sketch of the conjectured phase diagram is shown in Figure 4.2.

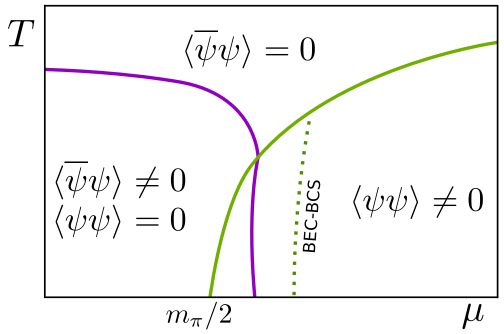

Figure 4.2.: A sketch of the two-colour QCD phase diagram. The violet line indicates the chiral transition and the green line the diquark condensation. The dotted line represents the BEC-BCS crossover.

In [22, 23] the phase diagram of two-colour QCD was mapped using the quark-meson model and the Polyakov-quark-meson model in a functional renormalization group approach. In the hadronic phase chiral symmetry is spontaneously broken and no diquarks have condensed. When increasing μ at low T the condensates remain constant up to $m_\pi/2$. This is called the Silver Blaze property [155, 156]. The naive expectation would imply that any non-zero μ alters the eigenvalues of the fermion matrix and thus the determinant, but in relativistic theories with a mass gap the thermodynamic partition function and all observables obtainable from it remain independent of the chemical potential as long as it is smaller than the mass gap. Below this value no zero temperature states can be excited. In two-colour QCD the mass gap is $m_\pi/2$, which coincides with half of the mass of the lightest baryon. This property is a generic feature of relativistic theories with a chemical potential and can be observed in purely bosonic theories as well.

Outside the Silver Blaze region and at small temperatures a second order diquark condensation takes place and a Bose-Einstein condensate (BEC) is formed. Shortly after this diquark onset, chiral restoration sets in. The restoration line is “bent” (“back-bending”). At even larger chemical potential quark-quark pairs form near the Fermi surface and a colour superconducting Bardeen-Cooper-Schrieffer (BCS) phase is observed. This was studied on the lattice in [157].

4.1. Anti-unitary symmetry of fundamental and adjoint QC$_2$D

In contrast to QCD a SU(2) Yang-Mills theory in the fundamental representation, in the following called two-colour QCD or QC$_2$D, provides an anti-unitary symmetry like

$$[C\gamma_5\tau_2 K, \mathcal{M}] = 0, \tag{4.1}$$

with the fermion matrix

$$\mathcal{M} = \gamma_\mu D_\mu + m + \mu\gamma_4, \tag{4.2}$$

the charge conjugation operator C, the complex conjugation K and the Pauli matrix τ_2. From this follows, that the fermion matrix is real.

The anti-unitary symmetry transformation obeys

$$(C\gamma_5\tau_2 K)^2 = 1 \tag{4.3}$$

such that the Dyson index of the continuum theory is $\beta_D = 1$ and its spectrum corresponds to the chiral Gaussian orthogonal ensemble (chGOE) random matrix theory.

Using that the generators of the gauge group SU(2) in the fundamental representation obey

$$\tau_2 T^j \tau_2^{-1} = -(T^j)^*, \tag{4.4}$$

where τ_k are the Pauli matrices, one can show that the fermion matrix is real if the chemical potential μ is real

$$\begin{aligned} \mathcal{M} &= C\gamma_5\tau_2 K\mathcal{M}\left(C\gamma_5\tau_2 K\right)^{-1} \\ &= C\gamma_5\tau_2\left(\gamma_\mu\partial_\mu + i\gamma_\mu A_\mu + m + \mu\gamma_4\right)\tau_2\gamma_5 C \\ &= \left(\gamma_\mu\partial_\mu + i\gamma_\mu A_\mu + m + \mu^*\gamma_4\right)^* = \mathcal{M}^*. \end{aligned} \tag{4.5}$$

Two-colour QCD thus has no sign problem and can be used to study the properties of non-perturbative gauge theories at finite chemical potential with Markov chain Monte Carlo methods.

In the adjoint representation the SU(2) gauge group is $N_c^2 - 1 = 3$ dimensional and the generators are given by the structure constants $(T^i)_{jk} = f_{ijk}$. The fermion matrix of adjoint two-colour QCD obeys

$$[C\gamma_5 K, \mathcal{M}] = 0, \tag{4.6}$$

and $(C\gamma_5 K)^2 = -1$ such that the Dyson index is $\beta_D = 4$. This indicates that the matrix elements of the Dirac operator in adjoint QC$_2$D are quaternion real and there is no sign problem present. Adjoint QC$_2$D corresponds to the chiral Gaussian symplectic ensemble.

4.2. The action of QC$_2$D with diquark sources

On a finite lattice a truly spontaneous symmetry breaking can not be observed as all phases are connected with finite probabilities. In order to observe a diquark condensation transition one therefore has to include an explicit symmetry breaking term, that breaks the baryon number conservation. The diquark source coupling is then to be extrapolated to zero.

The fermion action with an additional diquark source then reads [149]

$$S_f = \bar\psi D(\mu)\psi + \frac{\lambda_{qq}}{2}\left(\psi^T(C\gamma_5\tau_2)\psi + \bar\psi(C\gamma_5\tau_2)\bar\psi^T\right). \tag{4.7}$$

For staggered quarks the diquark term takes the form [3, 157]

$$\psi^T\tau_2\psi + \bar\psi\tau_2\bar\psi^T. \tag{4.8}$$

The fermion fields can be written in a Nambu-Gorkov basis

$$\Psi = \begin{pmatrix} \bar\psi^T \\ \psi \end{pmatrix} \text{ and } \Psi^T = \left(\bar\psi, \psi^T\right), \tag{4.9}$$

such that the action takes the form

$$S_f = \frac{1}{2}\left(\bar\psi, \psi^T\right)\begin{pmatrix} \lambda_{qq}(C\gamma_5\tau_2) & D(\mu) \\ -D^T(\mu) & \lambda_{qq}(C\gamma_5\tau_2) \end{pmatrix}\begin{pmatrix} \bar\psi^T \\ \psi \end{pmatrix} =: \frac{1}{2}\Psi^T A\Psi. \tag{4.10}$$

The fermion determinant is then given by

$$\det A = \det\left(D^\dagger(\mu)D(\mu) + \lambda_{qq}^2\right). \tag{4.11}$$

Using the pseudoreality of the gauge group $(C\gamma_5\tau_2)M(C\gamma_5\tau_2)^{-1} = M^*$ and $\det\begin{pmatrix} X & Y \\ W & Z \end{pmatrix} = \det(X)\det(Z - WX^{-1}Y)$ the fermionic part of the partition function is then given by the Pfaffian of the anti-symmetric matrix A [148]

$$Z_f = \int \mathcal{D}\bar\psi\mathcal{D}\psi e^{-S_f} = \int \mathcal{D}\Psi e^{-\frac{1}{2}\Psi^T A\Psi} = \mathrm{Pf}(A) = \sqrt{\det A}. \tag{4.12}$$

The diquark condensate can then be expressed like

$$\langle qq \rangle = \langle q^T \left(C\gamma_5 \tau_2 \right) q \rangle = \lim_{\lambda_{qq} \mapsto 0} \frac{\partial \ln Z}{\partial \lambda_{qq}} = \lim_{\lambda_{qq} \mapsto 0} \frac{\partial \ln \sqrt{\det A}}{\partial \lambda_{qq}} = \lim_{\lambda_{qq} \mapsto 0} \frac{1}{2} \operatorname{tr} \left(A^{-1} \frac{\partial A}{\partial \lambda_{qq}} \right). \tag{4.13}$$

A Banks-Casher like relation for the scalar diquark condensate was defined in [158, 159].

To avoid explicitly including Nambu-Gorkov spinors in our calculations we define

$$\tilde{A} := \begin{pmatrix} 1 & \\ & C\gamma_5\tau_2 \end{pmatrix} A \begin{pmatrix} C\gamma_5\tau_2 & \\ & 1 \end{pmatrix} = \begin{pmatrix} \lambda_{qq} & D(\mu) \\ -D^\dagger(\mu) & \lambda_{qq} \end{pmatrix} \tag{4.14}$$

and used the action $\tilde{S}_f = \frac{1}{2}\Psi^T \tilde{A} \Psi$ since the determinant remains $\det A = \det \tilde{A}$.

To ensure positive definiteness of the fermion matrix we double the number of flavours like

$$\mathcal{M} = \tilde{A}^\dagger \tilde{A} = \begin{pmatrix} \lambda_{qq}^2 + D(\mu) D^\dagger(\mu) & 0 \\ 0 & D^\dagger(\mu) D(\mu) + \lambda_{qq}^2 \end{pmatrix}, \tag{4.15}$$

which is diagonal in the Nambu-Gorkov basis. We thus drop one component and end up with two flavours again.

4.3. Bulk artifacts and the continuum limit

Most lattice gauge theories contain an artificial *bulk crossover transition*, that separates unphysical strong-coupling regime from a physical weak-coupling regime. This bulk transition was studied in a SU(3) lattice gauge theory with $N_f = 12$ staggered fermion flavours in the fundamental representation in [160], and it was found that an improvement of the fermion and gauge action made physics accessible that was otherwise obstructed by discretization artifacts.

In two-colour QCD the bulk transition poses a problem, since e.g. the deconfinement transition can already be observed with relatively coarse lattice spacings. This means that the inverse coupling typically is small enough to run into the unphysical bulk phase.

In this strong coupling regime no continuum limit is possible due to vortices and monopoles that distort the UV-behaviour of the gauge field. In the weak coupling regime, however, the short range interaction is dominated by asymptotic freedom such that the continuum limit can be approached with $\beta \to \infty$.

To quantify magnitude of discretization artifacts from the bulk phase we define the $Z(N_c)$ monopole density which reads

$$\langle z \rangle = 1 - \frac{1}{N_\square} \sum_{C \in \square} \prod_{P \in \partial C} \operatorname{sgn} \operatorname{tr} P \tag{4.16}$$

and measures the signs of plaquettes on the faces of elementary cubes, which are symbolized with $\square$. In the strong coupling regime those plaquette signs are aligned and the monopole density is large.

The bulk crossover transition is almost independent of the lattice volume: it only depends on the action discretization and the lattice spacing, or the inverse coupling respectively.

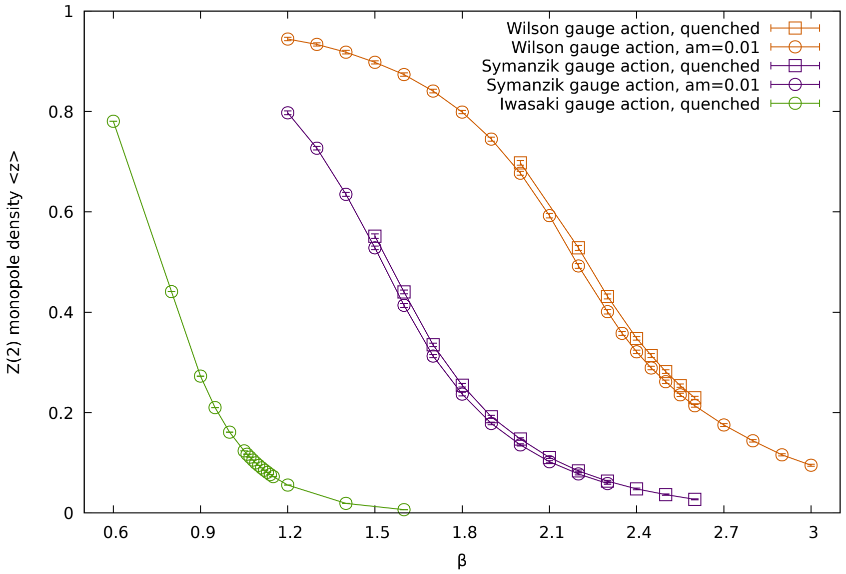

Figure 4.3.: The Z(2) monopole density for the Wilson and the Symanzik rectangle improved gauge action over β, computed on a $12^3 \times 8$ lattice, both quenched and with Wilson quarks, and the Iwasaki RG improved gauge action, computed on a 36×8 lattice in the quenched limit.

In Figure 4.3 we plotted the Z(2) monopole density over β for the Wilson, Symanzik and Iwasaki gauge actions, both quenched and with dynamical Wilson fermions. The monopole density drops as the inverse coupling approaches infinity but it depends very much on the choice of lattice action. The Symanzik rectangle action is a big improvement on the Wilson plaquette action already, but the optimal Iwasaki cubic action allows very small monopole densities at relatively small inverse couplings. It is thus necessary to find a setup, where the lattice spacing is sufficiently small and the physical volume is still large enough.

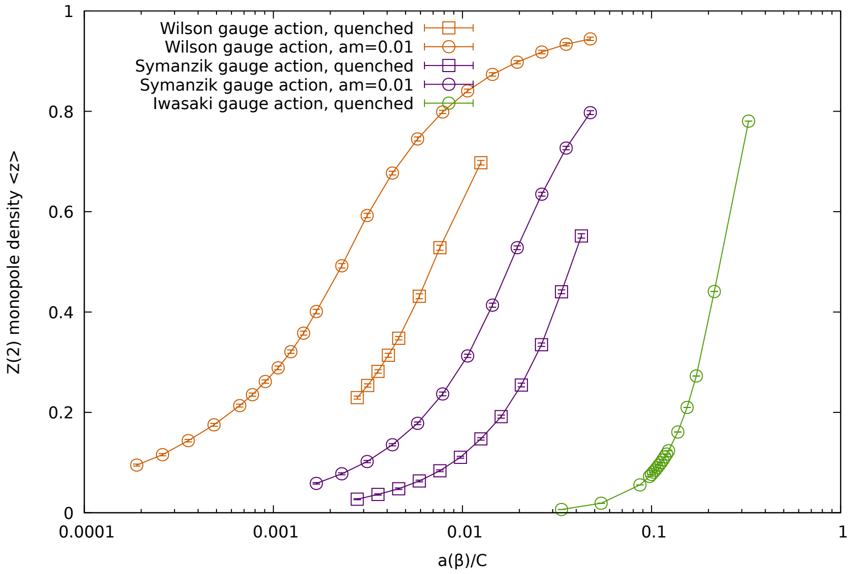

Figure 4.4.: The Z(2) monopole density for the Wilson, Symanzik and Iwasaki gauge action over a in arbitrary units. The presence of fermions in the theory increases the monopole already slightly.

In Figure 4.4 the monopole density is plotted over the lattice spacing in arbitrary units, where we have used equation (1.36). In this plot it becomes apparent that the presence of fermions in the theory increases the monopole density slightly.

In Section 4.4 we compare the Wilson plaquette action with the Symanzik rectangle action with a background of dynamical staggered quarks. Unfortunately using the RG-improved optimal Iwasaki action has proven to be rather expensive and was in this work only applied to quenched two-colour QCD, which is presented in Section 4.5.

4.4. Zero temperature $\mathrm{QC_2D}$ with staggered quarks

In the following section we will study two-colour QCD with $N_f = 2$ rooted staggered quarks in the fundamental representation at finite chemical potential, as described in Section 1.2.6. The staggered fermion discretization was chosen for this survey instead of the overlap discretization, since the Ginsparg-Wilson relation is not well-defined for $\mu > 0$.

In the staggered approach the γ-matrices have been replaced with staggered phases such that charge conjugation and γ_5 are now local operators. In the staggered framework γ_5 takes the form

$$\eta_5(x) = (-1)^{x_1+x_2+x_3+x_4}. \tag{4.17}$$

The anti-unitary symmetry is hence reduced to $[\tau_2 K, \mathcal{M}] = 0$ [161]. In contrast to two-colour QCD with fundamental quarks in the continuum, we find $(\tau_2 K)^2 = -1$, which is similar to adjoint $\mathrm{QC_2D}$, and the Dyson index is then $\beta_D = 4$. $\mathrm{QC_2D}$ with staggered quarks corresponds to a symplectic random matrix ensemble. We first have to investigate whether the anti-unitary symmetry of the theory is restored in the continuum limit.

Staggered quarks have in the past found wide application because they are computationally much cheaper than Wilson-like quarks. For example Kogut, Toublan and Sinclair studied the pseudo Goldstone spectrum at high densities with staggered quarks in 2003 [162] and compared it to predictions from a linear sigma effective Lagrangian in chiral perturbation theory. The lattice parameters therein are $N_s = 12$, $N_t = 24$, $\beta = 1.5$, $am_q = 0.025$ with $N_f = 4$ staggered fermions.

4.4.1. Lattice setup

We also study the aforementioned lattice parameters from [162] with a diquark source $a\lambda_{qq} = 0.0025$ using a fermion action as described in Section 4.2 with staggered quarks, but $N_f = 2$ tastes instead of $N_f = 4$. For this unimproved setup we employ the standard Wilson plaquette gauge action. We compare this lattice setup against an improved set of parameters, where $N_s = 16$, $N_t = 32$, $\beta = 1.7$, $am_q = 0.01$ and $\lambda_{qq} = 5 \cdot 10^{-3}$ using the Symanzik rectangle improved action and $N_f = 2$ staggered quarks.

With the improved setup the simulations take place on the weak coupling side of the bulk transition, since the monopole density $\langle z \rangle = 0.27340(66)$ is sufficiently low and bulk artifacts are not dominating. This particular parameter choice is motivated by the work of D. Scheffler: in [44, 163] these lattice parameters were used to study two-colour QCD at finite temperature outside the bulk phase and meson spectroscopy in this setup gave

$$\frac{m_\pi}{m_\rho} = 0.5816(27). \tag{4.18}$$

As we discussed in Section 4.3, these parameters are a good trade-off between a low monopole density and a sufficient physical volume.

4.4.2. The Wigner-Dyson class of staggered $\mathrm{QC_2D}$

The anti-unitary symmetry of the Dirac operator is reflected in the unfolded level spacing distribution, such that we can compare the ULSDs for the parameters sets we have discussed above. For $\beta_D = 4$, which corresponds to any-colour adjoint QCD or staggered two-colour QCD, the ULSD follows the Wigner-Dyson surmise of the Gaussian symplectic ensemble while for $\beta_D = 1$, which corresponds to continuum two-colour QCD in the fundamental representation, it follows the Gaussian orthogonal ensemble. We can thus check if the anti-unitary symmetry restores on the weak-coupling side of the bulk crossover transition.

In Figure 4.5 the ULSD of the staggered eigenmodes in the unimproved lattice setup is shown. Here the monopole density is large ($\langle z \rangle = 0.884040(95)$) and bulk effects are dominant. The ULSD does not contain an orthogonal part and is entirely described by the symplectic ensemble; the continuum symmetry can not be identified here.

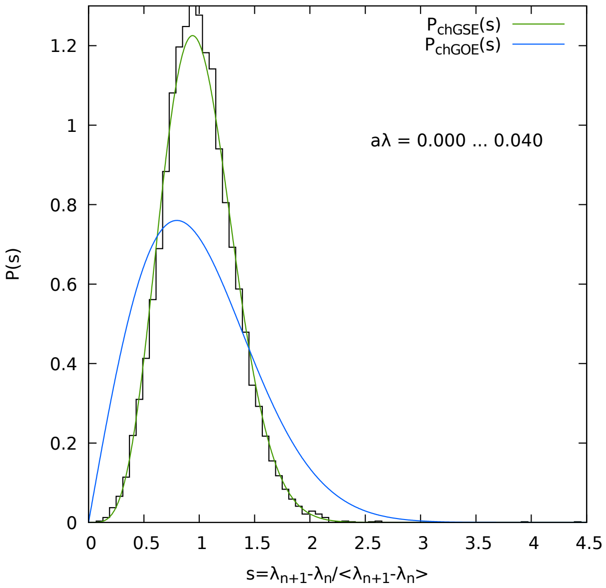

Figure 4.5.: The ULSD of the staggered quark modes in the bulk phase, where $N_s = 12$, $N_t = 24$, $\beta = 1.5$ with the Wilson gauge action, resembles the chiral symplectic ensemble ($\beta_D = 4$), which also corresponds to any-colour adjoint QCD.

With the improved lattice setup, on the other hand, the spectrum acquires modes in the low end which follow an orthogonal random matrix ensemble distribution, see Figure 4.6. The higher modes are still well represented by the Gaussian symplectic ensemble and seem to be not yet affected by the improvement.

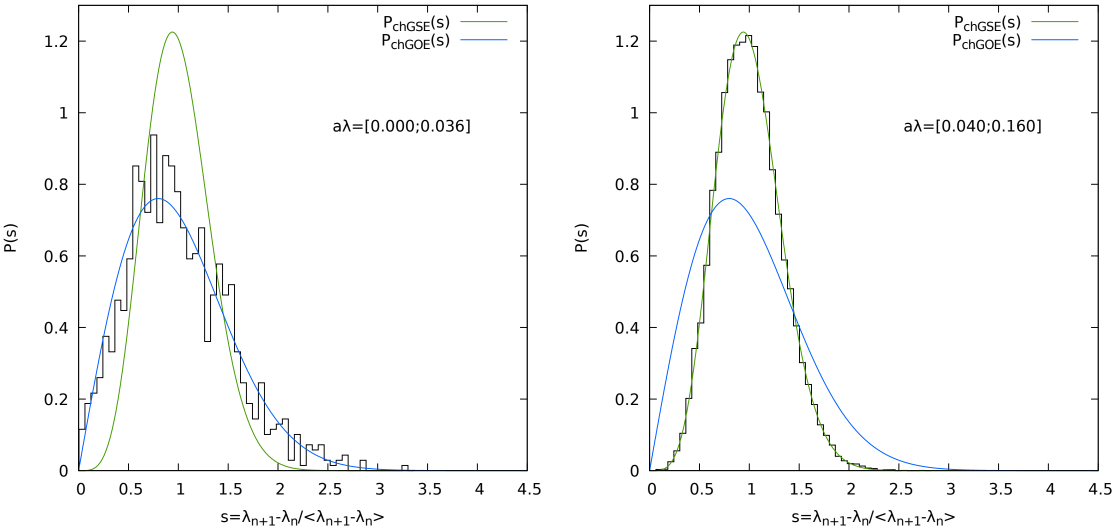

Figure 4.6.: The ULSD of the staggered quark modes with $N_s = 16$, $N_t = 32$, $\beta = 1.7$ and the Symanzik gauge action for $a\lambda \in [0; 0.036]$ (*Left*) and $a\lambda \in [0.04; 0.16]$ (*Right*). The lower part of the spectrum agrees well with the RMT prediction for the orthogonal ensemble, while the higher modes are still distributed according to the symplectic ensemble.

We find that the slightly finer lattice spacing and the improved gauge action have a great impact on the lower modes (which dominate the quark propagator): the lower end of the spectrum restores to the continuum symmetry of the Dirac operator and we expect that in the limit $a \to 0$ the anti-unitary symmetry becomes orthogonal for the whole spectrum.

4.4.3. The diquark condensation transition

In [86] Kogut *et al.* study the diquark transition in QCD-like theories with a non-linear sigma model in chiral perturbation theory (χPT). They predict a conserved combined condensate in leading order

$$\Sigma_\alpha = \sqrt{\langle \bar{q}q \rangle^2 + \langle qq \rangle^2} \equiv 2N_f G, \tag{4.19}$$

which is rotated by the vacuum alignment at the diquark condensation transition. This implies that the diquark condensate and the quark condensate are connected by a mixing angle like

$$\begin{aligned} \langle \bar{q}q \rangle &= 2N_f G \cos\alpha, \\ \langle qq \rangle &= 2N_f G \sin\alpha. \end{aligned} \tag{4.20}$$

The leading-order χPT Lagrangian with finite diquark source term can be minimized with

$$4\mu^2 \sin\alpha \cos\alpha = m_\pi^2 \sin(\alpha - \alpha_0) \tag{4.21}$$

where the diquark source and the mass term already generate a finite vacuum alignment angle $\tan\alpha_0 = \frac{\lambda_{qq}}{m_q}$ at vanishing chemical potential. This equation has analytic solutions, which are used to fit the χPT predictions to the condensates from our lattice calculations. From the vacuum energy one can identify the quark number density

$$n = 8N_f F^2 \mu \sin^2\alpha, \tag{4.22}$$

which can then be fitted as well.

In the unimproved lattice setup within the bulk phase we computed the quark number density and the condensates over $a\mu$ and fitted the leading order χPT predictions, which is shown in Figure 4.7.

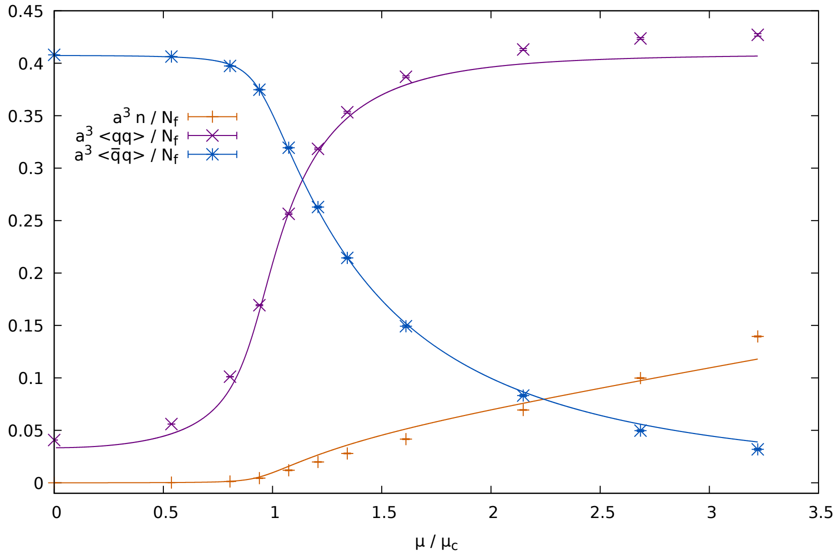

Figure 4.7.: The quark and diquark condensate and the quark number density over the relative chemical potential in the unimproved lattice setup, with the fit to the χPT predictions.

The fits were done with respect to the parameters α_0, G, F, $a\mu_c$ and we find $a\mu_c = 0.1862(12) = am_\pi/2$. The Silver Blaze property should be reflected below the diquark onset, but the condensates show a μ-dependence at $\mu \approx 0.8\mu_c$ already. However, the χPT predictions agree well with the measurements at small μ, but at larger μ there are deviations present. In next-to-leading order the combined condensate Σ_α becomes μ-dependent and its magnitude is a dynamical field. This was accounted for in [162], where a linear sigma model effective Lagrangian was used to fit the condensates and the quark number, which implied $\langle qq \rangle \propto \mu$ and $n \propto \mu^3$.

The vacuum alignment angle was available as a side product from the fit to the χPT predictions, see Figure 4.8.

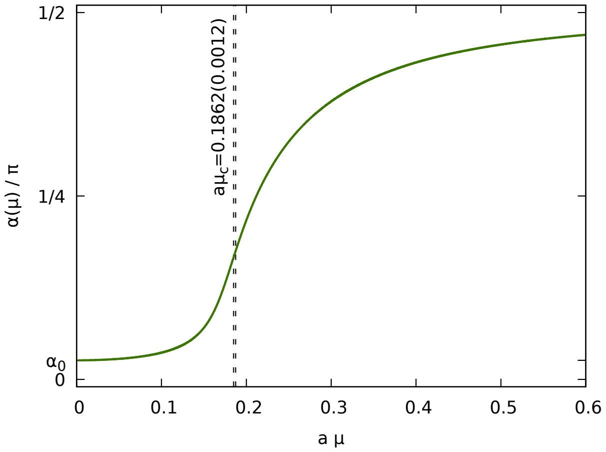

Figure 4.8.: The vacuum alignment angle over the chemical potential from a fit of the leading order χPT prediction to lattice data. At $\mu = 0$ it has already a non-vanishing value due to the finite quark mass and diquark source.

We thus find that the lattice results for the unimproved setup are in strong agreement with the chiral perturbation theory predictions.

In the improved lattice setup at $\beta = 1.7$ the monopole density is much smaller and we expect discretization artifacts to be much less prominent. In [3] we presented an extrapolation of the diquark condensate to $\lambda_{qq} \mapsto 0$, from which we extracted the position of the diquark condensation onset by a fit to the prediction to χPT like

$$\langle qq \rangle \propto \sqrt{1 - \left(\frac{\mu_c}{\mu}\right)^4}. \tag{4.23}$$

This fit is shown in Figure 4.9.

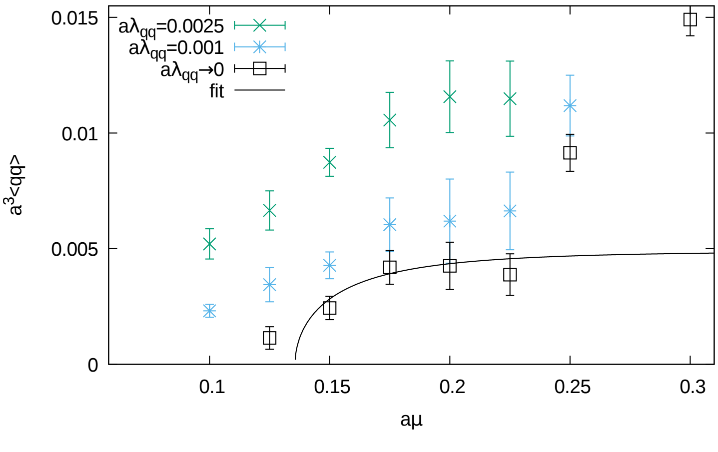

Figure 4.9.: The diquark condensate $\langle qq \rangle$ in the improved lattice setup extrapolated to vanishing source λ allows to fit to the prediction from χPT and extract $a\mu_c$ ($16^3 \times 32$ lattice at $\beta = 1.7$).

The diquark onset was fitted to $a\mu_c = 0.1356(86)$, which is consistent with the pion mass, that was extracted from the zero-momentum projected pion correlator $am_\pi/2 = 0.1428(26)$. The sudden increase of the diquark condensate at around $a\mu \approx 0.25$ was also observed in [157] and interpreted as evidence of the BEC-BCS crossover.

As we can see in Figure 4.10 the dependence of $\langle qq \rangle$ on the diquark source is relatively small. The diquark condensate rises until $\mu \approx 6.99\mu_c$ and then drops, which is caused by the effective "quenching" of the lattice at large chemical potential. In this region, the quark number density reaches its saturation value of maximum fermion occupancy on the finite lattice. From a fit the point of half filling was also determined to be $\mu_h \approx 6.35\mu_c$.

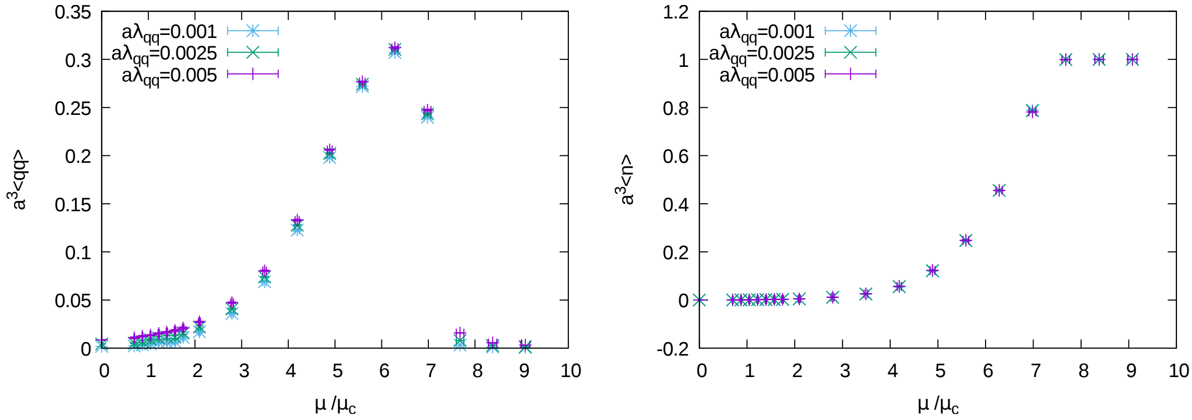

Figure 4.10.: *Left*: The diquark condensate depends only weakly on the diquark source. *Right*: The quark number density reaches its saturation due to the finite lattice volume at $\mu \approx 6.99\mu_c$ ($16^3 \times 32$ lattice at $\beta = 1.7$). From a fit the point of half filling was determined to be $\mu_h \approx 6.35\mu_c$.

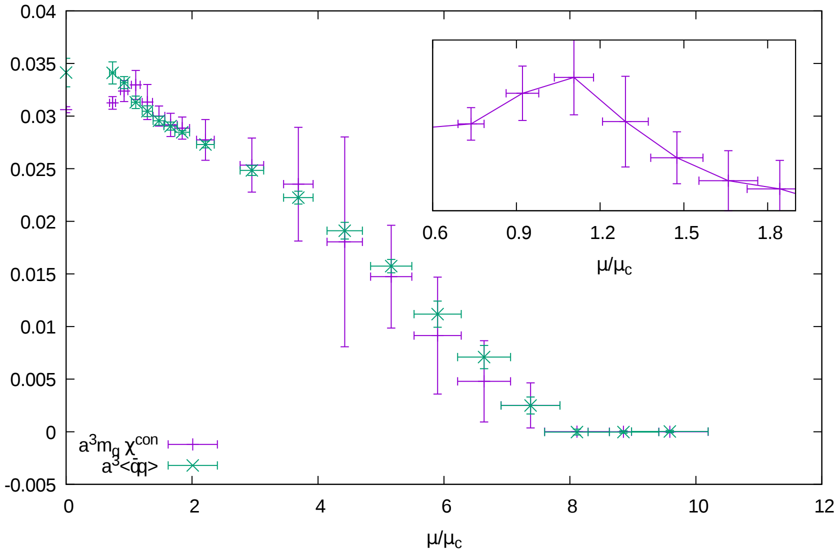

Figure 4.11.: The chiral condensate $\langle \bar{q}q \rangle$ and the connected chiral susceptibility χ^{con} in the improved lattice setup both contain a UV-divergence at large chemical potentials, while χ^{con} also contains a singular part close to the diquark onset.

The chiral condensate and the connected chiral susceptibility in the improved lattice setup at finite chemical potential are shown in Figure 4.11. On the finer lattice the chiral condensate contains a UV-divergent contribution, which is reflected in the decrease of the condensate above μ_c. The condensate requires additive renormalization. Unger [43] presented a possibility to renormalize the chiral condensate at finite temperature using the chiral susceptibility like

$$\begin{aligned}\langle\bar{q}q\rangle_{m_q} &= \langle\bar{q}q\rangle_0 + c_2 m_q + \frac{c_{\mathrm{UV}}}{a^2} m_q + \mathcal{O}(m_q^2)\\ \text{and } \chi_{m_q} &= c_2 + \frac{c_{\mathrm{UV}}}{a^2} + \mathcal{O}(m_q^2),\end{aligned} \tag{4.24}$$

such that the renormalized condensate reads

$$\Sigma = \langle\bar{q}q\rangle_{m_q} - m_q \chi^{\mathrm{con}}. \tag{4.25}$$

The UV-divergence at finite temperature mainly belongs to the connected part of the chiral susceptibility.

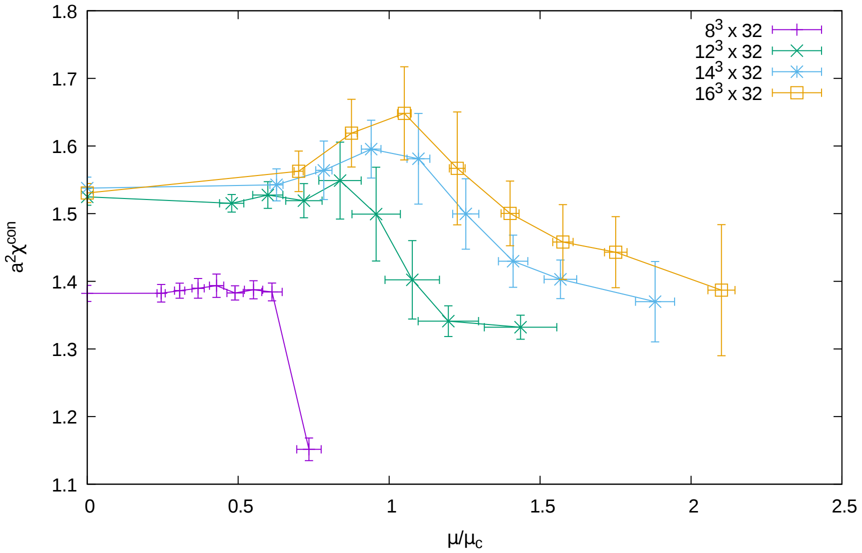

Figure 4.12.: The connected chiral susceptibility in the improved lattice setup contains a singular part close to the diquark transition which scales with the volume.

At finite chemical potential on the other hand the connected susceptibility also contains a singular contribution at the diquark transition, that is not apparent in the condensate. The height of this singular part scales with the volume as shown in Figure 4.12, and we expect it to become a true divergence in the infinite volume limit. Although the UV-divergent parts of both the condensate and the susceptibility appear to be equal, this singularity in proximity to the the diquark onset renders the renormalization scheme as in equation 4.24 inapplicable to finite μ.

A possible solution to this problem could be the renormalization of the observables with gradient flow. However, the spatial volume in this lattice setup is possibly too small compared to the temporal extent, such that the gauge fields can not sufficiently be smoothed without introducing systematic smoothing errors.

4.4.4. Quark modes at finite chemical potential

In the following we study the eigenmodes of the standard staggered Dirac operator on the gauge configurations generated with the improved lattice parameters. The staggered eigenvalues are purely imaginary and come in complex pairs; there is no projection procedure required. The configurations which were used are listed in Table 4.1. The quark modes were computed for $a\mu = 0$, $a\mu = 0.25$ and $a\mu = 0.5$. At $a\mu = 0.25$ the BEC-BCS crossover transition is suspected, since the diquark condensate shows a sudden increase in this region. The larger chemical potential is still well below the point of half filling (see Figure 4.10).

Table 4.1.: The configurations on which the staggered quark modes were computed.

	$a\mu$	μ/μ_c	# conf.	$\frac{\text{modes}}{\text{conf}}$
RS.16.32 $N_s = 16$, $N_t = 32$ $\beta = 1.7$ (Symanzik) $am_q = 0.01$ $a\lambda_{qq} = 5 \cdot 10^{-3}$	0.00 0.25 0.50	0 1.844(117) 3.687(234)	219 67 40	512 512 512

The spectral density for these chemical potentials is plotted in Figure 4.13. We find that at larger μ the eigenmodes bulk closer to zero. This indicates the formation of a condensate which breaks the flavour symmetry to $Sp(N_f/2)_V$, very similar to the Banks-Casher mechanism for the chiral condensate.

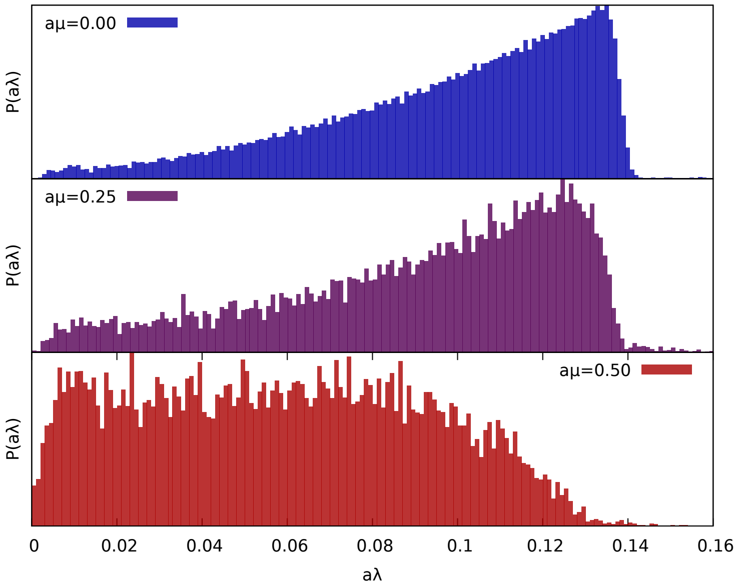

Figure 4.13.: The spectral density of the staggered Dirac operator for several chemical potentials.

Using the inverse participation ratio the relative eigenmode volume was computed and is shown in Figure 4.14.

At $\mu = 0$ and low temperature the Dirac operator is well described with an orthogonal random matrix (see Section 4.4.2) and all eigenmodes are delocalized. However, the lower modes occupy a smaller volume than the higher modes, which we assume reflects the transition from the orthogonal to the symplectic anti-unitary symmetry, which we have observed in Figure 4.6. No modes occupy the whole volume, which is a prominent difference to QCD at temperatures close to the chiral transition (compare with Section 2.3). At $a\mu = 0.25$ all modes occupy roughly the same volume, any residues of quark mode localization have vanished. Still the eigenmode volume is bound from above and at $a\mu = 0.5$ the eigenmode volume is consistent with a constant. The eigenmodes are still not filling the entire volume, which is possibly caused by the large temporal extent of the lattice. This allows the quark modes to propagate dynamically, even at large chemical potential.

We do observe, however, some μ-dependence in the eigenmode volumes: The chemical potential is counteracting localization effects and causes the quark modes to extend.

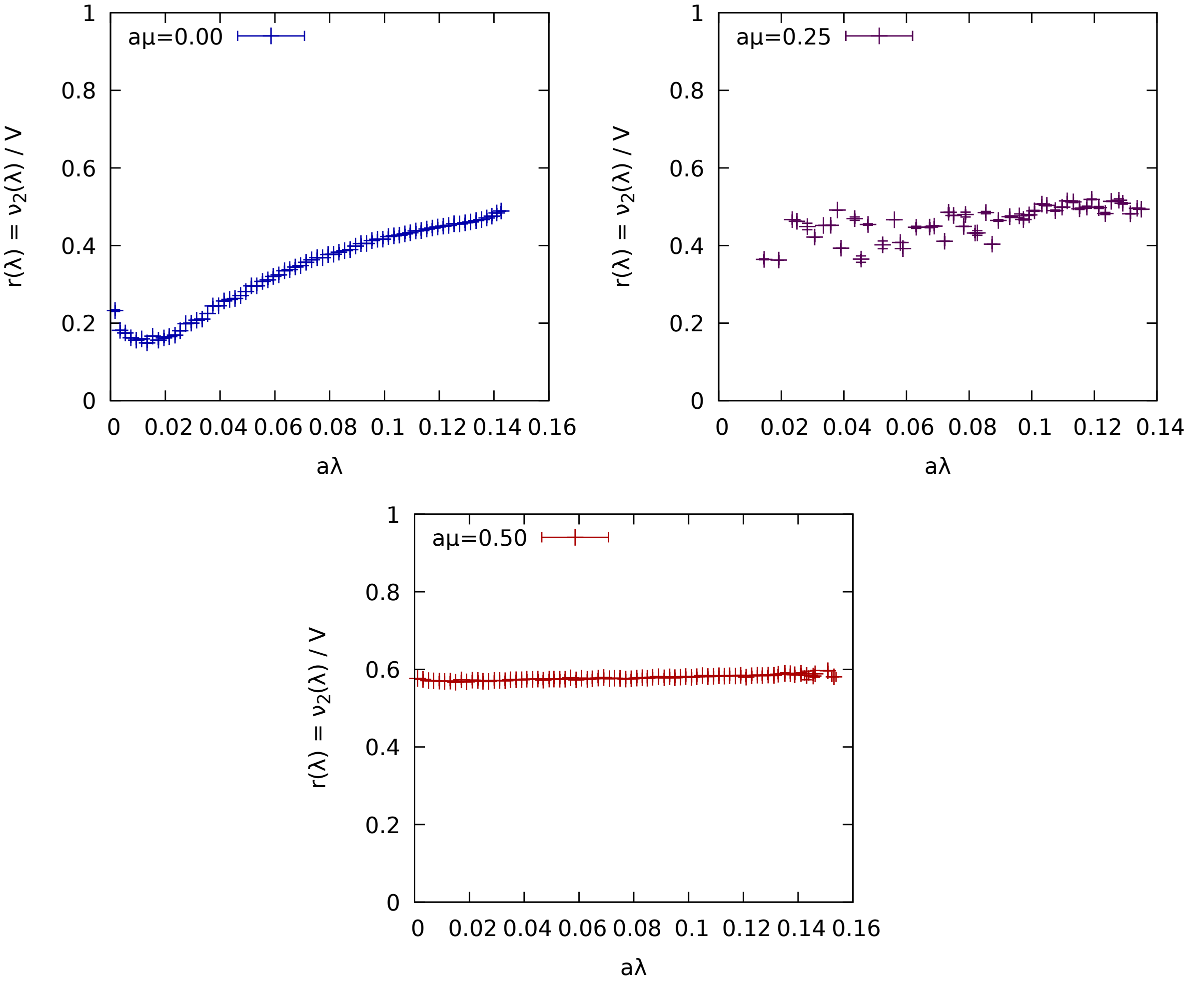

Figure 4.14.: The relative eigenmode volume over the eigenvalue for several chemical potentials.

Furthermore, the unfolded level spacing distribution at finite chemical potential (figure 4.15) indicates, that μ suppresses the level repulsion and the modes are "compressed". This could be caused by the presence of a Poisson-like sector in the spectrum.

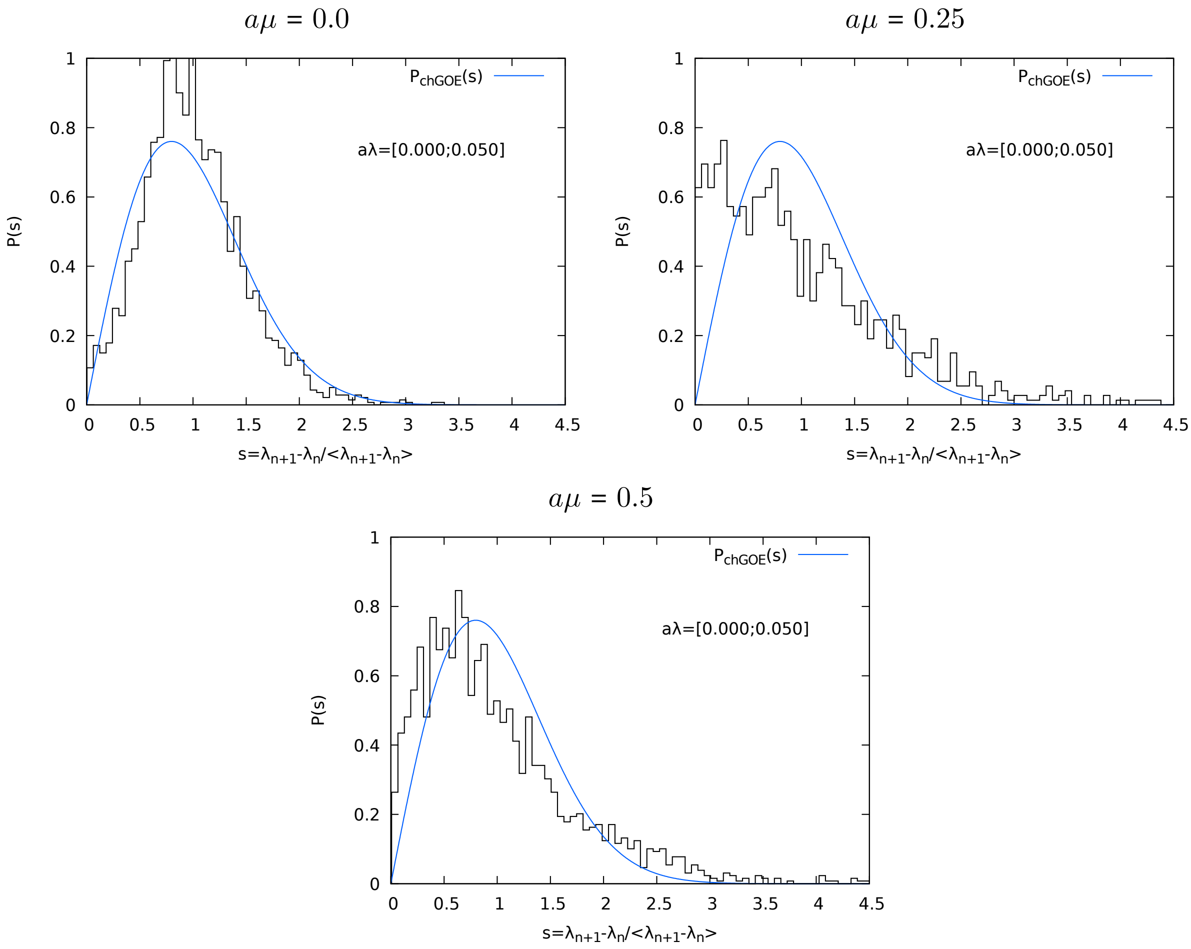

Figure 4.15.: The unfolded level spacing distribution in the low end of the spectrum, *Top left*: $a\mu = 0.0$, *top right*: $a\mu = 0.25$, *bottom*: $a\mu = 0.5$. At larger μ the level repulsion is suppressed, the levels are “compressed”.

4.5. Quenched $\mathrm{QC_2D}$ at finite temperature

This section is dedicated to the spectral properties of the overlap Dirac operator on a background of a quenched two-colour lattice gauge theory at finite temperature. We will study localization properties of quark wave functions and map the temperature dependence of the mobility edge. For this we chose a fixed scale approach, where the lattice spacing is fixed and the temperature is varied by adjusting N_t.

4.5.1. Fixed scale without physical parameters

Since two-colour QCD is not implemented in the real world, there is no experimentally available observable from which we could extract a physical scale. Nevertheless, we fix the scale to the pseudocritical inverse coupling β_c for the second order deconfinement transition by computing β_c in several volumes for some N_t and extrapolate to $N_s^3 \to \infty$. The lattice spacing can not be assigned a physical unit but a relative error was estimated.

For scale setting we choose $N_t = 16$ using the Symanzik rectangle action and $N_t = 8$ for the Iwasaki RG-improved action. The configurations were created with the Creutz heat bath algorithm (see Appendix A.1). We then compute the Binder cumulant [164] over the inverse coupling and determine the transition point from a fit. We also compute the susceptibility $\langle l^2 \rangle - \langle l \rangle^2$ and estimate the transition point with its peak position.

The infinite volume extrapolations of the pseudocritical inverse gauge coupling β_c for both setups are plotted in Figures 4.16 and 4.17.

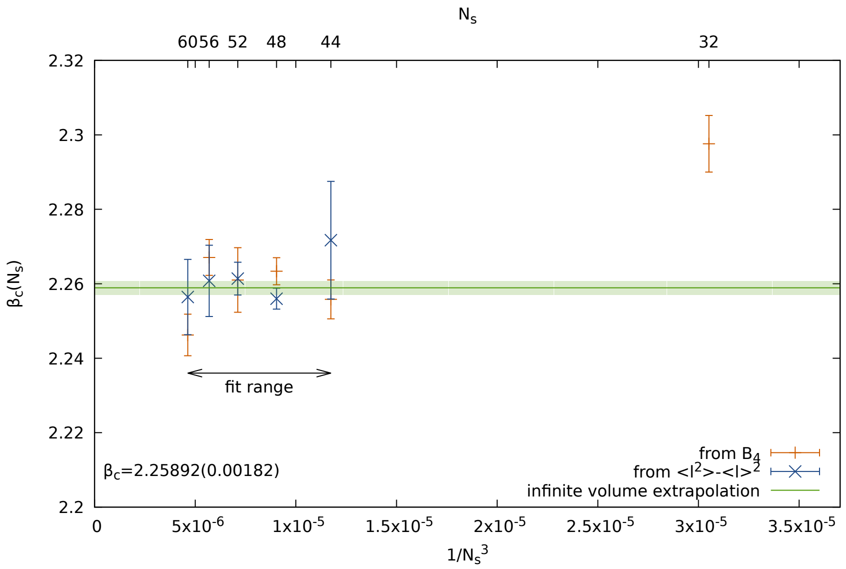

Figure 4.16.: The pseudocritical inverse coupling over the inverse volume for the Symanzik gauge action at $N_t = 16$.

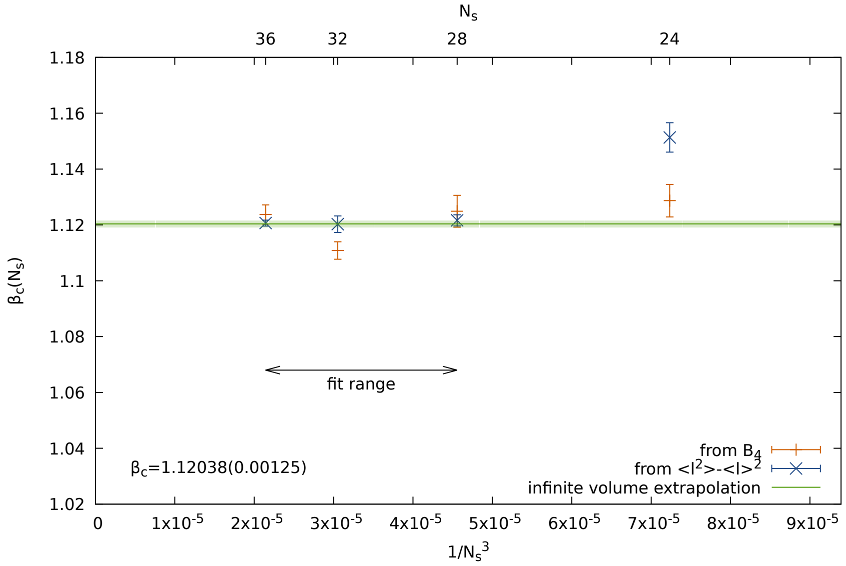

Figure 4.17.: The pseudocritical inverse coupling over the inverse volume for the Iwasaki gauge action at $N_t = 8$.

The relative error of the lattice spacing was estimated using the perturbative prediction of the lattice spacing in equation 1.36 like

$$\frac{\Delta a}{a} = \frac{1}{a}\left|\frac{\partial a}{\partial \beta}\Delta\beta\right| \text{ where } \beta = \frac{2N_c}{g^2}. \tag{4.26}$$

Each temperature $T = \frac{1}{aN_t}$ then has an error in arbitrary units, the relative error for the temperature is

$$\frac{\Delta T}{T} = \frac{1}{T}\left|\frac{\partial T}{\partial a}\Delta a\right| = \frac{\Delta a}{a} \tag{4.27}$$

and the error for the relative temperature is then

$$\Delta\left(\frac{T}{T_c}\right) = \sqrt{2}\frac{\Delta a}{a}\frac{T}{T_c}. \tag{4.28}$$

For the Symanzik gauge action with $N_t = 16$ we then obtain $\beta_c = 2.25892(182)$ and the relative error for the lattice spacing is $\frac{\Delta a}{a} = 0.00455932$. For the Iwasaki action we have $\beta_c = 1.12038(125)$ and $\frac{\Delta a}{a} = 0.00289439$.

4.5.2. Lattice setup

The Symanzik gauge action requires a relatively fine lattice constant to yield a small monopole density while the monopole density with the optimal Iwasaki action (including all cubic contributions) is very small and thus a coarser lattice can be studied. An overview of the configurations on which the eigenmodes of the overlap operator were studied is given in Table 4.2. All eigenmodes were computed at a gradient flow time $\tau = 0.1a^2$.

Table 4.2.: The quenched ensembles on which the eigenmodes of the overlap operator are studied, the number of configurations for each temperature and the number of eigenmodes per configuration.

Ensemble	N_t	T/T_c	# conf.	$\frac{\text{modes}}{\text{conf}}$
SYM.16 $N_s = 48$ $\frac{\Delta a}{a} = 0.00455932$	4	4.0000(258)	21	300
	8	2.0000(129)	6	128
IWS.8 $N_s = 32$ $\frac{\Delta a}{a} = 0.00289439$	3	2.6667(109)	20	300
	4	2.0000(082)	20	300
	5	1.6000(065)	20	300
	6	1.3333(055)	20	300
	7	1.1429(047)	20	300
	8	1.0000(041)	30	300
	9	0.8889(036)	20	300
	11	0.7273(030)	20	300

4.5.3. Finite size effects

To make sure that the localization phenomenon is not overshadowed by finite volume effects we study the quark eigenmodes for two different spatial volumes. As N_t is rather large in the SYM.16 ensemble the lattice constant in this ensemble is relatively small. It is therefore crucial to quantify how results may suffer from the limited physical volume. On the IWS.8 ensemble the lattice constant is more coarse, such that we need less lattice sites for a sufficiently large physical volume.

In Figure 4.18 we compare the Polyakov loop over the relative temperature for two different spatial volumes. The expectation values on both volumes agree very well, but the second moment of the Polyakov loop distribution shows a clear deviation. While we observe a clear peak at $T/T_c = 1$ for $N_s = 48$, this can not be seen for $N_s = 32$, which indicates that the correlation length is too large for this physical volume.

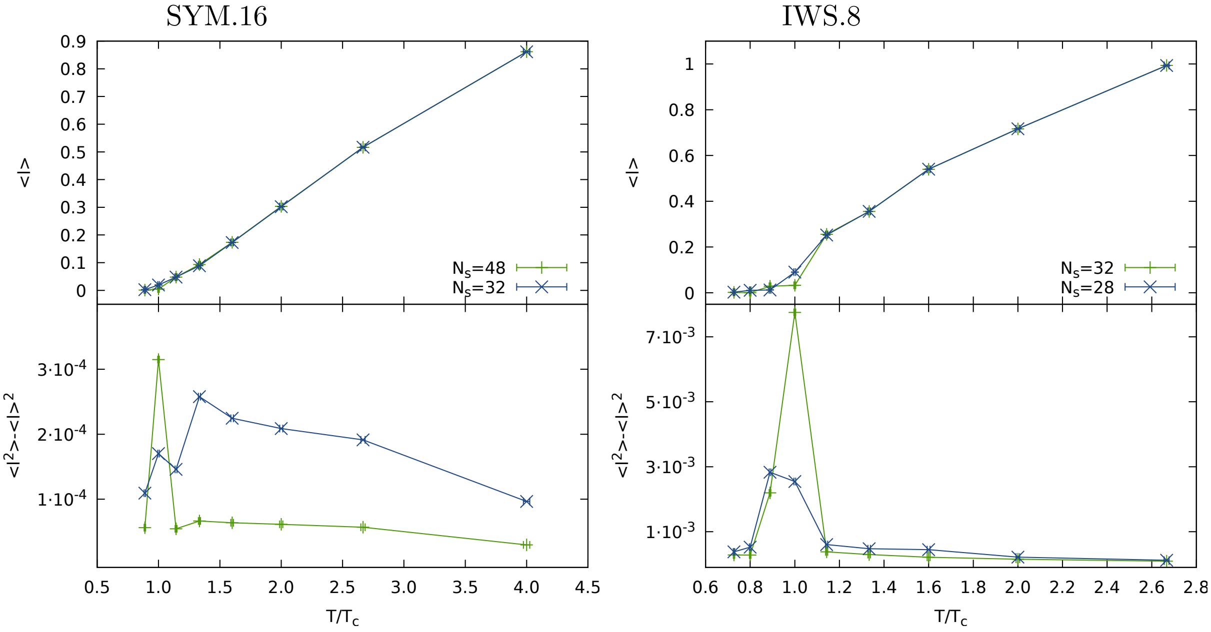

Figure 4.18.: The Polyakov loop expectation value (*Top panels*) and the susceptibility (*Bottom panels*) over T/T_c for the SYM.16 (*Left*) and the IWS.8 (*Right*) ensembles. While $\langle l \rangle$ deviates little for the two volumes, $\langle l^2 \rangle - \langle l \rangle^2$ clearly shows a different behaviour caused by finite size effects.

Furthermore we have computed the first 300 eigenmodes of the overlap Dirac operator on the SYM.16 ensemble for $N_t = 4$, which corresponds to $T = 4.000(276)T_c$ for two different spatial volumes, $N_s = 32$ and $N_s = 48$. At this temperature, the Banks-Casher gap should clearly be distinguishable, but in Figure 4.19 we can see that the gap is only open for the larger volume. In the smaller volume chiral symmetry seems to be broken by the finite volume, eigenvalues are pushed towards smaller values and bulk around zero.

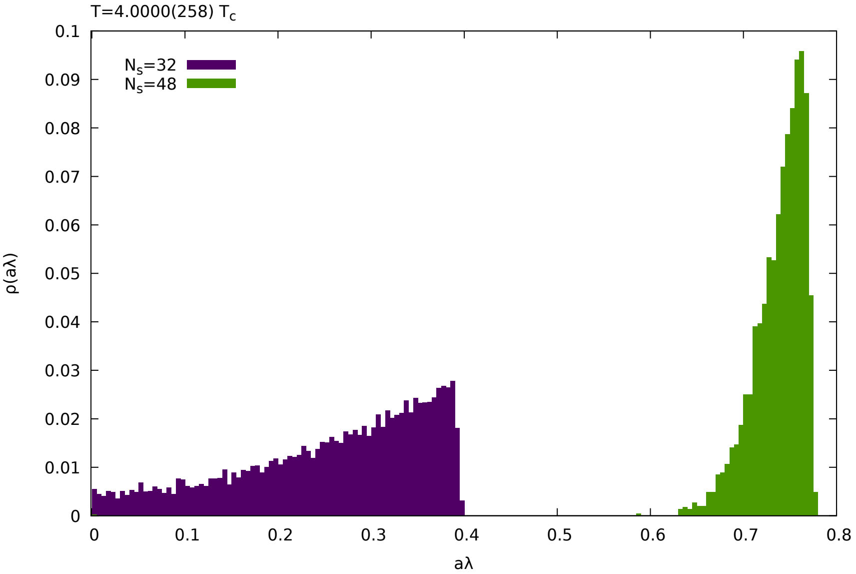

Figure 4.19.: The eigenvalue distribution of the overlap operator on the SYM.16 ensemble at $T = 4.000(276)T_c$ for $N_s = 32$ and $N_s = 48$. The Banks-Casher gap opens only for the larger volume.

We also compared the relative eigenvector volume for the two volumes, which is shown in Figure 4.20. At the smaller volume there of almost no localization effect to be seen, although at $N_s = 48$ a clear transition takes place. Since the eigenmode volume is very susceptible to finite volume effects, the localized regime is almost entirely distorted at $N_s = 32$.

By fixing the lattice constant according to some temporal extent of the lattice (in this case $N_t = 16$) the maximal correlation length was limited from above. We find, that localization studies should be performed on lattice configurations where $N_s/N_t \geq 3$.

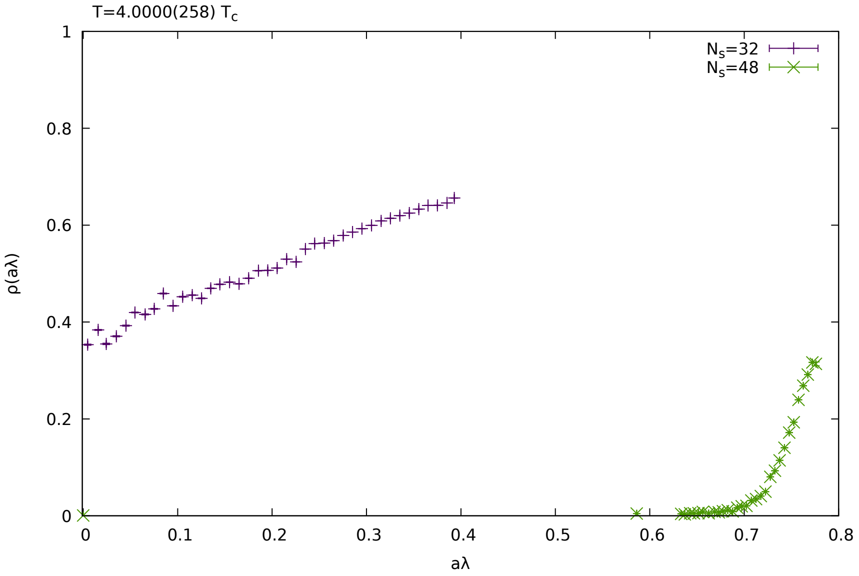

Figure 4.20.: The relative eigenmode volume determined from the IPR at $T = 4.000(276)T_c$ for two spatial lattice sizes $N_s = 32$ and $N_s = 48$. At the smaller volume there is almost no localization observed while at the larger volume a clear transition takes place at $a\lambda \approx 0.7$.

4.5.4. The Banks-Casher gap

The eigenvalues were again projected from the Ginsparg-Wilson circle onto the imaginary axis, as described in Section 2.1.2. The distribution of eigenvalues is shown in Figure 4.21 for the SYM.16 ensemble and in Figure 4.22 for the IWS.8 ensemble. We find, that at $T = T_c$ in the IWS.8 ensemble the Banks-Casher gap is still not open. A similar problem was observed in QCD (see Section 2.2). This is caused by the overlapping of quark wave functions in a finite volume, which causes their eigenvalues to obtain finite (and conjugate) shifts, very similar to the mechanism of chiral symmetry breaking in an instanton liquid.

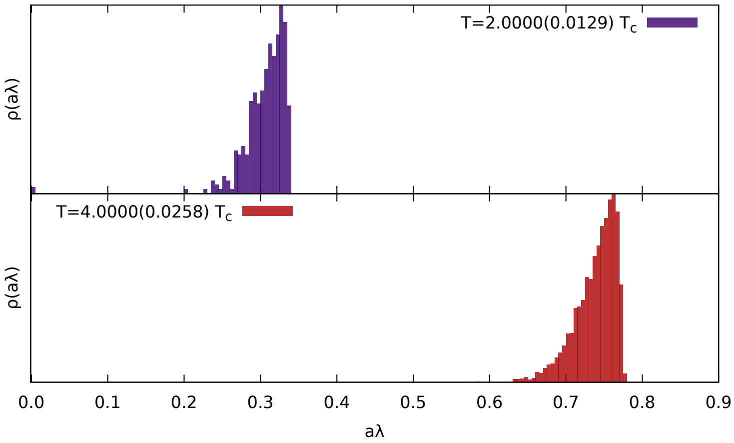

Figure 4.21.: The distribution of eigenvalues on the SYM.16 ensembles. At these large temperatures the Banks-Casher gap is well visible.

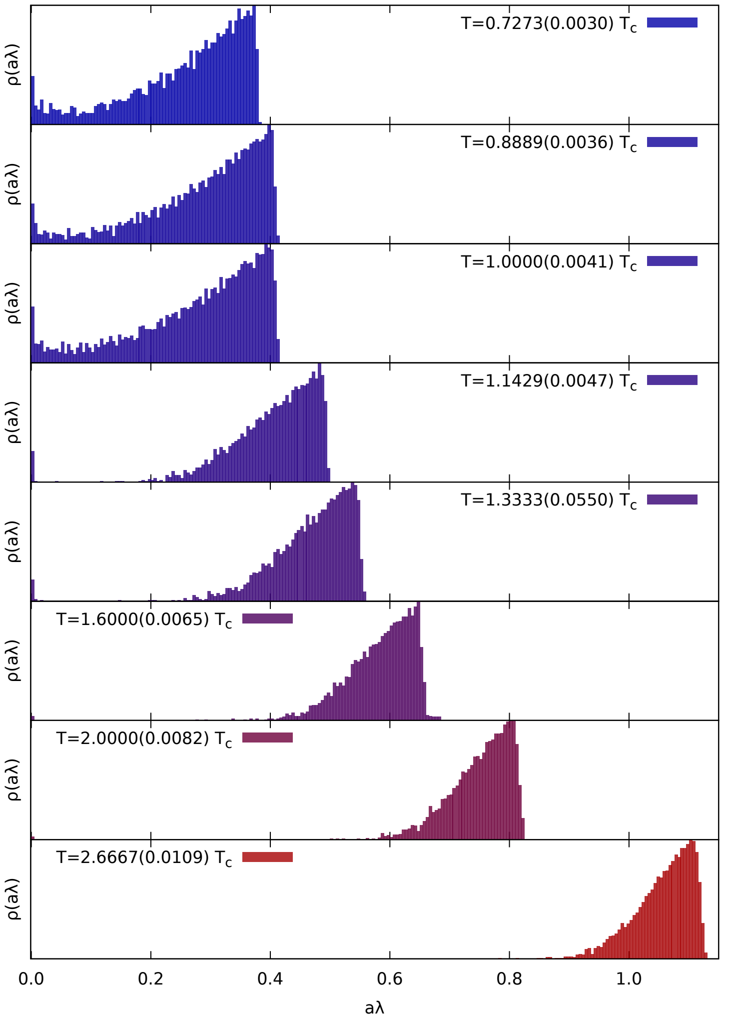

Figure 4.22.: The distribution of eigenvalues on the IWS.8 ensembles. At $T = T_c$ the Banks-Casher gap has not yet fully opened, which is accounted for by finite volume effects.

4.5.5. The mobility edge

Just like in Section 2.3 we use the relative eigenmode volume computed from the IPR to quantify the extent to which an eigenmode is localized. By a fit the inflection point of the relative volume was determined and used as an estimate for the position of λ_c. This works particularly well for larger temperatures, where the transition is clearly outlined but for small temperatures localization of modes is less clear.

The relative eigenmode volumes below and at T_c are shown in Figure 4.23 and for larger temperatures in Figure 4.24. For $T \leq T_c$ there does not seem to be a proper transition, but the low eigenmodes occupy a smaller volume than the ones at larger eigenvalues. However, no meaningful estimate for λ_c could be extracted from the inflection point. For $T > T_c$ the transition opens up at surprising large eigenvalues and it seems there is some kind of gap in λ_c; it "jumps" to finite values over T_c.

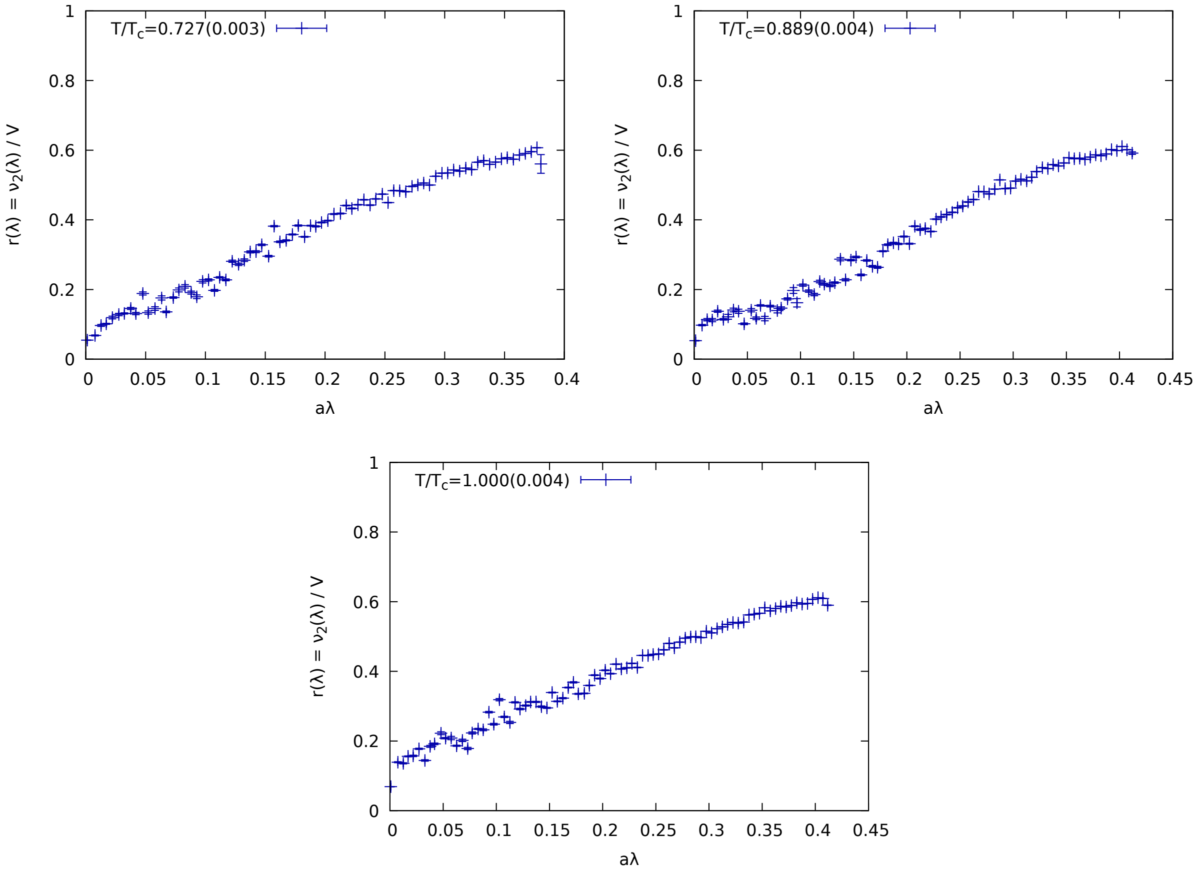

Figure 4.23.: The eigenmode volumes at $T \leq T_c$ on the IWS.8 ensemble. The regions of small volume occupation and extended modes are continuosly connected and no mobility edge could be defined.

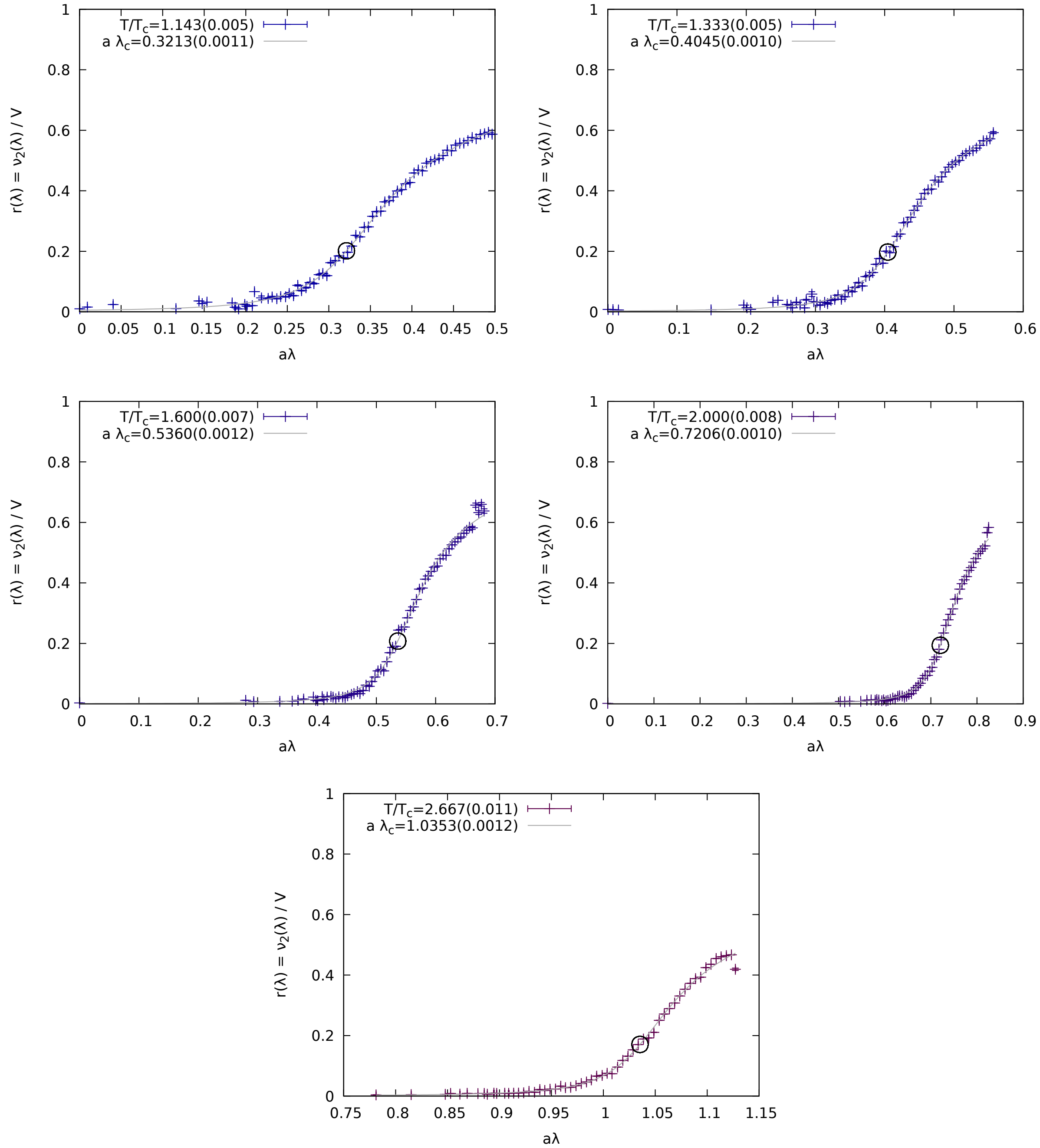

Figure 4.24.: The eigenmode volumes at $T > T_c$ on the IWS.8 ensemble.

In Figure 4.25 and Table 4.3 the mobility edge estimates are shown for each temperature. Just like in QCD, λ_c is linear in the temperature, but it does not vanish at the deconfinement transition. The linear extrapolation predicts a large portion of localized modes below T_c and must thus be inappropriate as we do not observe localized modes below the critical temperature. We conjecture, that λ_c drops to zero in a non-linear way, when the temperature is reduced; there must be some kind of curvature present that can not be resolved within this lattice setup.

However, at large temperatures the linear dependence of the mobility edge on the temperature is characterized by the slope

$$\left(\frac{a\lambda_c}{T/T_c}\right)_{\text{quenched QC}_2\text{D}} = 0.4693(036), \tag{4.29}$$

where T_c denotes the deconfinement temperature. The same quantity was computed in QCD (see Section 2.3), where the mobility edge also presents a linear dependence on the temperature

$$\left(\frac{a\lambda_c}{T/T_c}\right)_{\text{full QCD}} = 0.4281(218), \tag{4.30}$$

where T_c denotes the pseudocritical crossover temperature computed from the renormalized Polyakov loop in full QCD, which was taken from [115]. Although these two theories are vastly different (quenched vs. $N_f = 2+1+1$, SU(2) vs. SU(3)) these slopes are remarkably close to each other. This could be an indication that the linear slope of the mobility edge at large temperatures is caused by a universal mechanism.

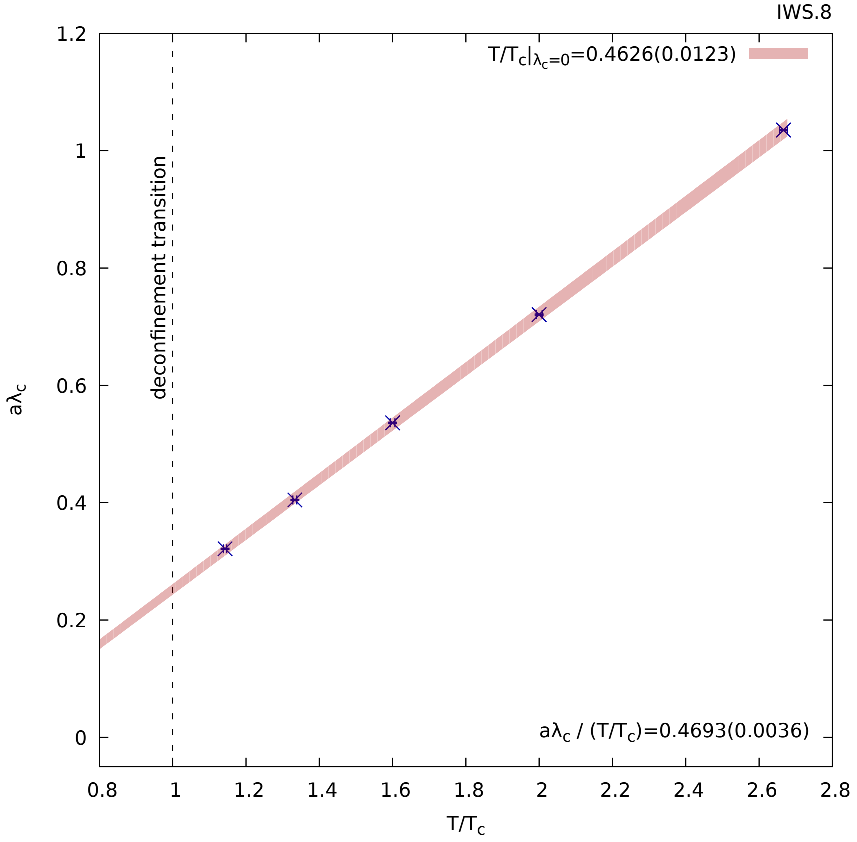

Figure 4.25.: The temperature dependence of the mobility edge in the IWS.8 ensemble. Above T_c the mobility edge is again linear, but there must be some non-linear drop to $\lambda_c = 0$ at $T = T_c$.

Table 4.3.: The estimates for the mobility edge, that were extracted from the relative eigenmode volume, over the temperature on the IWS.8 ensemble.

T/T_c	$a\lambda_c$
2.6667(109)	1.0353(12)
2.0000(082)	0.7206(99)
1.6000(065)	0.5360(12)
1.3333(055)	0.4045(10)
1.1429(047)	0.3213(11)

4.5.6. The unfolded level spacing distribution

The unfolded level spacing distributions on the IWS.8 ensemble are shown in Figure 4.26 for $T \leq T_c$ and in Figure 4.27 for $T > T_c$. The corresponding random matrix ensemble is orthogonal and the predicted level spacings are distributed like

$$P_{\text{chGOE}}(s) = \frac{\pi}{2} s e^{-\frac{\pi}{4}s^2}, \tag{4.31}$$

where the level repulsion contribution from small s is linear.

The red areas in the plots indicate localized, the blue areas indicate extended eigenmodes, both being separated by the mobility edge we have determined above. The agreement with the RMT prediction in the extended sector is great, while in the localized regime the Poisson distribution is difficult to resolve due to low statistics. However, a qualitative agreement can be observed.

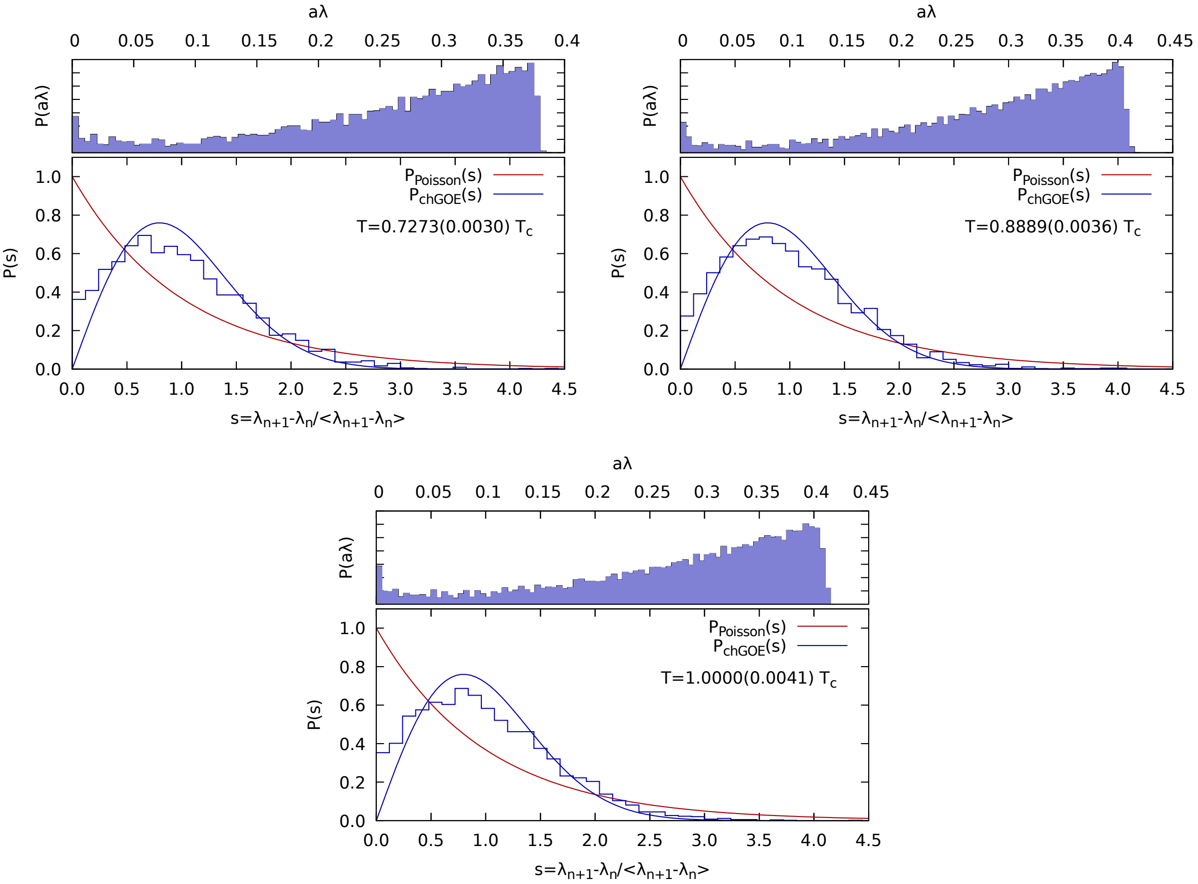

Figure 4.26.: The unfolded level spacing distribution for $T \leq T_c$ on the IWS.8 ensemble.

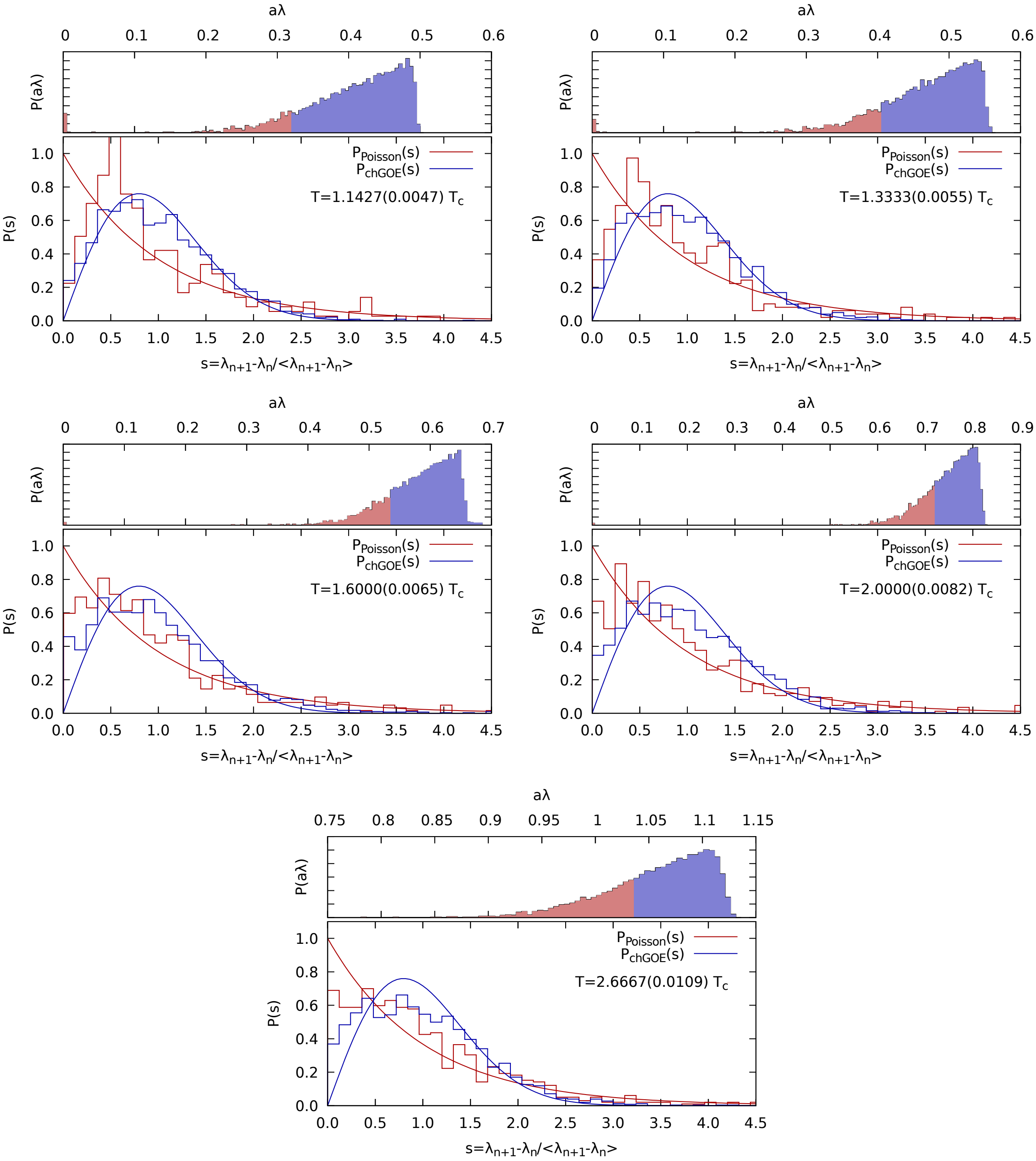

Figure 4.27.: The unfolded level spacing distribution for $T > T_c$ on the IWS.8 ensemble.

4.5.7. Localization and the Polyakov loop

In full QCD we observed a correlation between the local Polyakov loop $l(x)$ and the scalar- and pseudoscalar density of quark modes, see Section 2.6. In this setup localized quark modes are trapped in sinks of the Polyakov loop. For quenched two-colour QCD this correlation has also been observed in [128].

In Figure 4.28 we show the correlation between $\mathrm{Re}\, l(x)$ and four localized quark modes at $T = 1.3333(055) T_c$ from the IWS.8 meta ensemble. The gauge configurations have been smoothed with Iwasaki gradient flow to $\tau/a^2 = 1$ in order to remove distortions to the Polyakov loop.

We find that also in two-colour QCD this correlation is present, although the effect on the zero mode is relatively weak. The scalar density on the one hand presents regions where many points accumulate around a similar density, which corresponds to local clusters. The clusters with low densities appear to be less susceptible to the local Polyakov loop. On the other hand, the dense clusters are clearly anti-correlated with $\mathrm{Re}\, l(x)$ and are suppressed in regions where it bulks close to the centre element $+1$. We conclude that the same anti-correlation we have observed in QCD is present here, although its impact is less prominent.

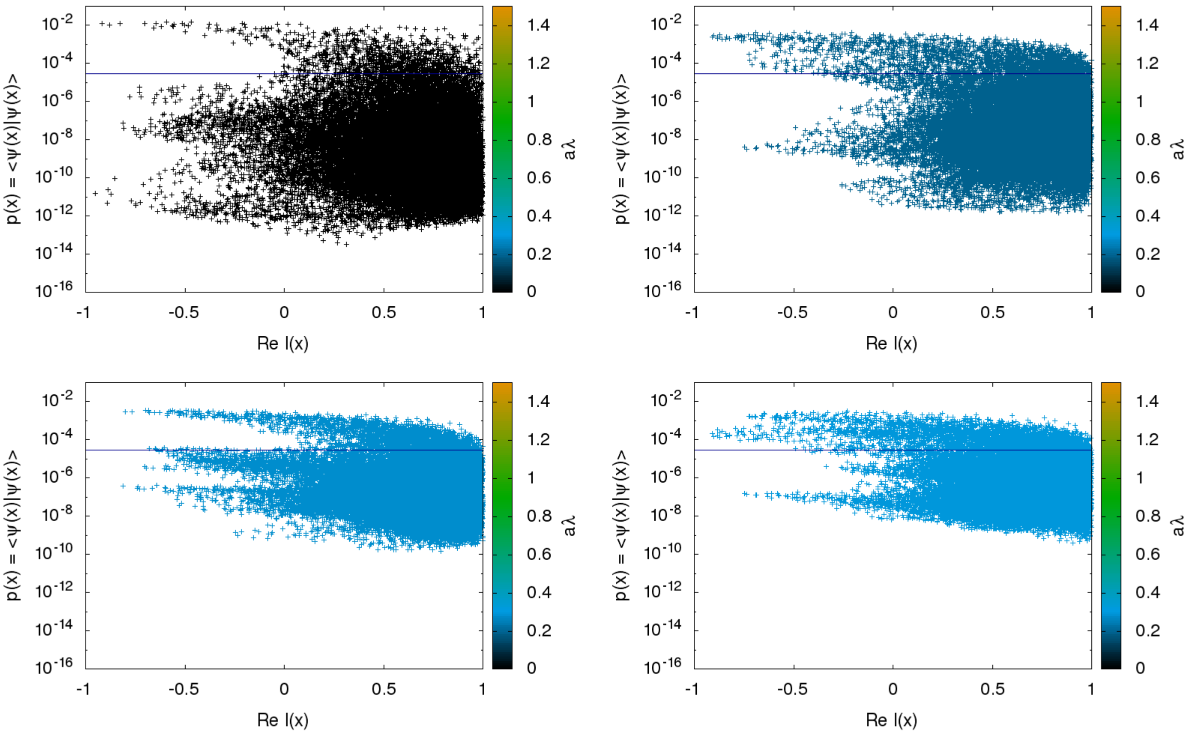

Figure 4.28.: The correlation between the scalar density and the local Polyakov loop at $T = 1.3333(055)T_c$ for four localized modes. *Top left*: $a\lambda = 0$, *Top right*: $a\lambda = 0.1965$, *Bottom left*: $a\lambda = 2.7878$, *Bottom right*: $a\lambda = 2.9621$.

4.6. Summary

In Section 4.4 we studied two-colour QCD with dynamical rooted staggered quarks at zero temperature and non-vanishing chemical potential. We compared two parameter sets, one within the bulk phase and one outside, and showed evidence that the anti-unitary symmetry of $\mathrm{QC_2D}$ with staggered quarks is restored in the continuum limit. Furthermore, we found that on the improved parameter set at finite chemical potential the quark condensate requires an additive renormalization which differs from finite temperature renormalization. The staggered quark modes at low temperatures are not properly localized, but we can observe a counteracting effect of the chemical potential on localization properties. However, at $\mu > 0$ level repulsion among the Dirac operator eigenmodes is weakened, which is a very different situation compared to finite temperature, where localized modes correspond to a vanishing level repulsion and extended modes strictly follow the Wigner-Dyson surmise.

In Section 4.5 we studied the structure of quenched two colour QCD at finite temperature and scanned the spectrum of the overlap operator for the Anderson transition. We fixed the scale in units relative to the lattice spacing for the Symanzik rectangle gauge action and the Iwasaki action and computed the eigenmodes of the overlap Dirac operator in a large temperature range.

While studying finite volume effects it was observed that a small physical volume of the lattice heavily distorts the structure of the eigenmodes, the Banks-Casher gap is closed above T_c and quark mode localization is suppressed.

We then mapped the temperature dependence of the mobility edge and found it to be linear, but it does not extrapolate to zero at the deconfinement temperature. We suspect a curvature term to be present in $\lambda_c(T)$. However, its slope at large temperatures is remarkably close to the slope of $\lambda_c(T)$ in QCD, which could indicate a more universal mechanism behind quark mode localization at large temperatures.

Finally, we conjecture that the Polyakov loop also in two-colour QCD causes localization by taking the role of the Anderson disorder potential.

5. Conclusion

In Chapter 2 we presented an investigation of the quark mode localization in the lower end of the spectrum of the QCD Dirac operator at temperatures above the chiral transition. For this we used the overlap operator on gauge configurations generated by the twisted mass at finite temperature (tmfT) collaboration and computed many eigenmodes for a very wide temperature range. We mapped the mobility edge λ_c and found that it is linear in T and vanishes at the chiral transition temperature. Furthermore, we observed that the localized modes below λ_c present a fractal dimension and have an oblate spatial structure. The chiral components of localized modes are strictly separated and connected clusters of homogeneous chirality have an exponentially decaying pseudoscalar density within. The level spacing distributions indicate that in the localized regime of the spectrum there is no level repulsion among the eigenmodes present, in contrast to the extended regime. The Chapter closes with a study of the correlation between the local Polyakov line and the (scalar and pseudoscalar) densities of the eigenmodes. It is found that the local Polyakov line is anticorrelated with the local distribution of quark modes and it takes the role of the disorder potential in the Anderson model, thus causing localization. This mechanism connects the deconfinement transition, whose (pseudo)order paramter is the Polyakov line, with the chiral transition since the low quark modes, which are "trapped" in Polyakov loop sinks, dominate the quark propagator and thus the condensate.

In Chapter 3 we used the same lattice setup to compare the fermionic and the gluonic definition of the topological charge, using gradient flow as a UV-smoothing method. The gluonic definition of the topological charge distribution differs from the charge distribution obtained from zero mode counting, but the differences become smaller at larger flow time. We found that localized quark modes carry almost the entire topological charge in a gauge configuration and suggested a method to identify localized self-dual objects within gauge configurations.

Finally, we studied the spectral properties of a QCD-like theory with the gauge group SU(2) in Chapter 4. This theory is of particular interest, as it has no sign problem and can be studied at finite chemical potential with Monte-Carlo methods. We used staggered quarks to study two-colour QCD at $\mu > 0$. We ensured that discretization artifacts from the bulk phase are sufficiently supressed and that staggered fermions restore the orthogonal anti-unitary symmetry in the continuum limit. With an appropiate lattice setup we found that the quark condensate at finite μ obtains an additive renormalization that is not present in finite temperature calculations. Furthermore we were able to conjecture that the chemical potential is counteracting quark mode localization, although level repulsion is supressed. This differs from the localization mechanism at finite temperature, where localized modes and vanishing level repulsion only occur together.

We also studied the finite temperature features of two-colour QCD, and computed overlap eigenmodes on a quenched gauge background. We studied finite volume effects to make sure that localization can properly be observed in our lattice setup, and then used a fixed scale approach to compute eigenmodes for temperatures above the deconfinement transition. At large temperatures we found that the moblity edge is again linear in T and its slope is comparable to the slope of $\lambda_c(T)$ in QCD with $N_f = 2 + 1 + 1$ quark flavours. At temperatures close to T_c we found that there must be a non-linear part in $\lambda_c(T)$ as well, since the linear extrapolation does not allow $\lambda_c(T_c) = 0$.

In this work many aspects of the spectral structure of the QCD (and two-colour QCD) Dirac operator were studied. Most prominently the localization phenomenon of low quark modes was connected with both chiral symmetry and the Polyakov line by drawing analogies with models from condensed matter physics and with the topological structure of QCD. Also the properties of quark modes in different “energy bands” were closely inspected. We presented similarities and differences between QCD and two-colour QCD and dealt with several difficulties that arise when studying these two theories on the lattice.

Coming from there, many open questions remain. Is there a general mechanism behind localization in Yang-Mills theories? How is the topological structure of QCD related to localization, chiral symmetry and deconfinement? What happens to the spectral structure of the Dirac operator at finite chemical potential?

Future surveys of quark mode localization within lattice gauge theories will hopefully shed light on these topics.

A. Generating gauge configurations

A.1. Local update algorithms

Local Monte Carlo update algorithms are a very valuable and fast method to solve the path integral in quantum theories, whose actions can be separated in local contributions. In the case of SU(N) Yang-Mills theories these algorithms are only applicable in pure gauge theories. In this “quenched limit” of the theory, the fermion determinant, which is a highly non-local object, is constant. The action can thus be decomposed with respect to a single link variable such that an update causes a change of the action like $\Delta S_g \propto U_\nu(x) - U'_\nu(x)$. This allows to update many link variables simultaneously without causing a race condition.

A widely used local Monte Carlo method is the *Metropolis algorithm*, that was first described by N. Metropolis in 1953 and generalized by W. K. Hastings in 1970 [165]. Applied to a lattice Yang-Mills theory, the update candidate link is sampled randomly by multiplying the original link with a random SU(N) update matrix, which is sampled symmetrically around unity. The candidate is the either accepted or rejected with a probability that depends on the change of the local action like $p_a \propto \exp\left(-\Delta S_g\right)$. If a link update candidate is rejected the original link remains unchanged and appears twice in the Markov chain. The acceptance rate of the Metropolis algorithm can be tuned with the width of the distribution of the update matrix.

The *heat bath algorithm* on the other hand provides an acceptance rate of 1, as the update candidate is constructed to be always accepted. In 1980 M. Creutz first described its application to SU(2) lattice gauge theory [166]. This particular version of the algorithm is commonly also referred to as *Creutz heat bath algorithm*. In the following we will look at the algorithm for a quenched SU(2) Yang-Mills theory, where the link variables U are represented by a quaternion matrix with four real parameters u_j. The equilibrium distribution of these variables reads

$$\int P(U_\nu) dU_\nu \propto \int_{-1}^{1} du_0 \sqrt{1-u_0^2}\, e^{\beta\sqrt{\det V_\nu}\, u_0} \int d\Omega_{\vec{u}}, \tag{A.1}$$

where $\Omega_{\vec{u}}$ is the solid angle of the parameters u_1, u_2 and u_3, β the inverse gauge coupling and V_ν is the sum of the surrounding plaquette-, rectangle- or cubic staples. The update matrix $\chi = (x_0, x_1, x_2, x_3)$ is randomly sampled following this distribution and the link is then updated like

$$U_\nu \to U'_\nu = \frac{1}{\sqrt{\det V_\nu}} \chi V_\nu^\dagger. \tag{A.2}$$

The heat bath algorithm can be applied to SU(3) lattice gauge theories as well. In this case the link variables are decomposed in SU(2) subgroups, which are independently updated as described before.

A.2. Hybrid Monte Carlo and equations of motion in molecular dynamics

When the fermion determinant is non-constant, new gauge configurations must be generated with a global method. The *hybrid Monte Carlo algorithm* generates gauge configurations by integrating the classical equations of motion of molecular dynamics along a fictitious time coordinate τ with Gaussian random momenta π. The molecular dynamics Hamiltonian reads

$$H = \frac{1}{2}\sum_{x,\mu} \operatorname{tr}(\pi_\mu(x)^2) + S. \tag{A.3}$$

The link variables are elements of the gauge group while the momenta are algebra valued,

$$U_\mu(x) = \exp\left(\sum_j^{N_c^2-1} U_\mu^j(x)T^j\right) \text{ and } \pi_\mu(x) = \sum_j^{N_c^2-1} \pi_\mu^j(x)T^j. \tag{A.4}$$

T_j denote the generators of the gauge group. The classical equations of motion for the momentum field then reads

$$\begin{aligned}\frac{d}{d\tau}\pi_\mu(x,\tau) &= \sum_j \frac{d\pi_\mu^j(x,\tau)}{d\tau}T^j \\ \text{with } \frac{d\pi_\mu^j(x,\tau)}{d\tau} &= -\frac{\partial H}{\partial U_\mu^j(x,\tau)} = -\frac{\partial S}{\partial U_\mu^j(x,\tau)} \equiv F_\mu^j(x,\tau),\end{aligned} \tag{A.5}$$

where $F_\mu(x)$ is called the *force term.* The Monte Carlo time evolution of the link variables is described by

$$\begin{aligned}\frac{d}{d\tau}U_\mu(x,\tau) &= \left(\sum_j \frac{dU_\mu^j(x,\tau)}{d\tau}T^j\right)U_\mu(x,\tau) \\ \text{with } \frac{dU_\mu^j(x,\tau)}{d\tau} &= \frac{\partial H}{\partial \pi_\mu^j(x,\tau)} = \frac{1}{2}\frac{\partial \sum_{y,\nu}\sum_k \left(\pi_\nu^k(y,\tau)\right)^2}{\partial \pi_\mu^j(x,\tau)} = \pi_\mu^j(x,\tau) \\ \Rightarrow \frac{d}{d\tau}U_\mu(x,\tau) &= \pi_\mu(x,\tau)U_\mu(x,\tau).\end{aligned} \tag{A.6}$$

In the following we will drop the explicit dependence on the Monte Carlo time.

A.2.1. Gauge sector

The gauge sector of the action can be written as a sum over the link variables $U_\mu(x)$ multiplied with the remaining parts of the surrounding Wilson loops, which shall be called "staples" $Q_\mu(x)$. The gauge action on the lattice generally reads

$$\begin{aligned}S_g &= -\frac{\beta}{N_c}\sum_x\sum_{\mu=1}^4\sum_{\nu\neq\mu} \operatorname{Re}\operatorname{tr} U_\mu(x)\left(c_0V_{\mu\nu}(x) + c_1W_{\mu\nu}(x) + \sum_{\rho\neq\mu,\rho\neq\nu}\left(c_2X_{\mu\nu\rho}^{\text{chair}}(x) + c_3X_{\mu\nu\rho}^{\text{cube}}(x)\right)\right) \\ &= -\frac{\beta}{N_c}\sum_x\sum_{\mu=1}^4 \operatorname{Re}\operatorname{tr} U_\mu(x)Q_\mu(x),\end{aligned} \tag{A.7}$$

where $V_{\mu\nu}(x)$ are the plaquette staples from the Wilson action, $W_{\mu\nu}(x)$ are the rectangle staples from the Symanzik action and $X_{\mu\nu\rho}^{\text{chair}}(x)$ and $X_{\mu\nu\rho}^{\text{cube}}(x)$ are the chair- and cube-like six-link Wilson loops from the Iwasaki RG improved gauge action. For the respective coefficients see Sections 1.2.2, 1.2.3 and 1.2.4.

The gauge sector thus contributes the force term

$$\begin{aligned}\frac{d\pi_\mu^j(x)}{d\tau} &= \frac{\beta}{N_c}\sum_{y,\nu}\frac{\partial U_\nu(y)}{\partial U_\mu^j(x)}Q_\nu(y) = \frac{\beta}{N_c}T^j U_\mu(x)Q_\mu(x)\\ \Rightarrow \frac{d\pi_\mu(x)}{d\tau} &= \frac{\beta}{N_c}\sum_j T^j U_\mu(x)Q_\mu(x)T^j = \frac{\beta}{N_c}U_\mu(x)Q_\mu(x)\Big|_{\mathrm{TA}} \equiv F_\mu(x),\end{aligned} \tag{A.8}$$

where the subscript TA indicates the projection of a group element to its traceless anti-hermitian part like

$$A\big|_{\mathrm{TA}} = \frac{1}{2}\left(A - A^\dagger\right) - \frac{1}{2N_c}\,\mathrm{tr}\left(A - A^\dagger\right). \tag{A.9}$$

A.2.2. Molecular dynamics with pseudofermions

The two-flavour pseudofermion action with a Dirac operator D generally reads

$$S_f = \sum_{y,z}\phi^\dagger(y)\left(D^\dagger D\right)^{-1}_{y,z}\phi(z). \tag{A.10}$$

The pseudofermion sector then contributes a force term

$$\begin{aligned}F_\mu^j(x) = -\frac{\partial S_f}{\partial U_\mu^j(x)} &= \sum_{y,z}\underbrace{\left(\phi^\dagger(D^\dagger D)^{-1}\right)(y)}_{=:\chi^\dagger(y)}\frac{\partial\left(D^\dagger D\right)_{y,z}}{\partial U_\mu^j(x)}\underbrace{\left((D^\dagger D)^{-1}\phi\right)(z)}_{=:\chi(z)}\\ &= \sum_{y,z}\chi^\dagger(y)\frac{\partial D^\dagger_{y,z}}{\partial U_\mu^j(x)}\left(D\chi\right)(z) + \sum_{y,z}\left(D\chi\right)^\dagger(y)\frac{\partial D_{y,z}}{\partial U_\mu^j(x)}\chi(z).\end{aligned} \tag{A.11}$$

The auxiliary vector χ is computed in each time step of the numerical integration of the equations of motion by solving

$$\left(D^\dagger D\right)\chi = \phi \tag{A.12}$$

on a random fermion source ϕ, which is sampled for each molecular dynamics trajectory, and thus every element of the Markov chain. The inversion of the fermion matrix is very expensive and is done using a Krylov subspace inverter. A common choice is the method of conjugate gradients [167] or similar algorithms based on this.

A.2.3. Dynamical staggered quarks

For standard staggered fermions the Dirac operator and its hermitian conjugate read

$$\begin{aligned}D_{y,z} &= m\delta_{y,z} + \sum_\nu\frac{\eta_\nu(y)}{2a}\left(U_\nu(y)\delta_{y+\hat\nu,z} - U_\nu^\dagger(y-\hat\nu)\delta_{y-\hat\nu,z}\right)\\ D^\dagger_{y,z} &= m\delta_{y,z} - \sum_\nu\frac{\eta_\nu(y)}{2a}\left(U_\nu(y)\delta_{y+\hat\nu,z} - U_\nu^\dagger(y-\hat\nu)\delta_{y-\hat\nu,z}\right)\end{aligned} \tag{A.13}$$

Using $U^\dagger U = 1$ and

$$\frac{\partial U_\nu(y)}{\partial U_\mu^j(x)} = \delta_{\nu,\mu}\delta_{x,y}T^j U_\nu(y) \tag{A.14}$$

we can write

$$\frac{\partial U_\nu^\dagger(y-\hat\nu)}{\partial U_\mu^j(x)} = U_\nu^\dagger(y-\hat\nu)\frac{\partial U_\nu(y-\hat\nu)}{\partial U_\mu^j(x)}U_\nu^\dagger(y-\hat\nu) = U_\nu^\dagger(y-\hat\nu)T^j\delta_{\nu,\mu}\delta_{x,y-\hat\nu} \tag{A.15}$$

and hence

$$\frac{\partial D_{y,z}}{\partial U_\mu^j(x)} = \frac{\eta_\mu(y)}{2a}\left(T^j U_\mu(y)\delta_{x,y}\delta_{y+\hat\mu,z} - U_\nu^\dagger(y-\hat\nu)T^j\delta_{x,y-\hat\nu}\delta_{y-\hat\nu,z}\right) = -\frac{\partial D_{y,z}^\dagger}{\partial U_\mu^j(x)}. \tag{A.16}$$

Using $\eta_\mu(x+\hat\mu) = \eta_\mu(x)$ we can plug this in the force term and obtain

$$\begin{aligned}\frac{d}{d\tau}\pi_\mu(x) &= \sum_j F_\mu^j(x)T^j \\ &=\frac{\eta_\mu(x)}{2a}\sum_j\left((D\chi)^\dagger(x)T^jU_\mu(x)\chi(x+\hat\mu)T^j - \chi^\dagger(x)T^jU_\mu(x)(D\chi)(x+\hat\mu)T^j\right) \\ &\quad+\frac{\eta_\mu(x)}{2a}\sum_j\left(\chi^\dagger(x+\hat\mu)U_\mu^\dagger(x)T^j(D\chi)(x)T^j - (D\chi)^\dagger(x+\hat\mu)U_\mu^\dagger(x)T^j\chi(x)T^j\right).\end{aligned} \tag{A.17}$$

This staggered force term can be written in a matrix form using outer products of colour vectors like

$$\begin{aligned}\frac{d}{d\tau}\pi_\mu(x) =&\frac{\eta_\mu(x)}{2a}U_\mu(x)\left(\chi(x+\hat\mu)(D\chi)^\dagger(x) - (D\chi)(x+\hat\mu)\chi^\dagger(x)\right)\Big|_{\mathrm{TA}} \\ &+\frac{\eta_\mu(x)}{2a}\left((D\chi)(x)\chi^\dagger(x+\hat\mu) - \chi(x)(D\chi)^\dagger(x+\hat\mu)\right)U_\mu^\dagger(x)\Big|_{\mathrm{TA}}.\end{aligned} \tag{A.18}$$

A.2.4. Dynamical Wilson quarks

The Wilson Dirac operator and its hermitian conjugate reads

$$\begin{aligned}D_{y,z} &= \left(m+\frac{4}{a}\right)\delta_{y,z} - \frac{1}{2a}\sum_\nu\left((1-\gamma_\nu)U_\nu(y)\delta_{y+\hat\nu,z} + (1+\gamma_\nu)U_\nu^\dagger(y-\hat\nu)\delta_{y-\hat\nu,z}\right) \\ D_{y,z}^\dagger &= \left(m+\frac{4}{a}\right)\delta_{y,z} - \frac{1}{2a}\sum_\nu\left((1+\gamma_\nu)U_\nu(y)\delta_{y+\hat\nu,z} + (1-\gamma_\nu)U_\nu^\dagger(y-\hat\nu)\delta_{y-\hat\nu,z}\right)\end{aligned} \tag{A.19}$$

Their derivatives with respect to the gauge field components are given by

$$\begin{aligned}\frac{\partial D_{y,z}}{\partial U_\mu^j(x)} &= -\frac{1}{2a}\left((1-\gamma_\mu)\delta_{x,y}T^jU_\mu(y)\delta_{y+\hat\mu,z} + (1+\gamma_\mu)U_\mu^\dagger(y-\hat\mu)T^j\delta_{x,y-\hat\mu}\delta_{y-\hat\mu,z}\right) \\ \frac{\partial D_{y,z}^\dagger}{\partial U_\mu^j(x)} &= -\frac{1}{2a}\left((1+\gamma_\mu)\delta_{x,y}T^jU_\mu(y)\delta_{y+\hat\mu,z} + (1-\gamma_\mu)U_\mu^\dagger(y-\hat\mu)T^j\delta_{x,y-\hat\mu}\delta_{y-\hat\mu,z}\right)\end{aligned} \tag{A.20}$$

such that the Wilson fermion force term becomes

$$\begin{aligned}\frac{d}{d\tau}\pi_\mu(x) &= \sum_j F_\mu^j(x)T^j \\ &= -\frac{1}{2a}\sum_j\left(\chi^\dagger(x)T^jU_\mu(x)(1+\gamma_\mu)(D\chi)(x+\hat\mu)T^j\right) \\ &\quad-\frac{1}{2a}\sum_j\left((D\chi)^\dagger(x)T^jU_\mu(x)(1-\gamma_\mu)\chi(x+\hat\mu)T^j\right) \\ &\quad-\frac{1}{2a}\sum_j\left(\chi^\dagger(x+\hat\mu)U_\mu^\dagger(x)T^j(1-\gamma_\mu)(D\chi)(x)T^j\right) \\ &\quad-\frac{1}{2a}\sum_j\left((D\chi)^\dagger(x+\hat\mu)U_\mu^\dagger(x)T^j(1+\gamma_\mu)\chi(x)T^j\right).\end{aligned} \tag{A.21}$$

Its matrix form reads

$$\begin{aligned}\frac{d}{d\tau}\pi_\mu(x) = &-\frac{1}{2a}U_\mu(x)\left(\left((1+\gamma_\mu)(D\chi)(x+\hat{\mu})\right)\chi^\dagger(x) + \left((1-\gamma_\mu)\chi(x+\hat{\mu})\right)(D\chi)^\dagger(x)\right)\Big|_{\mathrm{TA}} \\ &-\frac{1}{2a}\left(\left((1-\gamma_\mu)(D\chi)(x)\right)\chi^\dagger(x+\hat{\mu}) + \left((1+\gamma_\mu)\chi(x)\right)(D\chi)^\dagger(x+\hat{\mu})\right)U_\mu^\dagger(x)\Big|_{\mathrm{TA}}.\end{aligned} \tag{A.22}$$

A.2.5. Dynamical domain wall quarks

The domain wall Dirac operator contains a "parallel" and a "perpendicular" part like

$$D_{x,y;s,t} = \delta_{s,t}D^{||}_{x,y} + \delta_{x,y}D^{\perp}_{s,t} \tag{A.23}$$

such that the two-flavour pseudofermion action integrated over the additional domain wall dimension then looks like

$$S_f = \sum_{y,z}\sum_{s,t}^{N_5}\phi^\dagger(y;s)\left(D^\dagger D\right)^{-1}_{y,z;s,t}\phi(z;t). \tag{A.24}$$

The parallel part is the Wilson operator while the perpendicular part is independent from the gauge field, such that

$$\frac{\partial D_{x,y;s,t}}{\partial U_\mu^j(x)} = \delta_{s,t}\frac{\partial D^{||}_{x,y}}{\partial U_\mu^j(x)}. \tag{A.25}$$

Therefore the domain wall force term is the sum over the Wilson force terms for each space-time slice on the N_5 axis and reads

$$\begin{aligned}F_\mu^j(x) &= -\frac{\partial S_f}{\partial U_\mu^j(x)} \\ &= \sum_{y,z}\sum_{s,t}^{N_5}\chi^\dagger(y;s)\delta_{s,t}\frac{\partial\left(D^{||}\right)^\dagger_{x,y}}{\partial U_\mu^j(x)}(D\chi)(z;t) \\ &+\sum_{y,z}\sum_{s,t}^{N_5}(D\chi)^\dagger(y;s)\delta_{s,t}\frac{\partial D^{||}_{y,z}}{\partial U_\mu^j(x)}\chi(z;t).\end{aligned} \tag{A.26}$$

A.3. Rooting

To compute arbitrary powers of the fermion matrix the *Zolotarev approximation*, or rational approximation, can be used. This allows to adjust the number of mass-degenerate flavours in the fermion action and is of particular use for using staggered quarks, which without rooting represent four staggered tastes. The Zolotarev approximation reads

$$r_\gamma(\mathcal{M}) = \alpha_0 + \sum_j\frac{\alpha_j}{\mathcal{M}+\beta_j} \approx \mathcal{M}^\gamma \tag{A.27}$$

with the real parameters $\{\alpha_0,\alpha_1,...,\alpha_n,\beta_1,...,\beta_n\}$. Since the most conjugate gradient only converge on positive definite matrices, one usually uses the two-flavour fermion matrix $\mathcal{M} = D^\dagger D$ for this. The fermion force term then becomes

$$\begin{aligned}F_\mu^j(x) &= \sum_{y,z}\phi^\dagger(y)\frac{\partial r_\gamma(\mathcal{M})}{\partial U_\mu^j(x)}\phi(z) \\ &= -\sum_k\sum_{y,z}\underbrace{\left(\phi^\dagger(y)(\mathcal{M}+\beta_k)^{-1}\right)}_{=:\chi_k^\dagger(y)}\frac{\partial\mathcal{M}}{\partial U_\mu^j(x)}\underbrace{\left((\mathcal{M}+\beta_k)^{-1}\phi(z)\right)}_{=:\chi_k(z)}\end{aligned} \tag{A.28}$$

A.3.1. The multishift conjugate gradient solver

The rational approximation of the fermion matrix [35] requires the computation of the solutions y_k to

$$(\mathcal{M} + \beta_k)\, y_k = \phi \Rightarrow y_k = (\mathcal{M} + \beta_k)^{-1}\, \phi, \tag{A.29}$$

where ϕ is a pseudofermion source field. Such a solution can be found using the method of conjugate gradients [80]. As the Krylov subspace is invariant under positive shifts, the shifted search direction polynomials are proportional to each other and we can solve all shifted equations simultaneously [81,82]. This is a massive improvement compared to computing the shifted solutions separately.

An implementation of the multishifted conjugate gradient inverter in MATLAB is given in listing A.1

Listing A.1: An implementation of the Multishift Conjugate Gradient solver in Matlab.

```matlab
function [x, res] = cgm(A,b,m,eps)
N=length(b);
res=[];
converged = zeros(1,length(m)); % 0=false, 1=true
converged_total=0; % the number of converged shifts

% parameter initialization
alpha=0;
omega = zeros(1,length(m)) + 1;
omega_old = 1;
gamma_g = 0;
gamma_o = 0;
gamma = zeros(1,length(m));
ksi = zeros(1,length(m))+1;
ksi_old = zeros(1,length(m))+1;
eta = 0;
tmp = 0; % float buffer for ksi

x = zeros(N,length(m)); % solution vector, must be initialized with 0
p = zeros(N,length(m))+b; % search directions
s = zeros(N,1);

r = b; % residual of the smallest shift
res_sqr_old = r'*r;
res_sqr = res_sqr_old;

iter=0;
while converged_total<length(m) && iter < N

  % this assumes that the smallest shift
  % is stored in the beginning of the array
  s = A*p(:,1) + m(1).*p(:,1);
  alpha = p(:,1)'*s;
  omega_old = omega(1);
  omega(1) = -res_sqr_old/alpha;

  eta = omega(1)/omega_old * gamma_g;

  % update the smallest shift
  x(:,1) = x(:,1) - omega(1).*p(:,1);
  r = r + omega(1).*s;

  res_sqr = r'*r;

  gamma_g = res_sqr / res_sqr_old;
  gamma_o = gamma_g/omega(1);
  res_sqr_old = res_sqr;
  p(:,1) = r + gamma_g*p(:,1);

  % check residuals
  a = [];
  for k = 1:length(m)
    err = sqrt(res_sqr) * ksi(k);
```

```
    if(err <= eps)
      if converged(k)==0
        converged_total +=1;
        converged(k)=1;
      end
      err=0;
    end
    a = [a; err];
  end
  res = [res a];

  % update the other shifts (if they haven't converged yet)
  for k=2:length(m)
    if converged(k)==0
      tmp = ksi(k);
      ksi(k)=ksi(k)/(eta*(1-ksi(k)/ksi_old(k) )-(m(k)-m(1))*omega(1)+1);
      ksi_old(k) = tmp;
      omega(k) = omega(1)*(ksi(k)/ksi_old(k));
      gamma(k) = gamma_o*(ksi(k)/ksi_old(k))*omega(k);
      x(:,k) = x(:,k) - omega(k)*p(:,k);
      p(:,k) = ksi(k)*r + gamma(k)*p(:,k);
    end
  end
  iter += 1;
end
end
```

A.3.2. The Remez exchange algorithm

The Remez exchange algorithms can be used to determine the coefficients for rational and polynomial approximations from a min-max optimization. In this work it is used mostly for the coefficients of the Zolotarev approximation for rooting the fermion matrix, and the approximation of the sign function in the overlap operator using both rational functions and Chebyshev polynomials.

In the following we will consider the min-max approximation of a function $f(x)$ with a n-th degree polynomial $P_n(x)$ [168], which means to minimize the maximum error on an interval $x \in [a;b]$, or eigenvalues of a matrix respectively. The approximating polynomial reads

$$P_n(x) = \sum_{k=0}^{n} c_k (x-a)^k . \tag{A.30}$$

The Remez algorithm optimizes $n+2$ interpolation points

$$a \leq x_0 < \ldots < x_{n+1} \leq b, \tag{A.31}$$

on which the error function has a local maximum with alternating signs. This error function is then

$$f(x_j) - P_n(x_j) = (-1)^j E \text{ where } E = \pm \max_{x \in [a;b]} |f(x) - P_n(x)| . \tag{A.32}$$

The interpolating points $\{x_j\}$, the maximum error E and the polynomial coefficients $\{c_k\}$ are optimized in the following steps:

1. Initialize $\{x_j\}$ arbitrarily, i.e. equidistant
2. Computation of the coefficients of $P_n(x)$:
   The error function has an equal magnitude E at each x_j, but with alternating sign. Solve the $n+2$ linear equations

$$\sum_{k=0}^{n} c_k (x_j - a)^k + (-1)^j E = f(x_j) \tag{A.33}$$

for $\{c_k, E\}$, i.e. compute

$$\begin{pmatrix} c_0 \\ \vdots \\ c_n \\ E \end{pmatrix} = \begin{pmatrix} 1 & (x_0-a) & (x_0-a)^2 & \cdots & (x_0-a)^n & (-1)^0 \\ \vdots & & & \ddots & & \vdots \\ 1 & (x_n-a) & (x_n-a)^2 & \cdots & (x_n-a)^n & (-1)^n \\ 1 & (x_{n+1}-a) & (x_{n+1}-a)^2 & \cdots & (x_{n+1}-a)^n & (-1)^{n+1} \end{pmatrix}^{-1} f \begin{pmatrix} x_0 \\ \vdots \\ x_n \\ x_{n+1} \end{pmatrix}. \tag{A.34}$$

Note that the error magnitude E is not the global maximum error on the interval $[a;b]$ yet. The change of parameters and the error function is sketched in Figure A.1.

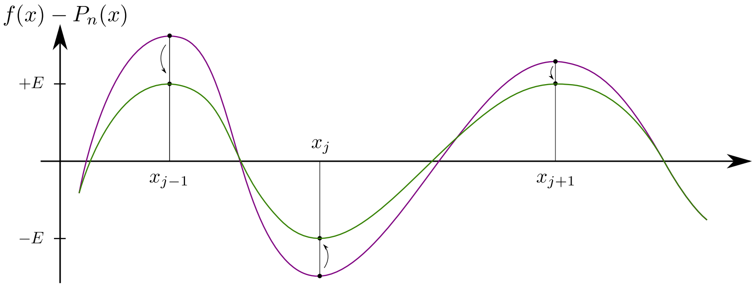

Figure A.1.: The coefficient update in the Remez algorithm: The error function takes a local maximum $\pm E$ at each interpolation point x_j.

3. Exchange step:
   The interpolation points $\{x_j\}$ are updated to a new set $\{x'_j\}$ which maximizes the error magnitude E between its roots. This is sketched in Figure A.2.

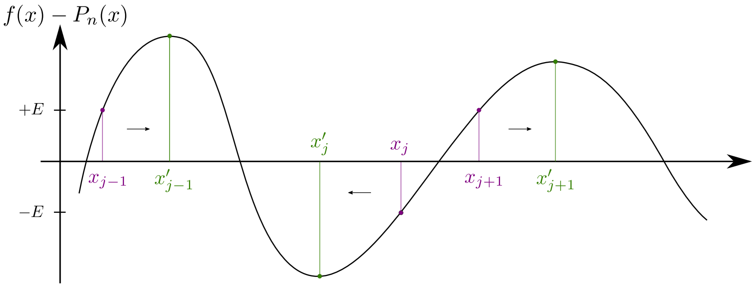

Figure A.2.: The exchange step in the Remez algorithm: The new interpolation points are chosen to maximize the error function.

4. Repeat from step 2 until E has reached the desired precision.

The Remez exchange algorithm can be used to compute the coefficients for a rational approximation as well. The approximating function is then given by $r(x) = \frac{p(x)}{q(x)}$, where $p(x) = \sum_k p_k x^k$ and $q(x) = \sum_k q_k x^k$ are polynomials. The error function reads

$$f(x_j) - \frac{p(x_j)}{q(x_j)} = (-1)^j E \tag{A.35}$$

and the coefficients can be computed by solving the nonlinear equations

$$\sum_{k=0}^{n} \left(p_k x_j^k - q_k x_j^k f(x_j) + (-1)^j E q_k x_j^k \right) = 0. \tag{A.36}$$

A.4. Symplectic integrators

Symplectic integrators solve Hamiltonian equations of motion for the canonical variables q and p. The Hamiltonian time evolution is a symplectic map, which means that it is a volume-preserving transformation of phase space. A symplectic integrator thus leaves the two form $dp \wedge dq$ conserved, and Liouville's theorem is obeyed throughout the numerical integration.

The time reversibility of symplectic integrators provides the detailed balance requirement, such that this integration scheme is well suited to solve the molecular dynamics equations of motion in the hybrid Monte Carlo algorithm.

A simple second order symplectic integration scheme is called the *leapfrog integrator*. The canonical variables $q(\tau)$ and $p(\tau)$ are integrated at interleaving times such that the integration with a step size $\Delta\tau$ looks like

$$\begin{aligned} q\Big((n+\frac{1}{2})\Delta\tau\Big) &= q\Big((n-\frac{1}{2})\Delta\tau\Big) + \Delta\tau p(n\Delta\tau) \\ p\left(n\Delta\tau\right) &= p\left((n-1)\Delta\tau\right) + \Delta\tau F\left((n-1)\Delta\tau\right). \end{aligned} \tag{A.37}$$

Here $F(\tau)$ denotes the force term from the Hamiltonian equations of motion and the first and last integration step for one of the variables is done with $\Delta\tau/2$. This interleaving scheme is sketched in Figure A.3.

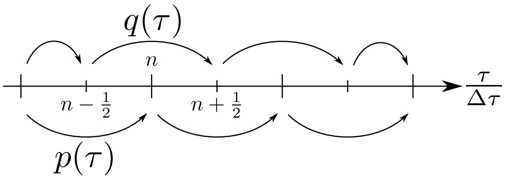

Figure A.3.: A sketch of the leapfrog integration method.

The action of a theory can often be split in separate parts, for example in a fermionic and a gluonic part. Integrating the force terms coming from these separate parts with different time scales can be very efficient. Such a nested multi-timescale leapfrog integration scheme is also called *Sexton-Weingarten integrator* [169], and in this work it is mostly used to distinguish the fermionic and the gluonic force term.

A.5. Gradient flow

The flow equation on a discrete lattice reads

$$\frac{d}{d\tau}V(\tau) = Z(V(\tau))V(\tau) \text{ where } V \in SU(N) \text{ and } Z \in su(N), \tag{A.38}$$

where the force term

$$Z_\mu(\tau,x) = \frac{\partial S}{\partial V_\mu(\tau,x)} \tag{A.39}$$

equates to the force term in molecular dynamics, but with respect to the flowed link variables. This flow equation can be integrated using a third order Runge-Kutta method like

$$\begin{aligned} W_0 &= V(\tau) \\ W_1 &= \exp \Delta\tau \left(\frac{1}{4} Z(W_0) \right) \\ W_2 &= \exp \Delta\tau \left(\frac{8}{9} Z(W_1) - \frac{17}{36} Z(W_0) \right) \\ V(\tau + \Delta\tau) &= \exp \Delta\tau \left(\frac{3}{4} Z(W_2) - \frac{8}{9} Z(W_1) + \frac{17}{36} Z(W_0) \right). \end{aligned} \tag{A.40}$$

B. Implementation of the overlap operator

The overlap Dirac operator reads

$$D = \frac{\rho}{a}\left(1 + \operatorname{sgn} K\right), \tag{B.1}$$

where K is the γ_5-hermitian kernel operator, see Section 1.3.3. The sign function must be approximated in some way. In this work either a polynomial or rational approximation was used.

B.1. Chebyshev polynomials

Approximating the sign function with Chebyshev polynomials is relatively cheap, compared to the Zolotarev approximation, since it always requires the same number of matrix multiplications with the kernel operator K, regardless of its condition number, which strongly depends on the temperature. Chebyshev polynomials fulfil the recurrence relation

$$T_{n+1}(x) = 2xT_n(x) - T_{n-1}(x) \text{ where } T_0(x) = 1 \text{ and } T_1(x) = x, \tag{B.2}$$

and can be used to approximate the sign function in the interval $[-1;1]$ like

$$\operatorname{sgn} K \approx \sum_n^N c_n T_n(x). \tag{B.3}$$

How the sign function is approximated with Chebyshev polynomials in several different orders N is shown in Figure B.1.

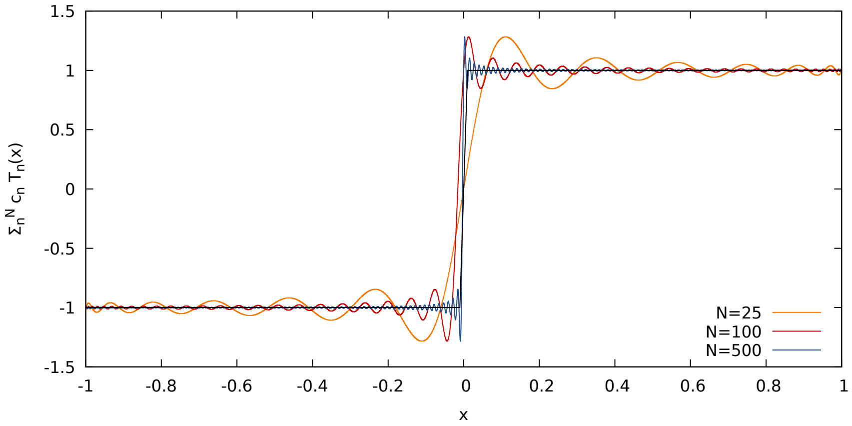

Figure B.1.: The approximation to the sign function in different orders of Chebyshev polynomials.

With a low order the low eigenmodes of the kernel operator are badly approximated with Chebyshev polynomials. One usually projects the kernel operator on its lowest eigenmodes to maintain a reliable precision in the low spectral range, see Section B.3.

B.2. Zolotarev approximation

In this work, however, the rational approximation was mostly used, since low-lying eigenmodes of the kernel operator are well maintained. For these computations it was not necessary to project to the lowest kernel operator eigenmodes. The sign function is approximated like sgn K = $\frac{K}{\sqrt{K^\dagger K}}$, where

$$\frac{1}{\sqrt{K^\dagger K}} = \frac{1}{\sqrt{(\gamma_5 K)^2}} \approx \alpha_0 + \sum_{j=1} \frac{\alpha_j}{(\gamma_5 K)^2 + \beta_j} =: r_{-\frac{1}{2}}((\gamma_5 K)^2), \tag{B.4}$$

such that sgn$K = Kr((\gamma_5 K)^2)$. The multishift conjugate gradient solver as described in Section A.3.1 was used to invert the squared kernel operator.

B.3. Projection to the low eigenmodes of the kernel operator

When projecting to the first N eigenmodes of the kernel operator, the sign function can, at least partially, be treated exactly, which greatly improves the precision of the chosen approximation [60]. For a Wilson kernel operator $K = D_W$, let $\gamma_5 D_W$ be the hermitian projection and

$$\gamma_5 D_W |\psi_W^j\rangle = \lambda_W^j |\psi_W^j\rangle \text{ with } \lambda_W^j \in \mathbb{R}. \tag{B.5}$$

We can then define a projector $P_N = \sum_j^N |\psi_W^j\rangle\langle\psi_W^j|$ to the first N eigenmodes of the hermitian kernel. The sign function can be separated in an approximated part $|\tilde{\eta}\rangle$ = sgn $D_W|\eta\rangle$ and an exactly treated part like

$$\begin{aligned}\text{sgn}D_W|\eta\rangle &= \text{sgn}D_W P_N|\eta\rangle + (1 - P_N)\underbrace{\text{sgn}D_W|\eta\rangle}_{=:|\tilde{\eta}\rangle} \\ &= \sum_j^N \text{sgn}\lambda_W^j |\psi_W^j\rangle\langle\psi_W^j|\eta\rangle + |\tilde{\eta}\rangle - \sum_j^N |\psi_W^j\rangle\langle\psi_W^j|\tilde{\eta}\rangle \\ &= |\tilde{\eta}\rangle + \sum_j^N \left(\text{sgn}\lambda_W^j\langle\psi_W^j|\eta\rangle - \langle\psi_W^j|\tilde{\eta}\rangle\right)|\psi_W^j\rangle.\end{aligned} \tag{B.6}$$

Bibliography

[1] L. Holicki, E.-M. Ilgenfritz and L. von Smekal, *The Anderson transition in QCD with $N_f = 2 + 1 + 1$ twisted mass quarks: overlap analysis*, `1810.01130`. (Cited on page vii.)

[2] L. Holicki, J. Wilhelm, B. Wellegehausen, D. Smith and L. von Smekal, *Continuum Goldstone spectrum of two-colour QCD at finite density with staggered quarks*, *In preparation* (2017) . (Cited on page vii.)

[3] L. Holicki, J. Wilhelm, D. Smith, B. Wellegehausen and L. von Smekal, *Two-colour QCD at finite density with two flavours of staggered quarks*, *PoS* **LATTICE2016** (2017) 052, [`1701.04664`]. (Cited on pages vii, 93, and 101.)

[4] T. Blum, A. Denig, I. Logashenko, E. de Rafael, B. L. Roberts, T. Teubner et al., *The Muon (g-2) Theory Value: Present and Future*, `1311.2198`. (Cited on page 1.)

[5] P. W. Higgs, *Spontaneous Symmetry Breakdown without Massless Bosons*, *Phys. Rev.* **145** (1966) 1156–1163. (Cited on page 1.)

[6] D. J. Gross and F. Wilczek, *Ultraviolet behavior of non-abelian gauge theories*, *Phys. Rev. Lett.* **30** (Jun, 1973) 1343–1346. (Cited on page 1.)

[7] H. D. Politzer, *Reliable perturbative results for strong interactions?*, *Phys. Rev. Lett.* **30** (Jun, 1973) 1346–1349. (Cited on page 1.)

[8] S. Scherer, *Introduction to chiral perturbation theory*, *Adv. Nucl. Phys.* **27** (2003) 277, [`hep-ph/0210398`]. (Cited on page 1.)

[9] T. Matsui, *Quest for the quark gluon plasma*, *Prog. Theor. Phys. Suppl.* **151** (2003) 11–20, [`nucl-th/0305096`]. (Cited on page 2.)

[10] S. Borsányi, Z. Fodor, C. Hoelbling, S. D. Katz, S. Krieg, C. Ratti et al., *Is there still any Tc mystery in lattice QCD? Results with physical masses in the continuum limit III*, *Journal of High Energy Physics* **2010** (Sep, 2010) 73. (Cited on page 2.)

[11] M. G. Alford, A. Schmitt, K. Rajagopal and T. Schäfer, *Color superconductivity in dense quark matter*, *Rev. Mod. Phys.* **80** (2008) 1455–1515, [`0709.4635`]. (Cited on page 2.)

[12] ALICE collaboration, *ALICE: Physics Performance Report, Volume II*, *Journal of Physics G: Nuclear and Particle Physics* **32** (2006) 1295. (Cited on page 2.)

[13] L. Kumar, *STAR Results from the RHIC Beam Energy Scan-I*, *Nuclear Physics A* **904-905** (2013) 256c – 263c. (Cited on page 2.)

[14] A. Kovalenko, V. Kekelidze, R. Lednicky, V. Matveev, I. Meshkov, A. Sorin et al., *Status of the NICA project at JINR*, *EPJ Web of Conferences* **191** (01, 2018) 01003. (Cited on page 2.)

[15] CBM collaboration, P. Senger, *QCD Matter Physics at FAIR*, *Nucl. Phys.* **A967** (2017) 892–895. (Cited on page 2.)

[16] Z. Fodor and C. Hoelbling, *Light hadron masses from lattice qcd*, *Rev. Mod. Phys.* **84** (Apr, 2012) 449–495. (Cited on page 2.)

[17] M. Constantinou, *Hadron Structure*, *PoS* **LATTICE2014** (2015) 001, [`1411.0078`]. (Cited on page 2.)

[18] A. Nicholson, E. Berkowitz, E. Rinaldi, P. Vranas, T. Kurth, B. Joo et al., *Two-nucleon scattering in multiple partial waves*, *PoS* **LATTICE2015** (2016) 083, [`1511.02262`]. (Cited on page 2.)

[19] E. Megias, E. Ruiz Arriola and L. L. Salcedo, *Polyakov loop in chiral quark models at finite temperature*, *Phys. Rev.* **D74** (2006) 065005, [`hep-ph/0412308`]. (Cited on page 3.)

[20] C. Ratti, M. A. Thaler and W. Weise, *Phases of QCD: Lattice thermodynamics and a field theoretical model*, *Phys. Rev.* **D73** (2006) 014019, [`hep-ph/0506234`]. (Cited on page 3.)

[21] B.-J. Schaefer, J. M. Pawlowski and J. Wambach, *The Phase Structure of the Polyakov–Quark-Meson Model*, *Phys. Rev.* **D76** (2007) 074023, [`0704.3234`]. (Cited on page 3.)

[22] N. Strodthoff, B.-J. Schaefer and L. von Smekal, *Quark-meson-diquark model for two-color QCD*, *Phys. Rev.* **D85** (2012) 074007, [`1112.5401`]. (Cited on pages 3, 91, and 92.)

[23] N. Strodthoff and L. von Smekal, *Polyakov-Quark-Meson-Diquark Model for two-color QCD*, *Phys. Lett.* **B731** (2014) 350–357, [`1306.2897`]. (Cited on pages 3 and 92.)

[24] H. Sanchis-Alepuz and R. Williams, *Recent developments in bound-state calculations using the Dyson-Schwinger and Bethe-Salpeter equations*, `1710.04903`. (Cited on page 3.)

[25] C. S. Fischer, *QCD at finite temperature and chemical potential from Dyson-Schwinger equations*, *Prog. Part. Nucl. Phys.* **105** (2019) 1–60, [`1810.12938`]. (Cited on page 3.)

[26] G. Aarts, F. Attanasio, B. Jäger and D. Sexty, *Complex Langevin in Lattice QCD: dynamic stabilisation and the phase diagram*, *Acta Phys. Polon. Supp.* **9** (2016) 621, [`1607.05642`]. (Cited on page 3.)

[27] E. Seiler, *Status of Complex Langevin*, *EPJ Web Conf.* **175** (2018) 01019, [`1708.08254`]. (Cited on pages 3 and 19.)

[28] AuroraScience collaboration, M. Cristoforetti, F. Di Renzo and L. Scorzato, *New approach to the sign problem in quantum field theories: High density QCD on a Lefschetz thimble*, *Phys. Rev.* **D86** (2012) 074506, [`1205.3996`]. (Cited on page 3.)

[29] M. Cristoforetti, L. Scorzato and F. Di Renzo, *The sign problem and the Lefschetz thimble*, `1210.8026`. (Cited on page 3.)

[30] C.-N. Yang and R. L. Mills, *Conservation of Isotopic Spin and Isotopic Gauge Invariance*, *Phys. Rev.* **96** (1954) 191–195. (Cited on page 3.)

[31] M. Asakawa, T. Hatsuda and Y. Nakahara, *Maximum entropy analysis of the spectral functions in lattice QCD*, *Prog. Part. Nucl. Phys.* **46** (2001) 459–508, [`hep-lat/0011040`]. (Cited on page 4.)

[32] P. Petreczky, A. Rothkopf and J. Weber, *Realistic in-medium heavy-quark potential from high statistics lattice QCD simulations*, *Nucl. Phys.* **A982** (2019) 735–738, [`1810.02230`]. (Cited on page 4.)

[33] G. Münster and I. Montway, *Quantum Fields on a Lattice.* Cambridge University Press, 1994. (Cited on page 5.)

[34] C. Gattringer and C. Lang, *Quantum Chromodynamics on the Lattice - An Introductory Presentation.* Springer, Berlin Heidelberg, 2010. (Cited on page 5.)

[35] M. A. Clark, *The Rational Hybrid Monte Carlo Algorithm.* PhD thesis, The University of Edinburgh, 2005. (Cited on pages 5, 10, 18, and 128.)

[36] O. Philipsen, *Lattice QCD at non-zero temperature and baryon density*, in *Modern perspectives in lattice QCD: Quantum field theory and high performance computing. Proceedings, International School, 93rd Session, Les Houches, France, August 3-28, 2009*, pp. 273–330, 2010. `1009.4089`. (Cited on pages 5 and 11.)

[37] F. Karsch, *Lattice QCD at high temperature and density*, *Lect. Notes Phys.* **583** (2002) 209–249, [`hep-lat/0106019`]. (Cited on page 5.)

[38] K. G. Wilson, *Confinement of Quarks*, *Phys. Rev.* **D10** (1974) 2445–2459. (Cited on page 6.)

[39] K. Symanzik, *Continuum Limit and Improved Action in Lattice Theories. 1. Principles and phi**4 Theory*, *Nucl. Phys.* **B226** (1983) 187–204. (Cited on page 6.)

[40] K. Symanzik, *Continuum Limit and Improved Action in Lattice Theories. 2. O(N) Nonlinear Sigma Model in Perturbation Theory*, *Nucl. Phys.* **B226** (1983) 205–227. (Cited on page 6.)

[41] S. Belforte, G. Curci, P. Menotti and G. P. Paffuti, *Monte Carlo Calculations With Symanzik's Improved Action for QCD*, *Phys. Lett.* **131B** (1983) 423–424. (Cited on page 6.)

[42] B. Berg, A. Billoire, S. Meyer and C. Panagiotakopoulos, *SU(2) Lattice Gauge Theory: Standard Action Versus Symanzik's Tree Improved Action*, *Commun. Math. Phys.* **97** (1985) 31. (Cited on page 6.)

[43] W. Unger, *The Chiral Phase Transition of QCD with 2 + 1 Flavors*, . (Cited on pages 6 and 102.)

[44] D. Scheffler, *Two-Color Lattice QCD with Staggered Quarks.* PhD thesis, TU Darmstadt, 2015. (Cited on pages 6, 18, and 97.)

[45] P. Weisz and R. Wohlert, *Continuum limit improved lattice action for pure Yang-Mills theory (II)*, *Nuclear Physics, Section B* **236** (1984) 397–422. (Cited on page 6.)

[46] B. Beinlich, F. Karsch and E. Laermann, *Improved actions for QCD thermodynamics on the lattice*, *Nucl. Phys.* **B462** (1996) 415–436, [`hep-lat/9510031`]. (Cited on page 6.)

[47] S. Aoki, M. Fukugita, S. Hashimoto, K. I. Ishikawa, N. Ishizuka, Y. Iwasaki et al., *Bulk first-order phase transition in three-flavor lattice QCD with O(a)-improved Wilson fermion action at zero temperature*, *Physical Review D - Particles, Fields, Gravitation and Cosmology* **72** (2005) 1–9, [`0409016`]. (Cited on page 6.)

[48] Y. Iwasaki, *Renormalization group analysis of lattice theories and improved lattice action: Two-dimensional non-linear O(N) sigma model*, *Nucl. Phys.* **B258** (1985) 141–156. (Cited on page 7.)

[49] Y. Iwasaki, *Renormalization Group Analysis of Lattice Theories and Improved Lattice Action. II. Four-dimensional non-Abelian SU(N) gauge model*, `1111.7054`. (Cited on page 7.)

[50] S. Ejiri, K. Kanaya, Y. Namekawa and T. Umeda, *Renormalization-group-improved action on anisotropic lattices*, *Phys. Rev. D* **68** (Jul, 2003) 014502. (Cited on page 7.)

[51] R. Sommer, *A New way to set the energy scale in lattice gauge theories and its applications to the static force and alpha-s in SU(2) Yang-Mills theory*, *Nucl. Phys.* **B411** (1994) 839–854, [`hep-lat/9310022`]. (Cited on page 8.)

[52] H. Nielsen and M. Ninomiya, *Absence of neutrinos on a lattice: (i). proof by homotopy theory*, *Nuclear Physics B* **185** (1981) 20 – 40. (Cited on page 9.)

[53] J. Kogut and L. Susskind, *Hamiltonian formulation of Wilson's lattice gauge theories*, *Phys. Rev. D* **11** (January, 1975) 395–408. (Cited on page 10.)

[54] R. V. Gavai, *Chemical Potential on the Lattice Revisited*, *Phys. Rev.* **D32** (1985) 519. (Cited on page 11.)

[55] N. Bilic and R. V. Gavai, *On the Thermodynamics of an Ideal Fermi Gas on the Lattice at Finite Density*, *Z. Phys.* **C23** (1984) 77. (Cited on page 11.)

[56] S. Hands, J. B. Kogut, M.-P. Lombardo and S. E. Morrison, *Symmetries and spectrum of SU(2) lattice gauge theory at finite chemical potential*, *Nucl. Phys.* **B558** (1999) 327–346, [`hep-lat/9902034`]. (Cited on pages 11 and 91.)

[57] S. Hands, P. Sitch and J.-I. Skullerud, *Hadron Spectrum in a Two-Colour Baryon-Rich Medium*, *Phys. Lett.* **B662** (2008) 405–412, [`0710.1966`]. (Cited on pages 11, 19, and 91.)

[58] S. Hands, S. Cotter, P. Giudice and J.-I. Skullerud, *The Phase Diagram of Two Color QCD*, `1210.6559`. (Cited on pages 11 and 91.)

[59] P. T. Matthews and A. Salam, *Propagators of quantized field*, *Il Nuovo Cimento (1955-1965)* **2** (Jul, 1955) 120. (Cited on page 12.)

[60] V. Weinberg, *Untersuchung der Struktur des QCD-Vakuums mit Hilfe von Overlap-Fermionen.* PhD thesis, Freie Universität Berlin, 2007. (Cited on pages 12 and 134.)

[61] J. J. M. Verbaarschot and T. Wettig, *Random matrix theory and chiral symmetry in QCD*, *Ann. Rev. Nucl. Part. Sci.* **50** (2000) 343–410, [`hep-ph/0003017`]. (Cited on pages 12 and 24.)

[62] A. Yu. Kotov, M. P. Lombardo and A. M. Trunin, *Fate of the η' in the Quark Gluon Plasma*, `1903.05633`. (Cited on page 12.)

[63] T. Banks and A. Casher, *Chiral Symmetry Breaking in Confining Theories*, *Nucl. Phys.* **B169** (1980) 103–125. (Cited on page 13.)

[64] P. H. Ginsparg and K. G. Wilson, *A Remnant of Chiral Symmetry on the Lattice*, *Phys. Rev.* **D25** (1982) 2649. (Cited on page 13.)

[65] P. Hasenfratz, *Prospects for perfect actions*, *Nucl. Phys. Proc. Suppl.* **63** (1998) 53–58, [`hep-lat/9709110`]. (Cited on page 13.)

[66] D. B. Kaplan, *A Method for simulating chiral fermions on the lattice*, *Phys. Lett.* **B288** (1992) 342–347, [`hep-lat/9206013`]. (Cited on page 14.)

[67] K. Jansen, *Domain wall fermions and chiral gauge theories*, *Physics Report* **273** (1996) 1–54, [`9410018`]. (Cited on page 14.)

[68] D. B. Kaplan, *Chiral Symmetry and Lattice Fermions*, in *Modern perspectives in lattice QCD: Quantum field theory and high performance computing. Proceedings, International School, 93rd Session, Les Houches, France, August 3-28, 2009*, pp. 223–272, 2009. `0912.2560`. (Cited on page 14.)

[69] HotQCD collaboration, A. Bazavov et al., *The chiral transition and $U(1)_A$ symmetry restoration from lattice QCD using Domain Wall Fermions*, *Phys. Rev.* **D86** (2012) 094503, [`1205.3535`]. (Cited on page 14.)

[70] V. Furman and Y. Shamir, *Axial symmetries in lattice QCD with Kaplan fermions*, *Nucl. Phys.* **B439** (1995) 54–78, [`hep-lat/9405004`]. (Cited on page 15.)

[71] RBC collaboration, C. Dawson, *Dynamical domain wall fermions*, *Nucl. Phys. Proc. Suppl.* **128** (2004) 54–58, [`hep-lat/0310055`]. (Cited on page 16.)

[72] D. J. Antonio et al., *First results from 2+1-flavor domain wall QCD: Mass spectrum, topology change, and chiral symmetry with Ls=8*, *Phys. Rev. D* **75** (2007) , [`0612005`]. (Cited on page 16.)

[73] H. Neuberger, *Exactly massless quarks on the lattice*, *Phys. Lett.* **B417** (1998) 141–144, [`hep-lat/9707022`]. (Cited on page 16.)

[74] H. Neuberger, *More about exactly massless quarks on the lattice*, *Phys. Lett.* **B427** (1998) 353–355, [`hep-lat/9801031`]. (Cited on page 16.)

[75] H. Neuberger, *An Introduction to lattice chiral fermions*, in *QCD and numerical analysis III. Proceedings, 3rd International Workshop, Edinburgh, UK, June 30-July 4, 2003*, pp. 3–13, 2003. `hep-lat/0311040`. (Cited on page 16.)

[76] S. Capitani, M. Gockeler, R. Horsley, P. E. L. Rakow and G. Schierholz, *Operator improvement for Ginsparg-Wilson fermions*, *Phys. Lett.* **B468** (1999) 150–160, [`hep-lat/9908029`]. (Cited on page 16.)

[77] D. H. Adams, *Theoretical foundation for the Index Theorem on the lattice with staggered fermions*, *Phys. Rev. Lett.* **104** (2010) 141602, [`0912.2850`]. (Cited on page 16.)

[78] D. H. Adams, *Pairs of chiral quarks on the lattice from staggered fermions*, *Phys. Lett.* **B699** (2011) 394–397, [`1008.2833`]. (Cited on page 16.)

[79] S. Meyn and R. Tweedie, *Markov chains and stochastic stability.* Springer-Verlag, London, 1993. (Cited on page 17.)

[80] J. R. Shewchuk, *An introduction to the conjugate gradient method without the agonizing pain*, tech. rep., Pittsburgh, PA, USA, 1994. (Cited on pages 19 and 128.)

[81] B. Jegerlehner, *Krylov space solvers for shifted linear systems*, *Physics* (1996) 16, [`9612014`]. (Cited on pages 19 and 128.)

[82] B. Jegerlehner, *Multiple mass solvers*, *Nuclear Physics B (Proceedings Supplements)* (1998) 1–3, [`9708029`]. (Cited on pages 19 and 128.)

[83] G. Parisi, *On complex probabilities*, *Phys. Lett.* **131B** (1983) 393–395. (Cited on page 19.)

[84] J. R. Klauder, *Stochastic quantization*, *Acta Phys. Austriaca Suppl.* **25** (1983) 251–281. (Cited on page 19.)

[85] S. Hands, I. Montvay, S. Morrison, M. Oevers, L. Scorzato and J. Skullerud, *Numerical study of dense adjoint matter in two color QCD*, *Eur. Phys. J.* **C17** (2000) 285–302, [`hep-lat/0006018`]. (Cited on pages 19 and 91.)

[86] J. Kogut, M. Stephanov, D. Toublan, J. Verbaarschot and A. Zhitnitsky, *Qcd-like theories at finite baryon density*, *Nuclear Physics B* **582** (2000) 477 – 513. (Cited on pages 19 and 99.)

[87] S. Hands, S. Kim and J.-I. Skullerud, *Deconfinement in dense 2-color QCD*, *Eur. Phys. J.* **C48** (2006) 193, [`hep-lat/0604004`]. (Cited on pages 19 and 91.)

[88] M. Pepe and U. J. Wiese, *Exceptional Deconfinement in G(2) Gauge Theory*, *Nucl. Phys.* **B768** (2007) 21–37, [`hep-lat/0610076`]. (Cited on page 19.)

[89] B. H. Wellegehausen, A. Maas, A. Wipf and L. von Smekal, *Hadron masses and baryonic scales in G_2-QCD at finite density*, *Phys. Rev.* **D89** (2014) 056007, [`1312.5579`]. (Cited on page 19.)

[90] M. Albanese, F. Costantini, G. Fiorentini, F. Flore, M. Lombardo, R. Tripiccione et al., *Glueball masses and string tension in lattice qcd*, *Physics Letters B* **192** (1987) 163 – 169. (Cited on page 20.)

[91] A. Hasenfratz and F. Knechtli, *Flavor symmetry and the static potential with hypercubic blocking*, *Phys. Rev.* **D64** (2001) 034504, [`hep-lat/0103029`]. (Cited on page 20.)

[92] A. Hasenfratz, R. Hoffmann and F. Knechtli, *The Static potential with hypercubic blocking*, *Nucl. Phys. Proc. Suppl.* **106** (2002) 418–420, [`hep-lat/0110168`]. (Cited on page 20.)

[93] C. Morningstar and M. J. Peardon, *Analytic smearing of SU(3) link variables in lattice QCD*, *Phys. Rev.* **D69** (2004) 054501, [`hep-lat/0311018`]. (Cited on page 20.)

[94] S. Durr, *Gauge action improvement and smearing*, *Comput. Phys. Commun.* **172** (2005) 163–186, [`hep-lat/0409141`]. (Cited on pages 20 and 79.)

[95] J. M. Pawlowski, I.-O. Stamatescu and F. P. G. Ziegler, *Cooling Stochastic Quantization with colored noise*, *Phys. Rev.* **D96** (2017) 114505, [`1705.06231`]. (Cited on page 20.)

[96] M. Lüscher, *Properties and uses of the Wilson flow in lattice QCD*, *JHEP* **08** (2010) 071, [`1006.4518`]. (Cited on pages 20, 21, 23, and 64.)

[97] M. Lüscher and P. Weisz, *Perturbative analysis of the gradient flow in non-abelian gauge theories*, *JHEP* **02** (2011) 051, [`1101.0963`]. (Cited on page 20.)

[98] M. Lüscher, *Future applications of the Yang-Mills gradient flow in lattice QCD*, *PoS* **LATTICE2013** (2014) 016, [`1308.5598`]. (Cited on page 20.)

[99] M. Luscher, *Chiral symmetry and the Yang–Mills gradient flow*, *JHEP* **04** (2013) 123, [`1302.5246`]. (Cited on page 20.)

[100] S. Borsanyi et al., *High-precision scale setting in lattice QCD*, *JHEP* **09** (2012) 010, [`1203.4469`]. (Cited on pages 24 and 64.)

[101] J. Goldstone, A. Salam and S. Weinberg, *Broken Symmetries*, *Phys. Rev.* **127** (1962) 965–970. (Cited on page 24.)

[102] M. L. Mehta, *Random matrices.* Elsevier Academic Press, 3rd editio ed., 2004. (Cited on page 24.)

[103] T. Guhr, A. Muller-Groeling and H. A. Weidenmuller, *Random matrix theories in quantum physics: Common concepts*, *Phys. Rept.* **299** (1998) 189–425, [`cond-mat/9707301`]. (Cited on page 25.)

[104] M. Catillo and L. Ya. Glozman, *Distribution of the Dirac modes in QCD*, in *35th International Symposium on Lattice Field Theory (Lattice 2017) Granada, Spain, June 18-24, 2017*, 2017. `1707.07055`. (Cited on page 25.)

[105] P. W. Anderson, *Absence of diffusion in certain random lattices*, *Phys. Rev.* **109** (Mar, 1958) 1492–1505. (Cited on page 26.)

[106] B. Kramer and A. MacKinnon, *Localization: theory and experiment*, *Reports on Progress in Physics* **56** (dec, 1993) 1469–1564. (Cited on page 26.)

[107] K. Slevin and T. Ohtsuki, *The anderson transition: Time reversal symmetry and universality*, *Phys. Rev. Lett.* **78** (May, 1997) 4083–4086. (Cited on pages 27 and 34.)

[108] S. N. Evangelou and D. E. Katsanos, *Energy level statistics in disordered metals with an anderson transition*, *Journal of Statistical Physics* **85** (Dec, 1996) 525–550. (Cited on page 27.)

[109] P. Markos, *Absence of diffusion in certain random lattices: Numerical evidence*, *ArXiv e-prints* (July, 2008) , [`0807.2531`]. (Cited on page 27.)

[110] J. Fröhlich and T. Spencer, *A rigorous approach to anderson localization*, *Physics Reports* **103** (1984) 9 – 25. (Cited on page 27.)

[111] L. Ujfalusi and I. Varga, *Finite-size scaling and multifractality at the Anderson transition for the three Wigner-Dyson symmetry classes in three dimensions*, *Physical Review B* **91** (May, 2015) 184206, [`1501.02147`]. (Cited on page 27.)

[112] W. E. Arnoldi, *The Principle of Minimized Iterations in the Solution of the Matrix Eigenvalue Problem*, *Quarterly of Applied Mathematics* **9** (1951) 17–29. (Cited on page 29.)

[113] Lehoucq, R. B. and Sorensen, D. C. and Yang, C., *APRACK users' guide: Solution of large scale eigenvalue problems with implicitly restarted Arnoldi methods.* 1997. (Cited on page 29.)

[114] F. Burger, G. Hotzel, M. Müller-Preussker, E.-M. Ilgenfritz and M. P. Lombardo, *Towards thermodynamics with $N_f = 2 + 1 + 1$ twisted mass quarks*, *PoS* **Lattice2013** (2013) 153, [`1311.1631`]. (Cited on page 29.)

[115] F. Burger, E.-M. Ilgenfritz, M. P. Lombardo, M. Muller-Preussker and A. Trunin, *Towards the quark–gluon plasma Equation of State with dynamical strange and charm quarks*, *J. Phys. Conf. Ser.* **668** (2016) 012092, [`1510.02262`]. (Cited on pages 29, 30, 33, 40, 45, and 115.)

[116] F. Burger, E.-M. Ilgenfritz, M. P. Lombardo and A. Trunin, *Chiral observables and topology in hot QCD with two families of quarks*, *Phys. Rev.* **D98** (2018) 094501, [`1805.06001`]. (Cited on page 29.)

[117] ETM collaboration, R. Baron et al., *Status of ETMC simulations with N(f) = 2+1+1 twisted mass fermions*, *PoS* **LATTICE2008** (2008) 094, [`0810.3807`]. (Cited on page 29.)

[118] ETM collaboration, R. Baron et al., *First results of ETMC simulations with N(f) = 2+1+1 maximally twisted mass fermions*, *PoS* **LAT2009** (2009) 104, [`0911.5244`]. (Cited on page 29.)

[119] R. Baron et al., *Light hadrons from lattice QCD with light (u,d), strange and charm dynamical quarks*, *JHEP* **06** (2010) 111, [`1004.5284`]. (Cited on page 29.)

[120] ETM collaboration, R. Baron et al., *Light hadrons from Nf=2+1+1 dynamical twisted mass fermions*, *PoS* **LATTICE2010** (2010) 123, [`1101.0518`]. (Cited on page 29.)

[121] C. Alexandrou, V. Drach, K. Jansen, C. Kallidonis and G. Koutsou, *Baryon spectrum with* $N_f = 2 + 1 + 1$ *twisted mass fermions*, *Phys. Rev.* **D90** (2014) 074501, [`1406.4310`]. (Cited on page 29.)

[122] R. Frezzotti and G. C. Rossi, *Twisted mass lattice QCD with mass nondegenerate quarks*, *Nucl. Phys. Proc. Suppl.* **128** (2004) 193–202, [`hep-lat/0311008`]. (Cited on page 29.)

[123] M. Giordano, T. G. Kovacs and F. Pittler, *Universality and the QCD Anderson Transition*, *Phys. Rev. Lett.* **112** (2014) 102002, [`1312.1179`]. (Cited on pages 34 and 60.)

[124] M. Giordano, S. D. Katz, T. G. Kovacs and F. Pittler, *The chiral transition as an Anderson transition*, *PoS* **LATTICE2014** (2014) 214, [`1410.8392`]. (Cited on pages 34 and 41.)

[125] S. M. Nishigaki, M. Giordano, T. G. Kovacs and F. Pittler, *Critical statistics at the mobility edge of QCD Dirac spectra*, *PoS* **LATTICE2013** (2014) 018, [`1312.3286`]. (Cited on page 34.)

[126] T. G. Kovacs and F. Pittler, *Poisson to Random Matrix Transition in the QCD Dirac Spectrum*, *Phys. Rev.* **D86** (2012) 114515, [`1208.3475`]. (Cited on pages 35 and 60.)

[127] L. Ujfalusi, M. Giordano, F. Pittler, T. G. Kovács and I. Varga, *Anderson transition and multifractals in the spectrum of the Dirac operator of Quantum Chromodynamics at high temperature*, *Phys. Rev.* **D92** (2015) 094513, [`1507.02162`]. (Cited on pages 42 and 58.)

[128] F. Bruckmann, T. G. Kovacs and S. Schierenberg, *Anderson localization through Polyakov loops: lattice evidence and Random matrix model*, *Phys. Rev.* **D84** (2011) 034505, [`1105.5336`]. (Cited on pages 63 and 118.)

[129] M. Giordano, T. G. Kovacs and F. Pittler, *An Ising-Anderson model of localisation in high-temperature QCD*, *JHEP* **04** (2015) 112, [`1502.02532`]. (Cited on page 63.)

[130] G. Cossu and S. Hashimoto, *Anderson Localization in high temperature QCD: background configuration properties and Dirac eigenmodes*, *JHEP* **06** (2016) 056, [`1604.00768`]. (Cited on page 63.)

[131] T. Schäfer and E. V. Shuryak, *Instantons in QCD*, *Rev. Mod. Phys.* **70** (1998) 323–426, [`hep-ph/9610451`]. (Cited on pages 75 and 77.)

[132] R. D. Peccei and H. R. Quinn, *CP Conservation in the Presence of Instantons*, *Phys. Rev. Lett.* **38** (1977) 1440–1443. (Cited on page 75.)

[133] R. D. Peccei and H. R. Quinn, *Constraints Imposed by CP Conservation in the Presence of Instantons*, *Phys. Rev.* **D16** (1977) 1791–1797. (Cited on page 75.)

[134] J. M. Pendlebury et al., *Revised experimental upper limit on the electric dipole moment of the neutron*, *Phys. Rev.* **D92** (2015) 092003, [`1509.04411`]. (Cited on page 76.)

[135] CP-PACS collaboration, A. Ali Khan et al., *Topological susceptibility in lattice QCD with two flavors of dynamical quarks*, *Phys. Rev.* **D64** (2001) 114501, [`hep-lat/0106010`]. (Cited on page 76.)

[136] D. Diakonov and V. Yu. Petrov, *A Theory of Light Quarks in the Instanton Vacuum*, *Nucl. Phys.* **B272** (1986) 457–489. (Cited on page 77.)

[137] E. V. Shuryak, *Correlation functions in the qcd vacuum*, *Rev. Mod. Phys.* **65** (Jan, 1993) 1–46. (Cited on page 77.)

[138] P. Gerhold, E. M. Ilgenfritz and M. Muller-Preussker, *An SU(2) KvBLL caloron gas model and confinement*, *Nucl. Phys.* **B760** (2007) 1–37, [`hep-ph/0607315`]. (Cited on page 77.)

[139] A. M. Garcia-Garcia and J. C. Osborn, *Chiral phase transition as an Anderson transition in the instanton liquid model for QCD*, *PoS* **LAT2005** (2006) 265, [`hep-lat/0509118`]. (Cited on page 77.)

[140] A. M. Garcia-Garcia and J. C. Osborn, *Chiral phase transition and anderson localization in the instanton liquid model for QCD*, *Nucl. Phys.* **A770** (2006) 141–161, [`hep-lat/0512025`]. (Cited on page 77.)

[141] A. M. Garcia-Garcia and J. C. Osborn, *Chiral phase transition in lattice QCD as a metal-insulator transition*, *Phys. Rev.* **D75** (2007) 034503, [`hep-lat/0611019`]. (Cited on page 77.)

[142] S. Durr, Z. Fodor, C. Hoelbling and T. Kurth, *Precision study of the SU(3) topological susceptibility in the continuum*, *JHEP* **04** (2007) 055, [`hep-lat/0612021`]. (Cited on page 79.)

[143] UKQCD COLLABORATION collaboration, D. A. Smith and M. J. Teper, *Topological structure of the su(3) vacuum*, *Phys. Rev. D* **58** (May, 1998) 014505. (Cited on page 85.)

[144] A. Athenodorou, P. Boucaud, F. De Soto, J. Rodríguez-Quintero and S. Zafeiropoulos, *Instanton liquid properties from lattice QCD*, *JHEP* **02** (2018) 140, [`1801.10155`]. (Cited on page 85.)

[145] E.-M. Ilgenfritz, K. Koller, Y. Koma, G. Schierholz and V. Weinberg, *Topological Structure of the QCD Vacuum Revealed by Overlap Fermions*, in *Proceedings, 4th Joint HLRB and KONWIHR Review and Results Workshop: Garching, Germany, December 8-9, 2009*, pp. 475–487, 2010. `0912.2281`. DOI. (Cited on page 85.)

[146] S. Morrison and S. Hands, *Two colors QCD at nonzero chemical potential*, in *Strong and electroweak matter '98. Proceedings, Conference, SEWM'98, Copenhagen, Denmark, December 2-5, 1998*, pp. 364–368, 1998. `hep-lat/9902012`. (Cited on page 91.)

[147] S. J. Hands, B. Kogut, S. E. Morrison and D. K. Sinclair, *Two-color QCD at finite fundamental quark number density and related theories*, *Nucl. Phys. Proc. Suppl.* **94** (2001) 457–460, [`hep-lat/0010028`]. (Cited on page 91.)

[148] J. B. Kogut, D. Toublan and D. K. Sinclair, *Diquark condensation at nonzero chemical potential and temperature*, *Phys. Lett.* **B514** (2001) 77–87, [`hep-lat/0104010`]. (Cited on pages 91 and 93.)

[149] T. Boz, P. Giudice, S. Hands, J.-I. Skullerud and A. G. Williams, *Two-color QCD at high density*, *AIP Conf. Proc.* **1701** (2016) 060019, [`1502.01219`]. (Cited on pages 91 and 93.)

[150] N. Yu. Astrakhantsev, V. G. Bornyakov, V. V. Braguta, E. M. Ilgenfritz, A. Yu. Kotov, A. A. Nikolaev et al., *Lattice study of static quark-antiquark interactions in dense quark matter*, `1808.06466`. (Cited on page 91.)

[151] S. Hands, I. Montvay, M. Oevers, L. Scorzato and J. Skullerud, *Numerical study of dense adjoint 2 color matter*, *Nucl. Phys. Proc. Suppl.* **94** (2001) 461–468, [`hep-lat/0010085`]. (Cited on page 91.)

[152] V. G. Bornyakov, V. V. Braguta, E. M. Ilgenfritz, A. Yu. Kotov, A. V. Molochkov and A. A. Nikolaev, *Observation of deconfinement in a cold dense quark medium*, *JHEP* **03** (2018) 161, [`1711.01869`]. (Cited on page 91.)

[153] V. G. Bornyakov, V. V. Braguta, E. M. Ilgenfritz, A. Yu. Kotov, I. E. Kudrov, A. V. Molochkov et al., *Confinement-deconfinement transition in dense SU(2) QCD*, *EPJ Web Conf.* **175** (2018) 07009. (Cited on page 91.)

[154] N. Strodtoff, *Critical Phenomena in the Phase Diagrams of QCD-like theories*. PhD thesis, TU Darmstadt, 2013. (Cited on page 91.)

[155] T. D. . Cohen, *Functional integrals for QCD at nonzero chemical potential and zero density*, *Phys. Rev. Lett.* **91** (2003) 222001, [`hep-ph/0307089`]. (Cited on page 92.)

[156] T. D. Cohen, *QCD functional integrals for systems with nonzero chemical potential*, `hep-ph/0405043`. (Cited on page 92.)

[157] V. V. Braguta, E. M. Ilgenfritz, A. Yu. Kotov, A. V. Molochkov and A. A. Nikolaev, *Study of the phase diagram of dense two-color QCD within lattice simulation*, *Phys. Rev.* **D94** (2016) 114510, [`1605.04090`]. (Cited on pages 92, 93, and 101.)

[158] T. Kanazawa, T. Wettig and N. Yamamoto, *Singular values of the Dirac operator in dense QCD-like theories*, *JHEP* **12** (2011) 007, [`1110.5858`]. (Cited on page 94.)

[159] T. Kanazawa, T. Wettig and N. Yamamoto, *Banks-Casher-type relation for the BCS gap at high density*, *Eur. Phys. J.* **A49** (2013) 88, [`1211.5332`]. (Cited on page 94.)

[160] A. Deuzeman, M. P. Lombardo, T. Nunes Da Silva and E. Pallante, *The bulk transition of QCD with twelve flavors and the role of improvement*, *Phys. Lett.* **B720** (2013) 358–365, [`1209.5720`]. (Cited on page 94.)

[161] M. A. Halasz and J. J. M. Verbaarschot, *Universal fluctuations in spectra of the lattice dirac operator*, *Phys. Rev. Lett.* **74** (May, 1995) 3920–3923. (Cited on page 97.)

[162] J. B. Kogut, D. Toublan and D. K. Sinclair, *Pseudo goldstone spectrum of 2-color* QCD *at finite density*, *Phys. Rev. D* **68** (Sep, 2003) 054507. (Cited on pages 97 and 100.)

[163] D. Scheffler, C. Schmidt, D. Smith and L. von Smekal, *Chiral restoration and deconfinement in two-color QCD with two flavors of staggered quarks*, *PoS* **LATTICE2013** (2014) 191, [`1311.4324`]. (Cited on page 97.)

[164] K. Binder, *Finite size scaling analysis of ising model block distribution functions*, *Zeitschrift für Physik B Condensed Matter* **43** (Jun, 1981) 119–140. (Cited on page 107.)

[165] W. K. Hastings, *Monte Carlo sampling methods using Markov chains and their applications*, *Biometrika* **57** (04, 1970) 97–109. (Cited on page 123.)

[166] M. Creutz, *Monte Carlo Study of Quantized SU(2) Gauge Theory*, *Phys. Rev.* **D21** (1980) 2308–2315. (Cited on page 123.)

[167] J. R. Shewchuk, *An introduction to the conjugate gradient method without the agonizing pain*, 1994. (Cited on page 125.)

[168] S. A. Tawfik, *Minimax Approximation and Remez Algorithm*, 2005. (Cited on page 129.)

[169] J. Sexton and D. Weingarten, *Hamiltonian evolution for the hybrid monte carlo algorithm*, *Nuclear Physics B* **380** (1992) 665 – 677. (Cited on page 131.)

Acknowledgements

First of all I would like to thank my family for enduring my absence during the last few months, and my friends who endured my presence. You have been patient and understanding and I am grateful for all of your support.

I would further like to thank my fiancee Oxana, without whom I wouldn't have made it this far. I am grateful for you being in my life and I am excited for the new challenges we are going to face together.

I would like to express my gratitude Ernst-Michael Ilgenfritz for his prolonged support and patience, for our very fruitful collaboration, for being available to me at any time and for taking responsibility where he didn't have to. Thank you.

Finally I would like to thank Lorenz von Smekal for giving me the opportunity to dive into this project.